Titre: Title:	Beam Shaping and Beam Scanning of C-Band Circularly Polarized Dual Reflector Antenna Using Reconfigurable Subreflector
Auteur: Author:	Marzieh Mehri Dehnavi
Date:	2021
Type:	Mémoire ou thèse / Dissertation or Thesis
Référence: Citation:	Mehri Dehnavi, M. (2021). Beam Shaping and Beam Scanning of C-Band Circularly Polarized Dual Reflector Antenna Using Reconfigurable Subreflector [Thèse de doctorat, Polytechnique Montréal]. PolyPublie. https://publications.polymtl.ca/9930/

URL de PolyPublie: PolyPublie URL:	https://publications.polymtl.ca/9930/
Directeurs de recherche: Advisors:	Jean-Jacques Laurin
Programme: Program:	Génie électrique

POLYTECHNIQUE MONTRÉAL

affiliée à l'Université de Montréal

Beam shaping and beam scanning of C-band circularly polarized dual reflector antenna using reconfigurable subreflector

MARZIEH MEHRI DEHNAVI

Département de génie électrique

Thèse présentée en vue de l'obtention du diplôme de *Philosophiæ Doctor*

Génie électrique

Décembre 2021

POLYTECHNIQUE MONTRÉAL

affiliée à l'Université de Montréal

Cette thèse intitulée :

Beam shaping and beam scanning of C-band circularly polarized dual reflector antenna using reconfigurable subreflector

présentée par **Marzieh MEHRI DEHNAVI**

en vue de l'obtention du diplôme de *Philosophiæ Doctor*

a été dûment acceptée par le jury d'examen constitué de :

Christian CARDINAL, président

Jean-Jacques LAURIN, membre et directeur de recherche

Ke WU, membre

Abdel Razik SEBAK, membre externe

ACKNOWLEDGEMENTS

I would like to thank my supervisor Professor Jean-Jaques Laurin for his endless patience, inspiration, valuable advice, technical support during this research. He taught me how to conduct the research and he guided me to develop the ideas of this research. I could not have finished this thesis without his excellent supervision.

Also, I would like to thank Prof. Christian Cardinal, Prof. Ke Wu, and Prof. Abdel Razik Sebak for their time to read and evaluate my thesis.

In addition, I would like to thank the technicians at Poly-Grames Research Center, Jules Gauthier, Traian Antonescu, Steve Dube, Maxime Thibault, and Jean-Sebastien Decarie. Without their help, I could not have completed this project.

Finally, I would like to thank my colleagues at Poly-Grames Research Center, who were always there for me with countless help and constructive discussions.

I am continuously grateful to my family and friends for their support, love, and encouragement.

RÉSUMÉ

L'objectif général de ce projet est d'étudier des solutions pour réaliser la formation et le dépointage du faisceau pour les antennes satellites en vol. La plupart des satellites actuels ont des antennes à gain élevé conçues avec des réflecteurs paraboliques. Dans ces antennes, la reconfigurabilité est réalisée avec des structures mécaniques volumineuses (encombrant) et lentes, c'est-à-dire, avec des systèmes de cardan (support tournant) pour le dépointage du faisceau et la permutation du sous-réflecteur pour la formation du faisceau.

Dans ce projet, notre objectif est de proposer une antenne à double réflecteur avec une parabole principale et une surface réfléchissante périodique reconfigurable comme sous-réflecteur qui permettra une modulation spatiale de phase (appelée sous-réseau réflecteur).

Les avantages souhaités de l'antenne proposée par rapport aux systèmes existants seront la plus grande flexibilité de reconfigurabilité, c'est-à-dire permettant une couverture "arbitraire", une vitesse et une légèreté. Cependant, il existe de nombreux défis pour trouver une solution qui conservera les caractéristiques souhaitées des systèmes de réflecteurs existants, telles qu'une faible polarisation croisée, une bande passante suffisante, et une efficacité énergétique élevée.

De plus, le système d'antenne proposé devra fonctionner en polarisation circulaire pour répondre aux exigences des systèmes satellitaires modernes. Cela nécessitera la conception de cellules réflectrices spéciales. Les éléments passifs conçus pour être entraînés par des micromoteurs réalisant la technique de rotation variable pour atteindre un réglage de phase complet de 360° sont sélectionnés pour le sous-réflecteur. La structure proposée dans ce travail balaye et forme le faisceau avec le petit sous-réseau réflecteur sans utiliser d'éléments électroniques de formation de faisceau RF, ce qui conduit à avoir la structure avec moins de perte d'insertion et moins de circuit de polarisation en courant continu (CC).

Dans le système à double réflecteur proposé, le balayage du faisceau est fourni en appliquant les techniques de focalisation en champ proche (NFF) et de décalage de phase progressif (PPS). Dans la technique NFF, le balayage du faisceau est assuré en déplaçant la source virtuelle créée par le sous-réflecteur du point focal du réflecteur principal. En appliquant la technique PPS, le balayage du faisceau est fourni en appliquant un déphasage progressif sur la surface du réflecteur. La technique NFF présente certains avantages en termes de polarisation croisée plus faible et de plage

de balayage plus large par rapport à la technique PPS. Ce travail démontre expérimentalement la plage de balayage du faisceau jusqu'à ± 3 degrés en appliquant la technique NFF avec la parabole à ouverture elliptique comme réflecteur principal avec les diamètres projetés de 15.18λ et 10.11λ pour les axes majeur et mineur, respectivement. Les deux méthodes conduisent à un balayage à angle étroit, adapté aux applications géostationnaires telles que les services Internet à large bande par satellite, la radiodiffusion télévisuelle et radiophonique et les prévisions météorologiques.

De plus, la formation et le dépointage du faisceau du système proposé sont réalisées en appliquant la technique de synthèse de faisceau basée sur PSO (Particle Swarm Optimization). La performance de la méthode proposée pour la formation du faisceau est illustrée en comparant les résultats PSO obtenus par MATLAB avec ceux obtenus avec la simulation de l'ensemble du système dans FEKO en utilisant une solution hybride « Méthode des moments (MoM) et optique physique (PO) ». De plus, la capacité de dépointage du faisceau de l'algorithme proposé est confirmée en comparant les résultats PSO obtenus par MATLAB avec les résultats de balayage du faisceau fournis par la technique NFF. La capacité de mise en forme du faisceau de l'algorithme PSO proposé est démontrée expérimentalement en élargissant le faisceau par rapport au motif de référence le long des axes u et v par $\Delta v = +0.15$ et $\Delta u = +0.05$ et en balayant le faisceau de Δv = +0.05 le long de l'axe v dans le uv plan.

ABSTRACT

The general objective of this project is to study solutions to allow beam steering and beam shaping for in-flight satellite antennas. Most current satellites have high gain antennas designed with parabolic reflectors. In these antennas, reconfigurability is accomplished with bulky and slow mechanical structures, e.g. gimbal systems for beam steering and sub-reflector permutation for beam shaping.

In this project, our objective is to propose a dual-reflector antenna with a main parabolic dish and a reconfigurable periodic reflecting surface as the subreflector that will allow spatial phase modulation (so-called sub-reflectarray).

Desired advantages of the proposed antenna over existing systems will be the greater flexibility in reconfigurability, i.e. allowing "arbitrary" coverage, speed, and lightweight. However, there are many challenges to find a solution that will keep the desired features of existing reflector systems, such as low cross-polarization, sufficient frequency bandwidth, sustainability in the harsh space environment, and high power efficiency.

Furthermore, the antenna system proposed will have to operate in circular polarization to meet the requirement of modern satellite systems. This will require the design of special reflectarray cells. The passive elements with full phase adjustment of 360° using variable rotation technique are selected for the sub-reflectarray, which are designed to be driven by micromotors. The proposed structure in this work scans and shapes the beam with the small sub-reflectarray without using electronic RF beamformer elements, which leads to having the structure with less insertion loss and less DC biasing in the network.

In the proposed dual-reflector system, beam scanning is provided by applying Near-Field Focusing (NFF) and Progressive Phase Shift (PPS) techniques. In the NFF technique, beam scanning is provided by displacing the virtual source created by the subreflector from the focal point of the main reflector. By applying the PPS technique, beam scanning is provided by applying progressive phase shift on the reflectarray surface. NFF technique has some advantages in terms of lower cross-polarization and wider scanning range compared to the PPS technique. This work experimentally demonstrates the beam scanning range of up to ±3 degrees by applying the NFF technique with the

elliptical aperture dish as the main reflector with the projected diameters of 15.18λ and 10.11λ for the major and minor axes, respectively. Both methods lead to narrow-angle scanning, suitable for geostationary applications such as broadband satellite internet services, TV and radio broadcasting, and weather forecasting.

Furthermore, the beam shaping and beam steering of the proposed system are implemented by applying the PSO (Particle Swarm Optimization)-based beam synthesis technique. The performance of the proposed method in beam shaping is illustrated by comparing the PSO results obtained by MATLAB with those obtained with the simulation of the whole system in FEKO using a hybrid "Method of Moments (MoM) and Physics Optics (PO)" solution. Also, the beam steering capability of the proposed algorithm is confirmed by comparing the PSO results obtained by MATLAB with the beam scanning results provided by NFF technique. The beam shaping capability of the proposed PSO algorithm is experimentally demonstrated by widening the beam with respect to the reference pattern along the u and v axes by $\Delta v = +0.15$ and $\Delta u = +0.05$ and scanning the beam by $\Delta v = +0.05$ along the v axis in the uv plane.

TABLE OF CONTENTS

LIST OF TABLES

LIST OF FIGURES

LIST OF SYMBOLS AND ABBREVIATIONS

MEMS	Micro-Electro-Mechanical Systems
PSO	Particle Swarm Optimization
VNA	Vector network Analyzer
DoF	Depth of Focus (DoF)
FFT	Fast Fourier Transform
PMA	Projection Matrix Algorithm
GA	Genetic Algorithm
SLL	Sidelobe Level
RHCP	Right Hand Circularly Polarized
LHCP	Left Hand Circularly Polarized
CP	Circular Polarization
AR	Axial Ratio
SGH	Standard Gain Horn
SAR	Synthetic Aperture Radar (SAR)
NFF	Near-Field Focusing
BDF	Beam Deviation Factor
PPS	Progressive Phase Shift
XPD	Cross-Polarization Discrimination

HPBW	Half Power Beamwidth
CATR	Compact Antenna Test Range
MSE	Mean Square Error
SFPB	Single Feed Per Beam
MFPB	Multiple Feeds Per Beam
SFMB	Single Feed-Multiple Beam

LIST OF APPENDICES

CHAPTER 1 INTRODUCTION

1.1 Background and description

Antennas based on parabolic reflectors are well-known as high gain antennas. Dual-reflector antennas with a flat subreflector and main parabolic dish are considered in this work. These antennas with reduced overall antenna volume are sufficient for space applications [1]. The antennas with the main parabolic dish and small sub-reflectarray have different applications, including compensating the large reflector's surface error in space applications, narrow beam scanning, and contoured beam applications [1, 2]. The application of interest in this work is to reconfigure the earth coverage of geostationary communication antennas.

Dual-reflector antennas with the parabolic dish as the main reflector take advantage of the wideband property of the parabolic dish since the bandwidth is only limited by the small flat sub-reflectarray. Therefore, these antennas have wider bandwidth than the antennas having the reflectarray as the main reflector [1]. Moreover, antennas with a small sub-reflectarray are reconfigurable, are easy to manufacture, and benefit from the high gain property of their main reflector which is a parabolic reflector.

1.2 Performance objective

An electronic or mechanical approach could implement beam scanning out of dual-reflector antennas. The mechanical approach is typically realized by the mechanical movement of the subreflector [3], while the electronic approach is made by applying proper phase shift on the sub-reflectarray elements [4].

In [3], the beam scanning out of the dual-reflector structure is obtained by using a flat metal subreflector. As shown in Figure 1.1, the antenna is made up of an offset parabolic reflector with an aperture diameter of 120 mm (38λ) and a flat subreflector [1]. By tilting the metal subreflector about X_r axis in Figure 1.2a, the beam steerings of 2.5 and 5 degrees are obtained. As shown in

Figure 1.2b, the gain reductions of 0.15 dB and 1.35 dB are obtained for 2.5° and 5° beam steerings, respectively, in the azimuth plane [3].

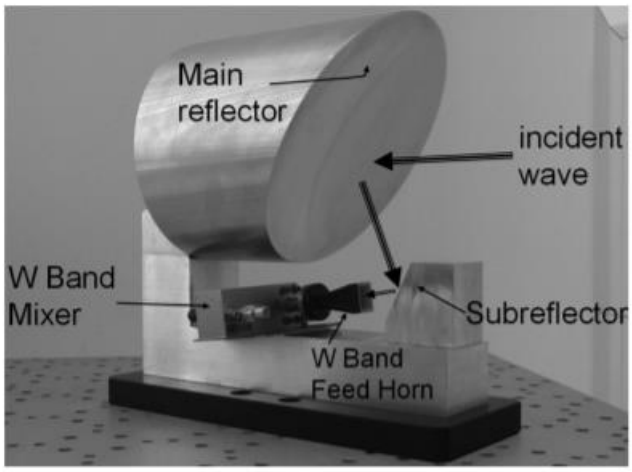

Figure 1.1 photograph of dual-reflector antenna ([3])

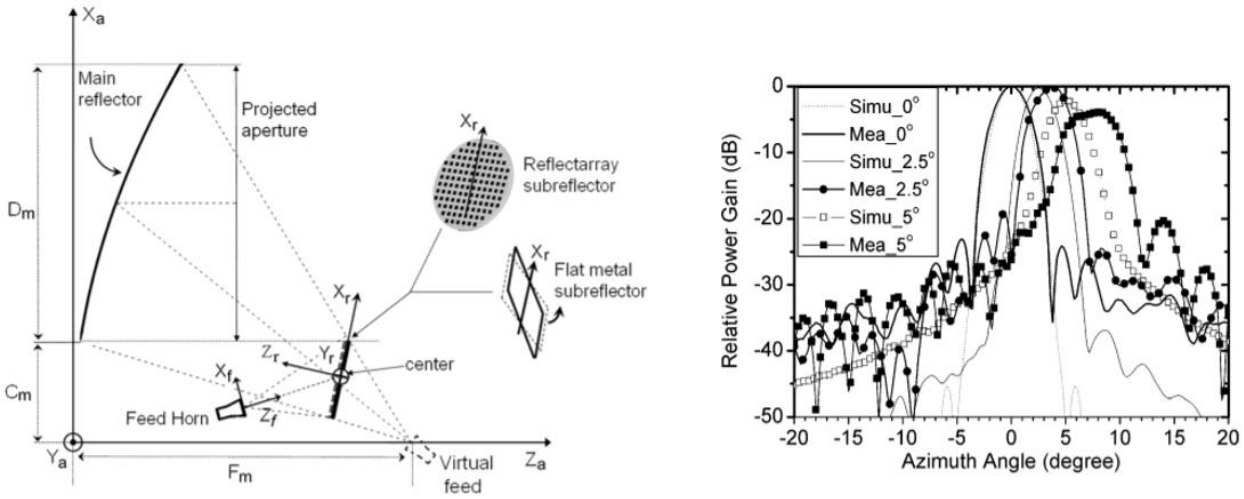

(a) (b)

Figure 1.2 (a) Schematic of the dual-reflector antenna with flat metal or reflectarray as the subreflector, (b) Measured and simulated radiation patterns of dual-reflector antenna (From [3])

Electronic approaches are appropriate for beam scanning in dual-reflector antennas with the reduced size reflectarray [4]. In [4], the beam scanning is obtained in azimuth and elevation planes out of the dual-reflector system by applying PPS on the sub-reflectarray. The configuration of the antenna is shown in Figure 1.3a, which is made of a 1.5 m aperture parabolic reflector and a rectangular sub-reflectarray (520 mm × 494 mm) at 11.95 GHz. A shown in Figures 1.3b and 1.3c, the beam scanning of 2 and -2 degrees are obtained with the gain loss of less than 1 dB in two planes.

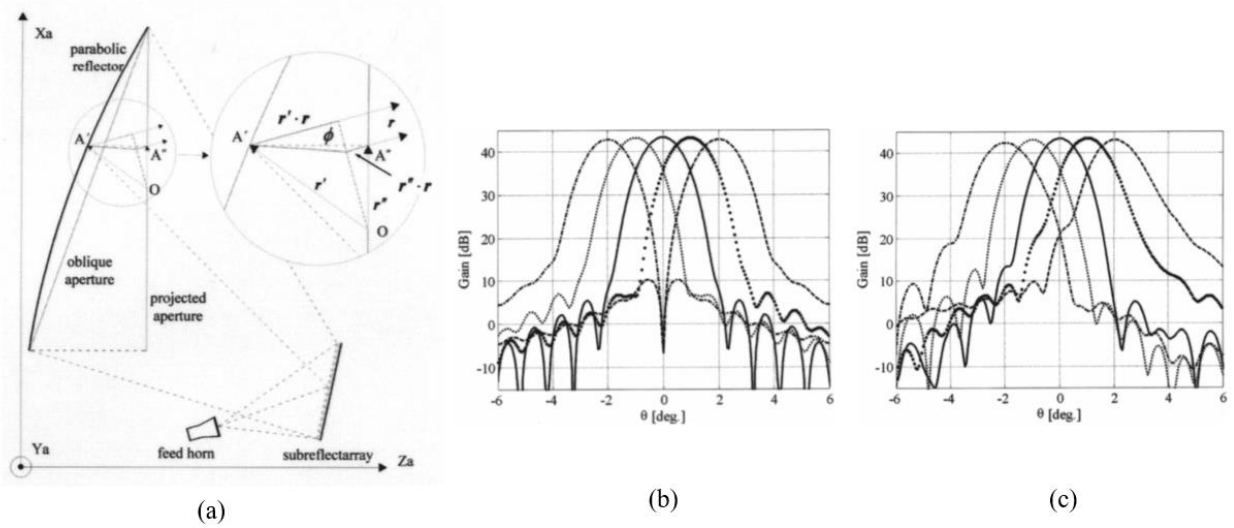

Figure 1.3 (a) Dual-reflector antenna structure with the reflectarray as subreflector, (b) The azimuth main cut for the Y_a axis scanning obtained by introducing a progressive phase on the reflectarray surface, (c) The elevation main cut for the X_a axis scanning obtained by introducing a progressive phase on the reflectarray surface. (From [4])

This work proposes an electromechanical approach by introducing a new technique with a broader beam scan range than Progressive Phase Shift (PPS) technique proposed in the literature [1, 4, 5]. The new method provides beam scanning out of dual-reflector antenna by using Near-Field Focusing (NFF) capability of the sub-reflectarray in the Gregorian dual-reflector configuration. Gregorian dual-reflector configuration is shown in Figure 1.4. In this configuration, sub-

reflectarray of the dual-reflector system mimics the behavior of the ellipsoidal subreflector in the Gregorian dual-reflector antenna. In this method, the radiated beam from a feed horn can be reflected by a subreflector to create a virtual source spot in the focal region of the main reflector. Displacement of the virtual source from the focal point of the main reflector leads to narrow-angle scanning, suitable for geostationary applications such as broadband satellite internet services, TV and radio broadcasting, and weather forecasting.

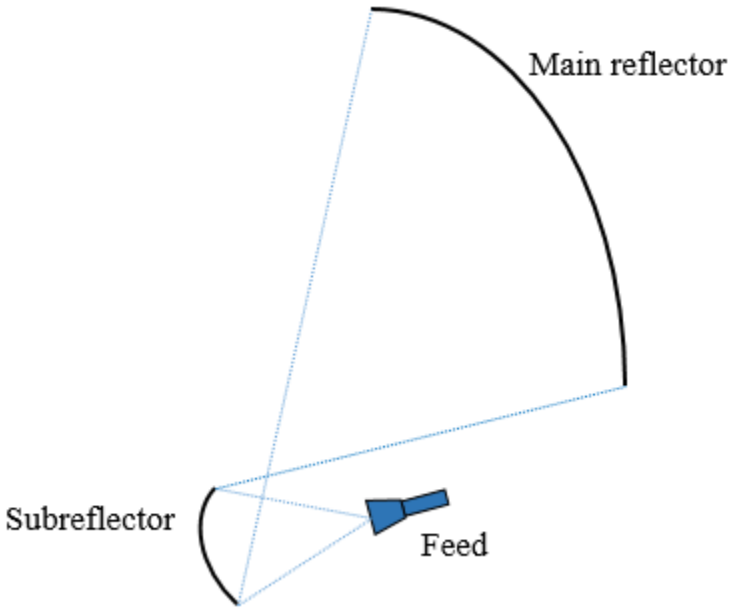

Figure 1.4 Offset Gregorian reflector antenna

The antenna system proposed will have to operate in circular polarization (CP) to meet the requirement of modern satellite systems. This will require the design of special reflectarray cells.

Variable rotation technique will be implemented in this work which obtains a proper phase adjustment in the bandwidth. Printed circular rings are used as subreflector elements instead of electronic beam forming elements due to their low cost, high power handling, and ease of reconfigurability. Miniature motors rotate the elements to scan the beam in the desired region.

The antenna has the functionality to achieve a high gain and has the property of beam shaping and beam scanning, which is a significant requirement for space and radar antennas.

1.3 Originality of the research

-C-band CP Reconfigurable reflectarray unit cell

A novel unit cell structure for C-band CP reconfigurable reflectarray has been proposed. The proposed structure enables 360° phase adjustment by implementing variable rotation technique and using mechanical actuation. Furthermore, the electromechanical unit cells are used in a dual-reflector system to realize beam scanning and shaping in desired angular regions without using RF electronic components. The use of electromechanical unit cells minimizes nonlinear effects that may occur in the case of high power illumination.

-NFF CP reflectarray

This work proposes C-band CP with NFF. The low-cost reflectarray with the property of easy reconfigurability provides the capability of steering the focused point by making field contribution add in-phase in the neighborhood of specified focal points. The difference between the desired and obtained positions of the focal point is due to the field spreading factor 1/R. The distance between the expected and obtained positions of the focal point vanishes as the distance from the center of the reflectarray to the desired focal point decreases.

-Beam Scanning Dual-Reflector Antenna with a CP Reconfigurable Reflectarray as Subreflector

A C-band reconfigurable CP dual-reflector structure, a potential candidate for new generation space antennas, is developed in this work. Different methods, including electronic and mechanical approaches, are provided for beam scanning of dual-reflector antennas. This work proposes NFF technique for beam scanning out of the dual-reflector antenna by electromechanical approach.

In [6], a reconfigurable reflectarray antenna using mechanically rotational elements is proposed. They have implemented two micromotor-controlled CP reflectarrays with the sizes of 225 and 756 elements in X-band. Finally, they concluded that the measurement results with the smaller

reflectarray size with fewer elements are more accurate due to the assembly accuracy. Consequently, there is an interest in using a micromotor system with a small reflectarray size. In our work, the reflectarray is used as the subreflector of the dual-reflector antenna. Therefore, a limited number of micromotors are used to reconfigure the beam compared to the antenna with the main reflectarray. Sub-reflectarray of the proposed dual-reflector antenna in our work is designed at C-band with 100 elements.

-Dual-Reflector with the beam synthesis capability using Particle Swarm Optimization (PSO) algorithm

The beam synthesis property of the proposed dual-reflector system is provided by introducing a PSO-based beam synthesis algorithm. A modified PSO algorithm has been proposed for beam synthesis of the proposed antenna, which meets two requirements: 1. minimize differences between the normalized synthesized and desired patterns, and 2. maximize the smoothness of the phase by forcing continuous phase distribution on the reflectarray. The beam synthesis capability of the proposed algorithm is experimentally validated for the proposed antenna.

1.4 Thesis Outline

Chapter 2 gives the literature review related to the main theme of the research. This chapter gives the introduction of the system, which is a dual-reflector antenna with the capability of beam steering and beam shaping. The designed sub-reflectarray has elements that are rotated by electromechanical actuators. Since the reflectarray is used as a subreflector of the system, a limited number of actuators are needed to adjust the phase distribution providing the beam shaping and beam scanning. The proposed system is low loss, easy to fabricate, and has a high power handling capability.

Chapter 3 presents the CP unit cell for the sub-reflectarray of the dual-reflector system. The performance of the unit cell is verified experimentally. Far-field focusing performance along with beam steering capability of the reflectarray is validated. A C-Band septum polarizer and feed horn with proper characteristics are fabricated and used as the feed of the system.

Chapter 4 introduces a dual-reflector antenna with the ability of beam scanning and beam shaping.

Different approaches are presented in Chapter 4 for beam scanning out of a dual-reflector system. Beam scanning using the NFF technique is introduced in this work as the most effective method for narrow beam scanning so far.

Chapter 5 introduces a PSO-based beam synthesis algorithm to provide the beam shaping for the proposed dual-reflector antenna. A modified PSO algorithm has been proposed to force continuous phase distribution on the reflectarray. The beam synthesis algorithm has been implemented by exporting element factors of the antenna array of the dual-reflector system.

Chapter 6 experimentally supports the beam synthesis capability of the dual-reflector antenna based on the algorithm proposed in Chapter 5.

Chapter 7 contains a general discussion on proposed methods in different stages of the works. Finally, it provides a conclusion and recommends possible future works.

CHAPTER 2 LITERATURE REVIEW

2.1 Introduction

The chapter aims to overview previous works related to dual-reflector antennas configuration and different techniques to implement the beam reconfigurability of dual-reflector antennas. The electronic or mechanical approaches could implement beam reconfigurability of the dual-reflector system without using a complicated feeding system of the phased array antenna. In this work, beam scanning of a dual-reflector antenna is implemented by an electromechanical approach [7, 8].

Sections below propose different methods that exist in the literature for beam reconfigurability of dual-reflector antennas. In addition, the subreflector elements design of the dual-reflector antenna is also covered in this chapter.

2.2 Dual-reflector structure with beam reconfigurability

Dual-reflector antenna has applications in satellite communication systems with reduced overall antenna volume [1]. These antennas are composed of a feed, subreflector, and a reflectarray or a parabolic dish as the main reflector. A Dual-reflector antenna with a parabolic dish as its main reflector covers a broader frequency band compared to an antenna with a big reflectarray as its main reflector.

Figure 2.1 shows the dual-reflector configuration used in this work with reflectarray as the subreflector and parabolic dish as the main reflector. This configuration combines the high gain and wideband property of parabolic antenna, and it is flexible in beam shaping and beam scanning while having reflectarray as the subreflector.

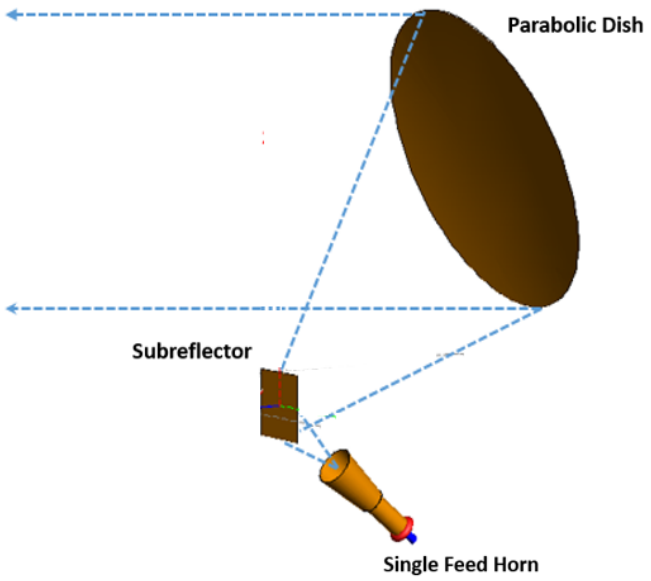

Figure 2.1 Dual-reflector antenna configuration with parabolic dish as the main reflector

In [3] and [4], Mechanical or electronic approaches provide beam scanning out of dual-reflector antennas at 94 GHz and 11.95 GHz, respectively. [3] provided beam scanning of a dual reflector antenna by the mechanical approach, which is obtained by the mechanical movement of the subreflector. The beam scannings of 2.5 and 5 degrees with the gain loss of 1.35dB and 0.15dB are obtained, which illustrates the limited scan range provided by this method. [4] implemented beam scanning of a dual reflector antenna by an electronic approach using the PPS technique. With this approach, the beam scanning of -2 to 2 degrees is obtained with a gain loss of less than 1dB.

In this work, we propose a new beam scanning approach with an electromechanical approach by taking advantage of the NFF property of the sub-reflectarray in the Gregorian dual-reflector structure. This method provides a wider scan range with the smaller aperture size of both subreflector and parabolic dish than the antenna structures in [3] and [4]. Moreover, the dual-reflector antennas proposed in [3] and [4] are linearly polarized, while this work implements a circularly polarized dual-reflector antenna.

2.3 Synthesis techniques

The beam synthesis property of the proposed antenna is studied in Chapters 5 and 6. Different beam synthesis algorithms exist in the literature, including Projection Matrix Algorithm (PMA), Fast Fourier Transform (FFT), Iterative Sampling Method, Genetic Algorithm (GA), Particle Swarm Optimization (PSO) Algorithm, etc. [9, 10, 11, 12].

Simple methods including, Woodward-Lawson and Fourier Transform techniques, do not allow sidelobe level (SLL) control directly [9]. Dolph-Tschebyscheff allows SLL control but for antenna array with isotropic elements [9]. In contrast with traditional optimization methods such as the least square approach for pattern synthesis, GA and PSO algorithms provide multiple design goals such as SLL, beamwidth, and null control [9, 13]. Particle Swarm Optimization (PSO) and Genetic Algorithm (GA), known as evolutionary phase synthesis algorithms, are widely used for antenna arrays. Compared to GA, PSO implementation is less complex and needs less computing time while conducting global and local searches simultaneously [9, 10]. This algorithm is effective in electromagnetic problems and is widely used in the design of microwave and antenna components (e.g. [14, 15]).

Beam synthesis algorithms are implemented based on the phase-only synthesis, the amplitude-only synthesis, or the complex technique by combining the phase and amplitude syntheses. Amplitude and phase synthesis techniques are efficient methods to achieve low sidelobes, nulls at specific directions with constrained main beam [16-20]. Phase-only synthesis techniques are widely used for phased arrays that provide beam scanning inexpensively, which minimizes excitation errors and preserves coherence [17]. The only-amplitude synthesis technique is implemented by using Taylor distribution and PSO in [18]. However, single parameter optimization may limit the effectiveness of SLL [20].

This work implements beam synthesis by introducing a phase-only synthesis PSO algorithm. The proposed algorithm gives the ability of beam scanning in the uv-plane as well as beam shaping.

2.4 Subreflector's element design

Reflectarrays are typically flat or slightly flat reflectors with potentially reconfigurable and low-cost properties. Using reconfigurable reflectarray has advantages in comparison to the phase arrays in terms of cost and efficiency. They combine the best features of aperture antennas and phased arrays by offering real time reconfiguration and scanning the beam pattern [21]. Consequently, there is high interest in reconfigurable reflectarrays using electronically tunable elements. However, Reconfigurable electronic elements have some limitations due to the complexity, loss, and power consumption. Therefore, in this work, we use mechanically controlled elements as reconfigurable elements for the reflectarray.

Figure 2.2 shows three basic approaches implemented in designing reconfigurable reflectarrays, including tunable resonator, guided-wave, and element rotation. In addition, they could employ different technologies such as semiconductor diodes, tunable dielectrics, and Micro-Electro-Mechanical-Systems (MEMS) that enable reconfigurability.

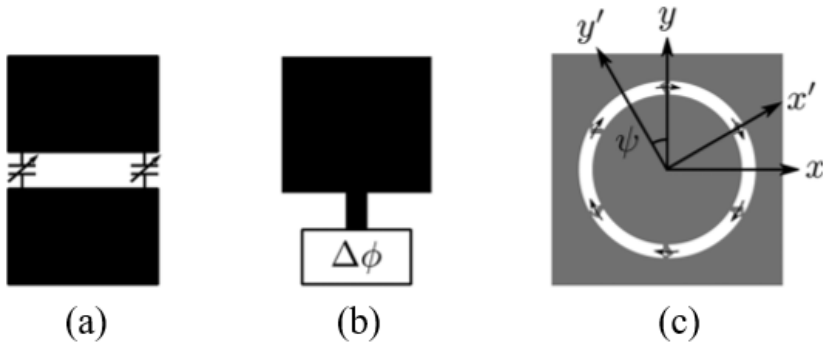

Figure 2.2 Reconfigurable reflectarray approaches (a) Tunable resonator, (b) Guided-wave, (c) Element rotation (Form [21])

The approach in Figure 2.2c is implemented for CP reflectarrays. Figure 2.3 shows CP dual-band reflectarray using the element rotation technique. Each element consists of two rings with different sizes integrated with RF MEMS switches, where each ring performs in one frequency band [22].

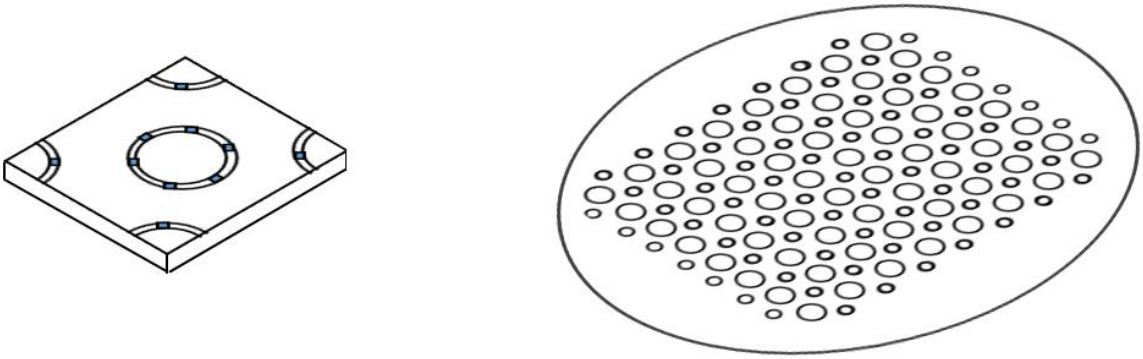

Figure 2.3 Dual-band reflectarray using RFMEMS [22]

Reflectarrays with analog control of MEMS switches suffer from a lack of sufficient reliability or temperature stability [23]. Replacing the analog control switches with two stage digital elements overcomes these shortages. The biasing complexity of the control elements is another issue in the design. Using switches with limited phase states provides the beam with low gain and high SLL due to the phase error. The phase error is the consequence of the limited phase state related to the phase quantization issue. Implementing a continuous phase state overcomes the phase error issue in terms of beam scanning accuracy, gain, and SLL. This could be solved by using passive microstrip elements where the continuous phase states of each element are obtained by rotating the elements by micromotors [21, 24, 25, 26]. We use a limited number of micromotors to rotate the limited number of passive sub-reflectarray elements in this work.

Considerable points in designing the reflectarrays are low cost, ease of manufacturing, and their potential for reconfigurability. Therefore, instead of using a ring structure with integrated RF MEMS, which allows implementing rotation [22], a single split metal ring element is used [27]. This metal ring element is rotated by micromotor to implement variable rotation technique for the phase adjustment of the reflectarray.

Table 2.1 summarizes the main technologies for enabling reconfigurability and some of their key parameters of the components as tuning elements [28]. Reconfigurable reflectarray employs the

components in the table to provide beam shaping and beam steering. The last column added to the table corresponds to the circular ring patch implemented in this work with less loss and a lower manufacturing cost. Due to the limited number of the sub-reflectarray elements of the dual-reflector system, a limited number of micromotors are needed for the phase adjustment of the system. Therefore, lower power consumption is expected with the dual-reflector system in Figure 2.1 compared to the system with the reflectarray as the main reflector.

Table 2.1 Selected technologies for reconfigurable reflectarray components and their impact on some key parameters

	RF MEMS	**PIN Diode**	**Varactor Diode**	**Liquid Crystal**	**Ferro Electric Material**	**CRP (Circular Ring Patch)**
References	[29, 30, 31]	[32]	[33]	[34, 35]	[36]	This work
Costs	Medium	Low	Medium /High	Low	High	Low
Loss	Very Low	Low	High	Medium	Medium	Low
Power Consumption	Negligible	High	Negligible	Negligible	Negligible	High
Technology Readiness	Foundry Requires	Market Available(COSTS)	Market Available (COSTS)	Special Facilities required	Special Facilities required	Market Available
Speed	Micro-seconds	Nano-seconds	Nano-seconds	Seconds	Milli-seconds	Seconds
Mounting Complexity	Low	Low	Low	Medium /High	Medium /High	Low
Biasing Complexity	High Voltage (60 V)	Low Voltage (1V)	Medium Voltage (0-30 V)	Medium Voltage (0-20V)	High Voltage (100V)	Low Voltage (3.3-5V)

Figure 2.4 shows two reflectarray elements using the element rotation principle [22]. The one on the left corresponds to the metal ring loaded with RF MEMS switches to enable the implementation of discrete rotation phase steps. The figure in the right corresponds to the single split metal ring, which is rotated by a micromotor that provides a continuous rotation phase state. The angle of rotation is ψ.

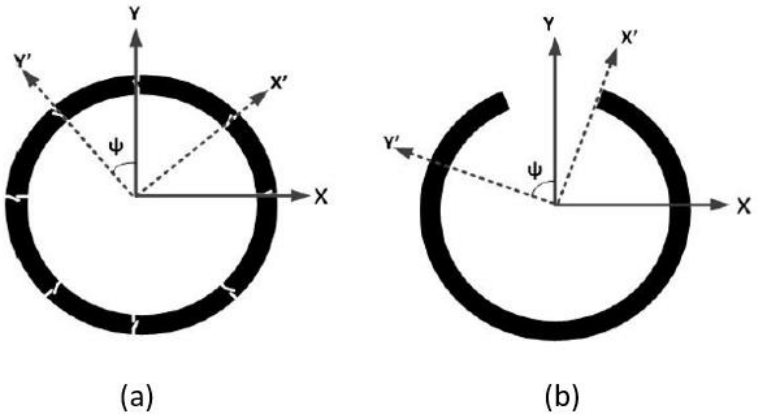

Figure 2.4 Reflectarray unit cell using element rotation principal (ψ is rotation angle): (a) RF MEMS as phase tuning elements, (b) phase tuning by variable rotation techniques

In [37], a Ka-band CP microstrip reflectarray with rectangular shape elements using the variable rotation technique is proposed. However, Using round shape elements keeps the minimum spacing between the elements while preventing physical interference between the elements.

In [6, 7], the round shape element is designed for X-band using a variable rotation technique. Two split metal rings are printed on RF-60A-0500 substrate with ε_r of 6.15 and $\tan\delta$ of 0.0038 where the suspended air substrate is supported by a pedestal made of Kapton with ε_r of 3.2 and $\tan\delta$ of 0.02 above 4 mm on the ground. The reflection loss obtained by each element in that structure is 0.2 dB.

In this work, we have designed CP microstrip elements with two layers of Duroid 6002 dielectric substrates with ε_r of 2.94 and $\tan\delta$ of 0.0012. In this structure, the motor driving shaft inserts into

the drilled hole area of the substrates with an Aluminum metal rod. The element return loss of 0.048 to 0.068 dB is obtained with this structure, which is less than the element loss in [6, 7].

The selected ring shape element is proper for CP plane wave and provides the phase adjustment by implementing the variable rotation technique. This technique is also know in the literature as the "Pancharatnam-Berry phase theory" [38].

With the Right-Hand Circularly Polarized (RHCP) incident wave on the element, the reflected wave is composed of Left and Right Hand Circularly Polarized (LHCP and RHCP) waves. It is assumed that the incident and reflected waves propagate in the -z and +z directions respectively. The reflected RHCP wave corresponds to the co-polarization term, while the LHCP wave corresponds to the cross-polarization term. The co- and cross-polarization reflected terms determined by reflection coefficients $\Gamma_{\text{Co-pol}}$ and $\Gamma_{\text{Cross-pol}}$ are related to the incident fields by eq. (2.1) to (2.4) [22, 37]:

$$\mathbf{E}^{\text{inc}} = \text{A}(\mathbf{a}_x + j\mathbf{a}_y)\, e^{jzk_0} \tag{2.1}$$

$$\mathbf{E}^{\text{ref}} = \left[\Gamma_{\text{Co-pol}}.\text{A}\right](\mathbf{a}_x - j\mathbf{a}_y)\, e^{-jzk_0} + \left[\Gamma_{\text{Cross-pol}}.\text{A}\right](\mathbf{a}_x + j\mathbf{a}_y)e^{-jzk_0} \tag{2.2}$$

$$\Gamma_{\text{Co-pol}} = \Gamma_{\text{Co-pol}}^{\psi=0} e^{+j2\psi} = \left(\frac{1}{2}(s'_{xx} - s'_{yy}) + js'_{xy}\right) e^{+j2\psi} \tag{2.3}$$

$$\Gamma_{\text{Cross-pol}} = \frac{1}{2}(s'_{xx} + s'_{yy}) \tag{2.4}$$

Primed scattering (s') parameters apply to x and y linearly polarized modes aligned with the coordinate system of Figure 2.4 for the element rotation angle of ψ. S parameters are the elements of a 2×2 matrix of the reflection coefficients in linear polarization, e.g. s'_{xy} (or s'_{yx}) is the reflected wave in x (or y) polarization resulting from the incident wave in the y (or x) polarization and s'_{xx} (or s'_{yy}) is the reflected wave in x (or y) polarization resulting from the incident wave in the x (or y) polarization. Equation (2.4) concludes that in order to obtain minimum (null) cross-polarization,

the reflection coefficient of two orthogonal linear reflected waves needs to have the same amplitude and a difference of 180 degrees in their phase.

2.5 Conclusion

This chapter proposed different methods to implement beam reconfigurability of dual-reflector antenna. As discussed, beam reconfigurability could be implemented by electronic or mechanical approaches. There is also high interest in reconfigurable reflectarrays using electronically tunable elements. However, due to the complexity, loss, and power consumption in using the tunable electronic elements, a single split metal ring element is used instead of using a ring structure with integrated RF MEMS [22]. This metal ring element is rotated by micromotor and allows implementing rotation.

The structure proposed in this work can allow beam scanning and shaping without using electronic devices, which leads to lower losses and increased power handling.

A new method for beam steering of the dual-reflector antenna will be proposed in the following chapters, which overcomes the very limited scan range for the dual-reflector antenna proposed in the literature. The beam synthesis property of the proposed antenna will be studied by implementing a modified PSO-based beam synthesis algorithm.

CHAPTER 3 C-BAND CIRCULARLY POLARIZED RECONFIGURABLE REFLECTARRAY USING ELECTROMECHANICAL ACTUATORS

3.1 Introduction

The most well-known high gain antennas are parabolic reflectors. Reflectarrays have been considered as suitable candidates to replace parabolic antennas due to their low cost, ease of manufacturing, and potential for reconfigurability. There is high interest in reconfigurable reflectarrays using electronically tunable elements. The structure proposed in this work can allow beam scanning and shaping without using electronic devices, which leads to lower losses and increased power handling. A single split metal ring element is used instead of using a ring structure with integrated RF micro-electro-mechanical systems (RF MEMS), which allows implementing rotation [22]. This metal ring element is rotated by micromotor.

This chapter presents the C-band CP reconfigurable reflectarray, which will be used as the subreflector of a dual-reflector system. Section 3.2 proposes the unit cell for reconfigurable reflectarrays. Then, the performance of the unit cell is presented and validated experimentally. Section 3.3 introduces the CP septum polarizer horn with proper characteristics to illuminate the reflectarray of the system. Section 3.4 proposes the reflectarray composed of the unit cell elements introduced in section 3.2. Afterward, the performance of the reflectarray is studied and supported experimentally. Section 3.5 present the electromechanical part for controlling the element of the system. Finally, Section 3.6 concludes the chapter.

3.2 C-band CP Reconfigurable Reflectarray Unit Cells

This section focuses on designing the unit cells of the reflectarray. The critical characteristic for designing the reflectarray is the bandwidth. By using single split ring metal elements and applying variable rotation technique explained in Chapter 2, wideband reflectarray is provided since the reflection phase of the elements is independent of the bandwidth (see eq. (2.3)) [39]. Also, the

performance of circularly polarized elements is defined by axial ratio (AR) bandwidth [27]. With CP elements, the variable rotation technique enables the reflected CP wave's full 360 degrees phase adjustment. Therefore, the phase adjustment is obtained by rotating the elements by an angle that is half of the desired phase shift according to eq. (2.3).

3.2.1 Unit Cell Design

The proposed reflectarray consists of identical split metal ring elements with different rotation angles. As shown in Figure 3.1, each unit cell consists of a cylindrical piece of a substrate with a printed metal ring. The substrate type is Duroid 6002 with ε_r = 2.94 and tan δ=0.0012. The motor driving shaft inserts into the drilled hole area of the cylinders and planar substrates. The metal cylinder will be directly driven by the motor in order to rotate the cylinder with the printed metal ring on the top of it. The period of the unit cell elements in the z and *y* directions should not exceed $\lambda_0 / 2$ too much at the desired frequency of operation in order to avoid grating lobes, where the λ_0 is free space wavelength ($\lambda_0 = 42.8\text{mm}$) at the design frequency of 7 GHz used in the experimental validations). Table 3.1 presents the dimensions of each unit cell. The thickness of the dielectric substrate of each unit cell significantly affects the bandwidth [39]. By increasing the substrate thickness, the bandwidth is increased. Also, the dimensions of the split metal ring element, including R_{out}, ΔR and θ_s, are optimization parameters to minimize the cross-polarization term and improve the axial ratio.

The infinite array of the unit cell is modeled using Floquet theory by defining master-slave boundary conditions in HFSS software from ANSYS. Bandwidth is a critical characteristic of each unit cell. It is defined as the frequency band where a difference of 20 dB is observed between the co- and cross-polarization levels of the reflected wave. This corresponds to an axial ratio (AR) of 1.74 dB or less for the reflected wave. Having the cylindrical rotating parts supported by a planar grounded dielectric substrate enhances the bandwidth compared to the case where they would be directly supported by the metallic ground plane.

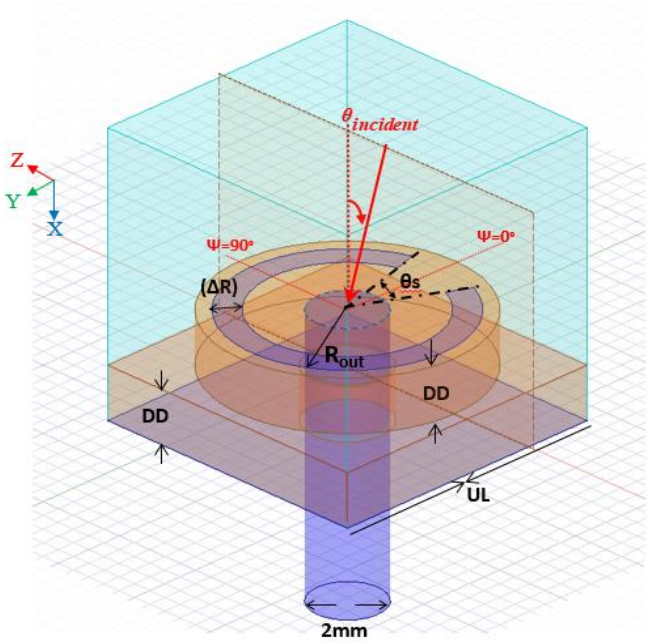

Figure 3.1 Unit cell structure (in the figure, the element rotation angle is $\psi = 0$)

Table 3.1 Unit cell structure parameters related to Figure 3.1

Parameter	**Value**
Dielectric-Thickness (Duroid 6002) (DD)	3.048 mm
θ_S (Gap)	40 degrees
Line Width (ΔR)	1.4 mm
R_{out}	6.3 mm
Unit Cell Size (UL)	15.75 mm
Dielectric-Cylinder Radius (CR)	7 mm

Since each element in the reflectarray structure may have a different rotation angle, the optimization parameter for the unit cell covers different angles of rotation. Of course, the simulation method by using Floquet theory implies the reflectarray with the same rotation angle of all the cells, which is not the case in practice. However, in reflectarrays with large *F*/D ratios, the

phase variation between neighbor cells is small. Also, the variable rotation technique leads to reflectarrays that are exempt from abrupt changes in unit cell geometry when passing between 360-degree phase transitions.

3.2.2 Unit cell performance

Figure 3.2a shows the amplitude of the reflected wave for different rotation angles covering the 360-degree range. The co-polarized curves show the reflection coefficient Γ_{RR}, corresponding to the level of reflected right-hand polarization for an incident right-handed polarized signal. The cross-polarized curves show Γ_{LR}, corresponding to the level of reflected left-hand polarization for an incident right-handed polarized signal. As shown in Figure 3.2a, the optimized structure achieves cross-polarization of -20 dB below the co-polarization level over a frequency band of 5.9 to 7.3 GHz (21%). Within that same band, the loss in the reflected co-polarized signal varies between 0.068 and 0.048 dB. Figure 3.2b shows the AR of the reflected wave in the same band. Each curve in Figure 3.2 corresponds to a different rotation angle of the moving part. It can be seen that during the rotation, the response gradually evolves from double resonant to a single resonant, and that the band is limited by the single resonant responses.

Figure 3.3a shows the phase shift of the co-polarized reflected wave as a function of the element rotation angle. Each blue dot corresponds to one rotation angle. The red dashed lines connecting the points have a slope of 2, which shows that the phase shift of the co-polarized reflected wave is twice the rotation angle of the element, as expected from eq. (2.3). Figure 3.3b shows the phase shift versus rotation angle for several frequency points in the range 6.2-7.2 GHz. The phase of the co-polarization signal increases by the same interval for all rotation angles when the frequency varies by 1 GHz. A plot of phase shift versus frequency in Figure 3.4 indicates that variation with frequency is linear, which means that the element rotation technique can lead to broadband reflectarrays.

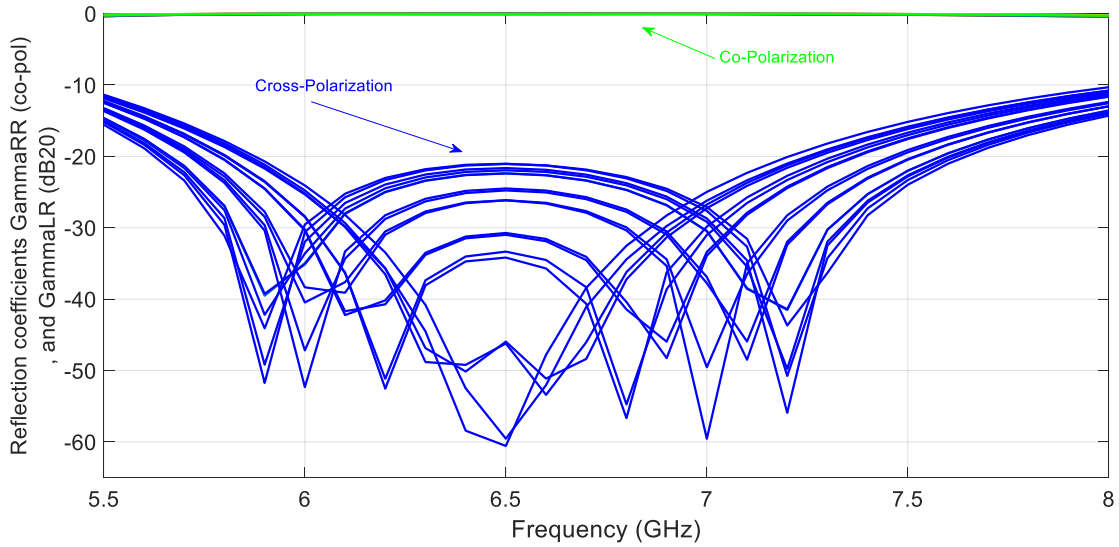

(a)

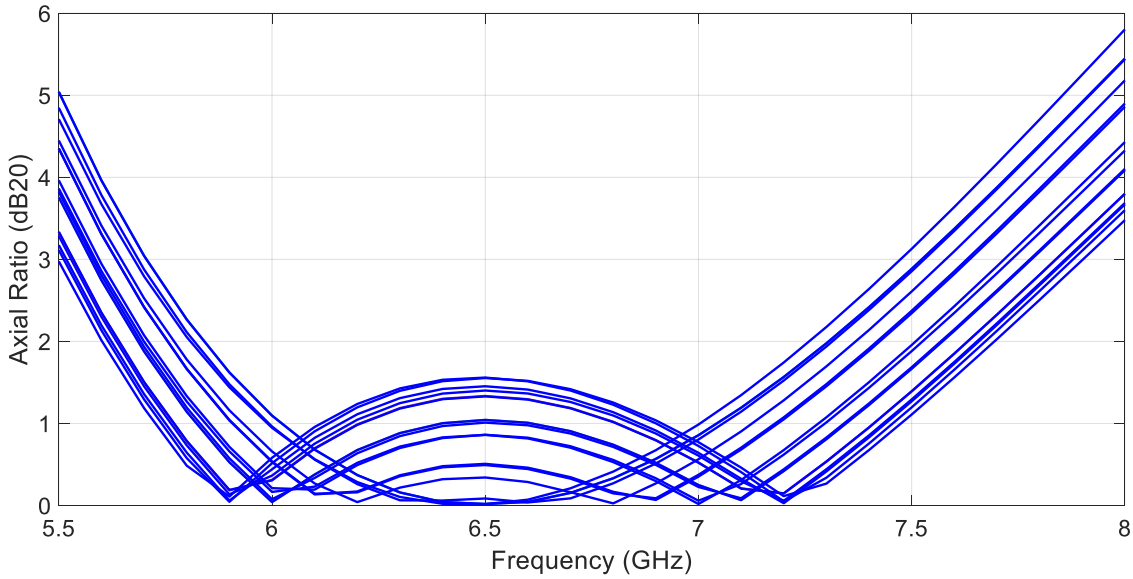

(b)

Figure 3.2 (a) Co- and cross-polarization amplitude of reflected waves for different rotation angles of the unit cell element, for normal incident angle, (b) AR vs frequency for different rotation angles of the unit cell element

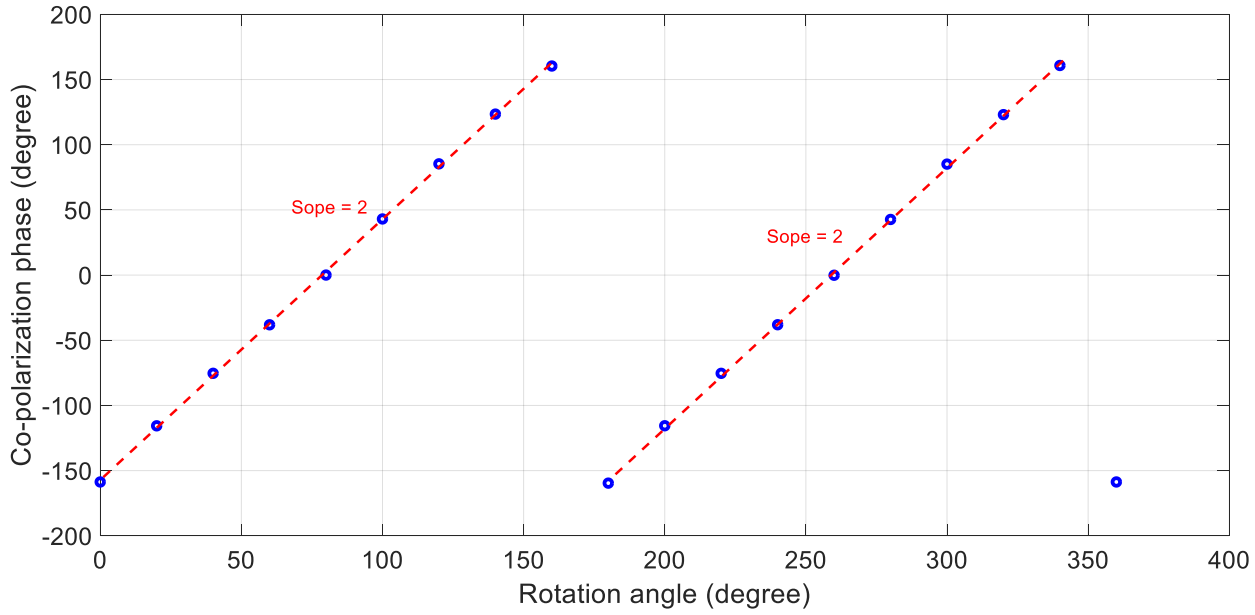

(a)

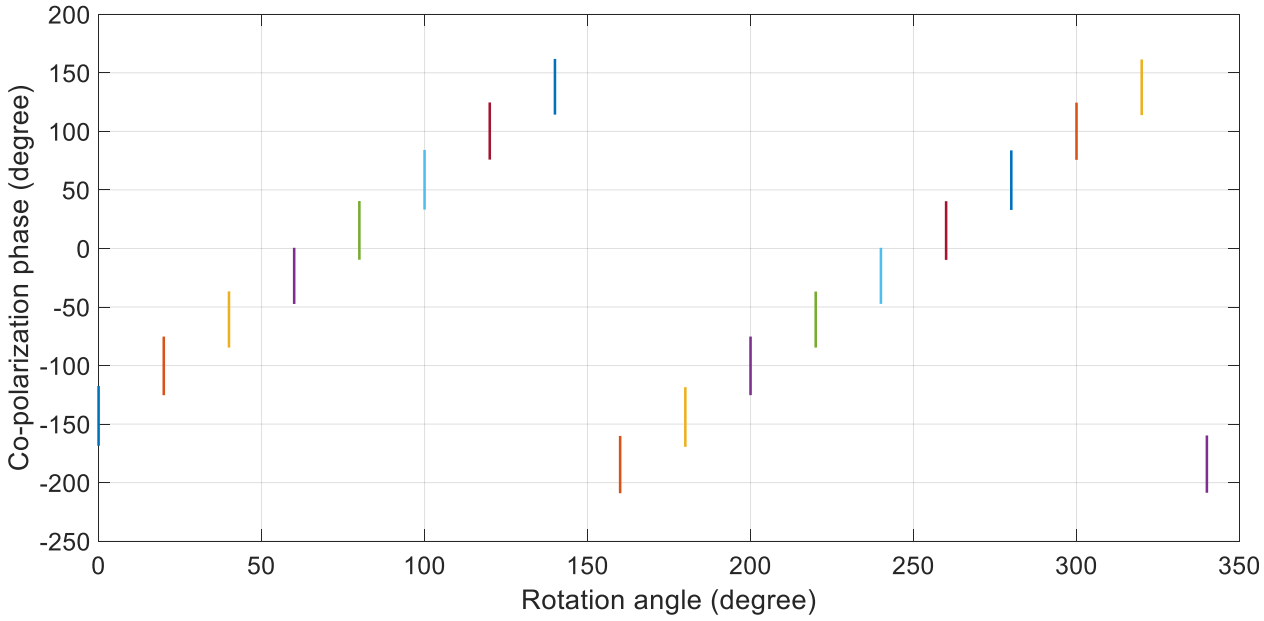

(b)

Figure 3.3 (a) Co-polarization phase graph for different rotation angles of the unit cell at 7 GHz, (b) Same results as 3.3.a but over the 6.2-7.2 GHz band. Each vertical bar corresponds to a set of frequency points within that band

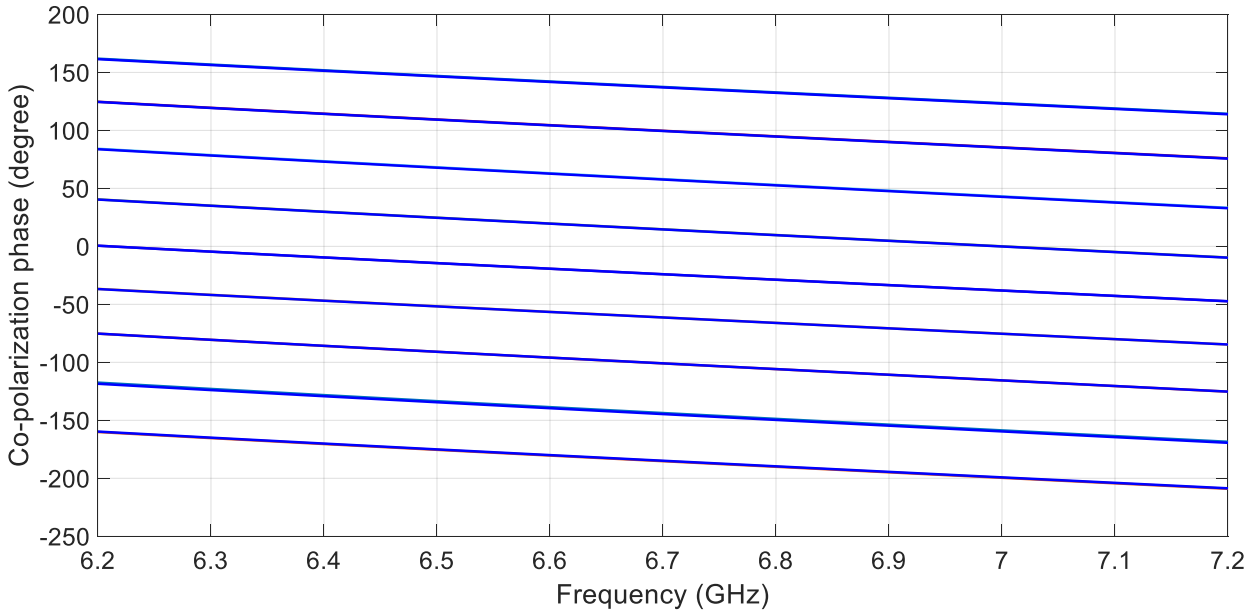

Figure 3.4 Co-polarization phase graph vs frequency for different rotation angles of the unit cell element over the 6.2-7.2 GHz band (each graph corresponds to one rotation angle and has a slope of -50 deg/GHz)

Oblique incident angle needs to be considered for the unit cells near the edge of the center-fed reflectarray. Figure 3.5 illustrate the reflection coefficients and axial ratio of the unit cells with the rotation angle of $\psi = 0^{\circ}$ for oblique incident angles of 0 to 35 degrees. Also, Figure 3.6 show the same parameters for the element with the rotation angle of $\psi = 90^{\circ}$. As shown in Figures 3.5 and 3.6, a difference of 20 dB between the co- and cross-polarization levels of the reflected wave corresponds to an AR of 1.74dB.

As shown in Figure 3.5b, with the element rotation of $\psi = 0°$, AR ratio values are more stable by increasing the oblique incident angle compared to Figure 3.6b with the element rotation of $\psi = 90^{\circ}$. For example, in Figure 3.5b, at the center frequency (7 GHz), the AR ratio stays below 2 dB for incident angles of 0 to 30 degrees, while in Figure 3.6b, AR is above 2 dB for incident angels of more than 25 degrees.

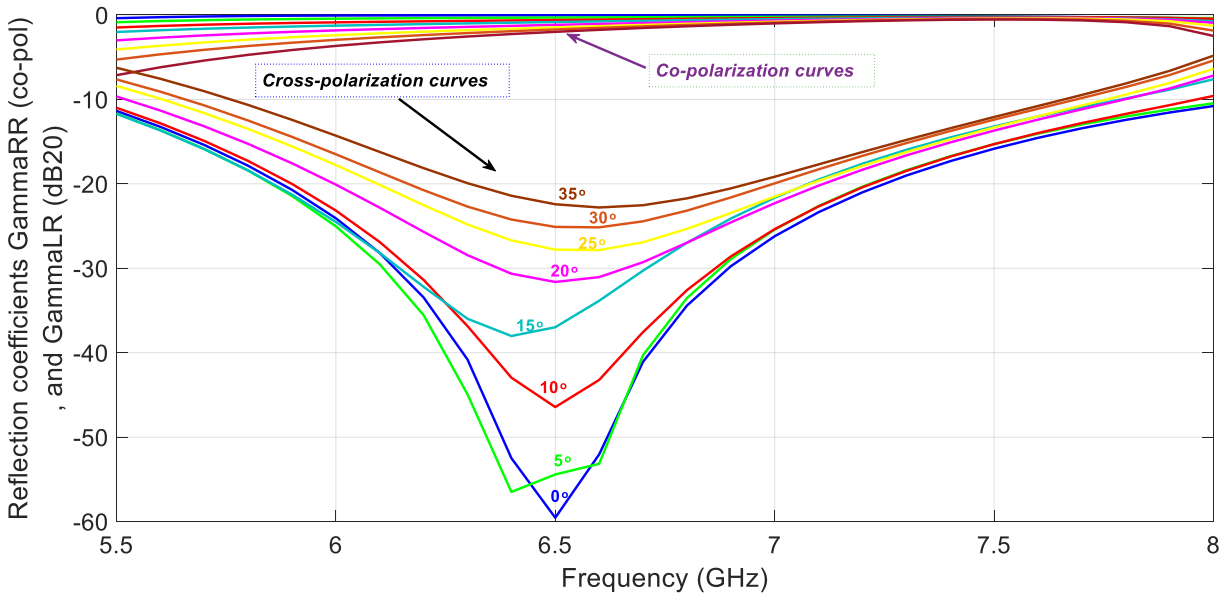

(a)

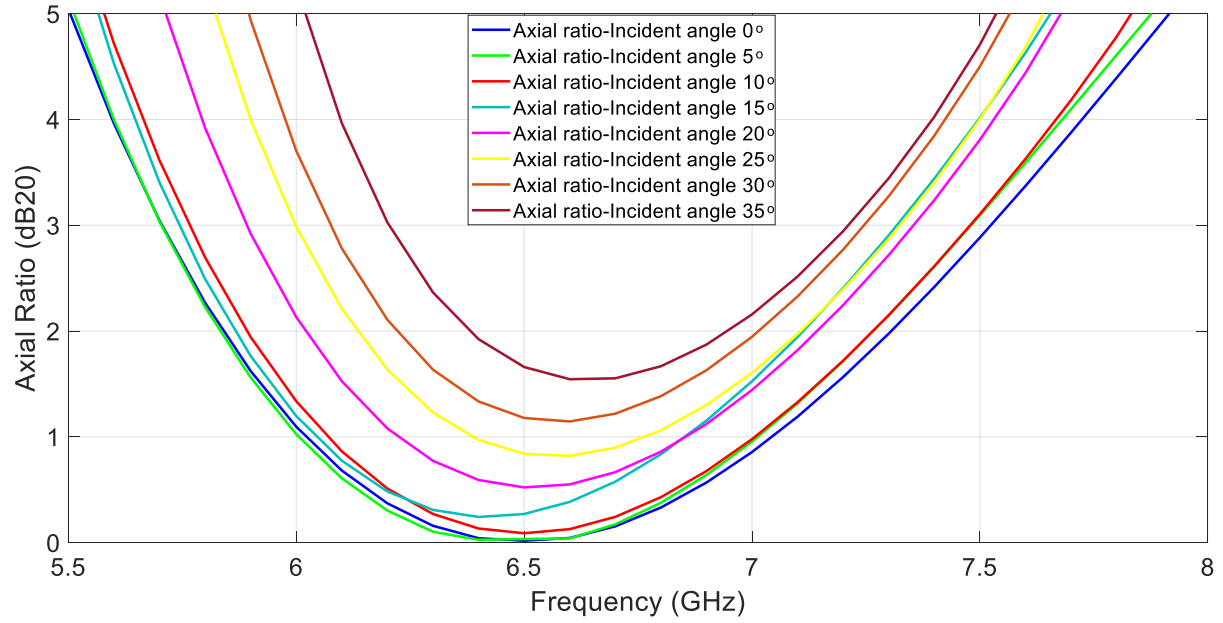

(b)

Figure 3.5 (a) Co- and cross-polarization amplitude graphs of the unit cell with the rotation angle of $\psi = 0°$ for oblique Incidence angles of 0-30 degrees (b) AR graph of the unit cell with the rotation angle of $\psi = 0°$ for oblique Incidence angles of 0-35 degrees

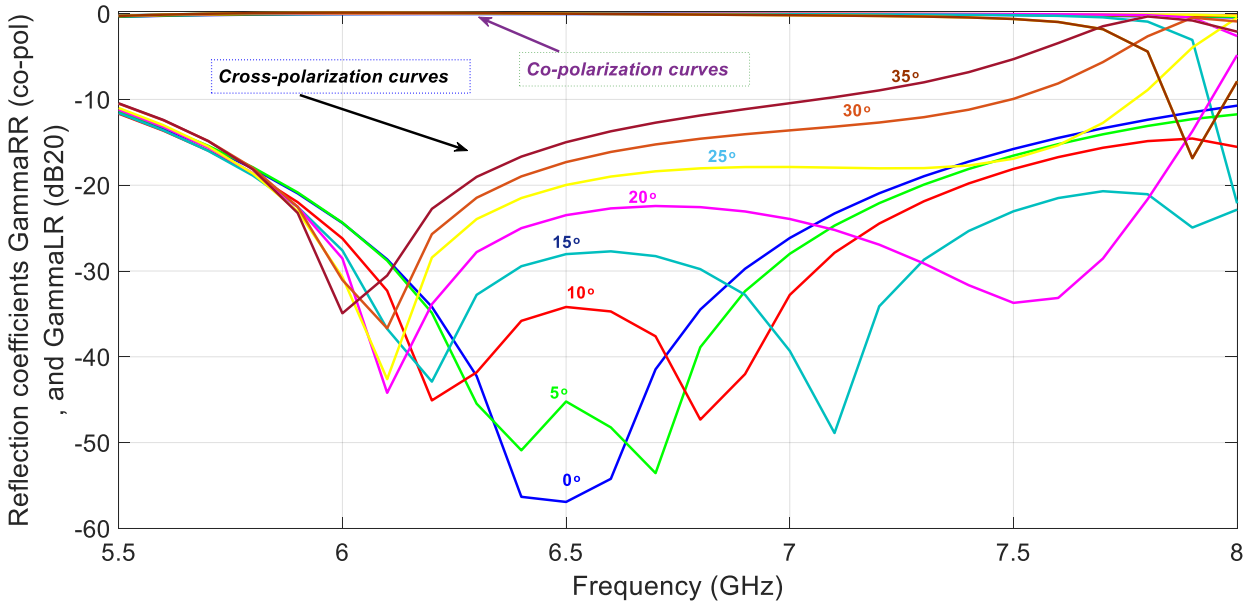

(a)

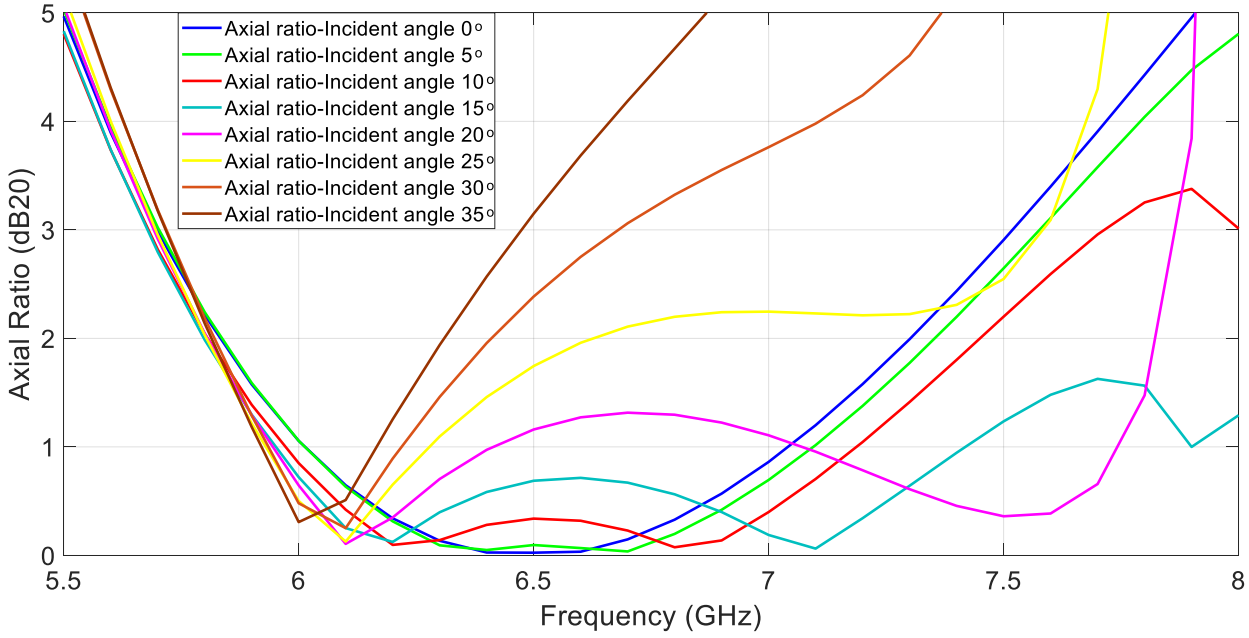

(b)

Figure 3.6 (a) Co and cross-polarization amplitude graphs of the unit cell with the rotation angle of $\psi = 90°$ for oblique Incidence angles of 0-30 degrees (b) AR graph of the unit cell with the rotation angle of $\psi = 90°$ for oblique Incidence angles of 0-35 degrees

3.2.3 Experimental Validation of the unit cells' performance

Unit cells' performance is evaluated by investigating two orthogonal reflected electric fields: are x and y linear polarizations. Two orthogonal terms of the reflected field, s_{xx} and s_{yy}, should have the same amplitude level and have the 180-phase difference to minimize the cross-polarization term of the reflected beam from the unit cells.

The performance of a reflectarray comprised of 100 (array of 10×10) of the unit cell introduced in Section 3.2.1 is evaluated experimentally in terms of cross-polarization level by applying two polarizations. For this purpose, the reflectarray is illuminated by linearly polarized C-Band Standard Gain Horn with the model number of 3160-06, as shown in Figure 3.7. In order to apply two polarizations, reflectarray is rotated by 90 degrees around the optical axis of the system. The feed is located at the focal point of a dielectric lens. Spherical wavefront emerging from the feed horn are converted into planar wavefront on another side of the lens.

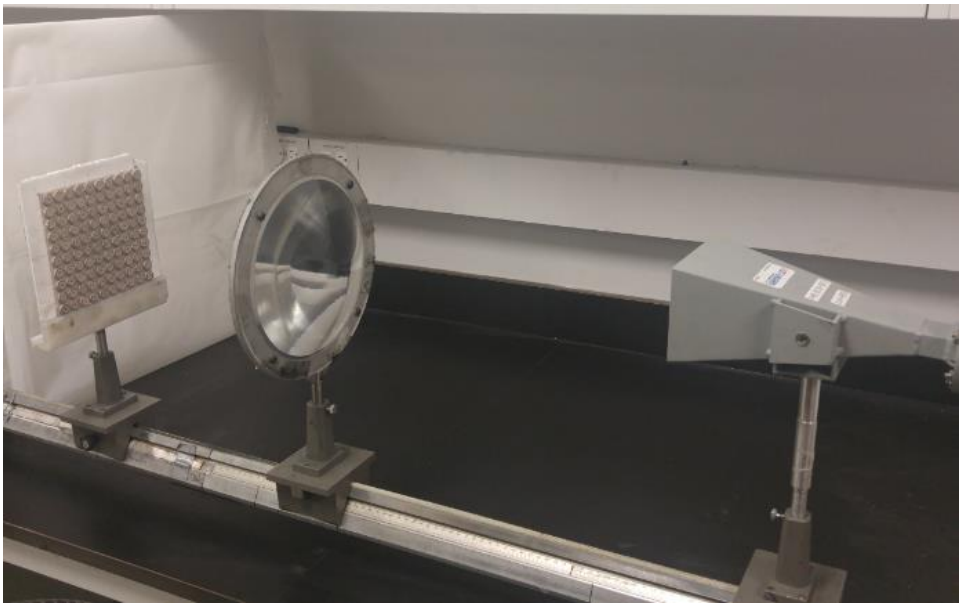

Figure 3.7 Setup for experimentally investigating the performance of the unit cells in terms of cross-polarization level

For measuring the reflected electric field from the reflectarray, the reference plane is adjusted on the top surface of the reflectarray. For this purpose, the time domain function on VNA (Vector Network Analyzer) is used. With the time domain function, we convert the signal reflected at the surface of the reflectarray from the frequency domain to the time domain. First, the proper part of the signal, which shows the reflection at the reflectarray surface, is time-gated. Then, the inverse Fourier transform function of VNA is used to convert the time-gated part of the signal from the time domain to the frequency domain. In the end, the displayed signal in the network analyzer is the reflection at the reference plane, which is on the top of the reflectarray surface in the desired frequency band.

We need two orthogonal reflected fields at the reference plane. For this purpose, first, all the cells are aligned with the same orientation angle of $\psi = 0°$. Then, all the cells will be oriented by 90 degrees. Finally, two cases that present two orthogonal reflected electric fields at the reference plane are compared, as shown in Figure 3.8.

Figure 3.8a shows that the two orthogonal electric fields have small differences in their amplitudes in the 6-8 GHz frequency band. Figure 3.8b shows a phase difference close to 180 degrees between two orthogonal reflected electric fields in the frequency band. Therefore, the low cross-polarization level of the reflected electric field is obtained according to eq. (2.4).

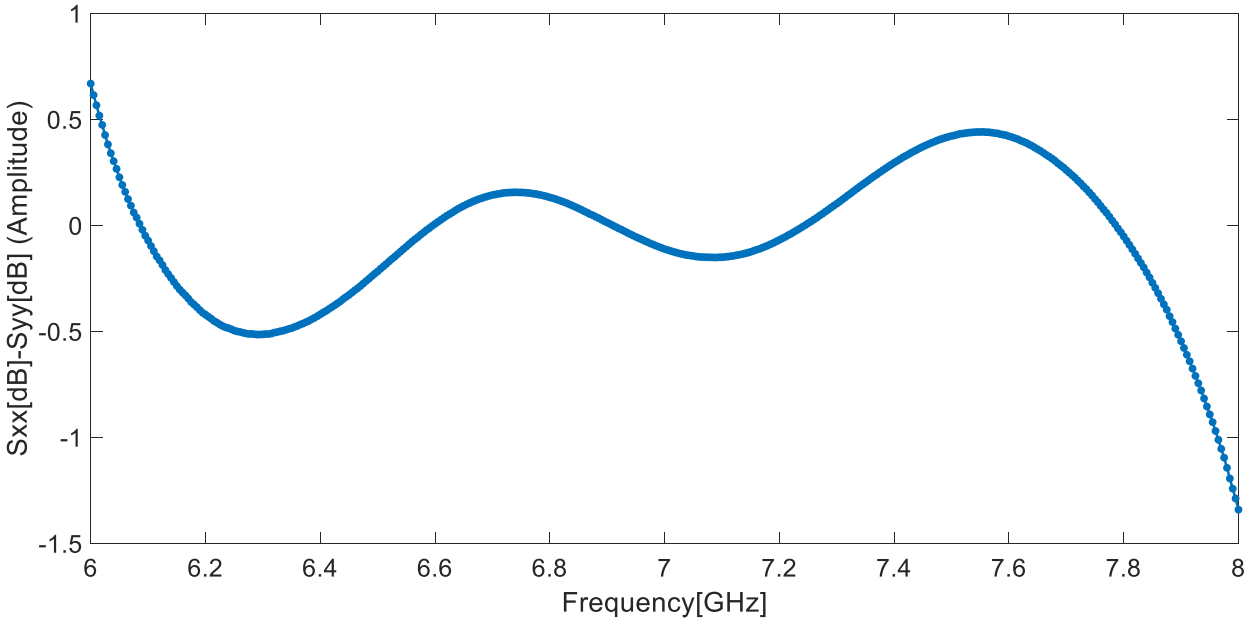

(a)

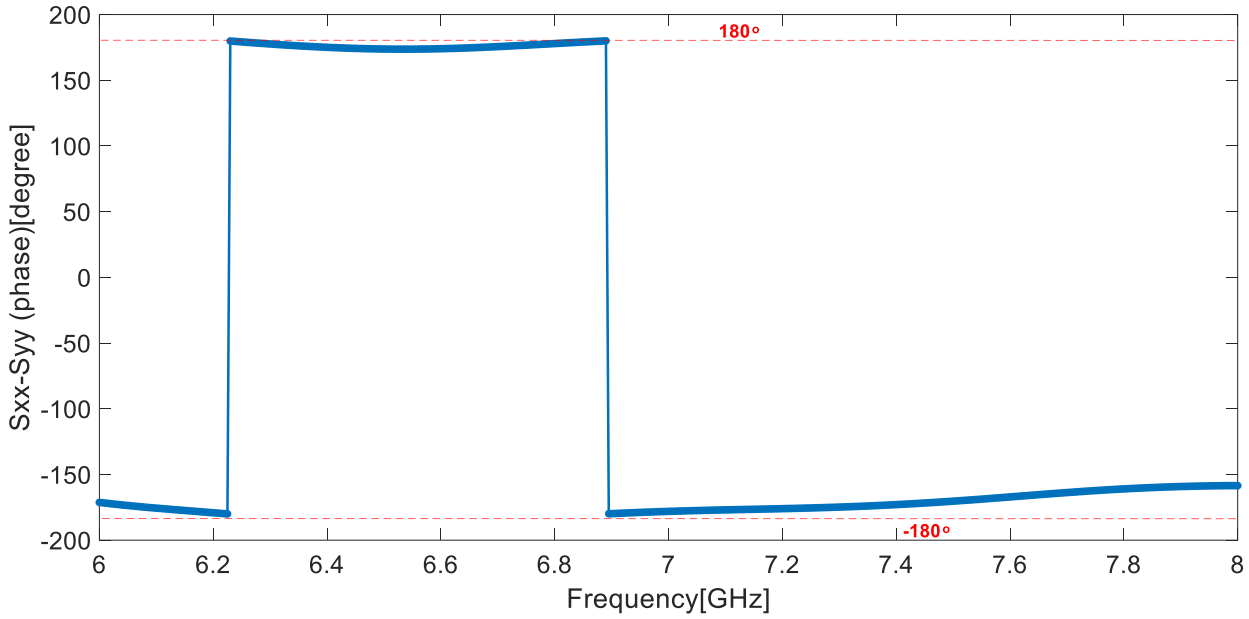

(b)

Figure 3.8 (a) Amplitude (a) and phase difference(s) of reflection coefficients for two orthogonal components of the electric field

In summary, the proposed unit cell for C-band CP reconfigurable reflectarray antennas exhibits a bandwidth of 15%, with the center frequency of 7 GHz, for a cross-polarization level 20 dB below the co-polarization level. The following section will introduce a CP septum polarizer feed horn with the proper features to illuminate the reflectarray.

3.3 CP feed horn

This section presents the design of the feed horn that will be used in all the experimental work involving the reflectarray.The designed horn implements a septum polarizer feed horn with proper characteristics in terms of half power beamwidth (HPBW) and gain for illuminating the C-band CP 10x10 reflectarray, used as the subreflector of dual-reflector structure. The performance of the fabricated feed horn is validated experimentally. Gain, SLL, beamwidth, AR and low spillover are the characteristics that need to be considered for the feed of the system.

3.3.1 Septum polarizer horn

The simulations done during the design of the horn have been carried-out with the surface integral equation solver of Altair FEKO®. By exciting a cylindrical waveguide with two orthogonal dominant modes (TE_{11}) with a 90 degrees phase difference, a CP wave will be produced. Proper dimensions for the circular cross section of the waveguide should be selected to propagate the dominant mode. However, in reality, linearly polarized electric fields are excited in the waveguide with a probe protruding from a coaxial cable. Therefore, a septum polarizer or an ortho-mode transducer (OMT) is needed for producing the CP wave. In contrast with the waveguide-based OMT, the septum polarizer inside the waveguide can create a CP wave without using an attenuator, phase shifter, and coupler to adjust two orthogonal electric fields.

A septum polarizer is a metal ridge that divides the waveguide with a rectangular or circular cross section into two parts (e.g., two semicircle cross sections for circular waveguide). A separate port feeds each part. The longitudinal and transverse cross sections of a cylindrical waveguide with a septum polarizer are shown in Figure 3.9. Using the waveguide with a circular cross section is

preferred in this work since there is no need for additional transition to connect the circular cross section of the CP horn aperture to the waveguide with a rectangular cross section. The precise design for the dimension of the metal ridge of the septum inside the waveguide is required. Left and right-hand CP waves will be created by feeding one of the coaxial ports of the feed horn while another port is connected to the matched load. In the septum polarizer horn design, good matching at each input port and maximum isolation between the two ports is required. These parameters can be optimized by adequately selecting the location of the coaxial probe in the waveguide as well as the shape and length of the probe. For a basic adjustment, $\lambda_g / 4$ for backshort distance and $\lambda_0 / 4$ for the extended probe length inside the waveguide are generally used, but these dimensions need to be adjusted for the impedance matching [40]. In this design, SMA connectors are used to feed the probes in the waveguide (See Figure 3.9).

The inner diameter of the cylindrical waveguide is 34mm. The SMA connector has Teflon as the dielectric, with ε_r of 2.1, $tan\,\delta$ of 0.0012, and the inner conductor and outer conductor diameters are 1.27 mm, and 4.1 mm, respectively. The optimized length of the cylinder-shaped probe is 9 mm, which is close to $\lambda_0 / 4$ at 7 GHz, and the radius of the probe is 1.1 mm. As shown in Figure 3.9a, the distance from the probe to the backshort of the waveguide is $\lambda_g / 4$. In our design, λ_0 and λ_g are equal to 42.8 mm and 63.5 mm, respectively.

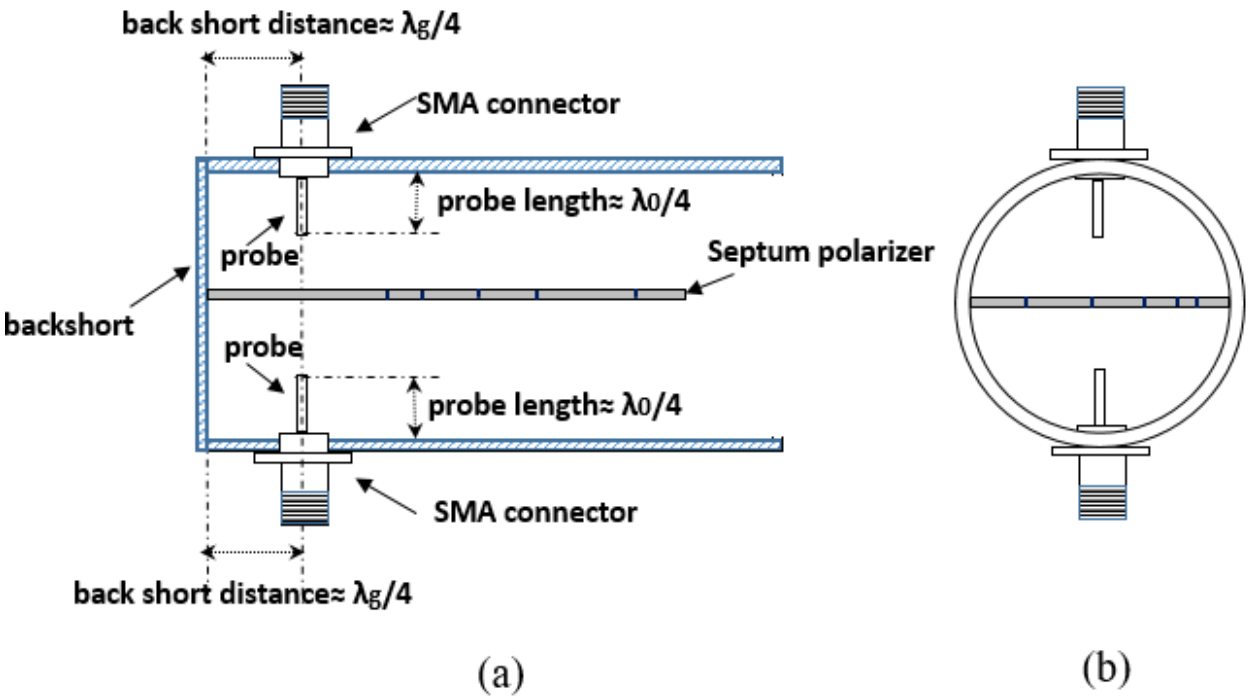

Figure 3.9 (a) Longitudinal (b) and transverse cross sections of the coaxial cable to circular waveguide transition, showing the septum polarizer

The top view of the septum polarizer is shown in Figure 3.10a. In this work, the septum polarizer in [41] is used after scaling for 7 GHz. The thickness of the septum is 0.0043λ. The dimensions of the septum are shown in Figure A.1 (Appendix A). The prototype of the waveguide with septum polarizer is shown in Figure 3.10b. Figure 3.10b shows that three edges of the polarizer (top, bottom and left side of the septum geometry in Figure 3.10a) are in contact with the metallic walls of the waveguide.

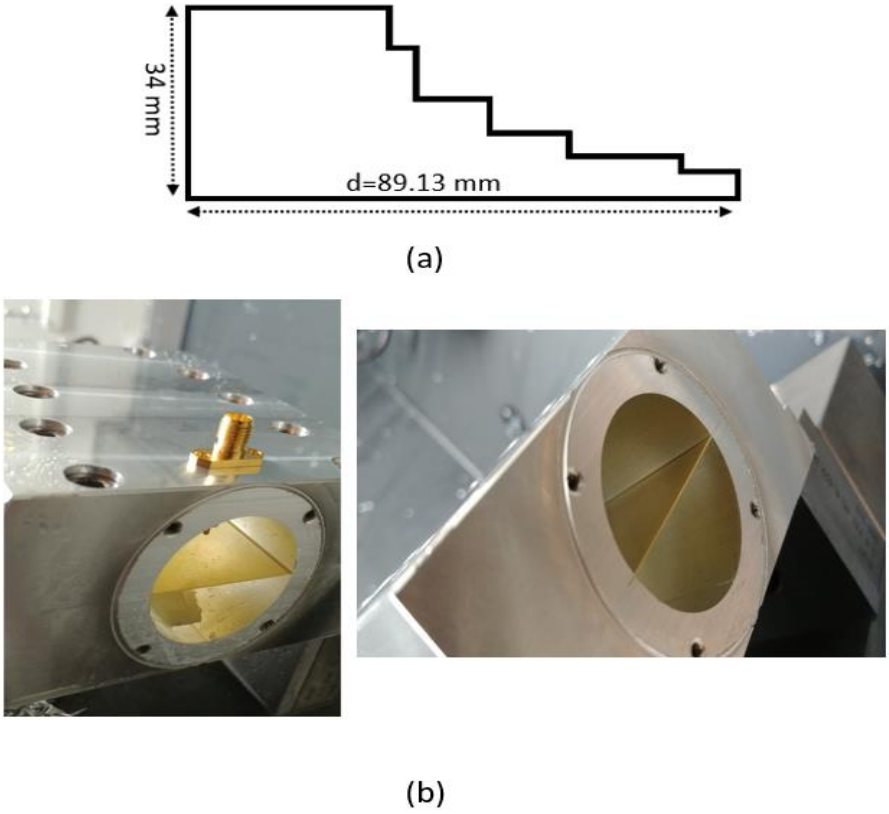

Figure 3.10 (a) Geometry of the septum polarizer (b) Prototype of the waveguide with septum polarizer

The operation of septum polarizer in transmission mode is explained by decomposition in even and odd modes as shown in Figure 3.11.

By exciting one of the coaxial ports, half of the TE11 mode is present on one side of the septum, and no fields are present on the other side. This asymmetric field distribution can be obtained by superposition of even and odd modes, as shown in the Figure 3.11 [42]. The even mode is excited when the currents on the two probes are in the same direction, while for the odd mode they are in opposite directions.

It can be demonstrated that the odd mode will lead to a horizontally polarized TE_{11} mode in the wavetuide, whereas the vertically polarized TE_{11} mode will be excited by the even mode. The reason for that is explained by looking at the current flow on the horizontal septum, the common

wall of the waveguide. For the even mode, the current flows in opposite directions on both sides of the common wall; therefore, there is no net current on the septum and therefore no distortion in the fields propagating from the region of the guide with septum to the region without septum. For the odd mode, the current flow in both sides of the common wall with the same directions. Therefore there is a net horizontal current on the septum. As the odd modes propagate towards the steps of the septum (see Figure 3.11); this current will generate horizontal E field between the septum and the waveguide wall. Gradually decreasing the septum width will lead to the formation of the horizontally polarized TE_{11} mode [43]. A vertically polarized field propagates inside the waveguide without change after passing through the septum, but horizontally polarized fields will have a phase difference at the end of the well septum slot. Septum polarizer with the appropriate dimension will produce a phase lag of 90 degrees between horizontal and vertical fields when the wave leaves the septum. By combining two orthogonal fields with 90 degrees phase difference, CP field will propagate towards the horn. CP waves of opposite senses of rotation are obtained by feeding each coaxial port respectively. For instance, if RHCP wave is propagated inside the horn by exciting port 1, LHCP will be propagated by exciting port 2.

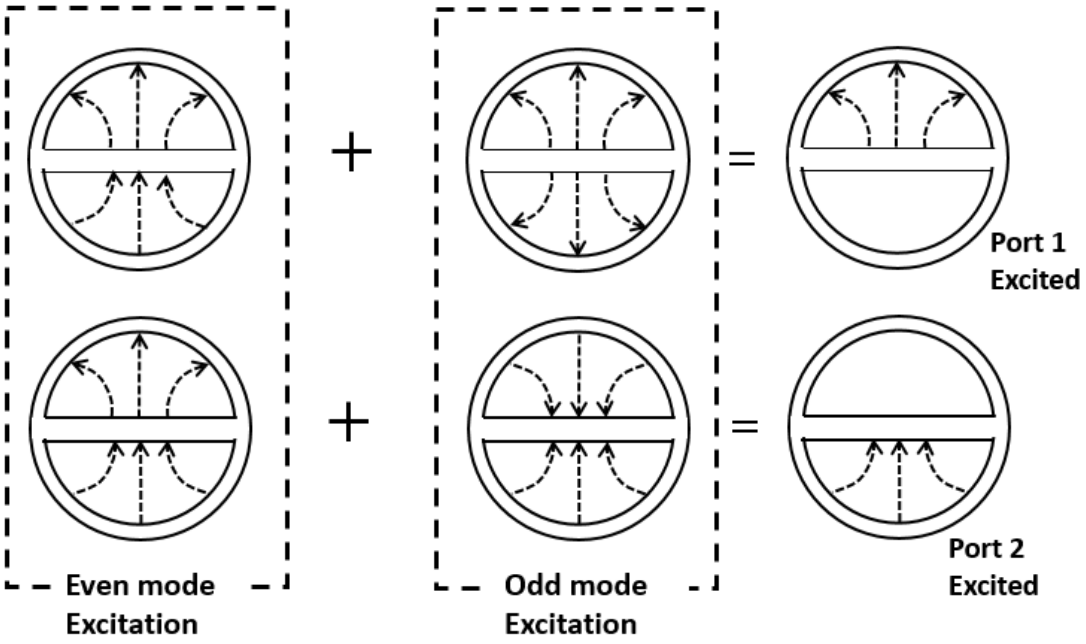

Figure 3.11 Decomposition into the even and odd modes for each port's excitation [42]

Figure 3.12 shows the difference between the amplitude and the phase of two orthogonal electric field components on the plane parallel to the top surface of the septum. For this simulation, one of the coaxial ports is excited while the other is terminated with a matched load. The value of 1 is observed for the magnitude of E_z / E_y , and the phase difference of -90 or 270 degrees is observed

between E_y and E_z. These simulation results confirms that the waveguide generates the CP wave with a septum polarizer.

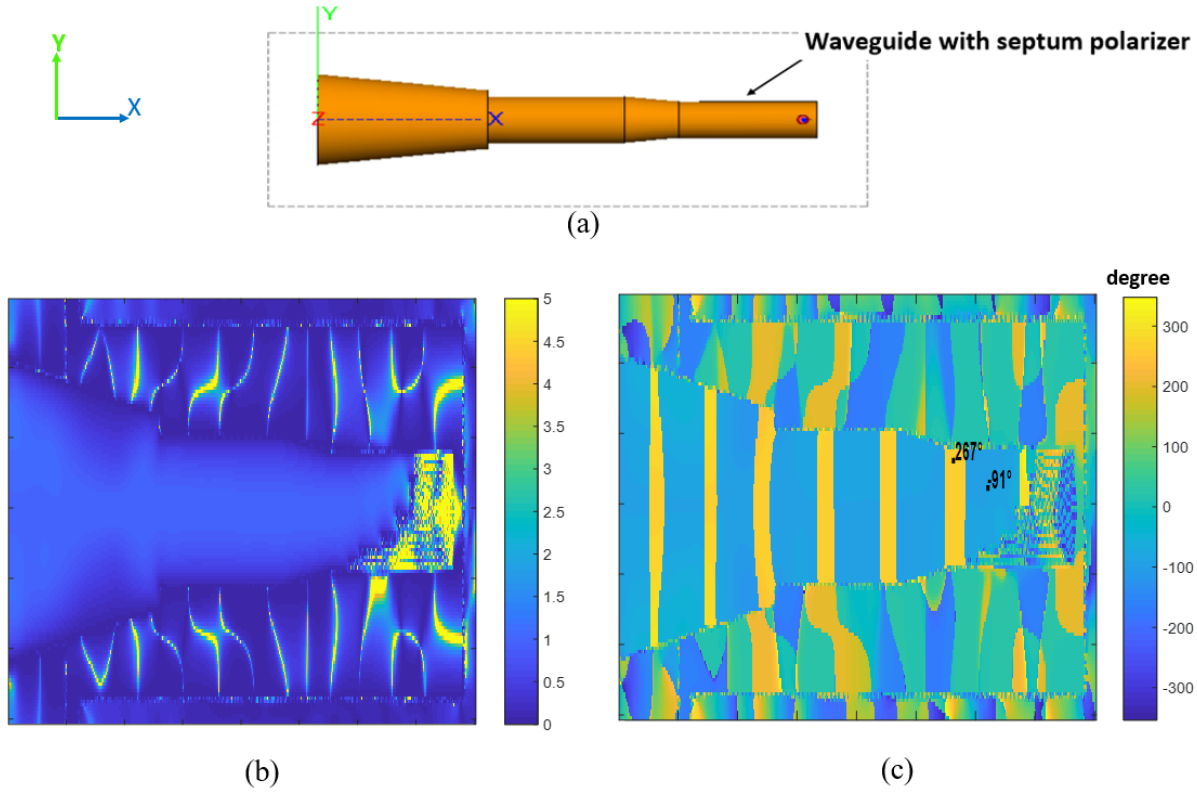

Figure 3.12 (a) Top view of the feed hon structure, (b) Comparison of the relative magnitudes between the E_y and E_z components (E_z / E_y), on the plane parallel to the top surface of the septum, (c) The phase difference between the E_y and E_z components on the plane parallel to the top surface of the septum

The CP horn is shown in Figure 3.13a. The dimensions of the horn's cross section, as well as the detailed geometry of the septum, are shown in Figure B.1 (Appendix B).

The prototype of the fabricated CP horn is shown in Figure 3.13b.

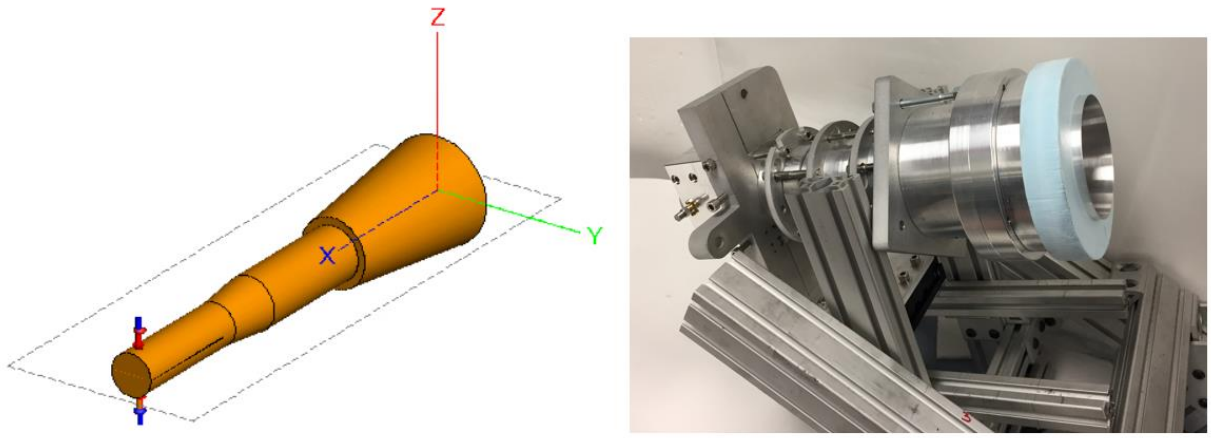

Figure 3.13 (a) Structure of the CP feed horn, (b) Prototype of the CP feed horn

The measured reflection coefficient at each port and isolation between the two ports are shown in Figure 3.14. the reflection coefficient of below -20 dB at each port, and isolation of about -25 dB is observed between the two ports in the frequency range of 6.2 to 8.3 GHz.

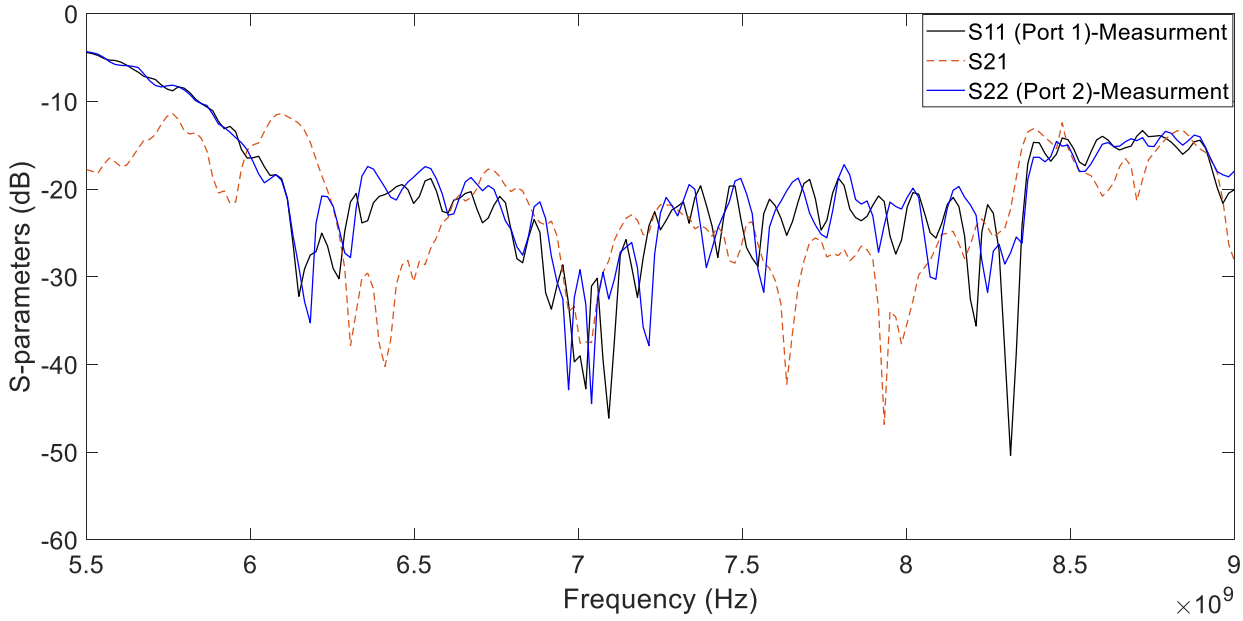

Figure 3.14 Measured reflection coefficients at each input port of the feed horn in Figure 3.13

The measured on-axis AR of the horn is shown in Figure 3.15, which is less than 1 dB in the frequency range of 6-7.8GHz. The axial ratio is obtained by roll axis rotation of the feed horn.

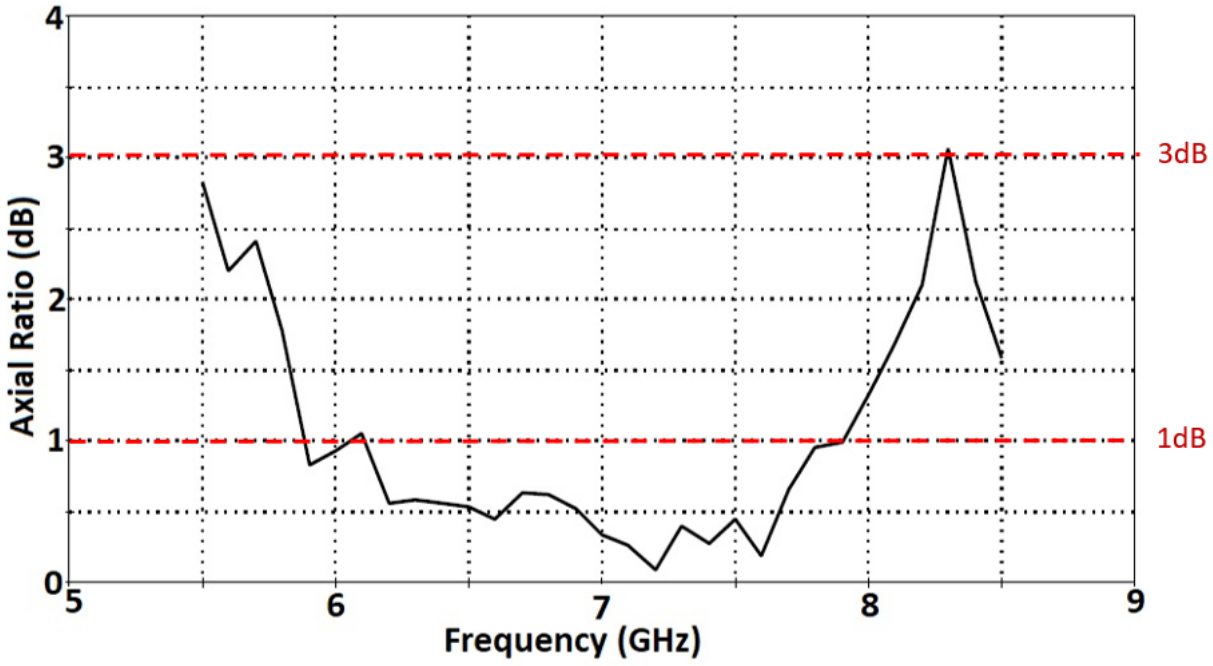

Figure 3.15 Measured on-axis AR of the feed horn in Figure 3.13

Figure 3.16 shows the radiation pattern of the measured and simulated feed horn with both polarizations in *xz* plane. By feeding each port, we could have either RHCP or LHCP. The simulated and measured frequencies are 7 GHz. The cross-polarization term of the measured pattern is higher than the simulation for both polarizations.

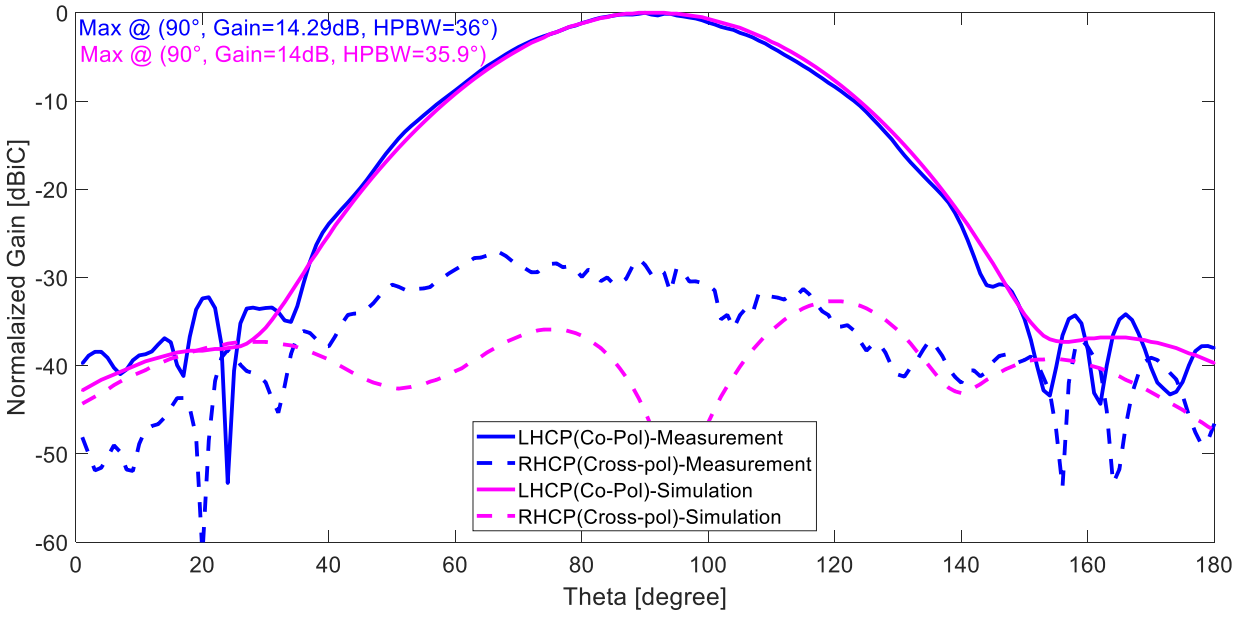

(a)

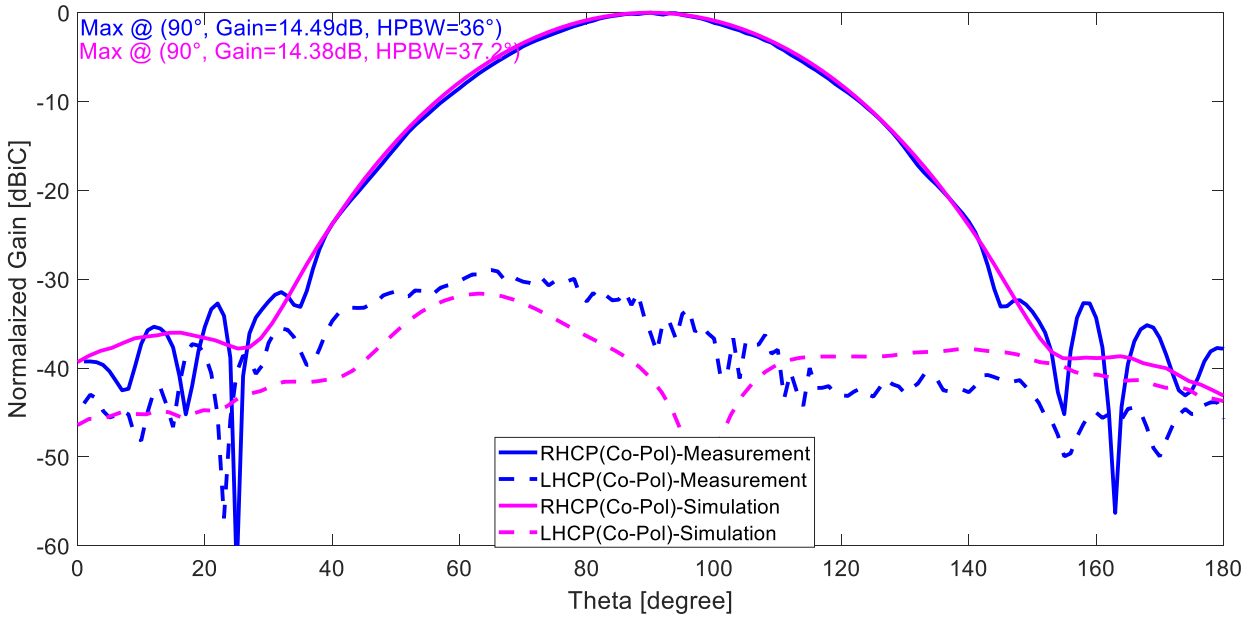

(b)

Figure 3.16 Measured and Simulated radiation pattern of the feed horn in Figure 3.13 at 7 GHz: (a) by feeding port 1 (RHCP is the co-polarization term and LHCP is the cross-polarization term), (b) by feeding port 2 (LHCP is the co-polarization term and RHCP is the cross-polarization term)

This section presented the septum polarizer feed horn. The gain and HPBW of the feed horn meet the requirement of the system to create proper edge illumination on the reflectarray with the optimum feed position, which will be discussed in the next section. The performance of the C-band CP reflectarray fed by the septum polarizer horn will be shown in the next section.

Edge illumination, gain, SLL, beamwidth, cross-polarization, and AR are the characteristics that should be considered in this system design.

3.4 C-band CP reconfigurable reflectarray

This section studies the performance of the reflectarray illuminated by the septum polarizer feed horn, introduced in the previous section. First, the performance of the system in terms of bandwidth, aperture efficiency, gain, beam scanning error versus frequency, and Cross-Polarization Discrimination (XPD), which is the ratio of co- to cross-polarization term will be explored. Afterward, the performance of the system will be studied experimentally. Furthermore, this work will examine the effect of phase quantization on the gain, SLL, and HPBW. Finally, the electromechanical system will be presented for controlling the elements of the reflectarray.

3.4.1 Center-fed configuration

In Figure 3.17, the spherical equivalent source of the CP feed horn introduced in section 3.3 illuminates the 100-cell C-band reflectarray in center-fed configuration. Using a spherical equivalent source of the feed for illuminating the reflectarray prevents the feed blockage, which is significant in the center-fed configuration. To use the equivalent spherical mode source, first, the horn antenna is simulated. Then, the far-field spherical expansion modes coefficients are exported to an .sph file as a spherical excitation. Finally, the horn antenna is removed from the system and replaced by the spherical equivalent source with the same orientation as the feed horn. The expansion of the spherical mode wave is presented in eq. (C.1) and eq. (C.2) in Appendix C [44, 45].

Some of the important performance indicators of reflector systems are the spillover of the feed radiation around the reflectarray and the taper of the illumination distribution on the reflectarray. The source position is a critical parameter in the reflector antenna that controls the slipover and taper efficiency. With small reflectarrays, choosing a proper value for the F/D parameter is more challenging (F corresponds to the distance from the horn phase center to the reflectarray, and D is the dimension of the reflectarray) [46]. For the proposed system, with a small aperture size reflectarray, by placing the reflectarray in the far-field of the feed horn at $2\frac{d^2}{\lambda}$, an edge illumination of -3 dB is obtained. *d* is the diameter of the feed horn aperture. This edge illumination level results in a low gain and high spillover. Figure 3.18 determines the optimum feed position for the reflectarray with the size of $3.67\lambda \times 3.67\lambda$ in the center-fed configuration ($\lambda = 42.8\text{mm}$). The whole model, including the equivalent source and reflectarray, is simulated by varying the F parameter, the distance between the source and reflectarray. In each F value, the reflectarray elements' rotation is re-adjusted to have a uniform reflected phase. The curve in the figure indicates that the optimum value obtained for F/D is 0.95, which is 0.44 of the far-field distance of the feed horn corresponding to 150 mm. This gives the edge illumination of -7 dB and the gain of 20.56 dB.

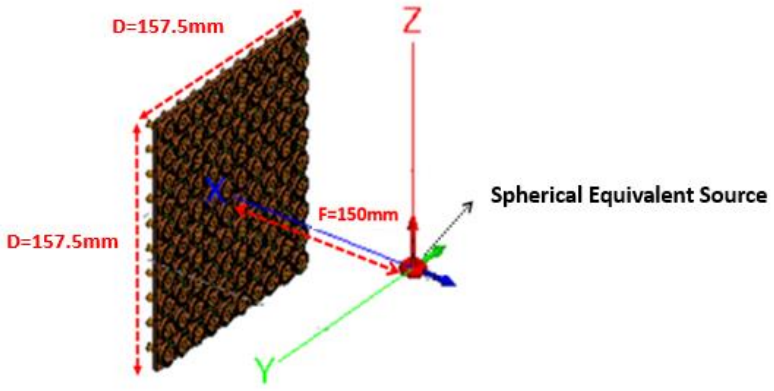

Figure 3.17 Center-fed configuration of the reflectarray and spherical equivalent source

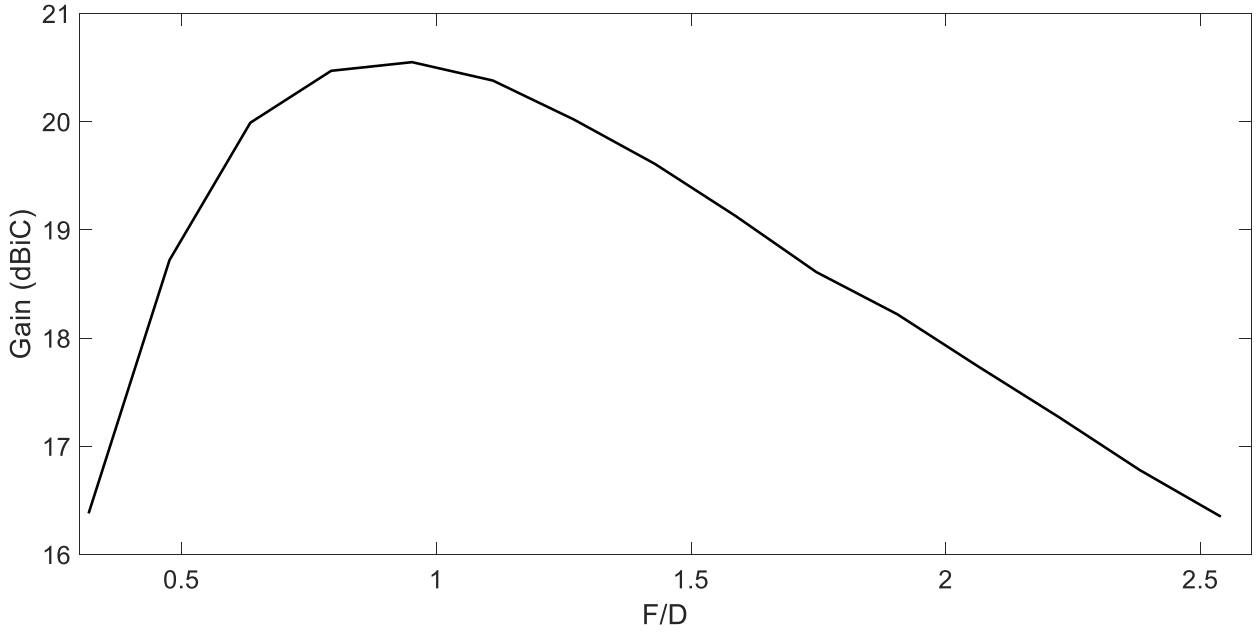

Figure 3.18 Simulated co-polarized CP gain vs F/D at 7 GHz of the system including the equivalent spherical wave source and the 100-element reflectarray

The gain of the reflectarray for the optimum F/D value in the frequency band of 5.5-8 GHz for the configuration in Figure 3.17 is shown in Figure 3.19a. In Figure 3.19, gain, XPD in HPBW, and aperture efficiency in the 5.5 GHz to 8 GHz frequency band are shown. A gain loss of less than 2.7 dB is observed within the frequency range of 5.5 GHz to 8 GHz with the center frequency of 7 GHz. A 1-degree beam deviation error is observed in the frequency band from 5.5 GHz to 8 GHz, and the direction of the main beam maximum is at 91 degrees in the xz plane. This deviation of the main beam from 90 degrees is due to the non-symmetry of the reflectarray's element factors.

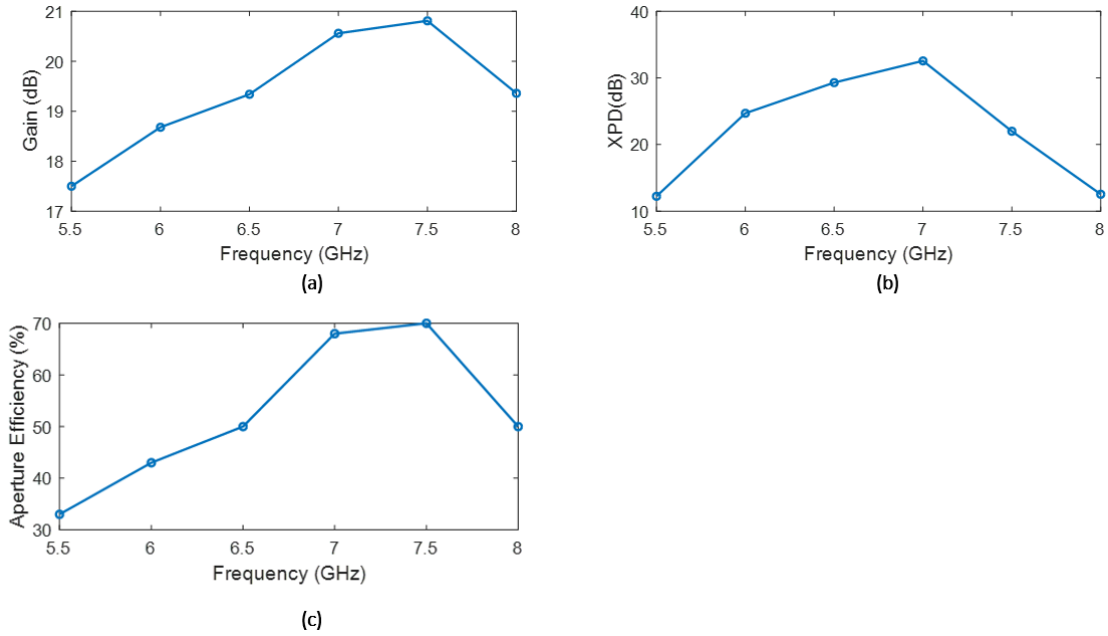

Figure 3.19 (a) Co-polarized gain vs Frequency, (b) XPD vs Frequency, and (c) Aperture efficiency vs Frequency

3.4.2 Beam steering performance of the reflectarray in the offset configuration

In this section, the beam steering capability of the reflectarray is studied with the offset configuration of the feed and the reflectarray. There is no need to use a spherical equivalent source in Figure 3.20 since there is no blockage by the feed in the offset configuration. For this purpose, the feed horn introduced in Section 3.3 is used to illuminate the reflectarray. As shown in Figure 3.20, the distance between the phase center of the source and reflectarray is 100 mm, and the clearance between the top edge of the feed horn and the bottom edge of the reflectarray is 26 mm. The proper distance between the horn and reflectarray is selected to obtain the high gain by optimizing spillover and taper efficiency. This configuration gives an edge illumination of 7 dB. The simulation of the antenna is done with FEKO at 7 GHz frequency. The beam steering angles of -45, -25, -15, 0 and $+15$ degrees in the xz plane, for the configuration in Figure 3.20 are shown in Figure 3.21. In that figure, 90 degrees represents zero steering, i.e. radiation in the $-x$ direction. The indicated negative (positive) steering angles are above (below) the $-x$ axis in the xz plane.

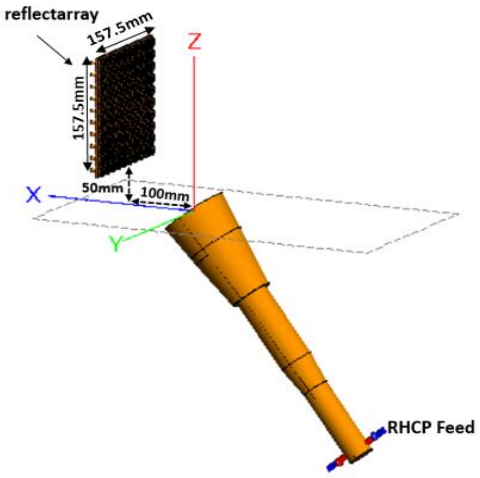

Figure 3.20 Offset configuration of the reflectarray and feed horn

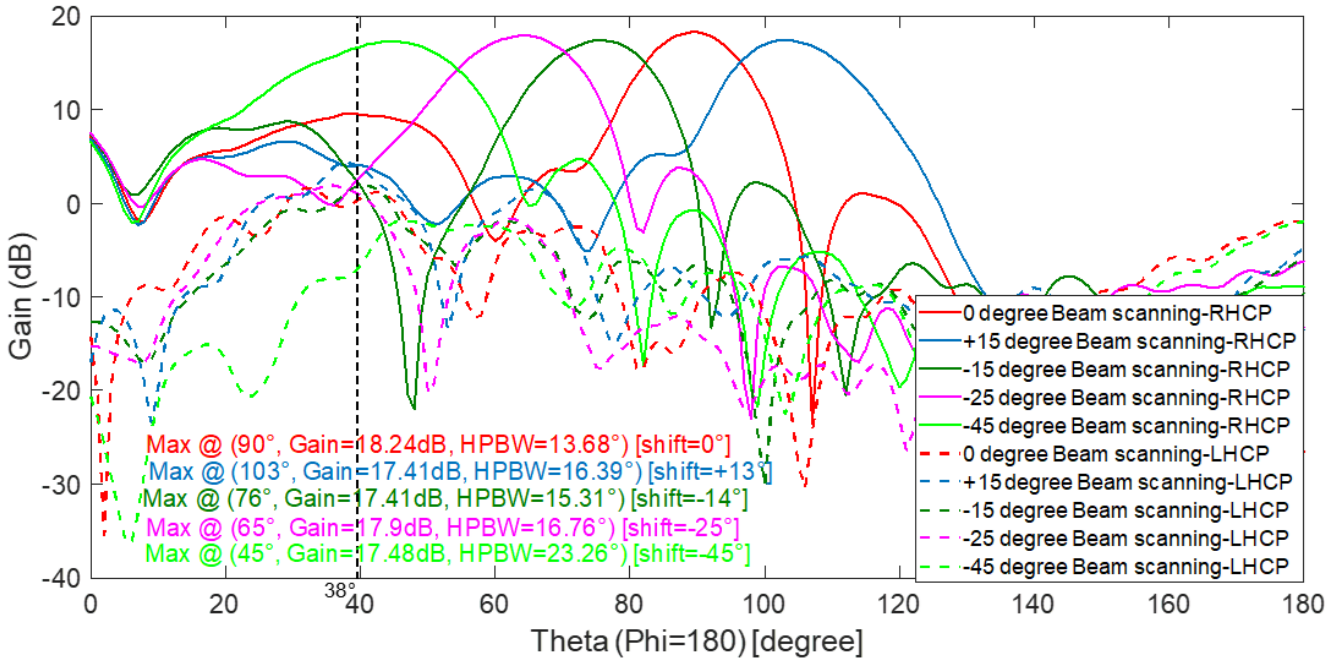

Figure 3.21 Beam steerings of –45, –25, –15, 0 and +15 degrees in the *xz* plane related to the configuration in Figure 3.20

As shown in Figure 3.21, the specular reflection appears as a cross-polarization term in the reflected beam at the angle of 38° according to Snell's law (the horn is pointed to the center of the reflectarray and formed the angle of 38° with the vertical yz plane). For the reflected beam with the scanned angle close to the specular reflection at $+38^{\circ}$, a lower XPD value is observed. Therefore, beam scanning should be avoided at angles close to the specular reflection.

Figure 3.21 shows that the scan loss of less than 0.8 dB was found for the beam scanned at -45 degrees. Also, realized steering angles are the same as the desired angles for beam steering angles of 0°, -25° and -45°, but only differ by 1° and 2° degrees for beam steering angles of -15° and $+15^{\circ}$. In Figure 3.21, with the RHCP feed, the desired polarization term is RHCP, and LHCP is considered the cross-polarization term.

3.4.3 Experimental validation of the reflectarray performance in the offset configuration

The performance of the reflectarray is offset configuration is studied and supported experimentally. The test configuration is shown in Figure 3.22. In this configuration, the distance between the horn and plane of the reflectarray is 150 mm, and the clearance between the top edge of the feed horn and the bottom edge of the reflectarray is 42 mm. Also, the size of the reflectarray is $3.67\lambda \times 3.67\lambda$ ($\lambda = 42.8\text{mm}$). The aperture of the feed horn is oriented towards the center of the reflectarray to minimize the spillover. Figure 3.23 show the good agreement between the measurement and simulation results in xy and zx planes. The frequency 7 GHz is selected at the simulated and measured frequency point. With the LHCP feed, the co-polarization term is LHCP, and RHCP is considered the cross-polarization term.

Deep nulls are observed in the simulation, which have disappeared in the measured beam. Also, the measured pattern has a higher SLL compared to the simulated pattern. Since in the measurement setup for simplicity, the rotation of the elements was done manually, step angles of 22.5° were selected for rotating each element. Therefore, the fade in the position of the nulls and higher SLL in the measurements may result from lower phase accuracy.

The cross-polarization level in the measurement is higher than the simulation due to the higher cross-polarization of the measured horn pattern compared to the simulated horn pattern in Figure 3.16.

The figure shows slight shifts of the measured main beam maximum angles compared to the simulation. Gain differences of few tenths of dBs between measured and simulated antennas can be attributed to measurement errors.

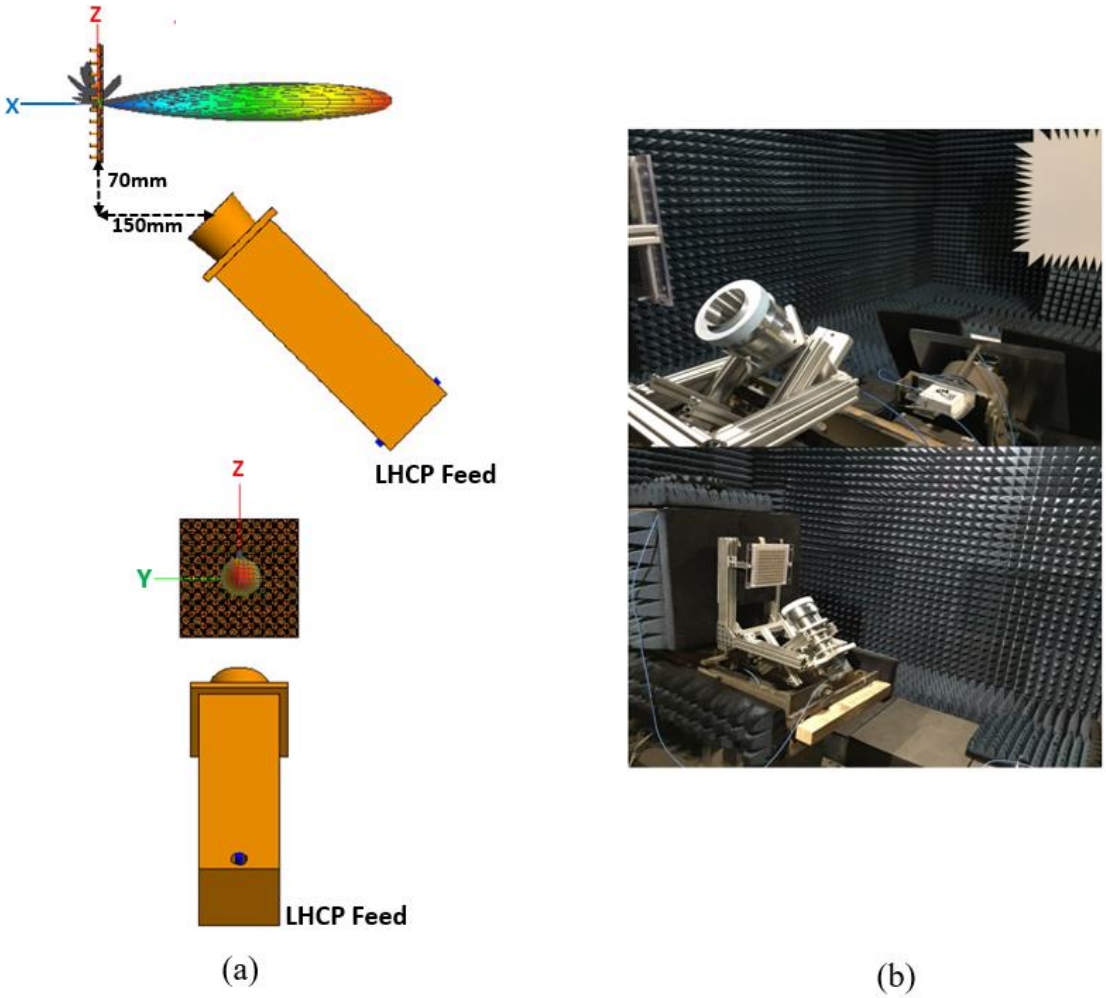

Figure 3.22 Offset configuration of the feed horn and reflectarray (a) simulation, (b) measurement

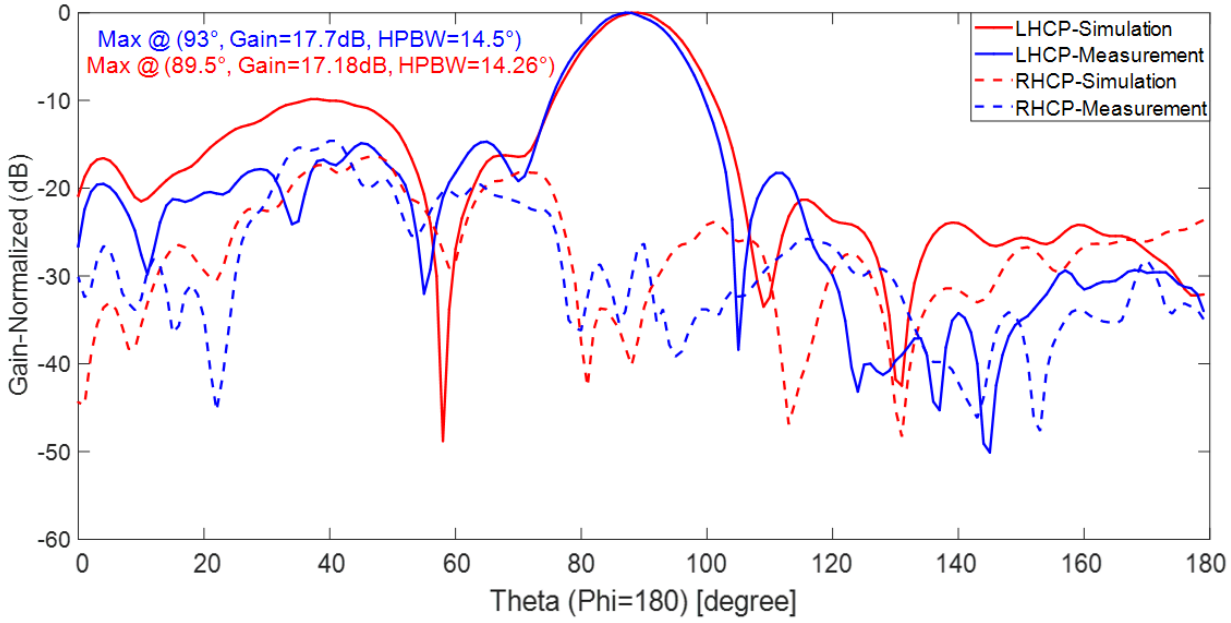

(a)

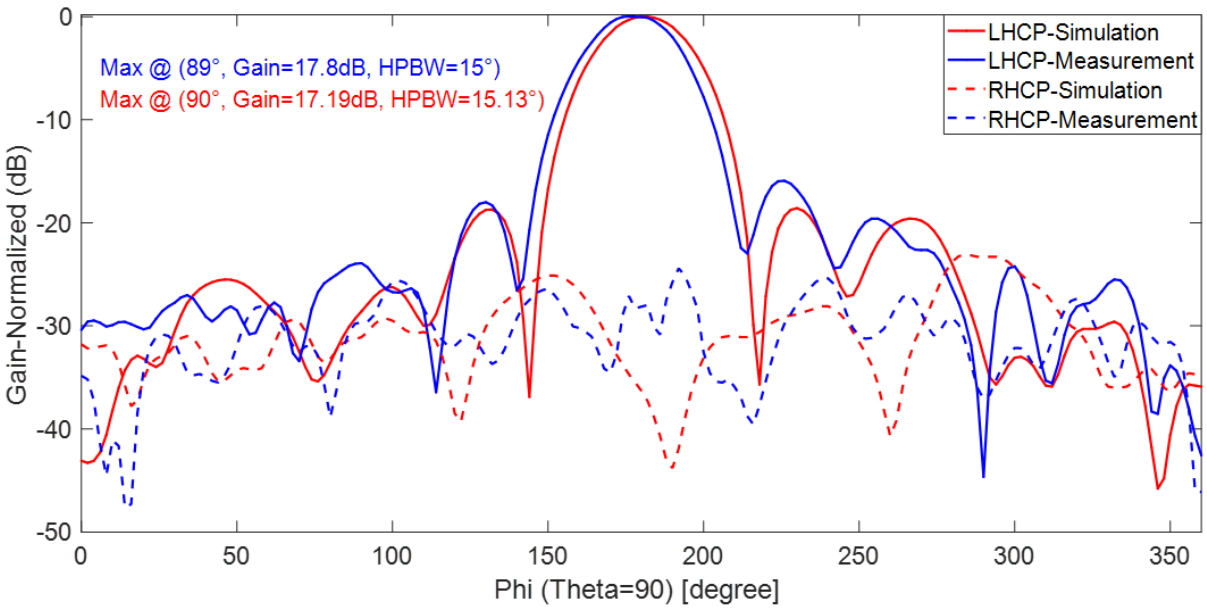

(b)

Figure 3.23 Radiation pattern related to the configuration in Figure 3.22 (a) in *zx* plane, (b) in *xy* plane

3.4.4 Dual reflector CP reflectarray

The unit cell design introduced in section 3.1 supports both RHCP and LHCP, which is confirmed by eq. (3.1) to (3.5) [22]. According to the variable rotation technique, the reflected beam in eq. (3.2) results from the incident beam in eq. (3.1). Incident beam comprised of both right-hand and left- hand CP waves traveling in the -z-direction. Therefore, reflected beam in eq. (3.2) consists of co- and cross-polarization terms of the RHCP and LHCP fields. Equations (3.4) to (3.5) define co- and cross-polarization terms in terms of linearly polarized S parameters. Equations (3.3) and (3.4) show that for RHCP and LHCP, the co-polarization term of the reflected electric field from each cell is 2 and -2 times the rotation angle of each element, respectively.

$$\mathbf{E}^{\text{inc}} = \mathrm{A}_{\mathrm{RH}}(\mathbf{a}_x + j\mathbf{a}_y)\, e^{jzk_0} + \mathrm{A}_{\mathrm{LH}}(\mathbf{a}_x - j\mathbf{a}_y)\, e^{jzk_0} \tag{3.1}$$

$$\begin{aligned}\mathbf{E}^{\text{ref}} &= \left[\Gamma_{\text{co-pol.RH}}\mathrm{A}_{\mathrm{RH}} + \Gamma_{\text{cross-pol}}\mathrm{A}_{\mathrm{LH}}\right](\mathbf{a}_x - j\mathbf{a}_y)\, e^{-jzk_0} \\ &+ \left[\Gamma_{\text{co-pol.LH}}.\mathrm{A}_{\mathrm{LH}} + \Gamma_{\text{cross-pol}}.\mathrm{A}_{\mathrm{RH}}\right](\mathbf{a}_x + j\mathbf{a}_y)e^{-jzk_0}\end{aligned} \tag{3.2}$$

$$\Gamma_{\text{co-pol.RH}} = \Gamma^{\psi=0}_{\text{co-pol.RH}} e^{+j2\psi} = \left(\frac{1}{2}(s'_{xx} - s'_{yy}) + js'_{xy}\right)e^{+j2\psi} \tag{3.3}$$

$$\Gamma_{\text{co-pol.LH}} = \Gamma^{\psi=0}_{\text{co-pol.LH}} e^{-j2\psi} = \left(\frac{1}{2}(s'_{xx} - s'_{yy}) - js'_{xy}\right)e^{-j2\psi} \tag{3.4}$$

$$\Gamma_{\text{cross-pol}} = \frac{1}{2}(s'_{xx} + s'_{yy}) \tag{3.5}$$

Therefore, proposed elements could support either RHCP or LHCP by changing the feed polarization. Figure 3.24 shows the far-field pattern of the reflectarray when illuminated by RHCP or LHCP feed. As shown in the figure, both RHCP and LHCP beams have a gain of 18dB with an HPBW of about 14^{o}. Also, XPD of 29 dB is observed for the beam with RHPC co-polarized term, while the XPD of 25dB is observed for the beam with LHCP co-polarized term.

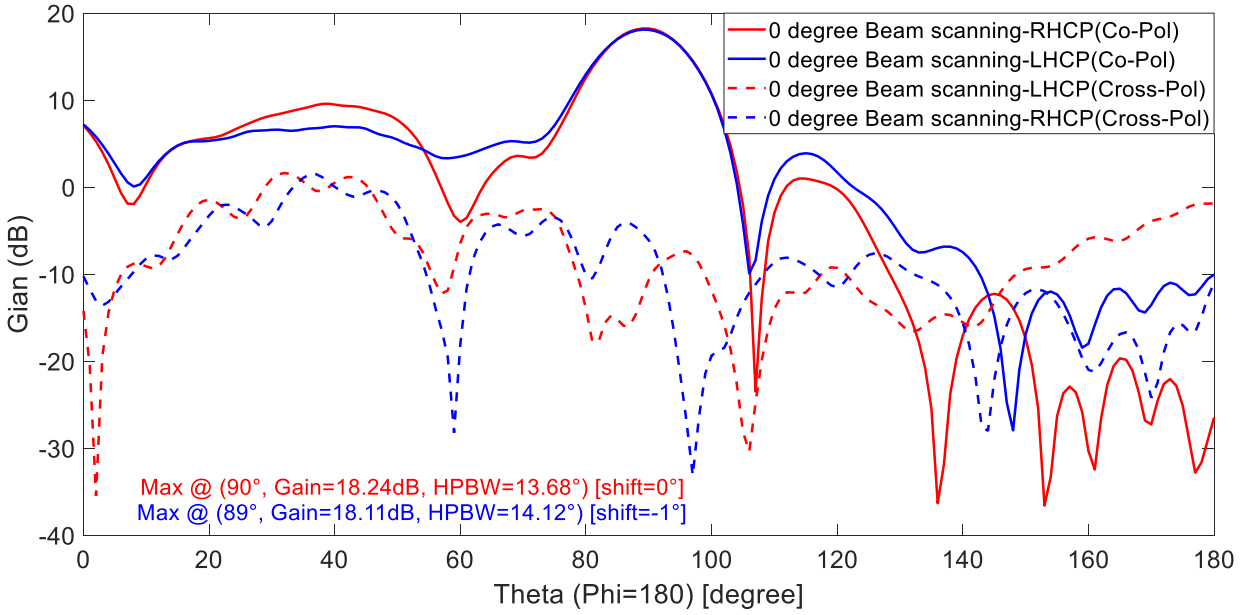

Figure 3.24 Radiation pattern related to offset configuration in Figure 3.20

3.4.5 Phase quantization effect

The performance of the reflectarray by applying 3, 2, and 1-bit phase quantization is evaluated with simulation results in this section. Figure 3.25 shows the normalized radiation pattern for the reflected beam from the reflectarray at boresight by applying continuous phase distribution, 1, 2, and 3-bit phase quantization. In Figure 3.25, with the RHCP feed, the desired polarization term is RHCP, and LHCP is considered the cross-polarization term.

In comparison to the no-quantization case, gain losses of 0.4 dB, 1.52 dB, and 4.8 dB appear for 3, 2, and 1-bit quantization, respectively. The deep null near θ=100 degrees is diminished for quantized cases. The improvement in SLL should be observed with better phase accuracy. However, higher SLL is observed for the small aperture size arrays [47]. Figure 3.25 confirms that higher SLL is observed for 1-bit quantization compared to the other cases. The SLL for 1-bit quantization is 5 dB higher than in the continuous phase case. HPBW is independent of the number of phase quantization and only depends on the size of the reflectarray [47]. This is nearly the case with the curves in Figure 3.25, but beamwidth variations remain visible.

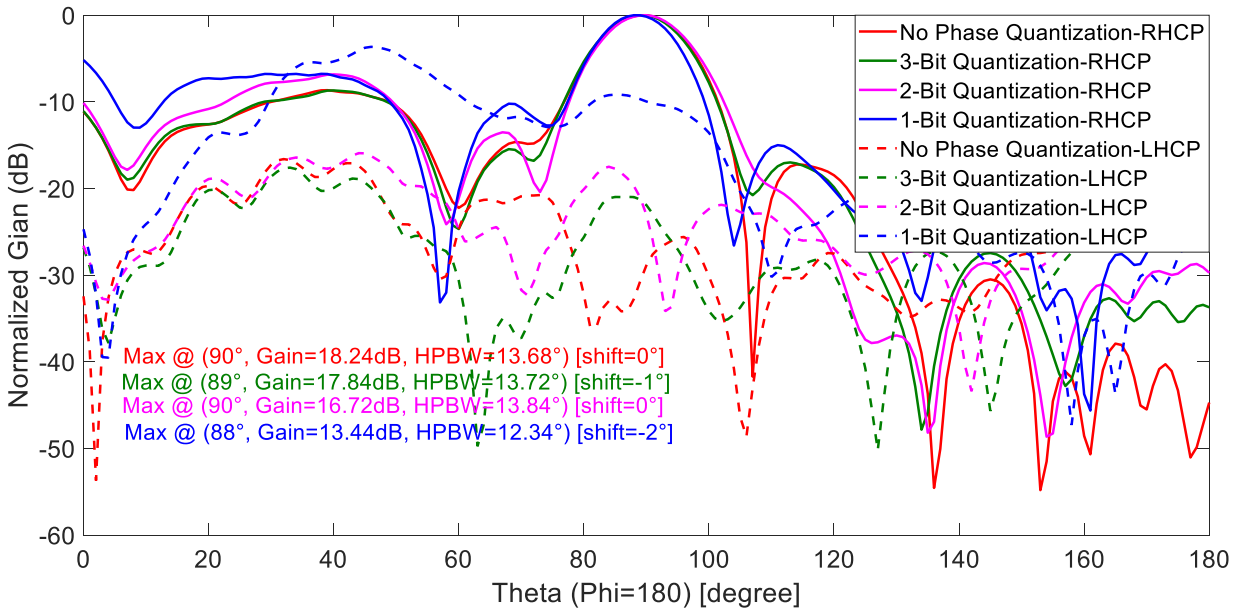

Figure 3.25 Normalized radiation pattern for the reflected beam from the reflectarray at boresight by applying continuous phase distribution, 1, 2, and 3-bit phase quantization

A shift in the direction of the main beam is observed for 1-bit quantization.

The cross-polarization level increases with lower bit quantizations. The reason for that is high uniformity in the alignment of the reflectarray elements with limited phase states. Figure 3.2a shows the changes in the cross-polarization level of the elements with different rotation angles.

The performance of the reflectarray with applied phase quantization is compared with previous works in Table 3.2. Usually, for smaller apertures with lower resolution, better phase accuracy is required to improve the array's gain loss and SLL. Therefore, the table shows the acceptable performance from the reflectarray proposed in this work compared to the literature.

Table 3.2 Comparison of array performance due to the phase quantization effect with reference papers

Ref No.	Reflectarray Size	Element numbers	Feed Polarization	Quantization	Loss
[6]	6.6λ octagonal	540	CP	3 Bit	0.2dB
[48]	11λ x 11λ	160X160	LP	1 Bit	3.9dB
[49]	10λ diameter Circular aperture	508	LP	1 Bit	>3.5dB
This work	3.78λ x 3.78λ square	100	CP	3 Bit	0.4dB
This work	3.78λ x 3.78λ square	100	CP	2 Bit	1.52dB
This work	3.78λ x 3.78λ square	100	CP	1 Bit	4.8dB

3.5 Motor Control System

This section introduces electromechanical actuators for rotating the elements of the reflectarray designed. The servo motor, which can be controlled with an accuracy of a 1-degree rotation angle for each element, is selected to meet the requirement for precision angular movement of each of the reflectarray elements. One hundred micromotors are used to rotate 100 elements of the reflectarray. The complete structure of the motor control system is presented in Appendix D [50]. The credit goes to Nicolas Pucci-Barbeau for designing and developing the electromechanical part of the system.

The 3D model for the motor control system is fabricated with a 3D printer, as shown in Figure 3.26, by considering the required gap between the elements. The choice of a stepped structure is the solution found to respect the spacing between the reflectarray elements by using servo motors. In this structure, connecting rods are needed between each motor and each reflectarray element.

The reflectarray is placed on the frame shown on top of the structure in Figure 3.26b.

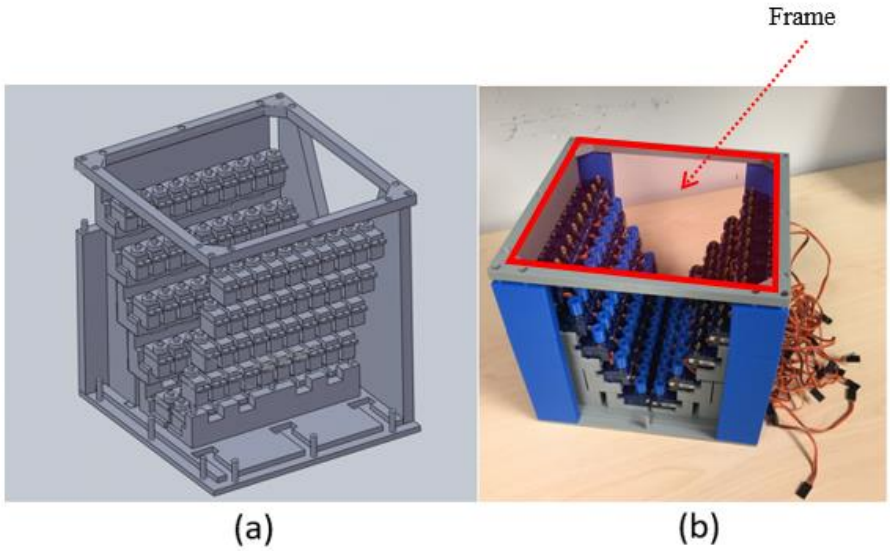

Figure 3.26 Electro-mechanical control system: (a) 3D view of the motor support structure, (b) Motor control system fabricated with a 3D printer

3.6 Conclusion

A C-band CP reconfigurable reflectarray with 100 elements has been presented in this chapter. The proposed reflectarray provides a 3-dB bandwidth of 28% with an average aperture efficiency of 55% and a gain variation of 17.5 dB to 21 dB in the frequency band from 5.5 GHz to 8 GHz.

A 100-cell reflectarray has been fabricated, and radiation pattern has been measured by studying the 3-Bit phase quantization effect on the radiation pattern. An increase in the SLL is also observed by reducing the number of phase states by switching from continuous phase distribution to 1-bit quantization. Quantization effect has been studied on reflectarray performance. The gain losses of 0.4 dB, 1.5 dB, and 4.8 dB are obtained for 3, 2, and 1 bit quantization, respectively.

Circular rings are used as reflectarray elements instead of electronic devices due to their low cost, high power handling, and ease of reconfigurability. Motors rotate the elements to scan the beam.

CHAPTER 4 BEAM SCANNING IN A DUAL-REFLECTOR ANTENNA WITH A C-BAND CIRCULARLY POLARIZED RECONFIGURABLE REFLECTARRAY AS SUBREFLECTOR

4.1 Introduction

High gain antennas relying upon parabolic reflectors are used extensively in radars and long-distance communications. The beam steering of these antennas is provided by mechanical movement of the dish and suffers from speed limitation and cost issues. In recent years, several dual-reflector structures have been proposed for beam scanning and beam shaping purposes. In a dual-reflector antenna structure, the main, the sub, or both reflectors can be replaced by reflectarrays. A dual-reflector antenna including a small sub-reflectarray and a main parabolic dish has better bandwidth and is easier to manufacture than a single large reflectarray. This antenna can also provide better performance than conventional dual-reflector antennas, including potential capabilities to scan and reconfigurable the beam, which is provided by adjusting the phase on the sub-reflectarray [51, 4].

This chapter proposes a high-gain and wideband dual-reflector structure with flexibility in beam shaping and beam synthesis realized with a reconfigurable reflectarray as the subreflector. Beam reconfigurability of the dual-reflector antenna is obtained by adjusting the phase shift of the limited-size reconfigurable sub-reflectarray elements by electromechanical approaches [52]. The proposed antenna system operates in circular polarization (CP) to meet the requirements of modern satellite systems. The CP property requires the design of special reflectarray cells presented in the previous chapter. The variable rotation technique is implemented in the design of the reflectarray unit cells, which leads to a proper phase adjustment over a broad bandwidth. A prototype of the sub-reflectarray was fabricated, and its performance has been validated experimentally in Chapter 3.

In this chapter, different methods are proposed for the scanning of a narrow beam with the proposed dual-reflector structure. Section 4.2 studies the Beam Deviation Factor (BDF) concept. Section 4.3 presents narrow-beam scanning out of the dual-reflector structure by introducing three methods. In

the first method, beam scanning is realized by moving a flat metal subreflector. The second method studies beam scanning of a dual-reflector system by applying a Progressive Phase Shift (PPS) across the sub-reflectarray aperture. In the third method, a new approach for beam scanning of the dual-reflector system is proposed by using Near-Field Focusing (NFF) technique. In the end, a comparison between the two last methods is presented. Section 4.4 experimentally demonstrates the narrow beam scanning performance of the proposed reflector system. In Section 4.5, the bandwidth performance of the proposed antenna will be discussed. Finally, Section 4.6 concludes the chapter.

4.2 Beam deviation factor (BDF)

Beam scanning of dual-reflector antennas could be obtained by taking advantage of the BDF concept without mechanical movement of the reflectors. Lateral feed displacement near the focal point in a system consisting of a feed and a parabolic reflector is an effective way to scan a narrow beam with low loss. The scan angle is quantified by the BDF concept. In Figure 4.1a, the parabolic reflector is illuminated by the horn feed having its phase center located at the focal point of the dish. When lateral displacement is applied to the feed, the reflected beam from the main reflector is tilted. Suppose the feed is displaced laterally from the focal point of the dish in the focal plane to form an angle θ_f as defined in Figure 4.1a. In this case, a good approximation of BDF for small displacement is calculated by eq. (4.1) [53]:

$$BDF = \frac{\theta_b}{\theta_f} = \frac{1 + 0.36 \times \left[4\frac{F}{D} \right]^{-2}}{1 + \left[4\frac{F}{D} \right]^{-2}} \tag{4.1}$$

where θ_b is the resulting deviation of the main beam direction. We will verify the accuracy of this equation by simulating a reflector system in FEKO. In these simulations, the LHCP horn introduced in Chapter 3 illuminates a parabolic dish in an offset configuration. In the hybrid simulation, the horn is simulated with the method of moments (MoM) and the reflector with physical optics (PO). In this case, PO and MoM/MLFMM solutions are coupled; therefore, mutual interactions between

the horn and the dish are taken into account. In Figure 4.1a, the projected diameter of the dish in the *yz* plane is 24λ (λ=42.8 mm), and *F/D* is 0.5. The angle of the horn with respect to the horizontal plane is $47°$. Thus, the spillover around the dish is minimized.

Moving the phase center of the feed with respect to the focal point of the dish by δ=±20 mm along the directions shown by the black arrows in Figure 4.1a corresponds to $\theta_f = \pm 2.12°$, for which a deviation θ_b of 1.83° is obtained from eq. (4.1). This is in good agreement with the FEKO simulations results depicted in Figure 4.1b where the obtained deviation angles are +1.8° and -1.9°.

Since the feed in the figure is LHCP, for the beam reflected from the dish, the RHCP term is considered co-polarization term, and LHCP is deemed to be the cross-polarization term.

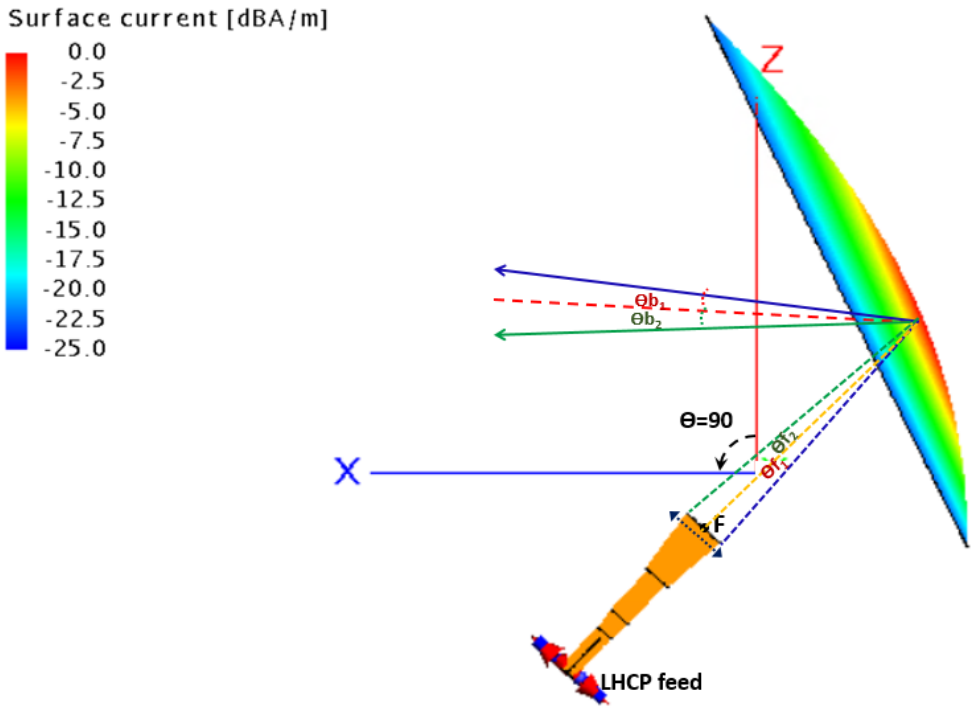

(a)

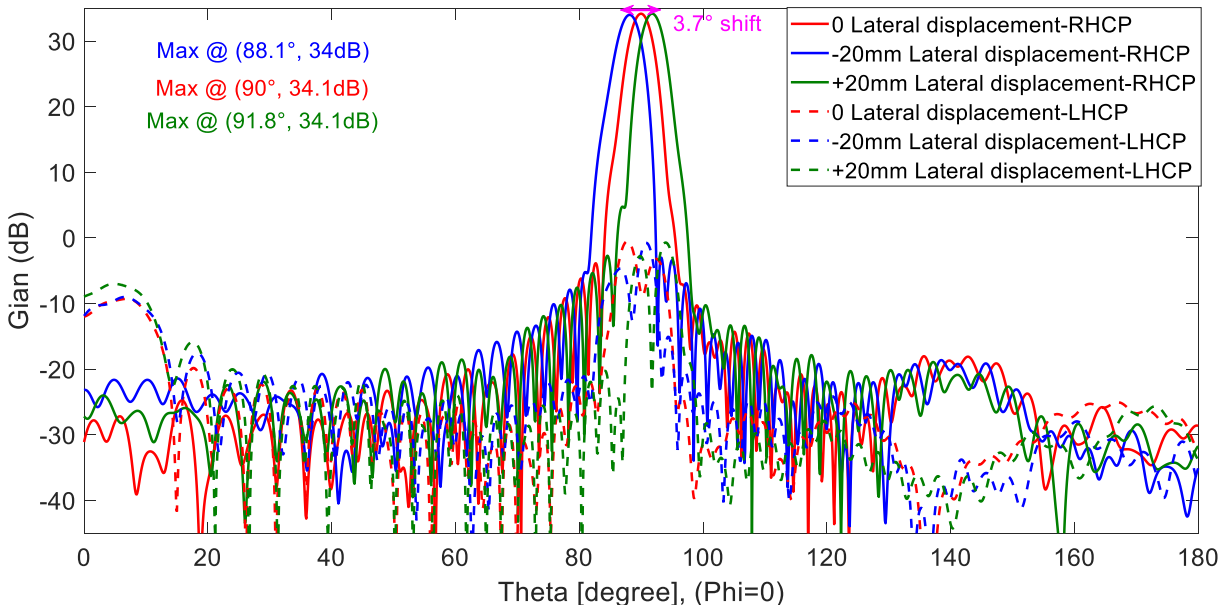

(b)

Figure 4.1 (a) Beam scanning by lateral feed displacement. The projected diameter of the dish in the *yz* plane is 24λ (λ=42.8 mm), and *F/D* is 0.5, (b) Radiation pattern of the scanned beam by lateral feed displacement of 0, +20 mm and −20 mm in the *xz* plane

4.3 Beam Scanning of dual-reflector antenna

This section studies three methods for realizing beam scanning with the dual-reflector antenna. In the first method, beam scanning is provided by tilting a flat metal subreflector. This is a simple way of scanning the beam out of the dual-reflector antenna without using the sub-reflectarray. However, this method suffers from a high amount of spillover around the subreflector emitted from the feed horn. The second method uses the same configuration, but the metal subreflector is replaced with a reflectarray in which the phases are adjusted to implement PPS. It will be seen that this method suffers from a high cross-polarization level with the scanned beams. A third approach is proposed . It is implementing the NFF technique with slight modification in the configuration used by the second method.

4.3.1 Beam scanning in dual-reflector structure with flat metal subreflector

This section considers the beam scanning in dual-reflector antennas using a flat metal subreflector [3, 4, 52]. This method is studied with simulations using the configuration shown in Figure 4.2, where the feed horn illuminates a flat metal subreflector in an offset configuration. The size of the metal subreflector is $3.67\lambda \times 3.67\lambda$ (same as the reconfigurable reflectarray used in the other two methods), and the projected diameter of the dish in the yz plane is 24λ. The phase center of the feed horn is placed at 3.45λ from the center of the subreflector (λ=42.8 mm). The proper distances between the horn, reflectarray, and dish are selected to minimize the spillover around the subreflector and the dish. As shown in Figure 4.2, if the focal point of the parabolic dish is placed at the virtual image of the feed phase center created by the subreflector, the main beam created by the main reflector points in boresight direction (i.e. $\varphi = 0°$ and $\theta = 90°$). By tilting the metal subreflector about *z* axis by few degrees, the virtual image of the phase center is moved away from the focal point of the dish, and the main beam is deflected off-boresight as shown in Figure 4.3.

The amount of the spillover around the subreflector is increased with a larger tilt angle of the subreflector. Therefore, a limited scan range is obtained with this configuration unless the subreflector size is increased [3, 52]. In this example, the dish *F/D* is 0.5. For subreflector tilt angles of 5 and -5 degrees, the simulated main beam steers by +1.7 and -1.6 degrees, while the deviation angle θ_b predicted by eq. (4.1) is 1.3 degrees on both sides. The difference between the deviation angle predicted by eq. (4.1) and obtained with simulations is due to the interference between the spillover beam around the subreflector and the reflected beam from the dish. In fact, since the CP radiation from the horn experiences two reflections on metallic surfaces, there are two changes of polarization sense. Consequently, the main beam polarization is the same as the spillover around the subreflector, and both radiations are towards the positive x half-space. Angle θ_f in eq. (4.1) is calculated using the configuration in Figure 4.1a by replacing the feed with the virtual image of the feed phase center. As shown in Figure 4.3, the same XPD values are observed for tilted and non-tilted cases. LHCP and RHCP are respectively the co-polarized and cross-polarized terms for the beam reflected from the parabolic dish. In the simulation, PO and MoM/MLFMM solutions are coupled; therefore, mutual interactions between the horn, the subreflector, and the dish are taken into account.

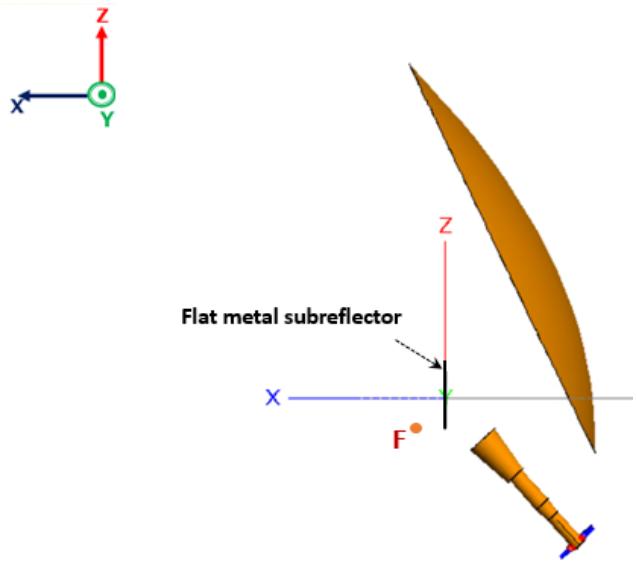

(a)

Figure 4.2 Dual-reflector antenna with a metal flat subreflector; the size of the metal subreflector is $3.67\lambda \times 3.67\lambda$ and the projected diameter of the dish in the *yz* plane is 24λ (λ=42.8 mm)

Figure 4.4 shows the current distribution magnitude on the dish for three cases. It can be seen in these projections of the system in the *yz* plane that the blockage of the reflected beam from the dish by the subreflector for the tilted cases is less compared to the non-tilted case. As a result, 0.1dB loss in the gain in Figure 4.3 is observed for the non-tilted case compared to the tilted cases. The offset of $\theta_b = -0.3°$ is observed in Figure 4.3 for the non-tilted case. This offset changes sign ($\theta_b = +0.2°$) when the polarization of the feed horn is switched from LHCP to RHCP. Beam squinting of circular polarization beams in the offset-fed configuration is a well-known phenomenon calculated by eq. (4.2) [54]. In this equation, θ_0 is the tilt angle of the feed, and *F* is the focal point of the dish.

$$\psi_S = \pm asin\left(\frac{\lambda sin(\theta_0)}{4\pi F}\right) \tag{4.2}$$

The value θ_0 in Figure 4.2 is 47 degrees. The beam squint angle of $\psi_s = -0.27°$ is obtained, which is close to the offset value of $\theta_b = -0.3°$ degrees found in Figure 4.3, for the non-tilted case. The reflected beam from the dish, which forms an LHCP beam, squints towards negative φ, while the RHCP radiated beam squints towards positive φ [55, 56].

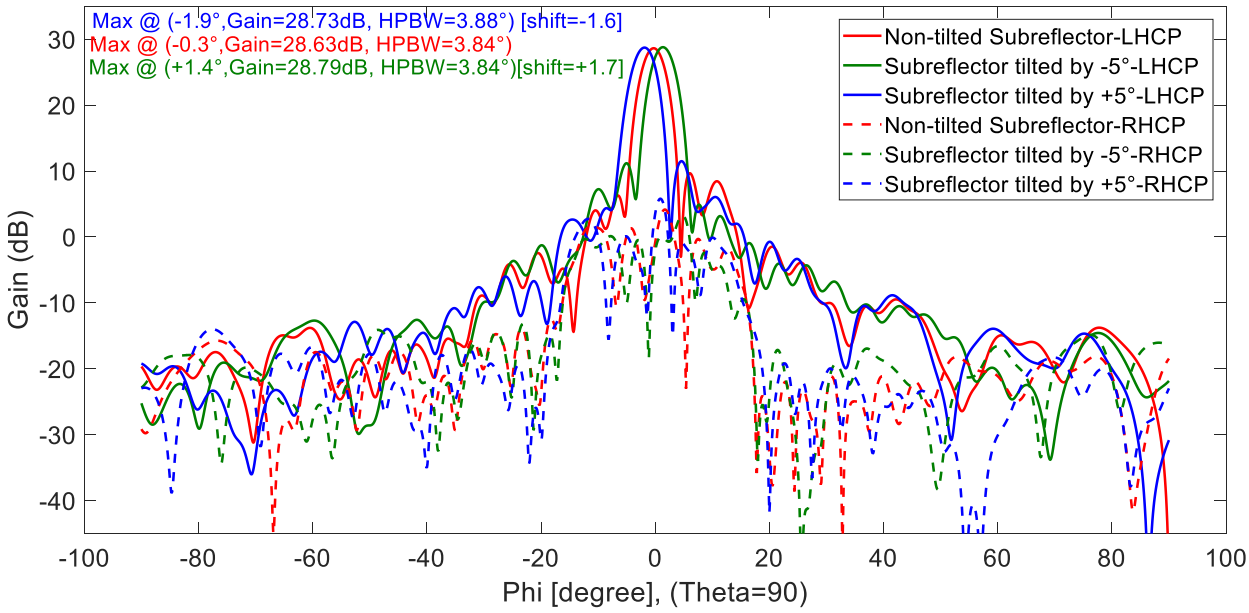

Figure 4.3 Beam scanning at $\theta = 90°$ by tilting the metal subreflector by the angles of $0°$, $-5°$, and $+5°$ about *z* axis

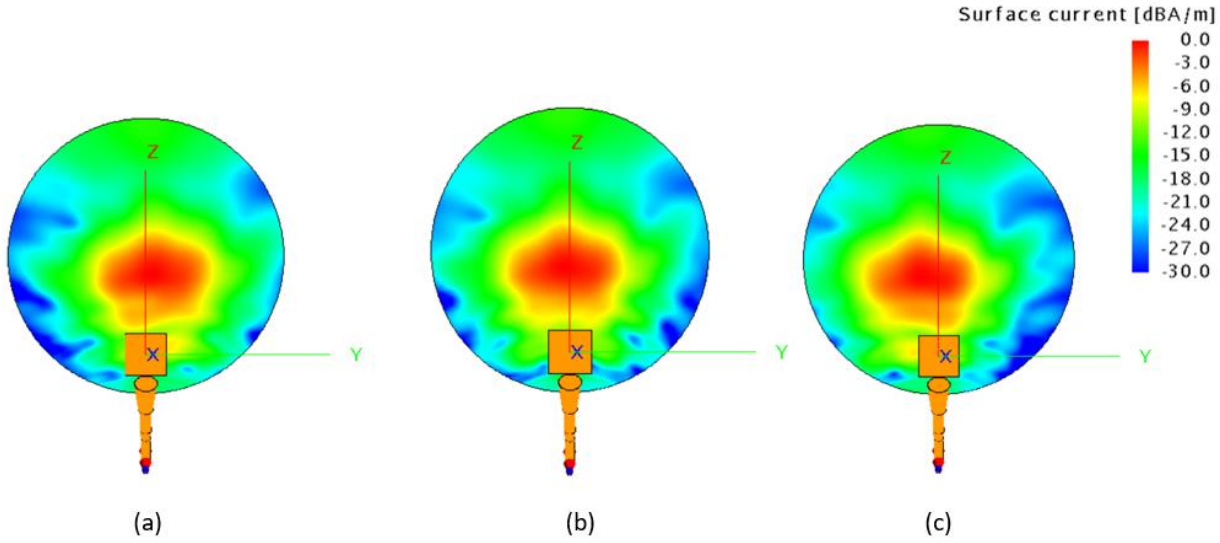

Figure 4.4 Normalized current distribution on the dish of dual-reflector antenna with beam scanning by tilting the metal subreflector by the angle of (a) $-5°$, (b) $0°$, and (c) $+5°$

4.3.2 Beam scanning in dual-reflector antenna by applying Progressive Phase Shift (PPS) on the sub-reflectarray

In this section, the flat metal subreflector is replaced by a reflectarray. The C-band CP reflectarray introduced in Chapter 3 is used as the subreflector. The reflectarray has 10×10 square elements with a periodicity of 15.75 mm (0.367λ) in a square lattice. Instead of tilting the subreflector, a PPS is applied along the reflectarray aperture to emulate the metal subreflector tilting [3, 4, 52]. The amount of spillover is less than the first method since the beam scanning is obtained without tilting the subreflector. In addition, in the configuration (see Figure 4.5), the subreflector is not changing the sense of polarization. Therefore, the spillover around the subreflector is contributing to the cross-polarization and will not interfere with the co-polarized radiation from the main reflector. The focal point of the dish in Figure 4.5 is placed in the virtual image position of the feed phase center in the un-tilted subreflector case. In this figure, the phase center of the feed horn is placed at 3.45λ from the center of the sub-reflectarray. In both configurations in Figures 4.2, and 4.5, the dish is placed close to the reflectarray since the focal point of the dish is behind the reflectarray.

Therefore, 3% of the main reflector's aperture is blocked by the reflectarray, which is small. Also, this blockage occurs on the edge of the aperture where the illumination is low.

The beam is tilted off-boresight by introducing a positive or negative phase gradient across the reflectarray aperture in the y, z, or an arbitrary direction. As an example, by applying phase differences of $0°$, $-34.2°$, and $+34.2°$ between adjacent elements along the along all the rows in the *y* direction, beam tilting caused by the PPS at the output of the reflectarray is $+15°$ and $-15°$, respectively. This gives the beam tilts of $-3°$ and $+3°$ out of the main reflector, respectively, about the boresight direction, as shown in Figure 4.6a. It should be noted that for a PPS of $0°$, Figure 4.6b shows the main beam direction at $\theta = 89°$ instead of 90°. For that phase shift the beam reflected from the dish is partially blocked by the subreflector. This can slightly distort the main beam and shift it maximum direction. When PPS= $\pm 34.2°$, the reflected beam is deflected away from the subreflector. In these cases the main beam points at 90° as expected. In the configuration in Figure 4.5, the spillover around the subreflector has the polarization the feed horn (LHCP). It is therefore contributing to the system's cross-polarization. In fact, a higher cross-polarization level is observed in Figure 4.6b compared to Figure 4.3 corresponding to the flat metal reflector case, for which spillover polarization is the same as the system's cross-polarization.

The cross-polarization level is increased at $\theta = 89°$ by scanning the beam, specially for the beam scanned at $-3°$, as shown in Figure 4.6a. Figure 4.7 shows the current distribution magnitude on the dish for three cases. The blue and green curves related to the beam tilts of $-3°$ and $+3°$ in Figure 4.6a as well as current distributions in Figures 4.7a and 4.7c are not mirrored images as expected. This is due to the non-symmetric alignment of the reflectarray elements with respect to the vertical axis (*z* axis). This asymmetry is due to the selection of the reference state for rotation angle of the elements equal to $\psi = 0°$ for non-tilted beam (see Figure 3.1), which corresponds to the blue curve in Figure 4.6a. Suppose the reference state for the rotation angle of the elements is selected at $\psi = 90°$. In that case, the alignment of the reflectarray elements by applying positive and negative phase gradient across the reflectarray aperture in the y direction will be symmetric with respect to the vertical axis, and mirrored images will be produced for the beam tilts of $-3°$ and $+3°$. With the offset configuration of the reflectarray and feed horn, the high cross-polarization level due to large incident angles of the beam on the reflectarray elements is observed. As shown

in Figure 3.6, with the element rotation of $\psi = 90°$, the higher level of the cross-polarization term of the reflected beam due to the oblique incident angles is observed compared to the element with the rotation angle of $\psi = 0°$ in Figure 3.5. Therefore, the reference state of $\psi = 0°$ is selected for element rotations to minimize the cross-polarization level.

In Figure 4.7, it can be seen in the projections of the system in the *yz* plane that the blockage by the subreflector is only over a small part of the aperture where the illumination is low. In the configuration in Figure 4.5, the virtual phase center is placed behind the reflectarray, and the direction of the reflected beam from the subreflector is determined by the law of reflection. Therefore, the current distribution on the dish is not concentrated around the center of the dish.

For the beam reflected from the parabolic dish, RHCP and LHCP are respectively the co-polarized and cross-polarized terms. The simulations have been done with the simulator FEKO, using physical optics of the dish and MoM/MLFMM for the horn and reflectarray. The PO and MoM/MLFMM solutions are coupled; therefore, mutual interactions between the horn, sub-reflectarray and the dish are taken into account.

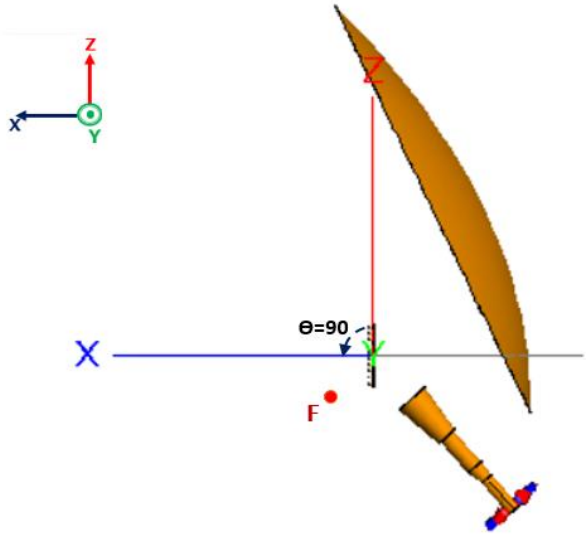

Figure 4.5 Configuration of dual-reflector antenna using PPS technique. The size of the sub-reflectarray is $3.67\lambda \times 3.67\lambda$ (λ=42.8 mm), and the projected diameter of the dish in the *yz* plane is 24λ with *F/D* of 0.5. The point identified by letter F is the focal point of the parabolic dish

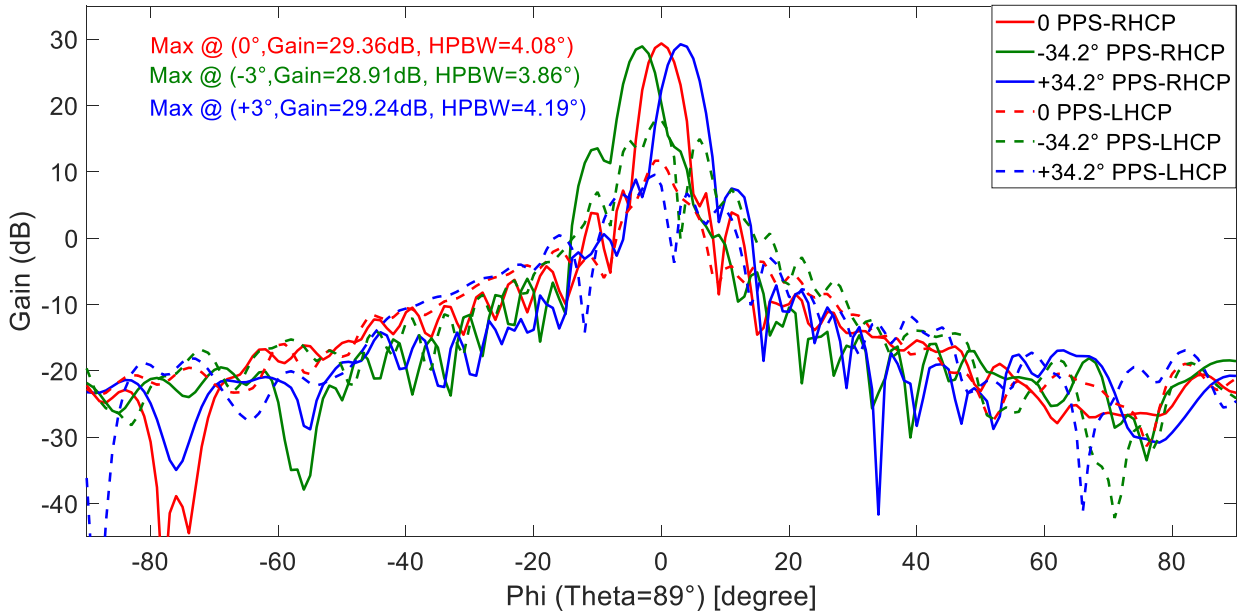

(a)

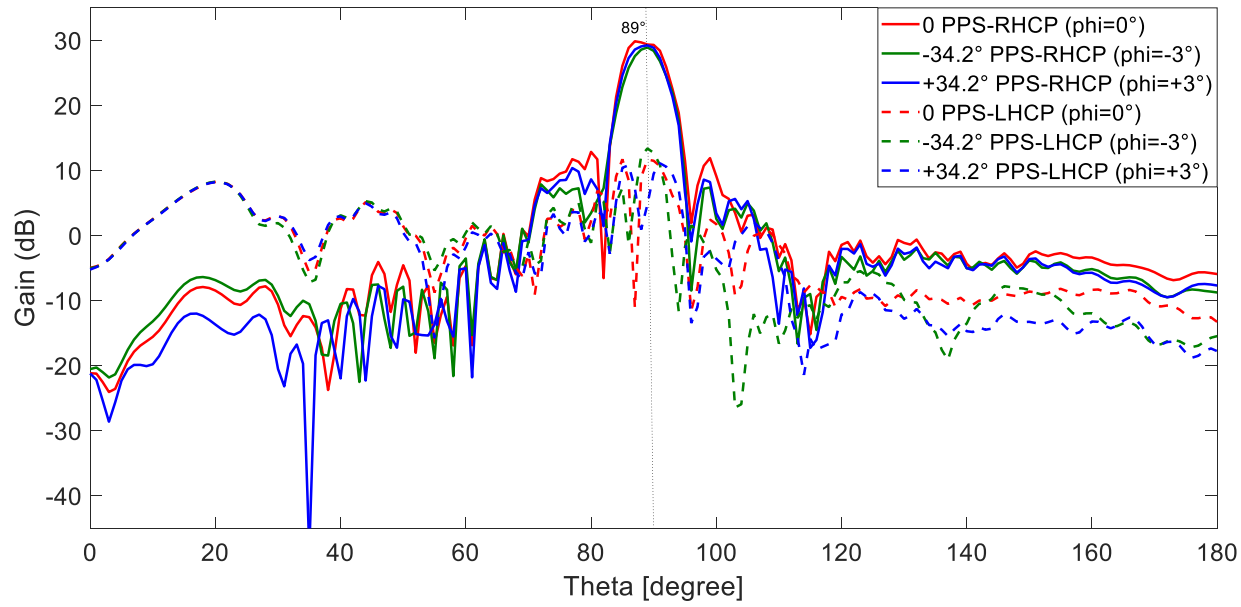

(b)

Figure 4.6 (a) Beam scanning at $\theta = 89°$ by applying PPS of $0°$, $-34.2°$, and $+34.2°$ along the y direction between adjacent elements of any row, (b) Main beam in the vertical planes related to three curves in Figure 4.6a

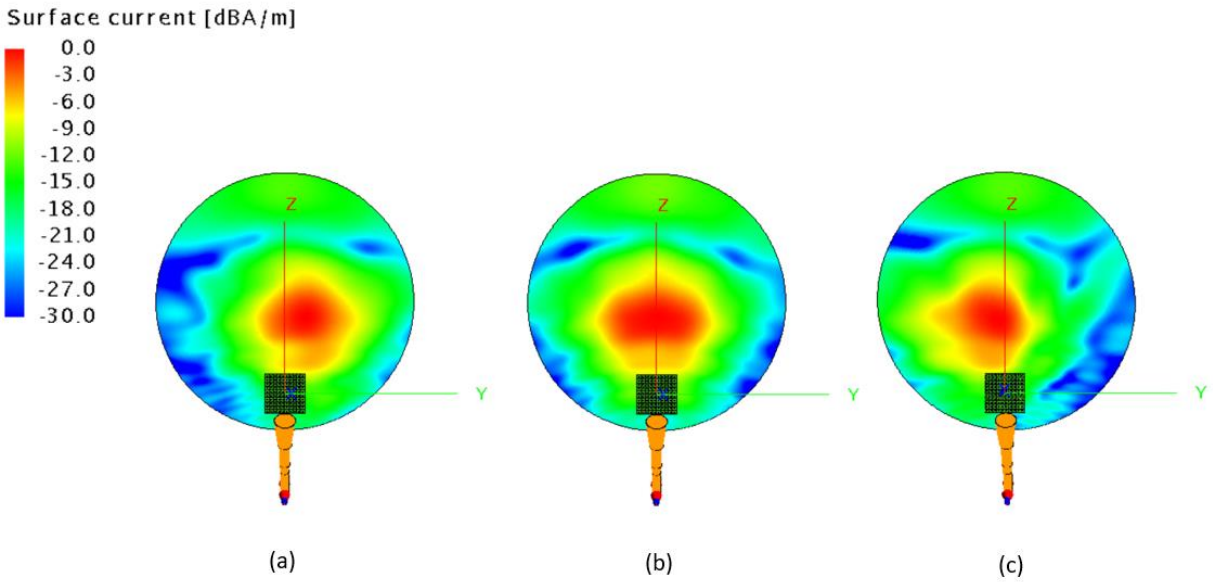

Figure 4.7 Normalized current distribution on the dish of dual-reflector antenna with beam scanning by applying PPS of (a) $+34.2°$, (b) $0°$, and (c) $-34.2°$ between adjacent elements of any row

4.3.3 Beam Scanning in dual-reflector antenna by applying the Near-Field Focusing (NFF) technique

The previous method of beam scanning has shortcomings, such as the high cross-polarization level of the scanned beams. This section proposes a method for beam scanning using the NFF technique. In a reflector system, NFF can be used to shift the position of the feeding structure (i.e. feed horn plus subreflector) phase center. For example, the radiated beam from a feed horn can be reflected by a subreflector to create a virtual source spot in the focal region of the main reflector. Beam scanning out of dual-reflector structure could be realized by moving the virtual source spot around the focal point of the main reflector [5, 57].

A C-band CP dual-reflector antenna with a reflectarray as subreflector with the ability of narrow beam scanning is proposed. The same reflectarray as the previous section is used. Before studying the beam scanning properties of the whole system, the NFF focusing property of the reflectarray

first will be evaluated. Then, beam scanning of the dual-reflector using the NFF focusing technique will be assessed with simulations, and also supported experimentally.

4.3.3.1 NFF Reflectarray

NFF is a well-known technique used in several applications: radio frequency identification (RFID) systems, gate access control systems, wireless power transmission, medical and industrial microwave applications [57, 58, 59]. NFF can also be applicable in satellite communication systems [60]. Antennas with high gain properties such as reflector antennas play a significant role in satellite communications.

This section studies the ability of the reflectarray antenna used as a subreflector to focus the beam at different distances from the aperture**.** The reflectarray comprising 10x10 cells using metallic slotted ring elements with a unit cell size of 15.75 mm is implemented in Chapter 3. As shown in Figure 4.8, a feed horn is placed at 200 mm from the plane of the reflectarray, and an offset of 100 mm is applied between the horn phase center and the bottom edge of the reflectarray.

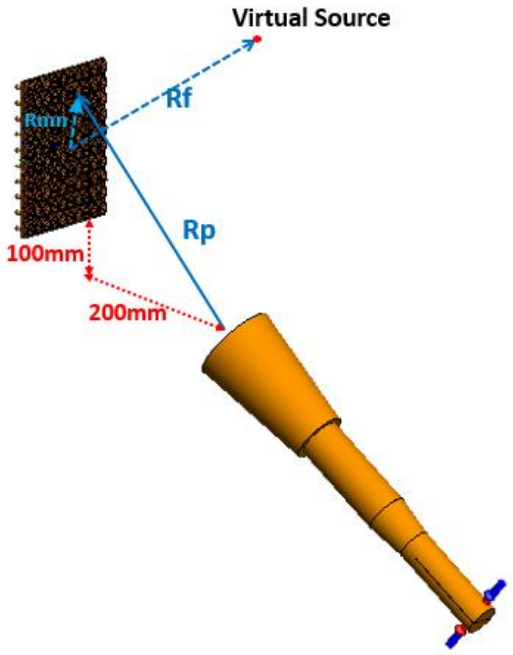

Figure 4.8 Horn and reflectarray structure [57]

To have all the elements contributions adding in-phase at a desired virtual source location, the phase shift distribution on the reflectarray surface should be applied according to eq. (4.3) for each element.

$$\phi = -2\pi / \lambda \times \left(R_p + \sqrt{(R_f)^2 + (R_{mn})^2 - 2\boldsymbol{R}_f . \boldsymbol{R}_{mn}} \right) \tag{4.3}$$

In eq. (4.3), R_p is the distance from the feed horn phase center to the mn^{th} element of the reflectarray. With the origin set at the center of the reflectarray, vector $\boldsymbol{R}_{mn}$ represents the coordinates of element (m, n) on the reflectarray, and vector $\boldsymbol{R}_f$ represents the coordinates of the virtual source point, in the vicinity of the reflectarray. This phase compensation mechanism results in an in-phase superposition of scattered fields from the reflectarray elements at the virtual source point.

A CP reflectarray antenna creating specific virtual source positions has been simulated in FEKO using the method of moments. As shown in

Figure 4.9a, showing the total near-field in the vicinity of the reflectarray in the $y = 0$ plane, a hot spot (electric field peak) appears near the desired virtual source points at coordinates of $\boldsymbol{R}_{f1} = (x = 50mm, z = 0)$, $\boldsymbol{R}_{f2} = (x = 100mm, z = 0)$, $\boldsymbol{R}_{f3} = (x = 50, z = 78.5mm)$ and $\boldsymbol{R}_{f4} = (x = 100mm, z = 78.5mm)$. A local plane wave front is expected to be present around the virtual source point formed with NFF [61, 62].

Figure 4.9b confirms the presence of locally plane wavefronts around the desired points.

Figure 4.10 shows the normalized and non-normalized power density along the *x* axis (perpendicular to array surface) for several near-field and far-field focused reflectarrays. The desired virtual source points in Figure 4.10 are considered on the *x* axis with $(x = 50mm, z = 0)$, $(x = 100mm, z = 0)$, $(x = 250mm, z = 0)$, and $(x \to \infty, z = 0)$ coordinates. In Figure 4.10a, for each curve, the radiation power density is normalized to its value at $x = 10 \times 2L^2 / \lambda$ where L is the reflectarray aperture size [63]. This distance is 10 times greater than the criterion generally used as a far-field condition for aperture antennas.

It can be observed that the achieved maximum power density is located close to the desired position ($\boldsymbol{R}_f$), but slightly closer to the aperture of the antenna, due to the field-spreading factor [63]. The focal shift that is the difference between the desired and obtained positions of the virtual source, increases as $R_f / (2L^2 / \lambda)$ increases. The Depth of Focus (DoF) that determines the range between the -3-dB axial points around the point of maximum power density [61] is obtained as 1.76λ when the desired virtual source point is at (x=50 mm, z=0). As shown in Figure 4.10b, for that same case, the focusing gain, defined as the ratio between the peak of non-normalized radiated power density of the NFF array and the non-normalized power density of far-field focusing array at $x = 2L^2 / \lambda$ [61] is 20.58 dB.

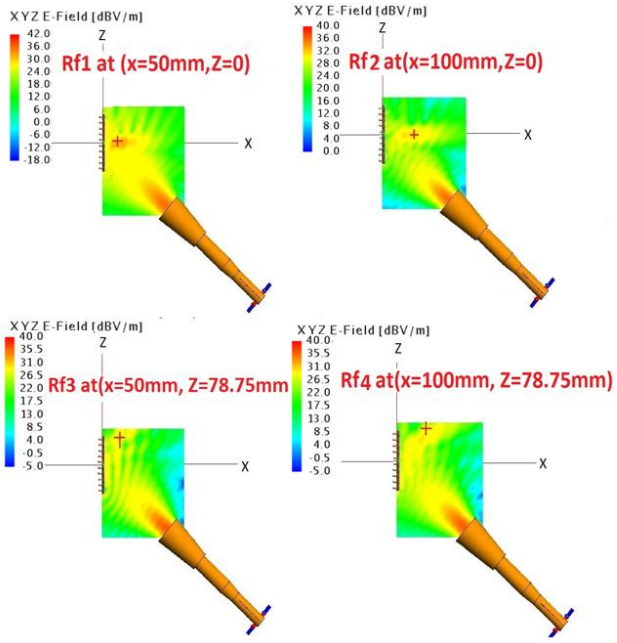

(a)

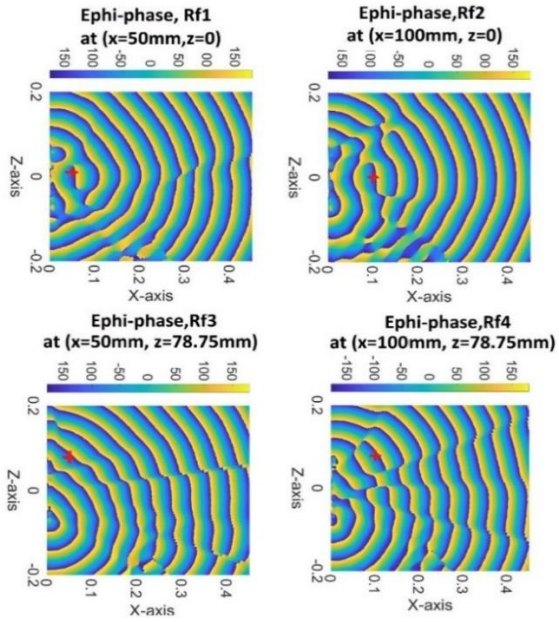

(b)

Figure 4.9 (a) Electric field magnitude (dBV/m), (b) Electric field phase (degree) on *xz* plane for NFF array with different focusing points. (Symbol + in the figures shows the desired virtual source points)

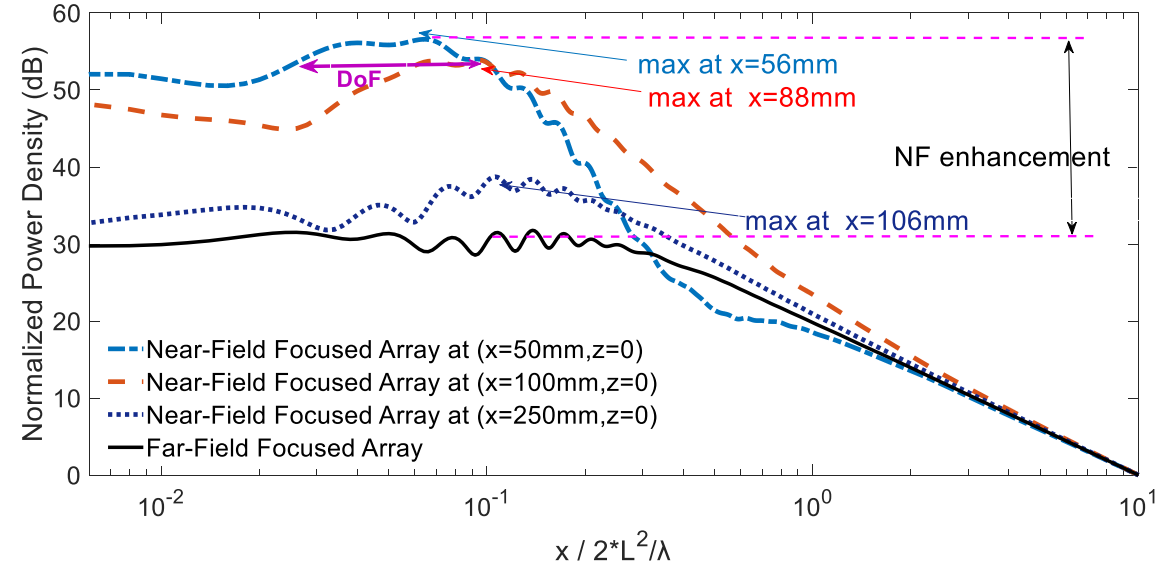

(a)

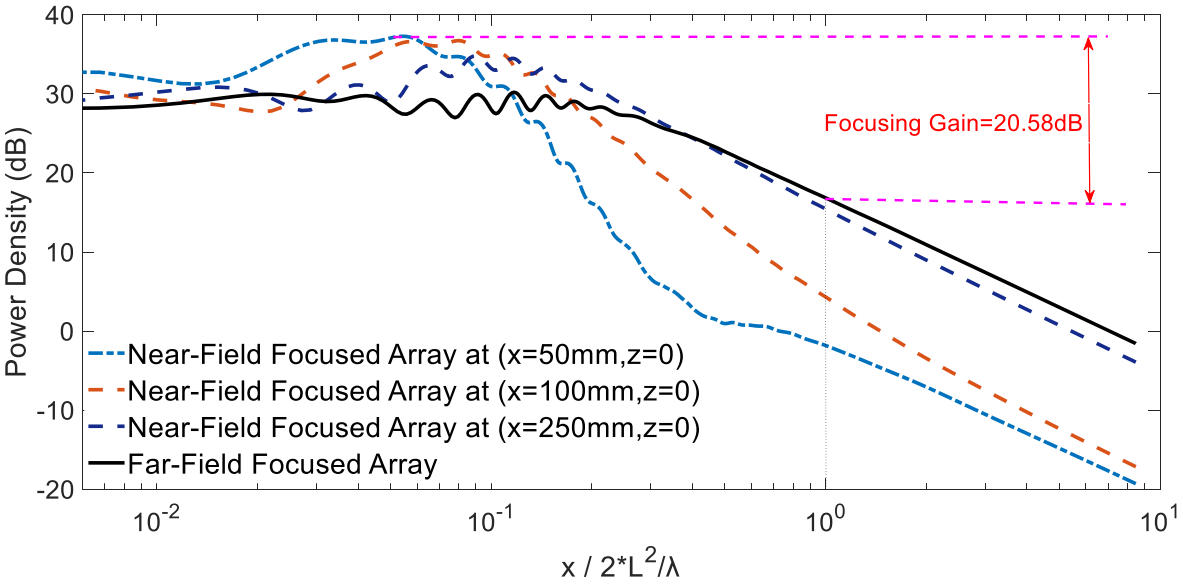

(b)

Figure 4.10 (a) Normalized, and (b) Non-Normalized power density (dB) radiated on *x* axis perpendicular to the array surface for near-field focused array with different virtual source points and for far-field focused array. The distance from the array surface (x) is normalized to the far-field region boundary ($2L^2/\lambda$)

The NFF property of the reflectarray has been validated experimentally by comparing the propagation direction of the measured and simulated far-field pattern of the reflectarray. In the structure shown in Figure 4.11a, the virtual source is created at (x=200 mm, z=138.75 mm) from the origin located at the center of the reflectarray. The coordinates of the virtual source are selected based on the dual-reflector antenna configuration that will be used for validation, and it is located at the focal point of the dish. The expected propagation direction in the reflected beam in the $\varphi = 0°$ plane is at $\theta = 55°$. Based on the far-field pattern, the propagation directions obtained from far-field measurements and simulation are respectively $\theta = 58°$ and $\theta = 54°$, respectively, as shown in Figure 4.12. This is a good agreement, considering the large beamwidth and the small electrical size of the reflectarray. The LHCP term is considered as the co-polarization term, and RHCP is regarded as the cross-polarization term. High cross-polarization level in the simulation between 80 and 120 degrees compared to measurement is due to specular reflection on the reflectarray. In the experimental test, this reflection can be blocked by the foam around the horn and the back metal plate at the extremity of the horn.

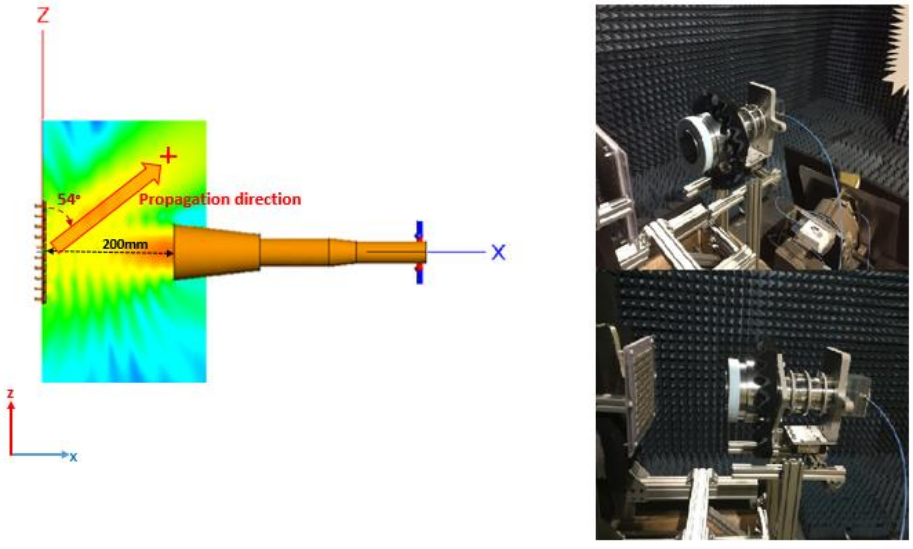

(a) (b)

Figure 4.11 (a) The structure of the horn and reflectarray with NFF (Symbol + in the figure shows the desired virtual source point), (b) The setup for measuring the far-field of the antenna structure in Figure 4.11a

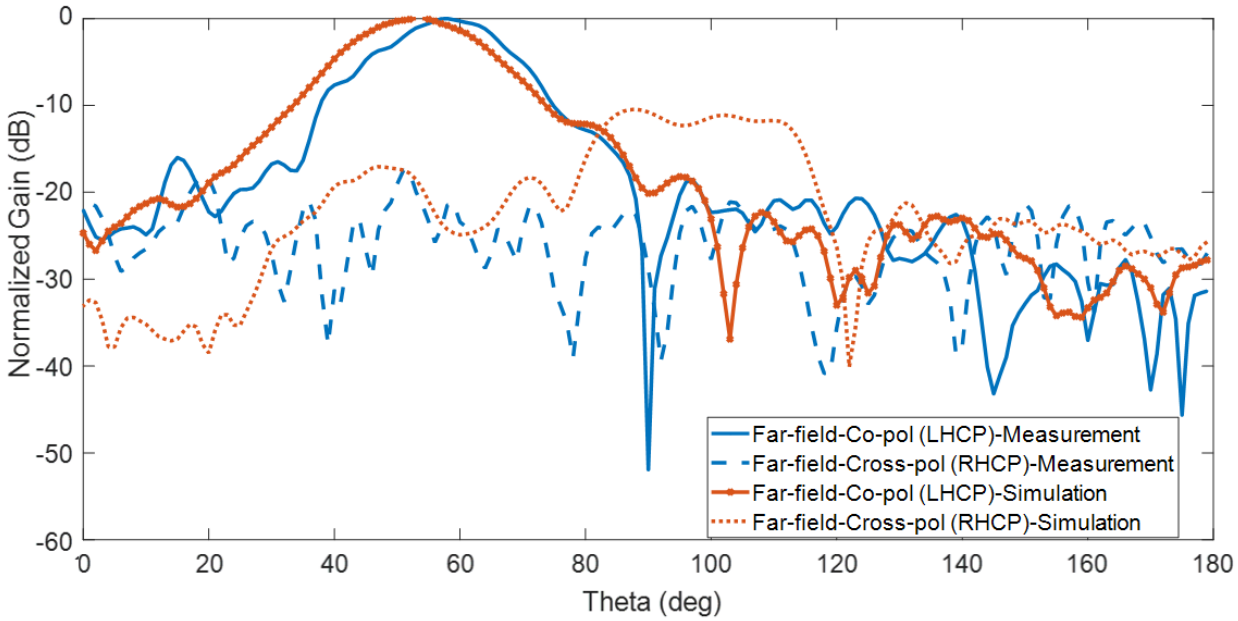

Figure 4.12 Simulated and measured far-field pattern (normalized) of the antenna in Figure 4.11, in plane $\varphi = 0°$

The reflectarray provides the capability of steering the focused point by making field contribution add in-phase in the neighborhood of specified virtual source point. In the next section, beam scanning of the dual-reflector antenna is obtained using the NFF property of the reflectarray as the subreflector of the system. The results of this section show that the application of NFF not only shifts the position of the virtual source, but it also redirects radiation in the direction of vector R_f. This second observation will be important to analyze the results of the next section.

4.3.3.2 Beam scanning in a dual-reflector antenna using the NFF technique

This section uses the NFF capability of the reflectarray antenna to scan the beam out of a dual-reflector system [52, 57]. In this method, a reflectarray used as a subreflector mimics the behavior of an ellipsoidal subreflector in a Gregorian dual-reflector configuration (see Figure 4.13).

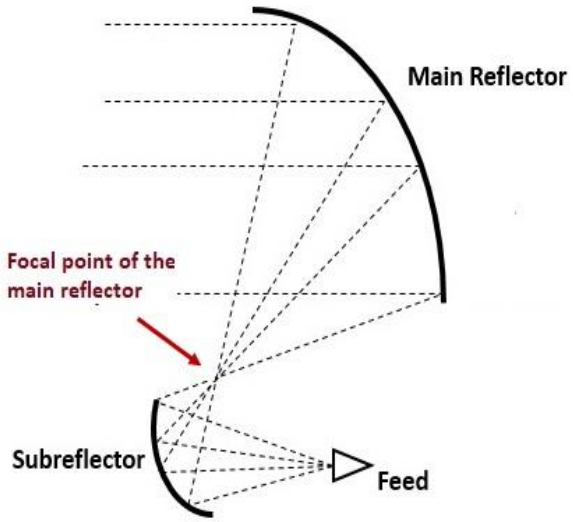

Figure 4.13 Offset Gregorian dual-reflector structure [64]

The configuration of the dual-reflector system proposed in this section is shown in

Figure 4.14. As in the previous examples, the distance between the feed horn and reflectarray is 200 mm. The projected diameter of the dish in the *yz* plane is 24λ at 7 GHz, and it has an *F/D* ratio of 0.5.

As seen in Section 4.2, the BDF concept is used to scan the beam by moving the virtual source phase center in the vicinity of the focal point of the main reflector. In the dual-reflector system of

Figure 4.14, beam scanning is obtained by using the NFF property of the reflectarray [57]. In this method, the focal point of the dish is placed in front of the reflectarray; therefore, the distance between the dish and reflectarray is larger compared to the configuration of PPS technique. In the configuration of

Figure 4.14, the incident illumination on the reflector comes from a virtual source. Let us now assume that the shaped subreflector in Figure 4.13 is replaced by a planar reconfigurable reflectarray. By controlling the phase distribution on the reflectarray, it is possible to shift the location of the virtual source phase center without mechanical movement of the subreflector. In the proposed system, a subreflector reflects a radiated beam from a feed horn to create a virtual source spot in the focal region of the main reflector. Displacement of the virtual source from the focal

point of the main reflector leads to narrow-angle scanning suitable for geostationary applications such as broadband satellite internet services, TV and radio broadcasting, and weather forecasting.

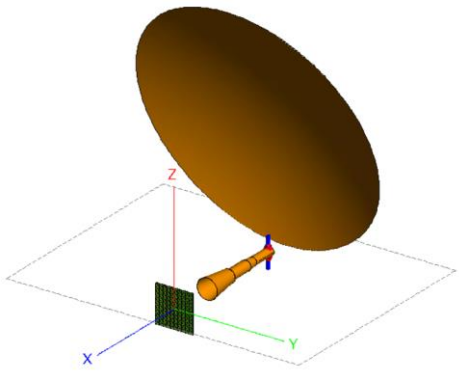

Figure 4.14 Dual-reflector antenna including horn, sub-reflectarray and solid parabolic dish. The size of the sub-reflectarray is $3.67\lambda \times 3.67\lambda$ (λ=42.8 mm), and the projected diameter of the dish in the yz plane is 24λ, with *F/D* of 0.5

Figure 4.15 shows the total near-field at *z*=138.75 mm plane in the vicinity of the focal point of the dish at (*x*=-200, *y*=0, *z*=138.75) for three cases of NFF. The hot spots (electric field peak) appear near the desired virtual source points at coordinates of (*x*=-200 mm, *y*= 0 mm, *z*=138.75 mm), (*x*=-200 mm, *y*=+30 mm, *z*=138.75 mm)**,** (*x*=-200 mm, *y*=-60 mm, *z*=138.75 mm), obtained by defining proper phase distribution on the reflectarray surface with eq. (4.3). The main beam direction of the whole system related to each case obtained by moving the virtual phase center in the +/-*y* directionson both sides of the dish's focal) is also shown in Figure 4.15. It can be seen that the displacement of the virtual source is accompanied by a change in the direction of the beam radiated from the spot. Therefore, the illuminated region of the main reflector will change, and spillover loss may occur of the shift of the virtual source point is too large.

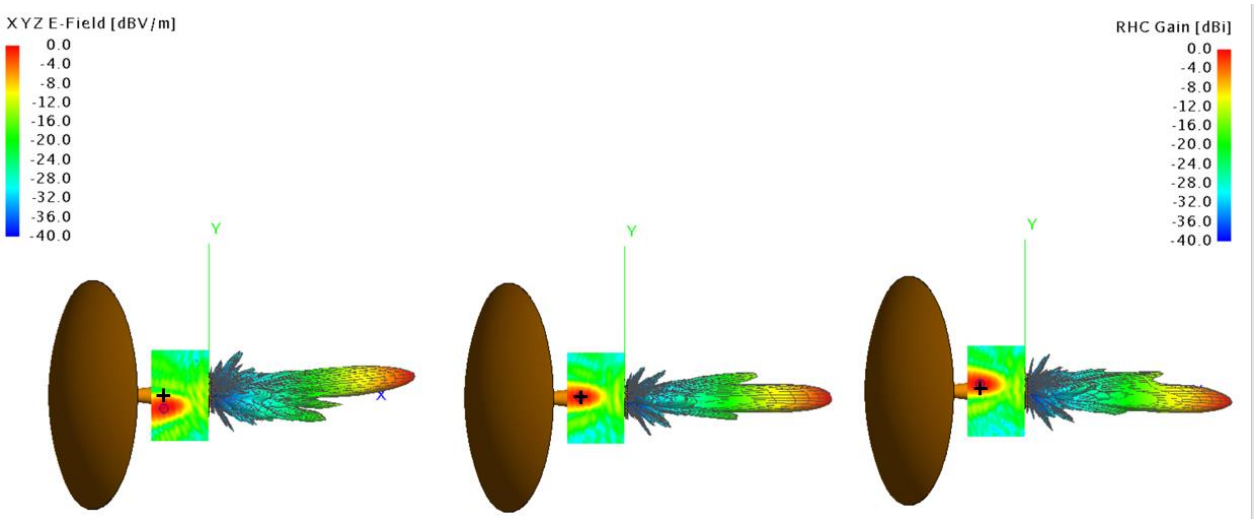

Figure 4.15 Displacement in the *y* direction of the virtual source phase center in plane *z*=138.75 mm , by +30 mm, 0 mm and -60 mm (symbol + in the figures shows (*x*=–200 mm, *y*=0 mm, *z*=138.75 mm), the coordinates of the dish focal point)

The radiation patterns of the beams in Figure 4.15 are shown in Figure 4.16. By moving the phase center by –60 mm and +30 mm along with *y* axis, the beam is steered by $+5^{\circ}$ and -3° off-boresight at $\theta = 89°$, as shown in Figure 4.16a. For these displacements of the phase center, the beam deviations θ_b calculated with eq. (4.1) are respectively equal to $+5.3°$ and $-2.67°$, which is close to the values obtained from the simulation. Figure 4.16b shows the main beam direction is at $\theta = 89°$. A gain value near 25.5 dB is obtained with the proposed system in the three cases. However, a larger gain was observed with the PPS method, as can be seen in Figure 4.6. In Figure 4.5, the compact configuration with the dish's focal point behind the subreflector leaves a smaller space between the reflectarray and the dish compared to the configuration in

Figure 4.14. This leads to less spillover losses on both the sub- and main reflectors. In addition, as shown in Figure 4.10b, for the near-field focused array, the power density in the far-field is reduced compared to the conventional far-field focused array. This explains the reduction in the gain of the dual-reflector antenna with NFF sub-reflectarray.

As mentioned, by moving the beam direction of the feed towards the center of the dish, the spillover loss is decreased. Since there is no control on the propagation direction by applying the NFF

technique, gain loss due to spillover around the dish is unavoidable. Spillover of LHCP from the feed around the edge of the small reflectarray is also present, as evidenced by the strong LHCP radiation between approximately 25 and 50 degrees in Figure 4.16, on each side of the main antenna beam. Of course, this is independent of the applied beam steering since these rays do not reach the reflectarray.

The current distribution on the dish related to scanned beams in Figure 4.16 is shown in Figure 4.17. The lower gain obtained by applying the NFF technique compared to the PPS technique is confirmed by comparing the current distribution on the dish for both cases. For the NFF technique, the current distribution on the dish is narrower compared to the PPS technique in Figure 4.7, which lead to a lower taper efficiency. This results in a wider beam for NFF technique which is confirmed by comparing the HPBW of the beams in Figure 4.6 and Figure 4.16. Therefore, the reflected beam from the dish with the NFF technique has less gain and directivity.

Figure 4.17 shows that a larger dish size is required for the PPS method with wider current distribution on the dish compared to the current distribution in the NFF method. In PPS, the reflected beam from the subreflector operates close to the specular reflection of the subreflector. This explains the lower cross-polarization of the beams in Figure 4.16a compared to Figure 4.6a. The other reason for the higher cross-polarization of the PPS technique compared to the NFF technique could be explained by looking at the cross-polarization term of the reflection coefficient of reflectarray elements in Figures 3.5 and 3.6. These Figures show the increment in cross-polarization level due to the oblique incident angle of the beam on the reflectarray elements. With the center-fed configuration of the horn and reflectarray in the NFF technique, lower incident angles of the beam on the reflectarray elements are observed compared to the PPS technique with offset configuration. Therefore, in the PPS technique, with the offset configuration of the feed horn and reflectarray, a higher cross-polarization level due to the larger incident angles of the beam on the reflectarray elements is observed. Again the simulations have been done with the simulator FEKO, by coupling PO and MoM/MLFMM solutions.

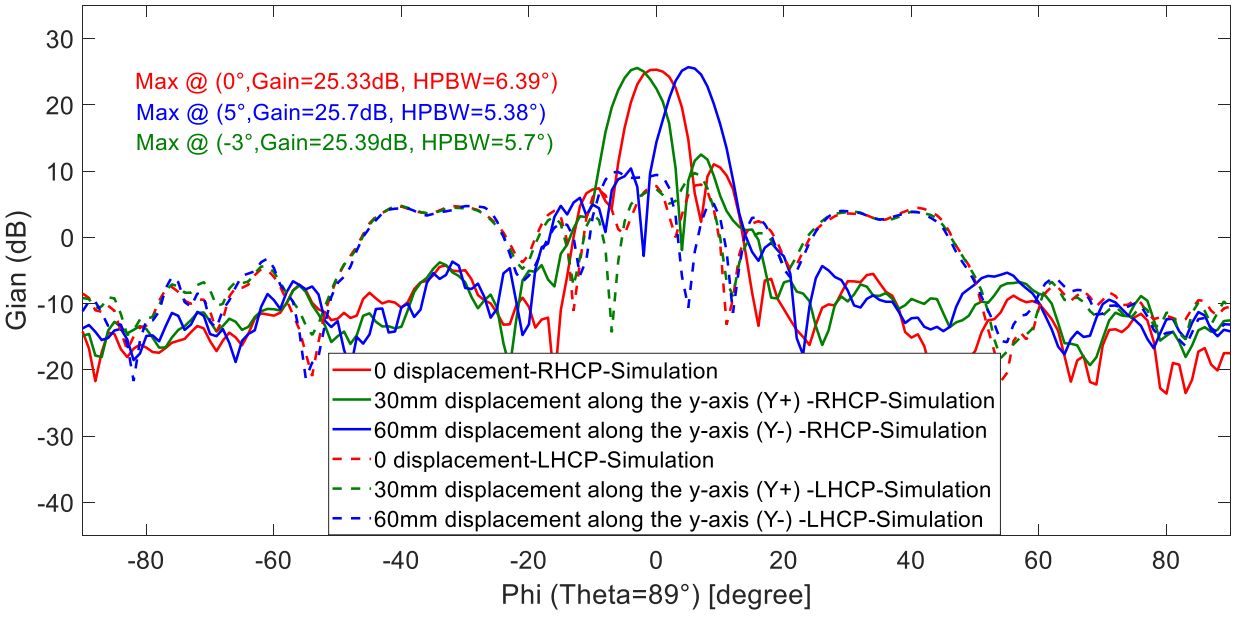

(a)

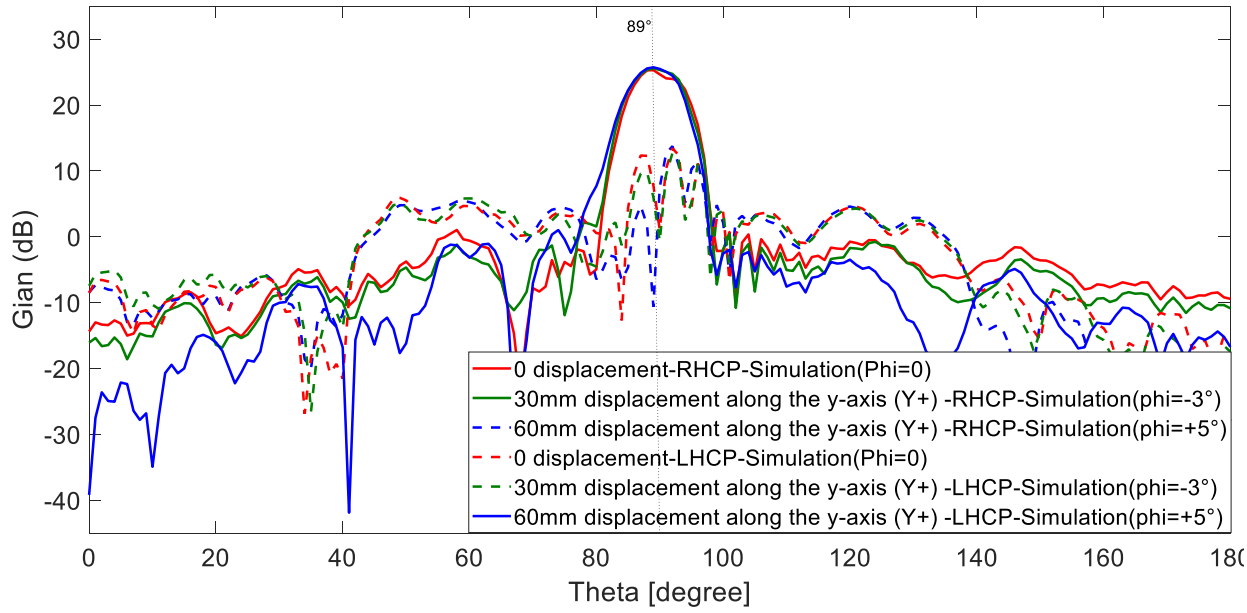

(b)

Figure 4.16 Beam scanning at $\theta = 89°$ by applying NFF technique for the virtual feed displacement of 0 mm, –60 mm, and +30 mm along the *y* axis , (b) Main beam in the vertical planes related to three curves in Figure 4.16a

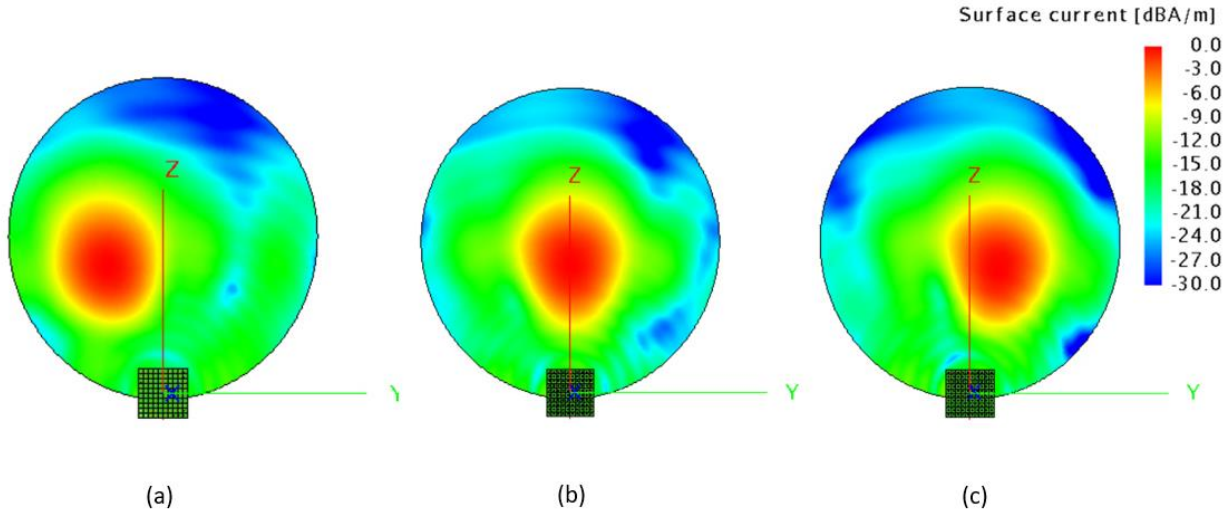

Figure 4.17 Normalized Current distribution on the dish for beam scanning at $\theta = 89°$ by applying NFF technique for the virtual feed displacement along the *y* direction of (a) –60 mm, (b) 0 mm, and (c) +30 mm with respect to the focal point of the dish located at (*x*=–200 mm, *y*=0, *z*=138 mm)

4.3.4 Comparison between the results obtained with the PPS and NFF techniques

Narrow beam scanning by applying PPS has some limitations in comparison to the NFF focusing method. Figure 4.18 shows the dual-reflector antenna configurations with narrow beam scanning capability using PPS and NFF techniques.

The configuration of Figure 4.18a exhibits more spillover around the reflectarray due to the offset configuration of the feed and reflectarray. With the NFF technique, it is possible to reduce spillover by having the feed horn in a center-fed configuration in front of the reflectarray (see Figure 4.18b).

Compared with the beam scanning range at $\theta = 89°$ for PPS (See Figure 4.6), the range of the scan angle at $\theta = 89°$ when applying NFF is wider since a lower cross-polarization level in the pattern has been observed (See Figure 4.16). With the PPS, the cross-polarization term has a high contribution to the current distribution on the dish since the reflected beam from the subreflector operates close to the specular reflection of the subreflector. In reflectarrays, specular reflection

occurs on the portions of the ground plane exposed to the incident field [65, 66]. This reflection causes a change in the sense of circular polarization, which is not the case for the reflectarray elements. Therefore, the scan range by applying the PPS technique is limited by the cross-polarization level, while in the NFF method, it is mainly determined by the dish size. The second reason for high cross-polarization with the PPS technique is related to the offset configuration of the feed horn and reflectarray in the PPS technique. The offset configuration in the PPS technique increases the cross-polarization level due to the larger incident angle of the beam on the reflectarray elements, which is different from the case of the NFF technique with center-fed configuration.

In NFF, beam scanning in two planes is possible and is only limited by the dish size. In contrast with NFF, in PPS, the beam scanning in both planes is limited by the high cross-polarization level, while in the vertical plane, it is also limited by greater feed blockage, as illustrated in Figure 4.18.

In the PPS method, more gain is obtained at the price of a higher cross-polarization level. The higher gain in the PPS technique is due to the compact configuration of the dual-reflector system in Figure 4.5, which leads to less spillover losses on both the sub- and main reflectors, compared to the NFF technique in

Figure 4.14. Moreover, narrower current distribution on the dish for the NFF technique confirms the wider beam and, therefore, a lower gain from the dish than the PPS.

Besides, NFF configuration allows more design flexibility. For example, the beamwidth can be modified by axial displacement of the virtual source phase center with respect to the focal point of the main reflector.

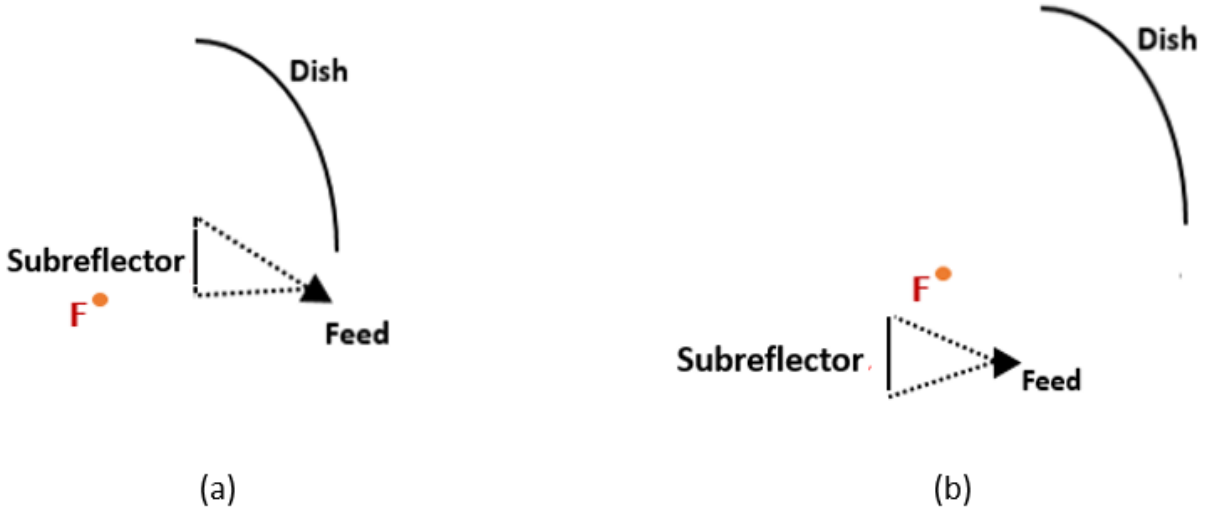

Figure 4.18 Dual-reflector configuration with reflectarray subreflector: (a) applying PPS technique and, (b) applying NFF techniques

The current distribution on the dish for both cases is shown in Figure 4.19. In Figure 4.19a the beam scanning of $+3°$ by implementing NFF technique is provided, while in Figure 4.19b the beam scanning of $+3°$ is obtained by PPS technique. In both of the cases, the reflectarray size of $3.67\lambda \times 3.67\lambda$, and the dish size of 24λ, with *F/D* of 0.5 are used (λ=42.8 mm). For the PPS, the maximum peak of both the beam and the current distribution on the dish are shifted in the +*y* side of the figure (see Figure 4.19b). This phenomenon is also observed in Figure 4.7. For the case of NFF, the main beam direction is on the opposite side of the current distribution on the dish, as shown in Figure 4.19a. This was also the case in Figure 4.17. This can be explained by looking at Figure 4.1a. When the feed is moved down in that figure, we see that the beam of the main reflector is shifted upward. Similarly, if in the configurations of Figure 4.5 (PPS) and

Figure 4.14 (NFF) the virtual source is moved in the -*y* direction with respect to the focal point, the beam will be steered on the other side, i.e. to a positive φ angle. Looking at in Figure 4.7 (or Figure 4.19b) (PPS), we see that the reflectarray has steered the subreflector beam to the positive *y* region of the dish. Considering the virtual image of the feed behind the subarray, such steering is obtained

by moving the virtual image in the negative *y* direction. Consequently, the main reflector beam will be steered to a positive φ angle. Now let us consider the NFF case of Figure 4.17 (or Figure 4.19a). In this case NFF moves the virtual source to a negative *y* value, and consequently the main reflector beam is again steered to a positive φ angle. What is counterintuitive in this case is that the current distribution on the dish is also shifted towards the negative *y* region. This can be understood by looking at the examples in Figures 4.11 and 4.15. As already pointed out, when the focusing realized by the subreflector is in a certain direction, the amplitude of the scattered wave will be stronger along that direction. This is why we see stronger currents on the negative side in Figure 4.19a, where the focusing was done at *y*=-30 mm. However, although the amplitude is stronger on the negative *y* side, the phase distribution of the incident field on the dish is that of a source located on the negative *y* side. As a result the main reflector beam is also steered to a positive φ angle.

Another interesting difference between PPS and NFF is that beam scanning using PPS corresponds to the Cassegrain dual-reflector configuration where the virtual source is located behind the subreflector, whereas beam scanning using NFF corresponds to the Gregorian dual-reflector configuration with the virtual source [67] shifted in front of the subreflector. This can be observed in Figure 4.19.

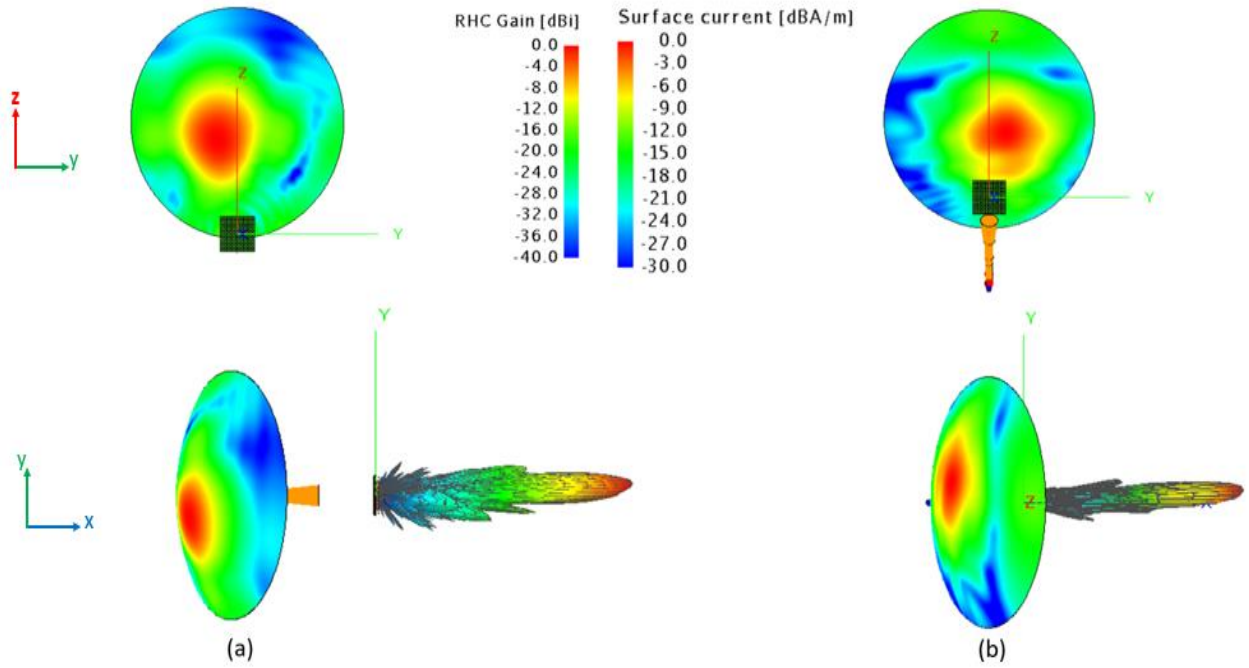

Figure 4.19 Normalized current distribution on the dish for beam scanning (a) by applying NFF for the scanned beam of $+3°$, and (b) by applying PPS for the scanned beam of $+3°$

4.4 Experimental validation of beam scanning of the reflector system

The dish antenna size used in the measurement setup is smaller than the dish size in Figure 4.14 due to the limited quiet zone size of the compact antenna test range (CATR) of the Poly-Grames Research Centre. The offset parabolic dish with the circular aperture in Figure 4.14 will be cut in an elliptical shape to fit inside the CATR quiet zone.

4.4.1 Localization of the focal point of the offset satellite dish

To fit a TV satellite dish in our experimental setup, we first need to characterize the dish before building our reflector system. For example, to demonstrate BDF experimentally with the

subreflector, the focal point of the dish should be known precisely. In this section, the focal point of the offset dish used in the experimental validations will be determined.

The commercial offset satellite TV dish in Figure 4.20a with the dimension of $750\text{mm} \times 813\text{mm}$ is used. It has a focal distance of 492 mm, and the offset angle is $22.75°$. The rim of the offset dish is an ellipse with the minor and major axes sizes of W and D, respectively. The orthogonal projection of the ellipse in yz plane in Figure 4.20b is a circle with the diameter of W shown on the right side of the figure [68]. The offset angle of the parabolic dish antenna given in the datasheet is calculated by the following equation [68]:

$$\cos(\theta) = W / D \tag{4.4}$$

where W and D are the width and length related to the dimension of the dish and θ is the offset angle of the dish shown in Figure 4.20b.

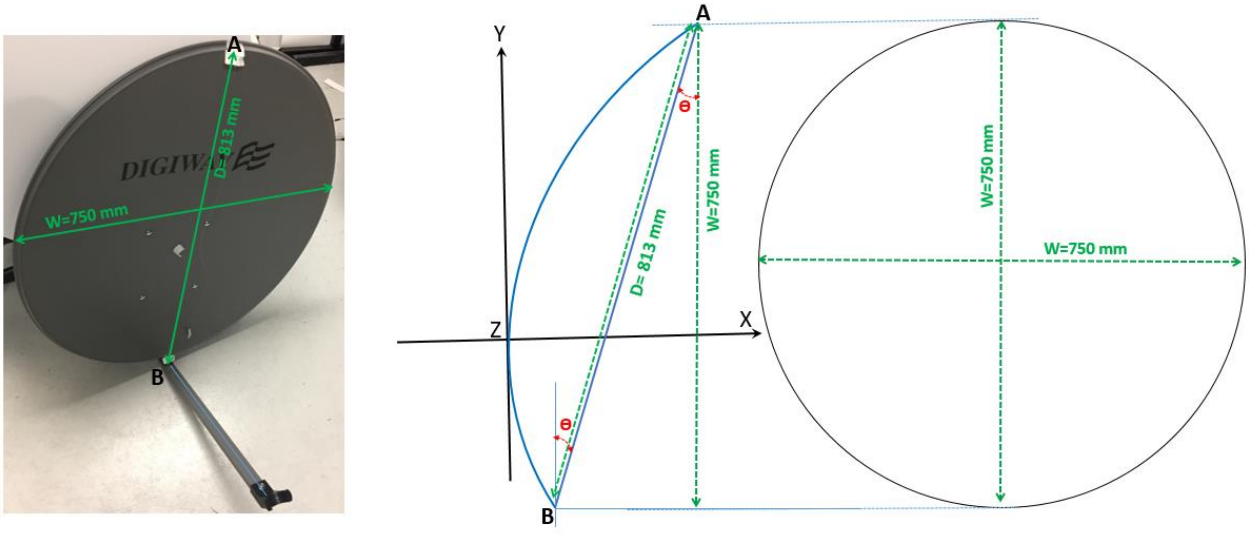

(a) (b)

Figure 4.20 (a) Commercial offset satellite TV dish, (b) 2D cross section of the offset dish [68]

Figure 4.21 shows the geometry of the offset parabolic dish and the parameters required to calculate the correct position of the focal point.

Let us consider a 2D cross section of the offset dish in the vertical plane containing the focal point. In Figure 4.21, (X_o, Y_o) are the coordinates of the bottom edge of the dish in a coordinate system centered on the vertex of the parabola (point $(0, 0)$). From [68] we have:

$$Y_O = 2 * a \tan(\theta) - W / 2 \tag{4.5}$$

and from the equation of parabola, we have:

$$X_o = Y_o^2 / 4a \tag{4.6}$$

where *a* is the focal length of the parabola. Every point on the parabola has the same distance from the focal point as it has from the directrix line, which is perpendicular to the *x* axis and passing by point $(-a, 0)$.

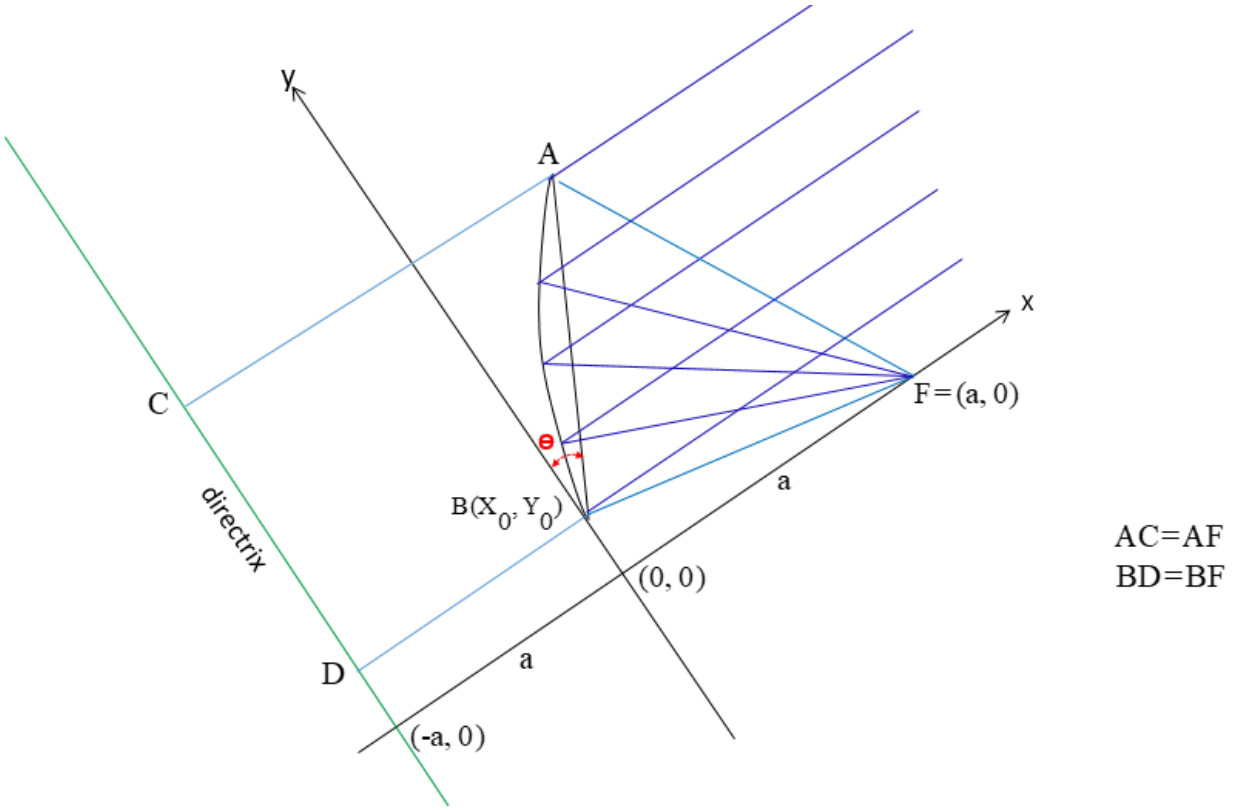

Figure 4.21 Offset dish geometry [68]. Letter "a" refers to the focal length noted "*a*" in the text

BF, the distance from lower rim of the dish to the focal point, is obtained by adding a, the focal length, to the x-coordinate:

$$BD = BF = X_o + a \tag{4.7}$$

Cord *AB*, which connects point *A* at the upper rim of the dish to point *B* at the lower rim of the dish, has the angle of θ with the *y* axis. Therefore, *AF*, the distance from the upper rim to the focal point of the dish, is obtained by:

$$AF = AC = X_o + a + AB.sin(\theta) \tag{4.8}$$

Applying the equations to the dimension of the offset satellite dish in Figure 4.20 gives $AF = 807.11\text{mm}$ and $BF = 492.7\text{mm}$. The focal point of the dish is found by using the string with a total length of $AF + BF$ [69]. A knot is be tied on the string at the distances of AF and BF to each end of the string. Two ends of the string will be fixed at the upper and lower points on the rim of the dish, as shown in Figure 4.22. By keeping the string taut in the symmetry plane of the dish, the knot will be at the focal point of the dish, as shown with the red circle in Figure 4.22.

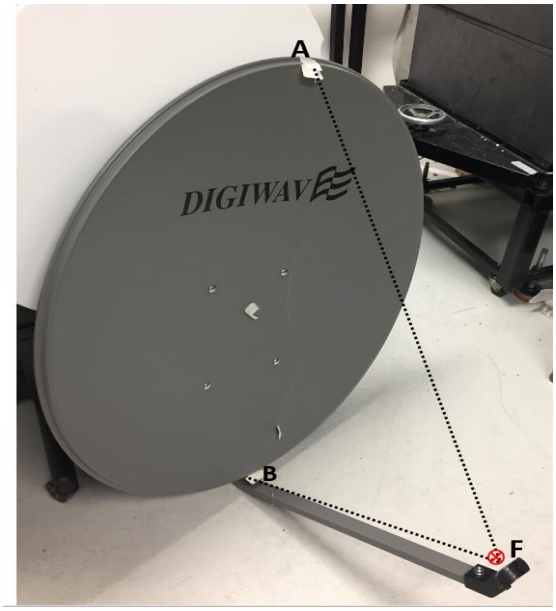

Figure 4.22 Satellite dish antenna with the string to find the feed position

The offset parabolic dish with the circular aperture in Figure 4.22 will be cut in an elliptical shape due to the limited quiet zone inside the anechoic chamber. The shape of the ellipse to be cut is marked on the dish's surface in Figure 4.23a. The projected diameter of the major and minor axes of the elliptical shape is 650 mm and 433 mm, respectively.

The distances from the top and lower points on the rim of the elliptical dish to the focal point, called $A'F$ and $B'F$ in Figure 4.23b, are two parameters to be determined. For this purpose, a new string (shown with blue colour in Figure 4.23a) marking with a tied knot is used. As shown in Figure 4.23a, the knot of the blue string is tight to the knot of the black string. At this time, the black string with the total length of $AF + BF$ is kept taut in the plane of symmetry of the dish, and the knot on the string is pointing to the focal point of the dish. Now, two ends of the blue string will be cut and fixed to the upper and lower points on the rim of the ellipse shape marked on the dish. Therefore, the blue string with a total length of $A'F + B'F$ is obtained. The focal point of the elliptical shape dish shown in Figure 4.23b is found by attaching the ends of the blue string with the total length of $A'F + B'F$ to the upper and lower edges of the elliptical shape reflector while keeping the string taut in the plane of symmetry of the dish. Therefore the knot on the blue string will be located at the focal point of the dish. The distances obtained for $A'F$ and $B'F$ are 622 mm and 491 mm, respectively.

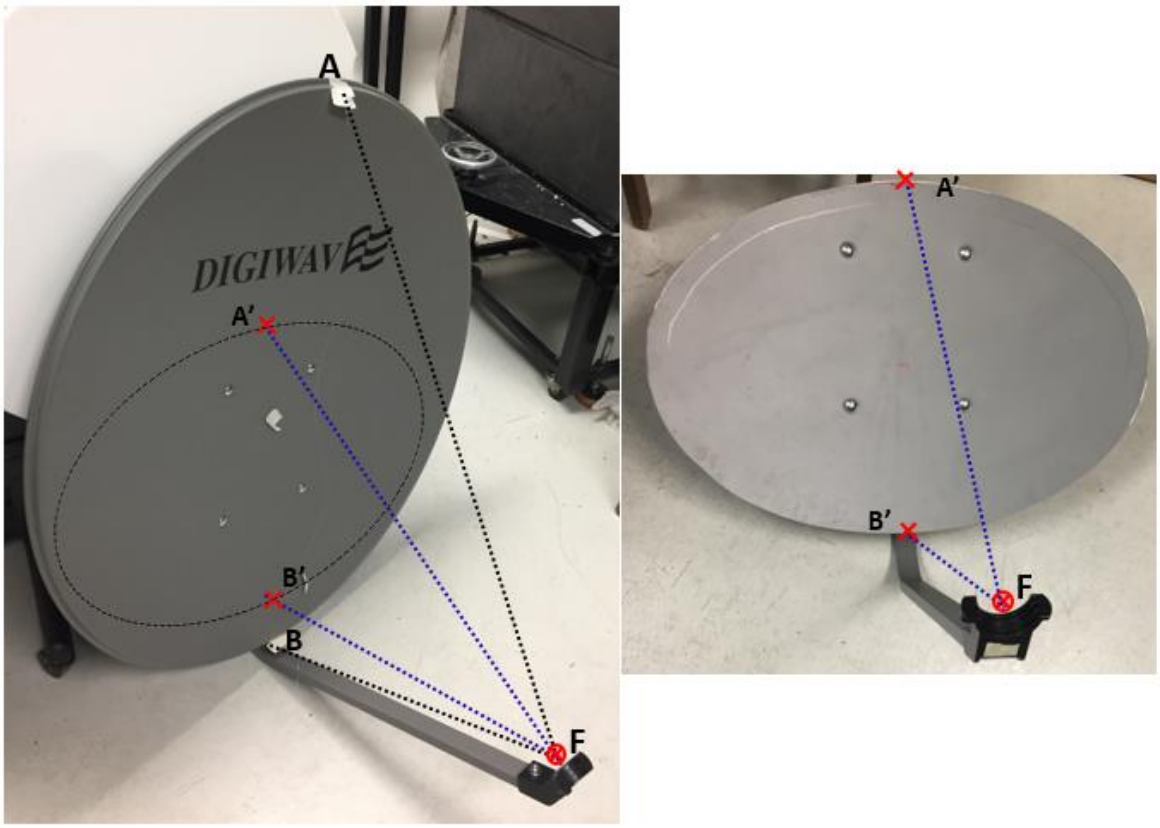

Figure 4.23 (a) Satellite dish antenna with an elliptic shape marked on it, (b) Elliptical reflector obtained after cutting the original dish. The blue string is used to find the focal point

4.4.2 Experimental validation of the BDF estimation

In this section, the BDF concept will be studied experimentally using the setup illustrated in Figure 4.24. In this figure, the *z* axis corresponds to the *y* axis in Figure 4.21. The elliptical shape reflector shown in Figure 4.23b is used. The major and minor axes of the reflector projected in *yz* plane are 15.18λ and 10.11λ, respectively, whereas the focal distance is 11.14λ at the design frequency of 7 GHz. The CP feed horn introduced in Chapter 3 is used.

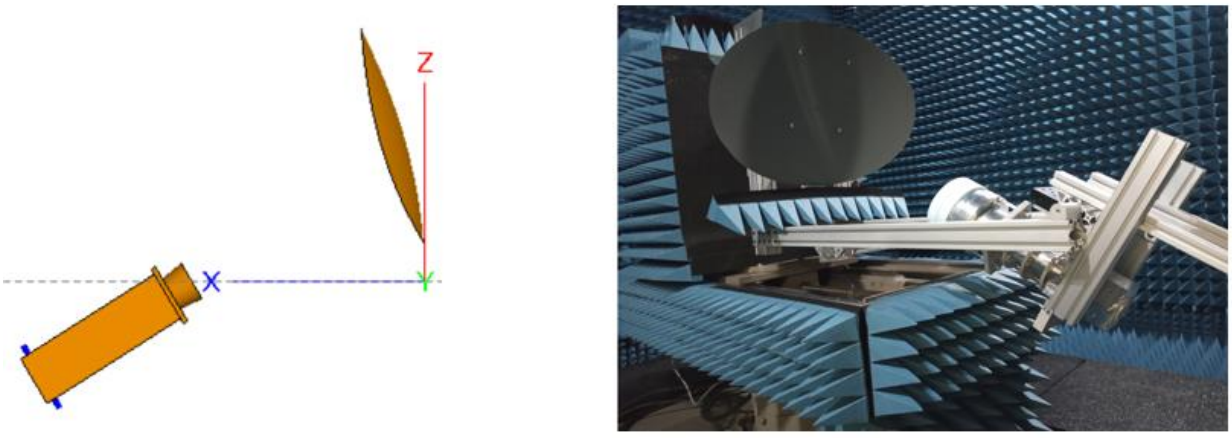

Figure 4.24 (a) The structure of the dish and the feed horn used to study BDF concept, (b) Setup of the structure used in the experiments

The feed horn is displaced between –5 mm and +17 mm along the *y* axis with respect to the focal point of the dish. The displacements of –5 mm and +17 mm correspond to $\theta_f = -0.54°$ and $+1.82°$. The corresponding beam deviations in the *xy* plane predicted by (4.1) are $\theta_b = +0.51°$ and $-1.73°$, respectively. Figure 4.25a shows simulation results obtained with Altair FEKO, using a hybrid approach where the horn is handled with the method of moments and the reflector with physical optics. Beam deviations of $+0.5°$ and $-1.7°$ due to the feed displacement of –5 mm and +17 mm were found, which is in good agreement with the simple prediction formula. Although not clearly visible in the figure, an offset of $\theta_b = +0.2°$ of the main beam is predicted for $\theta_f = 0°$. This offset changes sign ($\theta_b = -0.2°$) when the polarization of the feed horn is switched from RHCP to LHCP. Therefore, the offset in θ_b is due to feed polarization rather than the asymmetry in the setup and BDF effect. Beam squinting of circular polarization beams in the offset-fed configuration is a well-known phenomenon. The offset predicted by eq. (4.2) with θ_0 of $31°$ is $+0.21°$, which is close to

$\theta_b = +0.2°$. The radiated beam forms RHCP which is radiated by LHCP feed squints towards the left side in xy plane; left and right is defined for the observer who is looking in the direction of the wave propagation, $+x$ [55].

Since the feed horn for the simulation in Figure 4.24a is LHCP, for the beam reflected from the dish, the RHCP term is considered co-polarization term, and LHCP is deemed to be the cross-polarization term.

Figure 4.25b experimentally supports the predicted beam deviation results in Figure 4.25a. The figure illustrates the beam deviations of $+0.7°$ and $-1.7°$ due to the feed displacement of –5 mm and +17 mm respectively. As shown in Figure 4.25b, a measured offset of $\theta_b = -0.6°$ instead of the simulated value of +0.2° is observed for $\theta_f = 0°$. Similarly, the measured beam directions for feed displacements of -5 mm and +17 mm are shifted at +0.1° and -2.3° respectively rather than the simulated values of +0.7° and -1.5°. These differences are partly due to misalignment in the measurement setup. The beamwidth obtained from the measurement setup in Figure 4.25b is slightly greater (average of 4.9° compared to 4.49°) than the beamwidth obtained from the simulation in Figure 4.25a. This could be due to the limited quiet zone size of the existing CATR, causing a reduction of the antenna effective aperture. The beamwidth difference leads to a reduction in the measured gain compared to the simulation.

Higher cross-polarization levels in the measurement compared to the simulation result from the higher cross-polarization level of the fabricated feed horn compared to the simulated horn, as explained in Chapter 3.

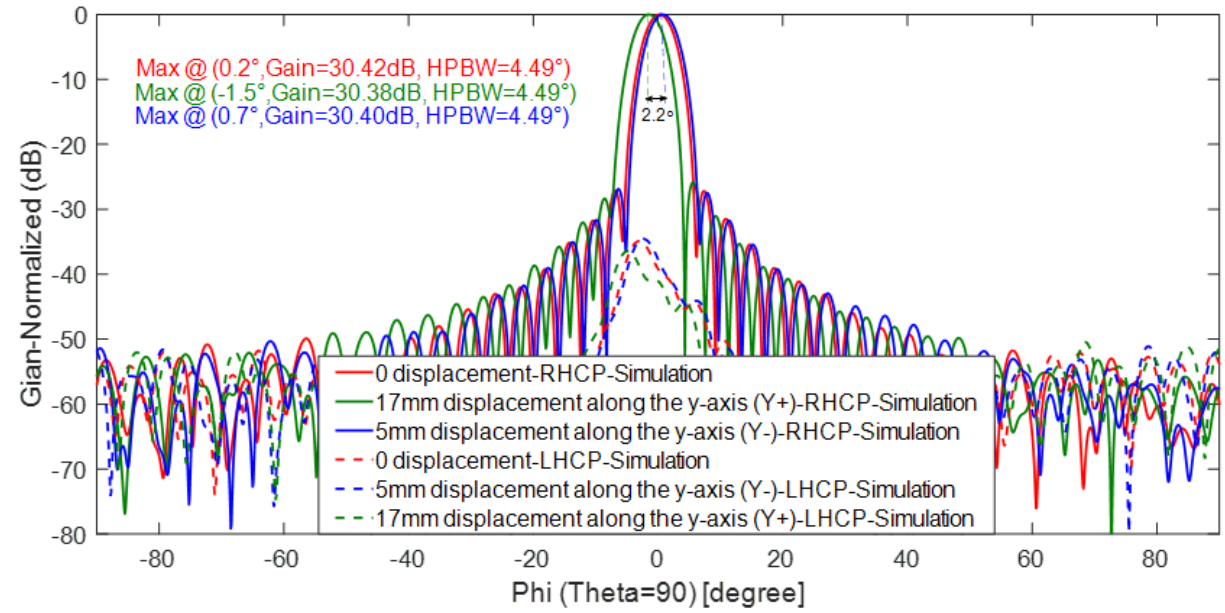

(a)

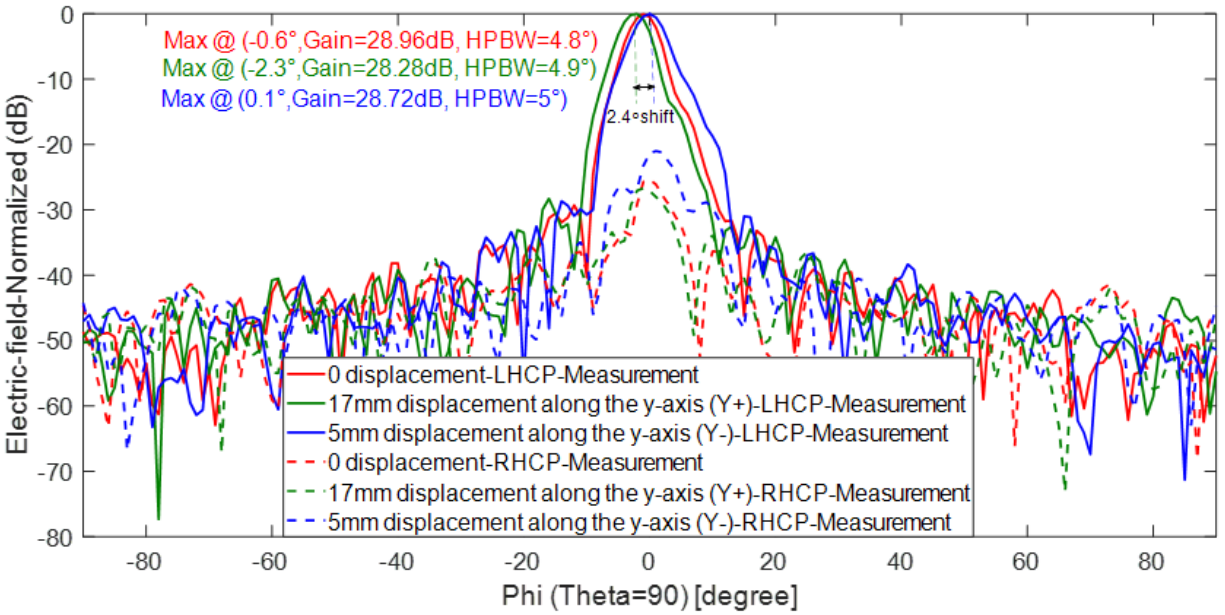

(b)

Figure 4.25 Beam deviation due to the feed horn displacement in Figure 4.24a by –5 mm, 0 mm and +17 mm along the *y* axis with respect to the focal point of the dish. (a) Simulations, (b) Measurements

4.4.3 Experimental validation of the beam scanning capability of the dual-reflector antenna implementing NFF

This section experimentally supports the beam scanning property of dual-reflector antenna using the NFF technique. For this purpose, the structure in Figure 4.26 based on the elliptical dish in Figure 4.23b is used. As already mentioned, the dish size of the measurement setup in Figure 4.26 is smaller than the simulated dish size in Figure 4.14 due to the limited quiet zone inside the anechoic chamber. More details on this limitation will be given in Chapter 6. Reflectarray elements are rotated manually by steps of $11.25°$ degrees for the phase adjustment. As a first step, we will present simulation results based on a model similar to the one used in the experimental validations. Then, as a second step, measurements with the real antenna will be presented. The simulation frequency is 7 GHz in all cases. Bandwidth performance will be investigated in Section 4.5.

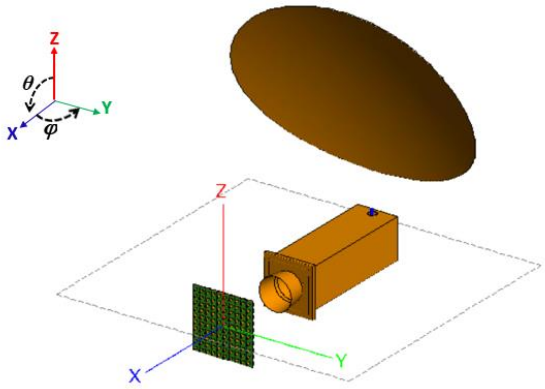

Figure 4.26 Dual-reflector antenna including horn, sub-reflectarray and elliptical shape parabolic dish, the size of the sub-reflectarray is $3.67\lambda \times 3.67\lambda$ (λ=42.8 mm), and the distance between the feed horn and reflectarray is 200 mm

In this example, to evaluate the beam scanning performance of the structure, the beam reflected from the reflectarray is focused at the focal point of the dish located at (x=–100 mm, y=68.75 mm), and it is then moved with respect to that point. Displacements of the virtual phase center in the y and z directions are considered. As shown with simulations in Figure 4.27, the main beam is steered

at $\varphi = -1°$, $-3°$, and $+3°$ at $\theta = 89.4°$, for corresponding virtual feed displacements of +10 mm, +30 mm, and -30 mm respectively along the *y* axis. Corresponding normalized current distributions on the dish are shown in Figure 4.28. These results show the beam steering in the horizontal plane is effective. The current distribution on the dish in Figure 4.28 complies with the phenomena explained in Figure 4.19a for NFF. In the next section, the beam steering in the vertical plane is investigated. Since the dish diameter cannot completely cover the total current distribution on the dish for the beam steering in the vertical plane, only one case will be considered for beam scanning in the vertical plane.

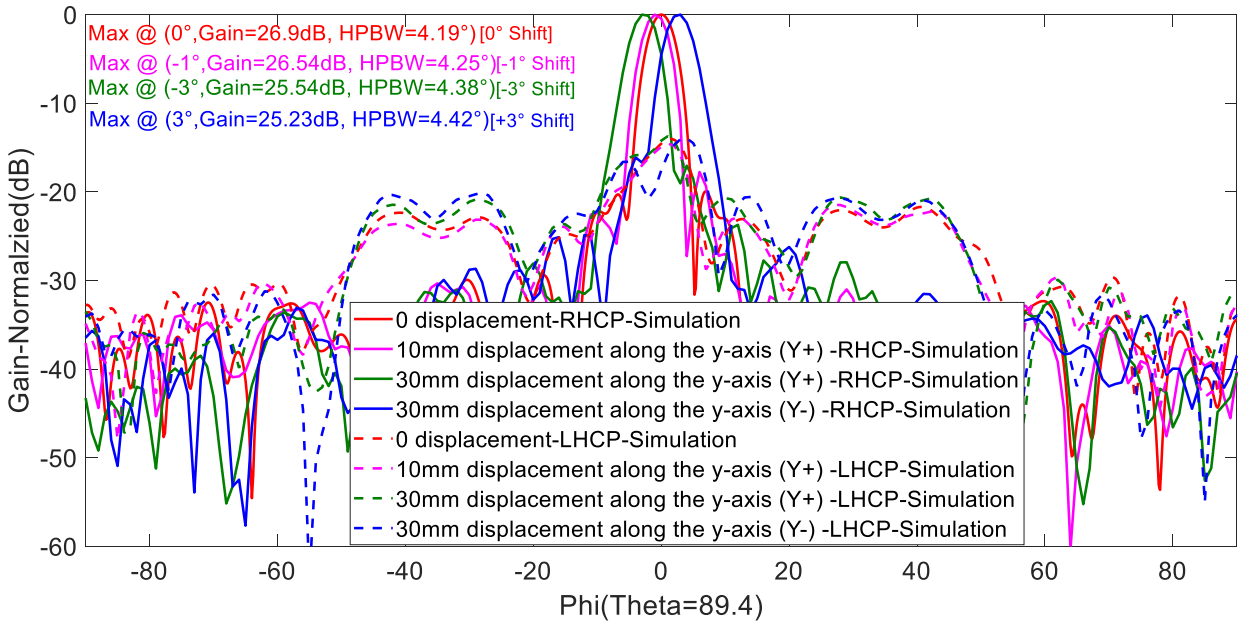

Figure 4.27 Simulated beam scanning at $\theta = 89.4°$ for the structure in Figure 4.26 by applying NFF technique for the virtual feed displacements of 0 mm, +10 mm, +30 mm, and -30 mm along the *y* axis

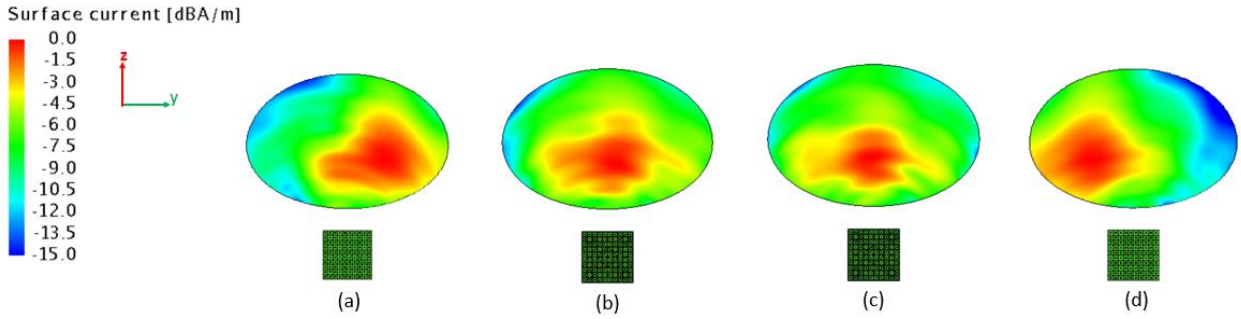

Figure 4.28 Normalized current distributions on the dish for the scanned beams of (a) $-3°$, (b) $-1°$, (c) $0°$ and (d) $+3°$ at $\theta = 89.4°$

Figure 4.29 shows the beam scanning for displacements of 0 mm and +10 mm of the virtual phase center in the *z* direction. For zero displacement (i.e. the non-scanned beam), the main beam points at $\theta = 89.4°$ instead of 90° in the $\varphi = 0°$ plane. This offset is due to asymmetry in the alignment of the reflectarray elements. As shown in Figure 4.28, the beam is steered to $\theta = 90°$ in $\varphi = 0°$ plane when the displacement is +10 mm along the *z* axis. There is a limitation in beam scanning in $\varphi = 0°$ plane due to the small minor axis of the elliptically shaped dish. Normalized current distributions on the dish related to the scanned beams of $0°$ and $+0.6°$ at $\varphi = 0°$ are shown in Figure 4.30.

Since the feed horn for the simulation in Figure 4.26 is LHCP, for the beam reflected from the dish, the RHCP term is considered co-polarization term, and LHCP is deemed to be the cross-polarization term. Spillover from the feed around the subreflector therefore contributes to cross-polarization, and show as strong contributions on each side of the main beam in Figures 4.27 and 4.29.

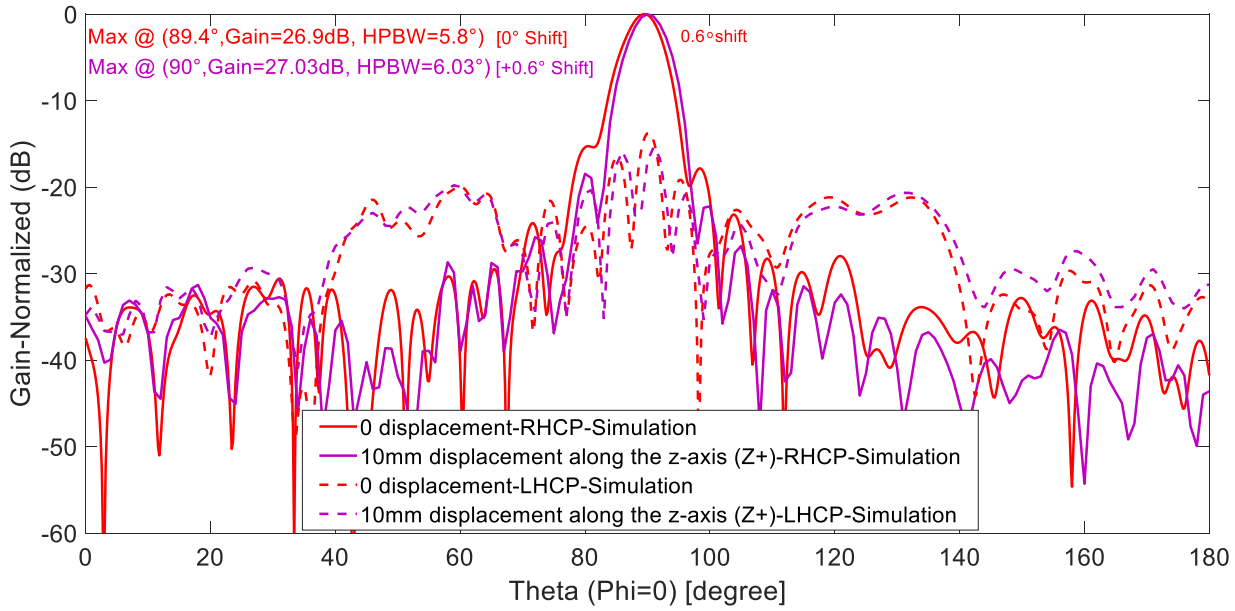

Figure 4.29 Beam scanning in $\varphi = 0°$ plane for the structure in Figure 4.26 by applying NFF technique for virtual source displacements of 0 mm and +10 mm along the *z* axis

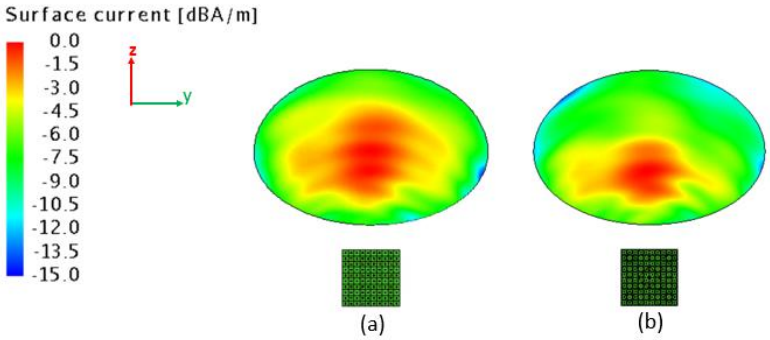

Figure 4.30 Normalized Current distribution on the dish for the scanned beams of (a) $+0.6°$ and (b) $0°$ in the $\varphi = 0°$ plane

To experimentally support the simulation results obtained in Figures 4.27 and 4.29, the setups in Figure 4.31 related to the structure in Figure 4.26 are used.

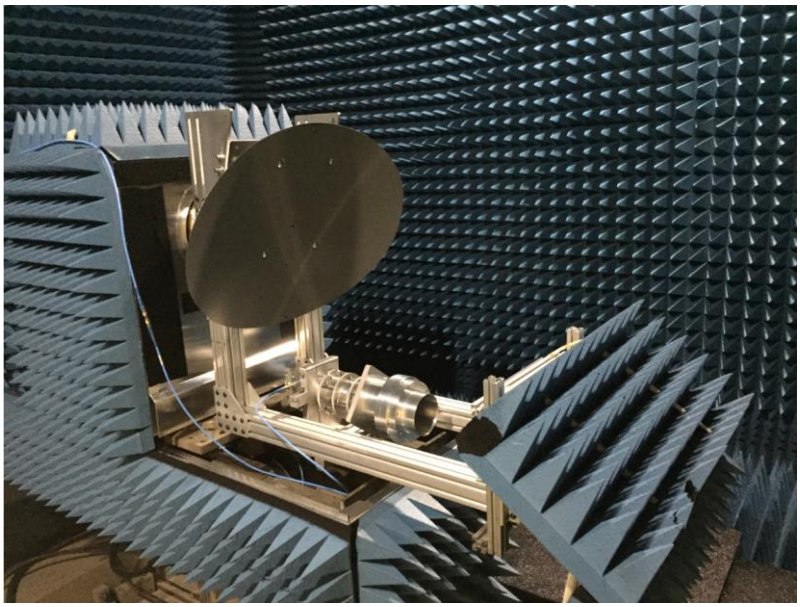

(a)

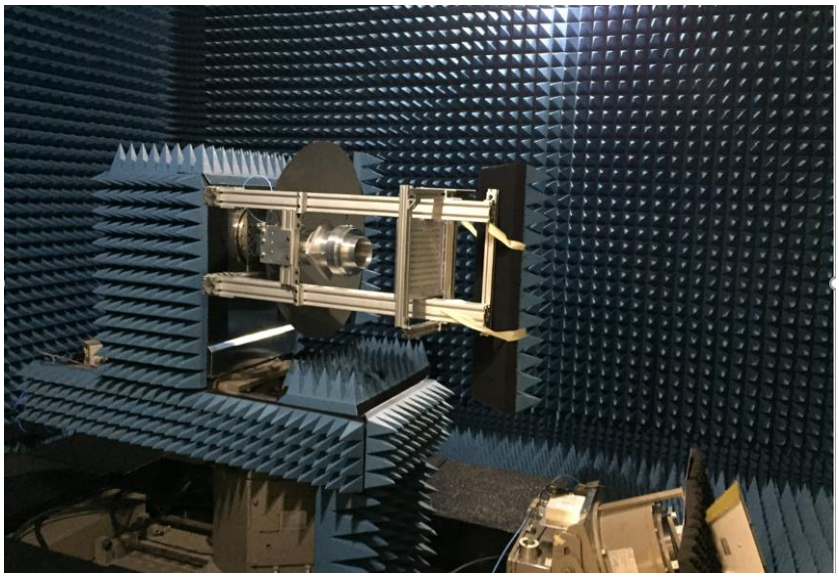

(b)

Figure 4.31 (a) Setup of the structure in Figure 4.26 to experimentally validate beam scanning results in Figure 4.27. This setup is used to scan in the horizontal *xy* plane, (b) Setup of the structure in Figure 4.26 to experimentally validate beam scanning results in Figure 4.29. This configuration is used to characterize beam steering in the vertical *yz* plane

The mounting fixture used to put together the horn, reflectarray and dish reflector was not present in the simulation model. To minimize scattering of the reflectarray mounting hardware during the tests, absorber panels have been added at the front end of the fixture, as shown in Figure 4.31. A consequence of this is that spillover from the feed will be highly attenuated during measurements. Figure 4.32 shows an offset of $\varphi = 0.5°$ in $\theta = 90°$ plane for the non-scanned beam, corresponding to zero displacement of the virtual phase center with respect to the focal point of the dish. This measured offset could be due to the misalignment of the antenna in the measurement setup. As shown in Figure 4.32, beam steerings of $-1°$, $-3.2°$ and $+2.7°$ in the $\theta = 90°$ plane are obtained

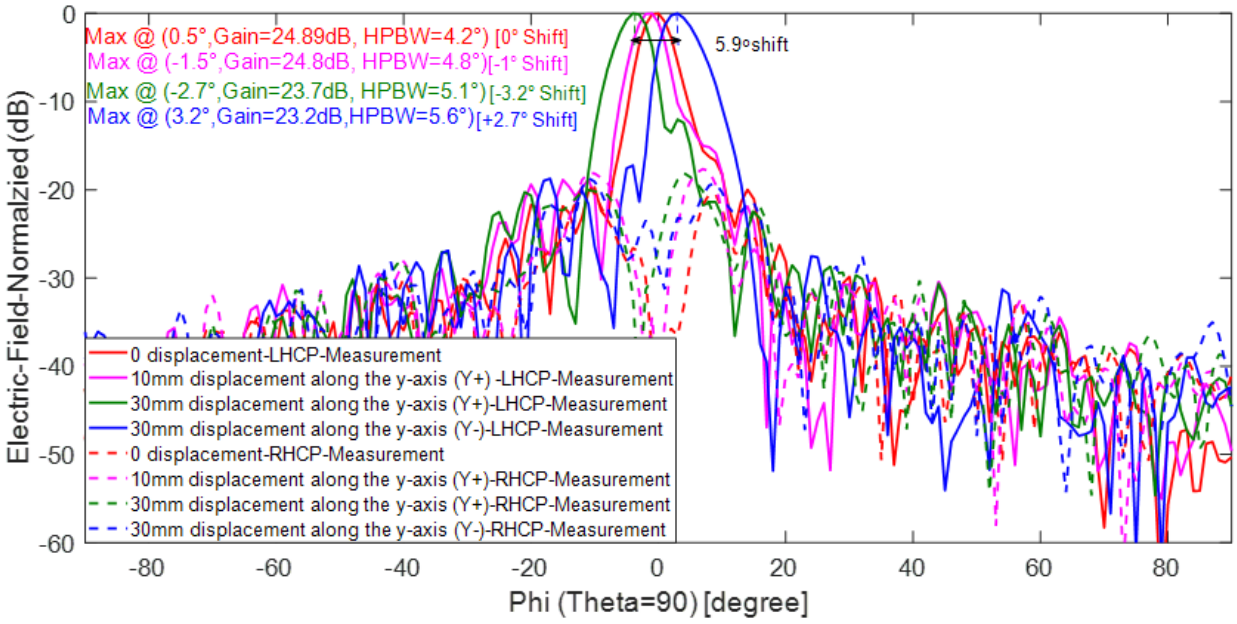

Figure 4.32 (a) Beam scanning in $\theta = 90°$ plane for the structure in Figure 4.26 by applying NFF technique for the virtual feed displacements of 0 mm, +10 mm, +30 mm, and -30 mm along the *y* axis

with respect to the reference curve (in red) for virtual feed displacements of +10 mm, +30 mm, and -30 mm along the *y* axis respectively. Non-symmetric main beam directions for displacements of +30 mm and -30 mm could be due to either asymmetry in the alignment of the reflectarray elements

or the misalignment of the antenna in the measurement setup. In comparison with the simulated cases of Figure 4.27, the cross-polarization level in the direction of the main beams is lower by more than 10 dB in the measurements, and the high cross-polarized lobes in the 25° to 50° intervals are not present. This is due to absorber material surrounding the reflectarray in the measurements, as will be discussed in more details in Chapter 6.

Figure 4.33 shows the beam scanning for the displacement of 0 mm and +10 mm of the virtual phase center along the *z* direction for. For zero displacement, corresponding to the non-scanned beam, the main beam points at $\theta = 89.6°$ in $\varphi = 0°$ plane. This offset, also observed in the simulations (Figure 4.29), could be due to either the asymmetry in the alignment of the reflectarray elements or misalignment of the antenna in the measurement setup. As shown in Figure 4.33, the beam is steered by $0.5°$ in $\varphi = 0°$ plane for a phase center displacement of +10 mm along the *z* axis.

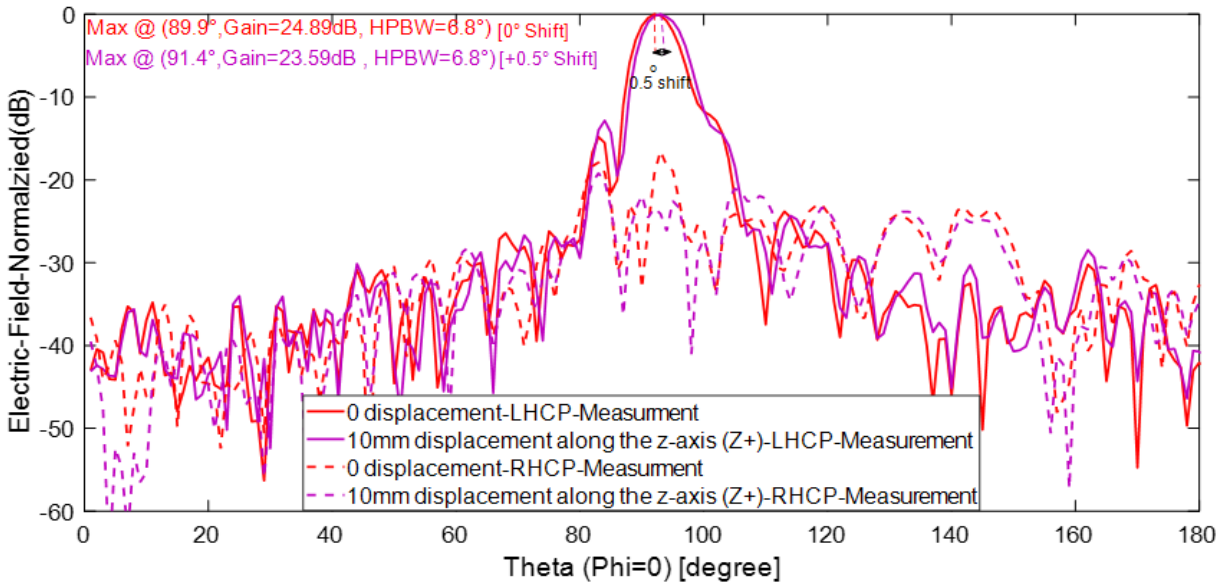

Figure 4.33 Measured beam scanning in the $\varphi = 0°$ plane for the structure in Figure 4.26 by applying NFF technique for the virtual feed displacements of 0 mm and +10 mm along the *z* axis

Table 4.1 shows HPBW and gain related to the simulated and measured scan beams in Figures 4.28, 4.29, 4.32 and 4.33.

Table 4.1 HPBW and gain for the simulated and measured scan beams in Figures 4.28, 4.29, 4.32 and 4.33

	Virtual Source Offset	Main Beam Direction		Beam Shift	HPBW at $\varphi=0^\circ$	HPBW at $\theta\simeq 90^\circ$	Gain
Simulation	0	$\theta=89.4^\circ$	$\varphi=0^\circ$	$\Delta\varphi=0^\circ,\Delta\theta=0^\circ$	5.8°	4.19°	26.9 dB
	10 mm Y+	$\theta=89.4^\circ$	$\varphi=-1^\circ$	$\Delta\varphi=-1^\circ$		4.25°	26.54 dB
	30 mm Y+	$\theta=89.4^\circ$	$\varphi=-3^\circ$	$\Delta\varphi=-3^\circ$		4.38°	25.54 dB
	30 mm Y-	$\theta=89.4^\circ$	$\varphi=+3^\circ$	$\Delta\varphi=+3^\circ$		4.42°	25.23 dB
	10 mm Z+	$\theta=90^\circ$	$\varphi=0^\circ$	$\Delta\theta=+0.6^\circ$	6.03°		27.03 dB
Measurement	0	$\theta=89.6^\circ$	$\varphi=0.5^\circ$	$\Delta\varphi=0^\circ,\Delta\theta=0^\circ$	6.8°	4.2°	24.89 dB
	10 mm Y+	$\theta=90^\circ$	$\varphi=-1.5^\circ$	$\Delta\varphi=-1^\circ$		4.8°	24.8 dB
	30 mm Y+	$\theta=90^\circ$	$\varphi=-2.7^\circ$	$\Delta\varphi=-3.2^\circ$		5.1°	23.7 dB
	30 mm Y-	$\theta=90^\circ$	$\varphi=3.2^\circ$	$\Delta\varphi=+2.7^\circ$		5.6°	23.2 dB
	10 mm Z+	$\theta=88.6^\circ$	$\varphi=0^\circ$	$\Delta\theta=+0.5^\circ$	6.8°		23.59 dB

In the measurement setup, the rotation angle increment of 11.25° is considered for the reflectarray unit cells. This corresponds to increments of 22.5° in the applied phase shifts. Such Phase 4-bit quantization can increase the SLL and broaden the main beam. The lower gain and larger HPBW in the measured beams compared to the simulations are partly due to the phase quantization effect.

As shown in Table 4.1, the gain obtained from the measurements is about 2 dB lower than the simulation. Besides the phase quantization effect, this loss could be due to the uncertainty in the measurement, such as the limited quiet zone size of the CATR, the phase error due to the small reflectarray, and the error we had for SGH measurement. The phase error results in a larger HPBW in the measurements compared to the simulation. This effect is observed in the figures and leads to a reduction in directivity.

The axial ratio of the incident field generated in the CATR may not be good over the whole quiet zone. The CP is synthesized in calculations by combining two measurements with orthogonal linear polarizations with phase quadrature. Since vertical and horizontal fields are not equal over the whole quiet zone, AR is not perfect, and therefore incident CP is not pure.

The dish surface is not a smooth since it is cut out from a low-cost parabolic TV dish. Therefore, the shape could be distorted or rough.

XPD in the measurement is improved by the absorber covering the area behind the reflectarray. The absorber blocks the spillover of cross-polarization term around the reflectarray. This effect will be confirmed in Chapter 6 by simulating the whole system by including a Salisbury screen around the reflectarray. Also, metallic supports in the measurement setup can cause additional scattering and increasing cross-polarization levels. The scattered fields are partially absorbed by absorbing material behind the reflectarray.

4.5 Bandwidth performance of the dual-reflector antenna

Reflectarray elements were set to steer the beam at the four different angles in the $\theta = 90°$ plane specified in Figure 4.32, at a frequency of 7 GHz. Then, the antenna was tested over the 6 to 7.8 GHz range at intervals of 0.1 GHz without changing the unit cells' rotation angles. This is the band where $AR < 1\text{dB}$ for the feed horn, according to Figure 3.15. Figure 4.34a shows results for the co-polarized gain. Unfortunately, the gain is still increasing at the upper end of the band; therefore, it is not possible to determine the upper end of the 3dB bandwidth. However, the bandwidth is limited by the axial ratio of the system, which is less than 3dB in the 6 to 7.8 GHz range. Based on the figure, 3dB gain bandwidth is greater than 13%, 16%, 13% and 16% respectively for the beams steered at 0, -2, -3.2 and +2.7 degrees. Also, the bandwidth of 16% is obtained for the beam steering of 0 degrees from the simulation results.

The XPD (in the direction of the main beam) and HPBW associated with the steered beams in Figure 4.32a are provided in Figure 4.34b. Contrary to the gain, it can be seen that the XPD is a narrow-band characteristic, and it degrades rapidly away from the design frequency. Figure 4.34c shows the beam steering error versus frequency in the bandwidth associated with the measurement

of the scanned beams provided in Figure 4.32. In some cases, these errors can be large compared to the specified amount of steering. Since the unit cells have shown broadband performance (see Chapter 3), it can be concluded that both XPD and steering directions are sensitive to path length variations with frequencies.

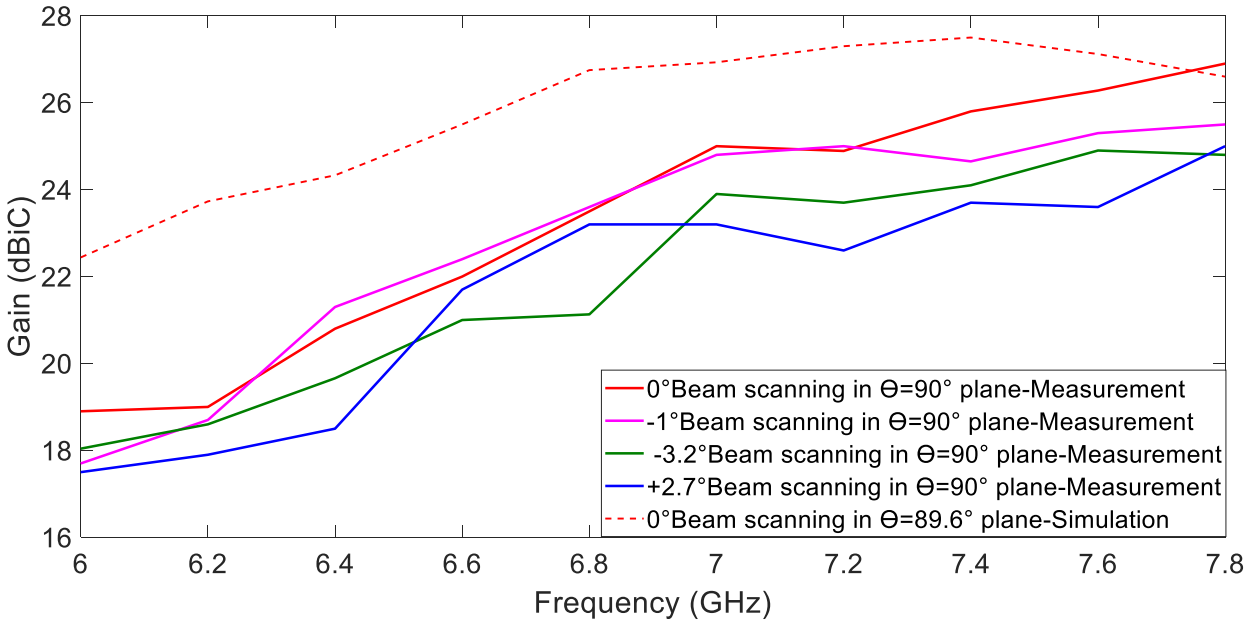

(a)

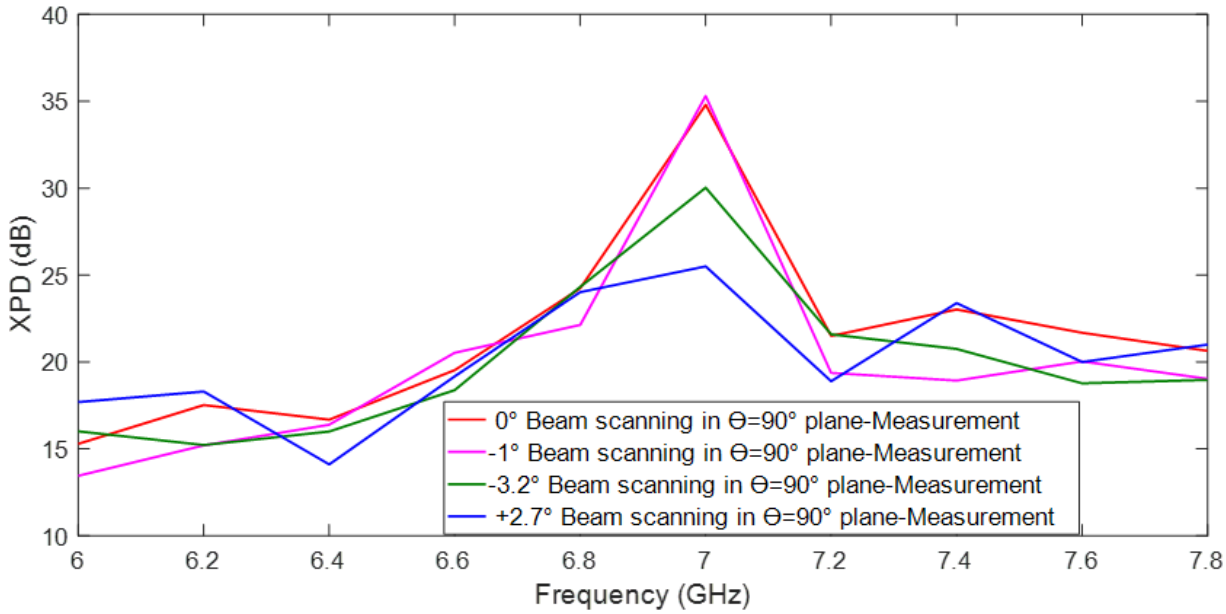

(b)

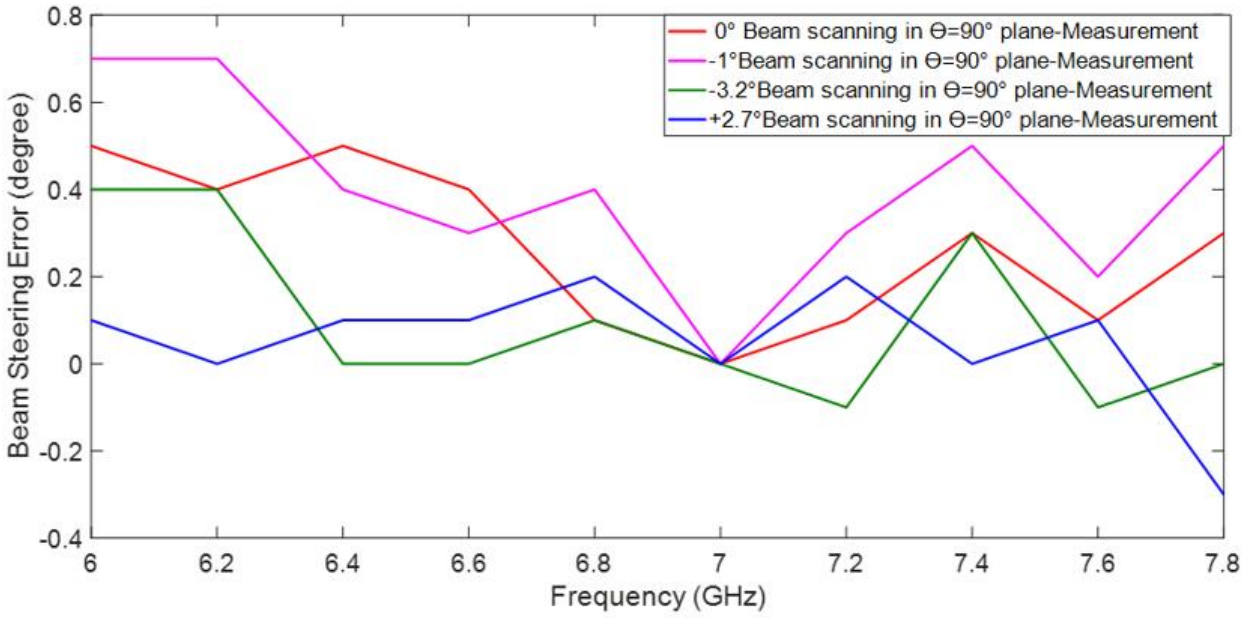

(c)

Figure 4.34 (a) Measured co-polarized gain in the frequency band, (b) XPD in the frequency band, (c) Beam steering error vs frequency. All results for the scanned beams provided in Figure 4.32

4.6 Conclusion

This chapter presented a C-band reconfigurable CP dual-reflector structure as a potential candidate for new generation steerable antennas. Narrow beam scanning of the dual-reflector antenna with a reflectarray subreflector using NFF is proposed.

Compared to the traditional PPS method, NFF allows covering a more extensive scan range with the ability to change the beamwidth, which is applicable in beam steering for geostationary applications. In the NFF technique, there is less spillover around the reflectarray and the dish. In NFF, the beam scanning in two planes is possible and is only limited by the dish size, while with PPS, the beam scanning in both planes is limited by the high cross-polarization level and limited

by the feed blockage in the vertical plane. Higher gain is obtained from the PPS method is at the expense of higher cross-polarization level and limited scan range.

The proposed structure keeps the desired features of existing reflector systems, such as low X-pol, wide frequency bandwidth, and high gain. The beam scanning of 6 degrees for the dual-reflector system has been validated experimentally in the anechoic chamber. A measured 3 dB gain bandwidth greater than 13% is reported for the proposed system.

CHAPTER 5 BEAM SYNTHESIS OF A C-BAND CIRCULARLY POLARIZED DUAL-REFLECTOR ANTENNA USING A RECONFIGURABLE SUBREFLECTOR

5.1 Introduction

In this chapter, the phase-only synthesis technique is used for beam shaping of a C-Band CP dual-reflector antenna for earth coverage applications. In this chapter, synthesis relies on Particle Swarm Optimization (PSO) by using the element factors of a 100-element reflectarray. The proposed algorithm gives the ability of beam scanning as well as beam shaping in the uv plane. Beam scanning and shaping of the dual-reflector antenna is realized with a phase synthesis technique, whereas Chapter 4 proposed beam scanning of a dual-reflector antenna by adjusting the phase distribution of the sub-reflectarray using NFF and PPS techniques [52].

Section 5.2 briefly describes the PSO algorithm. Section 5.3 presents the procedure for implementing the PSO algorithm for a dual-reflector antenna in which the subreflector is a reconfigurable reflectarray. Moreover, the performance of the proposed method is illustrated by comparing the patterns calculated with with MATLAB using the phases obtained from PSO with those obtained with the simulation of the whole system in FEKO using a hybrid "Method of Moments (MoM) and Physics Optics (PO)" solution. Afterward, to address the degradation of the optimized far-field patterns due to the discontinuities in the reflectarray phase distribution, a solution to force a continuous phase distribution among the reflectarray surface is proposed. The performance of this modified algorithm is explored by scanning and shaping the beam. Finally, Section 5.4 concludes the chapter.

5.2 Particle Swarm Optimization (PSO) basics

Although optimization methods are not the focus of this thesis, it is useful to give some background on the method used to optimize the antenna patterns. PSO is an evolutionary algorithm inspired by the concept of the search of birds hunting for food [15]. The first step for implementing this

algorithm is to define the population number. That is the number of "particles" moving in the search space to find the best solution to the problem. The best solution is the one giving the lowest cost value. The iterative algorithm stops the process when the best cost reaches the goal value or when a maximum pre-defined iteration number is reached. The Mean Square Error (MSE) between desired and synthesized patterns is used as a cost function to be minimized.

Each potential solution in the algorithm is called a 'particle'. PSO search in the solution space to find the optimum solution. In the phase synthesis problem, each particle consists of a set of phase shifts to be applied to all the reflectarray elements. A small reflectarray with 100 elements is considered in this work, so each particle is a vector of 100 unknown phase values. Each of these phases is comprised between $-\pi$ and π. The velocity parameter controls the moving tracks of each particle. Velocity (*v*) and position (*r*) are two parameters dedicated to each particle in the algorithm. Each of the parameters is a 100-size element matrix that is updated in each iteration n as follows:

$$\boldsymbol{v}_i^{n+1} = \omega \cdot \boldsymbol{v}_i^n + c_1 \cdot r_1 \odot (\boldsymbol{p}_i^n - \boldsymbol{x}_i^n) + c_2 \cdot r_2 \odot (\boldsymbol{g}_i^n - \boldsymbol{x}_i^n) \tag{5.1}$$

$$\boldsymbol{x}_i^{n+1} = \boldsymbol{v}_i^{n+1} + \boldsymbol{x}_i^n \tag{5.2}$$

where ω is the inertia weight which is a scalar value, c_1 and c_2 scalars are the acceleration coefficients, r_1 and r_2 are random matrices with the size of d equal to 100 with real numbers in the range of [0,1]. The position and velocity of i-th particle with the dimension d equal to 100 are given by $\boldsymbol{x}_i = (x_{i1}, x_{i2}, ..., x_{id})^T$ and $\boldsymbol{v}_i = (v_{i1}, v_{i2}, ..., v_{id})^T$, respectively. $\boldsymbol{p}_i$ is the position vector giving the best cost of the i[th] particle called personal best position, and g is the global best position vector with the best cost value among all particles in the current and previous iterations.

The right-hand side of eq. (5.1) includes three terms; the first term is related to the initial velocities of particles. The second part is associated with each particle's behavior, and the third part is "social", which expresses the cooperation among the particles [70, 71, 72].

The algorithm begins by assigning, for all the particles, 100 arbitrary values to the position vector and assigning zeros to the velocity vector. These values will be updated in each iteration. Two best

positions, including global and personal best solution parameters, update the particles as potential solutions. The set of 100 phases in each particle is updated in each iteration. After the last iteration, the optimized phase distribution related to the particle with the global best cost is used to calculate the far-field pattern.

Since the problem is a minimization problem, the global best cost is initialized to infinity. The value will be updated in each iteration with the smallest number among all the particles' best costs during the current and previous iterations. Figure 5.1 shows the flowchart of the PSO process for the pre-defined iteration number. As shown in the flowchart, in each iteration, the particle best's cost value is compared with the global best cost, the best cost among all the particles in all previous and current iterations. If the particle best cost is less than the global best cost, the global best's cost will be updated with the particle's best cost. The algorithm will be continued by updating the position and velocity of each particle in each iteration.

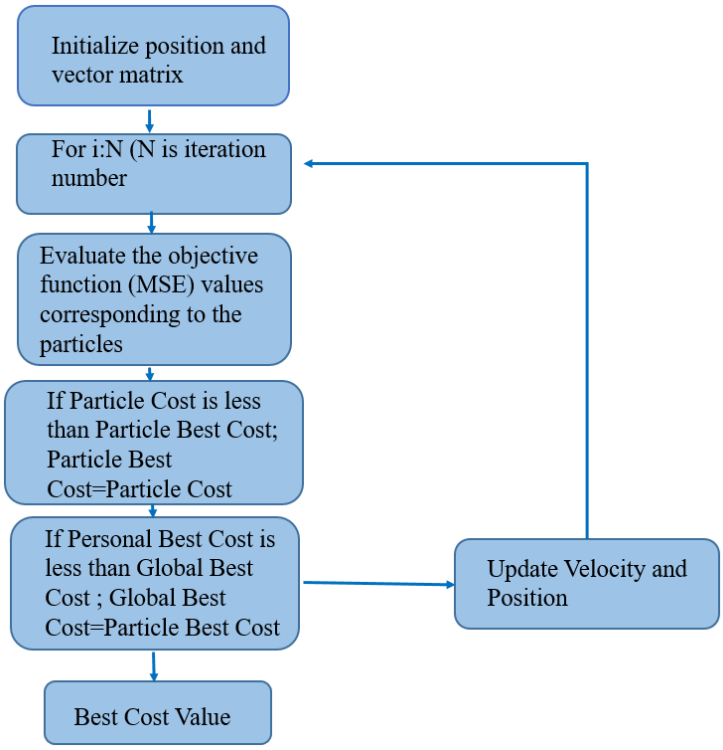

Figure 5.1 Flowchart of the PSO algorithm [15]

5.3 Implementation of the PSO algorithm for beam synthesis of the antenna

This section describes the main process of the beam synthesis applied to the antenna system illustrated in Figure 5.2. This figure is similar to Figure 4.14, but with the *uv* plane displayed on the left side. Coordinates *u* and *v* are the direction cosines used to designate far-field directions. The system includes a horn, a reconfigurable subreflector consisting of the reflectarray for which the phases have to be optimized, and a solid parabolic dish. The system operates in CP. See Chapter 3 for a description of the horn and reconfigurable CP reflectarray elements. The size of the square subreflector is $3.67\lambda \times 3.67\lambda$ (λ=42.8 mm), and the projected diameter of the dish in the *yz* plane is 24λ (102.7 cm) at the design frequency of 7 GHz. The dish F/D ratio is 0.5. The reflectarray has 10×10 square elements with a periodicity of 15.75 mm in a square lattice. For such a small array, a large fraction of the elements is close to the array edges, so assuming identical far-field patterns for all the elements is inaccurate in the beam synthesis. Therefore, to implement a beam synthesis algorithm, each reflectarray element's embedded element factor is an important parameter to be considered.

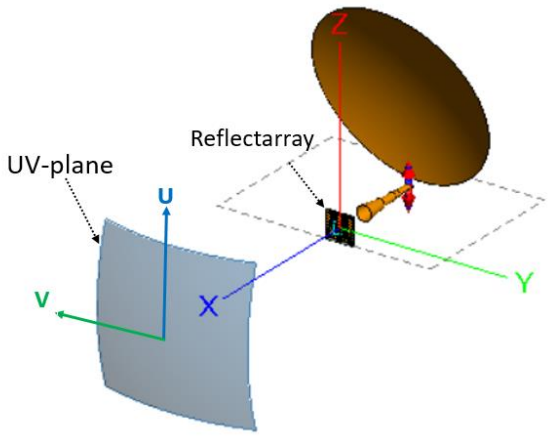

Figure 5.2 Dual-reflector antenna including horn, sub-reflectarray and solid parabolic dish, *u* and *v* are direction cosines in the far-field, as illustrated in the coordinate system

5.3.1 Criteria for implementing beam synthesis algorithm for the proposed system

Element factors of reflectarray elements contributing to the far-field pattern are parameters to be calculated in this section for beam synthesis purposes. A simplified radiation source model that accounts for the specific element factors of all the array elements is proposed. In this model, the element factor $f_n(u,v)$ is defined as the contribution of the nth reflectarray element to the whole system's radiation pattern. It consists of the fields scattered by the reflectarray element that is then reflected by the parabolic dish. Therefore, the far-field pattern is a weighted sum of all the element factors as given by eq. (5.3):

$$F(u,v) = \sum_{n=1}^{N} a_n f_n(u,v) + F_{struc}(u,v) \tag{5.3}$$

where *u* and *v* are the coordinates shown in Figure 5.2.

$F_{struc}(u,v)$ is a complex contribution to far-field pattern coming from parasitic scattering, e.g., specular reflection on reflectarray, diffraction by the reflectarray, back radiation of the horn reflected by the dish, etc. It accounts for all the phenomena that are not affected by the excitation of the array elements.

Functions $f_n(u,v)$ are the complex element factors associated with the N elements of the reflectarray in the far-field of the dish.

The a_n's are complex coefficients associated with each reflectarray element and is defined as $|a_n|e^{j\varphi_n}$. The magnitude of a_n is set by the illumination source incident on the n^{th} element and the phase φ_n can be controlled by element rotation. In the reference case used in the calibration phase (see 1a below), all the φ_n's are considered zero, and therefore the a_n's are real positive. φ_n is the difference between the phase of element *n* resulting from rotation of the element and the phase of element *n* in the reference rotation angle used in the calibration, to be defined in eq. (5.4) below.

The following steps are used to determine functions f_n and F_{struc} using simulations of the antenna system, and then to use eq. (5.3) to synthesize desired radiation patterns using PSO. It is assumed that the structural scattering term does not depend on the phase settings of the reflectarray elements, so the two terms of eq. (5.3) can be treated independently. Before running PSO, the radiation pattern terms f_n and F_{struc} in eq. (5.3) need to be determined. This is done through simulations with the following procedure.

1. Determination of $F_{struc}(u,v)$
    a. Adjust the rotation angles of the reflectarray to generate a narrow beam in the far-field, for instance by having near-field focusing at the focal point of the dish. In this case, calculate pattern F^+ by simulation of the whole system. This pattern corresponds to:

$$F^+(u,v) = \sum |a_n| e^{j\varphi_n} f_n(u,v) + F_{struc}(u,v) \tag{5.4}$$

    For this reference case, we consider that the phases of all coefficients a_n are zero, i.e. $\{\varphi_n\} = 0$. Therefore we have:

$$F^+(u,v) = \sum |a_n| f_n(u,v) + F_{struc}(u,v) \tag{5.5}$$

    b. Rotate all the elements by 90 degrees in the same sense of rotation. That will add a phase of 180 degrees to all a_n coefficients. In this case, the simulated pattern will correspond to:

$$F^-(u,v) = \sum -|a_n| f_n(u,v) + F_{struc}(u,v) \tag{5.6}$$

    c. Extract $F_{struc}(u,v)$ by post processing:

$$F_{struc}(u,v) = \frac{F^+ + F^-}{2} \tag{5.7}$$

So, with only two simulations, with all the elements not rotated and then rotated by 90 degrees, F^+ and F^- can be obtained,. The same $F_{struc}(u,v)$ should be found in all cases, at least approximately. If it is found that $|F_{struc}(u,v)| \ll |F(u,v)|$ in all the (u,v) range of interest, the $F_{struc}(u,v)$ can be neglected in (5.3). Otherwise, it should be kept for the next steps.

2. Determination of the element patterns $f_n(u,v)$ for the N elements

   a. Use the same setting as in part 1a ($\{\varphi_n\} = 0$), except for element number k. Rotate element k by 90 degrees. This effectively changes the phase of the k^{th} element (i.e. a_k) by 180 degrees. Using (5.3) therefore:

$$F_k(u,v) = \sum_{n \neq k} |a_n| f_n(u,v) - |a_k| f_k(u,v) + F_{struc}(u,v) \tag{5.8}$$

   b. Based on the result of step 2a, and assuming the magnitude of a_k is known, (5.9) can be obtained:

$$f_k(u,v) = \frac{F^+ - F_k}{2|a_k|} \tag{5.9}$$

   The magnitude of a_k is obtained from the intensity of the horn illumination in the desired polarization in element *k*. This can be obtained by simulating the horn without reflectarray and sampling the field amplitude of the horn at the location of the element *k* which corresponds to a_k.

   c. Repeat steps 2a and 2b for the N elements of the reflectarray. This gives the set of element patterns that can then be used in the phase synthesis.

These "element patterns" correspond to the far-field of the elements embedded in the whole system (horn, reflectarray and dish). As implied by eq. (5.9), 100 simulations of the whole system (horn +

reflectarray + dish) sitting at the same physical location are necessary to obtain each f_k. Therefore, there is no need for the usual path length factors $\exp(j\beta\mathbf{r}_k'\bullet\hat{\mathbf{r}})$ in the sum, because the terms $\mathbf{r}_k'$ are constant. The path length factors can then be considered included in the element factors f_k.

3. Use PSO (or another optimization method) to find the set of phases $\{\varphi_n\}$ to be applied to coefficients a_n to generate a desired far-field pattern $F_d(u,v)$. The MSE to minimize can be based on the magnitude only of the normalized patterns, i.e.:

$$MSE = \sum_{u,v} \left\| F_{d,normalized}(u,v) \right| - \left| F_{normalized}(u,v) \right\|^2 \tag{5.10}$$

where $F_{d,normalized}$ is the normalized desired pattern and $F_{normalized}$ is the normalized optimized pattern. The obtained phase distribution $\{\varphi_n\}$ should be added to the reference phase state of the elements to realize the desired pattern.

The non-normalized pattern can be rewritten as:

$$F(u,v) = F_{struc}(u,v) + \sum_{n=1}^{N} |a_n| e^{j\varphi_n} f_n(u,v) \tag{5.11}$$

During the iterative process, the sum in eq. (5.10) is calculated over a number of selected points in the *uv* plane. For all the examples shown in this thesis, 256 sample points in the uv plane equally spaced in the range, $(u,v) = ([-0.3,0.3],[-0.3,0.3])$ were used. This range has been selected based on the geometry of the system and the wavelength. It covers the main beam of the focused beam and allows demonstrating efficient beam steering.

As mentioned in steps 1a and 1b above, two simulations are run to calculate F_{struc} of the dual-reflector antenna in Figure 5.2. In the first simulation, F^+ will be obtained where all the elements are in the reference state. The second simulation gives the pattern related to F^- where all the elements are rotated by 90 degree from their primary state. F_{struc} is calculated by eq. (5.7). Figure 5.3 show plots of F_{struc} and F^+ obtained from simulations of the antenna system in FEKO. An

average difference of approximately 20 dB between the amplitude level of F_{struc} and F^{+} can be observed. Therefore, the F_{struc} term was considered negligible and was ignored in the of the beam synthesis examples presented in the rest of the chapter.

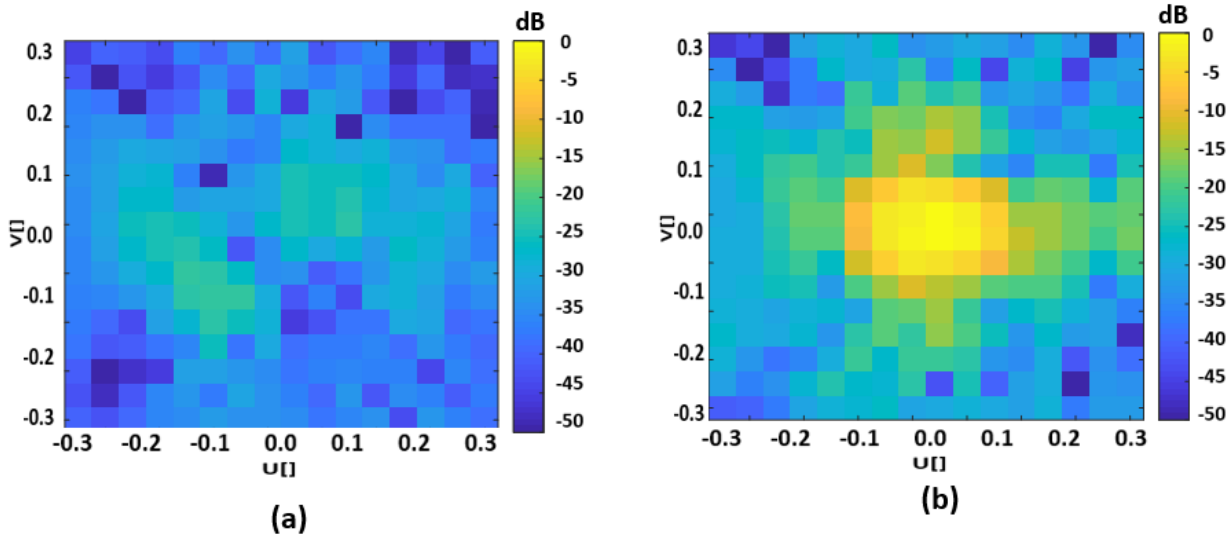

Figure 5.3 (a) Amplitude of F_{struc}, (b) Amplitude of F^{+}. Both patterns are normalized with respect to the maximum of F^{+}

In the reference state, the phases of the elements are adjusted using the standard path equalization reflectarray formula, is such a way that the reflected beam from the reflectarray is focused at the focal point of the dish. The reference radiation pattern of the dual-reflector antenna, F^{+}, in FEKO is shown in Figure 5.4, which is the same data used to plot Figure 5.3b in MATLAB, without interpolation and smoothing.

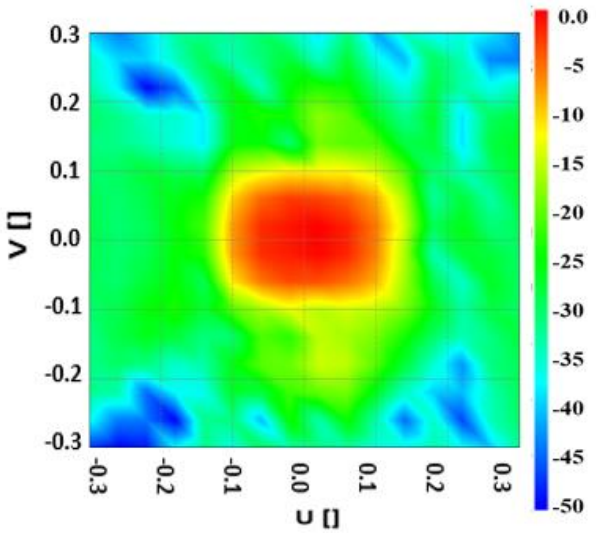

Figure 5.4 Reference pattern in uv plane related to the structure in Figure 5.2

In Figure 5.5, the amplitude (on a linear scale) and phase of element factors of the 100 reflectarray elements are shown in the uv range of $(u,v) = ([-0.3, 0.3], [-0.3, 0.3])$. The desired term of the beam is RHCP reflected by the dish. The position of each pattern in the figures correspond to the position of the corresponding reflectarray element in the y-z coordinate system of Figure 5.2. Each pattern is plotted in the far-field *u*-*v* coordinates, also displayed in Figure 5.2. These coordinates are repeated at the bottom right of Figure 5.5. It can be seen from these plots that the elements on the edge of the array have weaker contributions. This is not due to the illumination amplitude since it is taken into account in eq. (5.9). The elements on the edge of the array have different couplings with neighbors than those in the center, which may modify their pattern. Also, they are farther from the dish focal point, so their radiation is not well collimated.

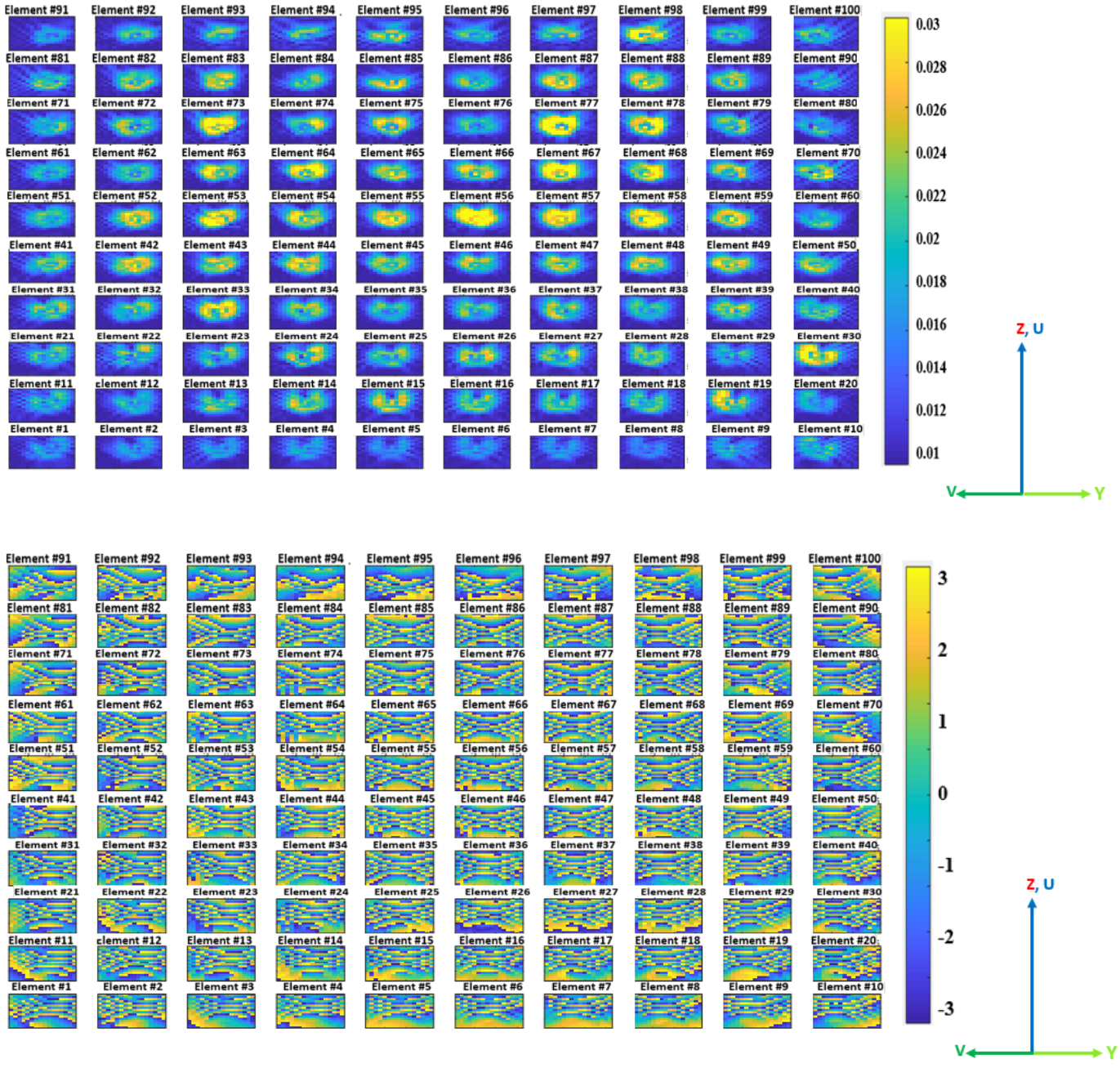

Figure 5.5 (a) Element factor f_n of the 100 elements of the reflectarray (Electric field amplitude (V/m)), *Z*, *Y*, *U* and *V* axes are according to the coordinate system in Figure 5.2: (a) Amplitude on a linear scale, (b) Phase (radians)

5.3.2 Performance of the proposed beam synthesis technique

This section presents the results of the beam synthesis technique proposed in the previous section. The performance of the algorithm will be evaluated by comparing the patterns calculated with eq. (5.3) using the element's phases obtained with PSO. The whole PSO optimization process to determine these optimal phases as well as final pattern $F(u,v)$ are calculated with MATLAB. Then, the set of 100 optimal phases are used to apply corresponding rotations to the unit cells in order to simulate the whole system in FEKO.

For evaluating the performance of the algorithm, a simple problem where the reference pattern in Figure 5.4 is defined as the desired pattern is considered. The algorithm is started with a random phase distribution and is expected to converge to a proper phase distribution of 100 zero-phase ($\pm 2m\pi$) values used to generate the pattern of Figure 5.4. A zero-phase distribution will not change the primary rotation angle of the elements and result in the reference pattern as the desired pattern. The PSO is implemented with a population number of 2000 particles (each one consisting of a set of 100 phases, i.e. one for each reflectarray element) and a maximum iteration number of 5000. The algorithm stops when the maximum iteration number is reached. Figure 5.6 shows the convergence of MSE, and Figure 5.7a shows the distribution of $\cos\varphi_n$ on the reflectarray elements for the particle having the smallest MSE after 5000 iterations. A smooth decrease of MSE can be observed in the whole optimization process. It can be seen that after 5000 iterations, the MSE still decreases, but very slowly. Therefore, letting the iterations run for a longer time would not improve antenna patterns significantly. The expected $\cos\varphi_n$ distribution is uniform, with unit amplitude. Instead, Figure 5.7a shows a quasi-random distribution. The normalized far-field pattern in Figure 5.7b calculated by PSO with phase distribution in Figure 5.7a using eq. (5.11) is, however, close to the desired pattern. Using the phase calculated by PSO, rotations are applied to the reflectarray elements, and then hybrid (MoM + PO) simulation of the antenna is done with FEKO. It is found that the resulting pattern, shown in Figure 5.7c, is quite different from the expected reference pattern of Figure 5.4. The main beam with a rectangular shape centered at (0,0) is slightly shifted in the negative *v* direction, and in addition, a lobe approximately 5 dB lower is created near (*u*, *v*) =(0.05, 0.15).

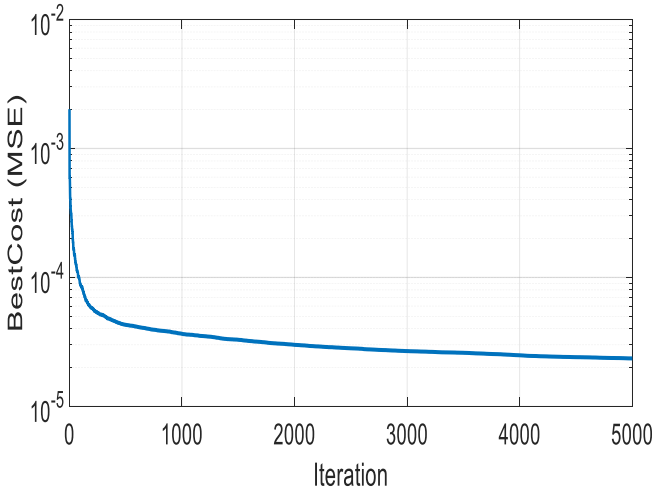

Figure 5.6 MSE of the optimized pattern with the reference pattern as desired pattern

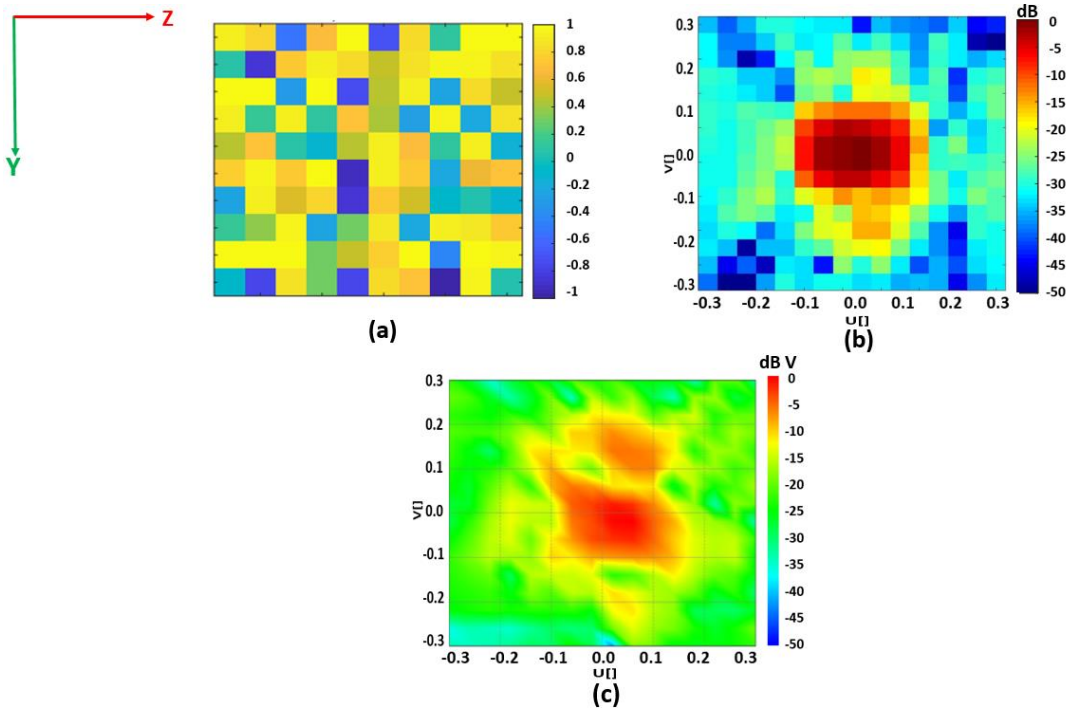

Figure 5.7 (a) Distribution of $\cos\varphi_n$ on the reflectarray elements of the optimized pattern with the reference pattern as the desired pattern, (b) Normalized amplitude of the optimized pattern calculated by PSO, (c) Radiation pattern obtained by hybrid simulation of the antenna in FEKO using the phase distribution in Figure 5.7a

Although the calculated pattern of Figure 5.7b using phases generated by PSO is similar to the one calculated with known phases in Figure 5.3b, the simulated antenna model using theses phases is not in good agreement. It was conjectured that the poor results obtained with the hybrid simulation come from the rapidly varying phase visible in Figure 5.7a. In fact this figure shows adjacent pixels with large differences. The phase response of reflectarray unit cells is generally calculated with the assumption of infinite arrays of identical cells, which is not the case when the phase varies rapidly and not linearly from cell to cell. This mutual interaction effect between unit cells is, of course, not included in the simplified model embodied by eq. (5.3). In order to make the model and the real reflectarray have a more similar behavior, one strategy could be to force the real reflectarray to have more similar cells, or equivalently, to have less abrupt variations or discontinuities in the phase settings distribution. Section 5.3.3 proposes an approach to minimize large phase variations between adjacent cells.

5.3.3 Modification to the algorithm by forcing continuous phase distribution

This section proposes a solution to modify the proposed beam synthesis algorithm in the previous section. The modified algorithm should meet two requirements: 1. minimize differences between the normalized synthesized and desired patterns, and 2. maximize smoothness of the phase distribution on the reflectarray. The penalty function (eq. (5.10)) used in the previous section only considered the first requirement. When calculating a metric for phase smoothness, one has to be careful with the inevitable phase transitions of 2π occurring in the calculations. To avoid this difficulty, it was chosen to force smoothness of $\exp(j\varphi)$, where φ is the phase correction introduced by the unit cell. The exponential form has no discontinuity at 2π phase jumps. The phase correction can be with respect to an initial phase distribution, for example, a distribution that gives a well-focused beam.

A smooth phase is desired, not a uniform phase, because phase gradients are necessary to achieve beam steering. So, we do not want to penalize phase gradient, but rather fast variations of the phase gradient, for instance, a point in the phase distribution (let's call this point a phase pole) that is very different from the phase at the surrounding points. Continuous phase gradient with no poles means

that the gradient has no divergence. So, the aim is to minimize the divergence of the phase gradient, i.e. the Laplacian of the phase distribution, i.e.:

$$\nabla \bullet \nabla \varphi = \nabla^2 \varphi = 0 \tag{5.12}$$

Or rather, to avoid non-physical 2π phase jumps:

$$\nabla^2 \exp(j\varphi) = 0 \tag{5.13}$$

The easy way to calculate the Laplacian numerically is by using finite differences. This can be written as eq. (5.14) at point (x_i, y_j):

$$\nabla^2 \exp(j\varphi_{i,j}) \approx \exp(j\varphi_{i,j}) - \frac{1}{4}(\exp(j\varphi_{i-1,j}) + \exp(j\varphi_{i+1,j}) + \exp(j\varphi_{i,j-1}) + \exp(j\varphi_{i,j-1})) \tag{5.14}$$

Of course, point (x_i, y_j) should have four neighbours in the grid, so the points on the corners and edges of the grid are excluded from the MSE calculation.

A phase-smoothing term is added to the cost function to minimize the divergence of the phase gradient. This is the last term in eq. (5.15)

$$MSE = \sum_{u,v} \left\| F_{d,normalized}(u,v) \right| - \left| F_{normalized}(u,v) \right\|^2 + \alpha \sum_{i,j} \left| \nabla^2 \exp(j\varphi_{i,j}) \right| \tag{5.15}$$

Absolute value is applied on the Laplacian because we are interested to minimize its magnitude at each point of the reflectarray grid, and not its complex value. Constant α is a regularization parameter to be adjusted. Several numerical experiments with several cases are needed to adjust the α value, starting with low value and increasing progressively. α should not be too large because it may "over-smooth" the phase and decrease the relative weight of the first term in the MSE forcing pattern fitness.

The validation case where the reference pattern is defined as the desired pattern is repeated with this new MSE function. The value of α is first selected in the same range as the MSE value obtained in Figure 5.6 after 5000 iterations. Figure 5.8 shows the convergence of the new MSE

function after 5000 iterations. Figure 5.9a shows the phase distribution of the optimized pattern with the updated MSE using PSO. An α value of 5×10^{-5} , a population number of 2000 and an iteration number of 5000 are selected for this example. The results indicate that the algorithm converged to the expected nearly-constant phase distribution. Figure 5.9a shows the distribution of $\cos\varphi_n$. The yellow color illustrates phases of zero. The normalized far-field pattern in Figure 5.9b calculated by PSO with phase distribution in Figure 5.9a using eq. (5.11) is close to the desired pattern. Figures 5.9c and 5.9d show the obtained radiation pattern and current distribution on the dish calculated by FEKO with the hybrid method (MoM + PO) by applying the phase distribution shown in Figure 5.9a. Figure 5.9d shows symmetric current distribution on the dish with the edge illumination of -20dB. This figure is used as the reference to compare with current distribution on the dish for synthesized beams.

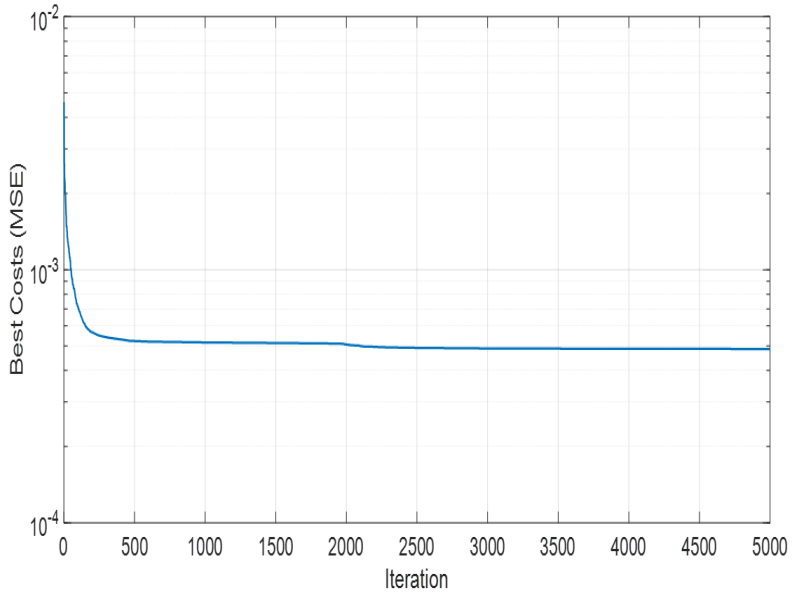

Figure 5.8 MSE of the optimized pattern with the reference pattern as the desired pattern after adding a phase-smoothing term to the cost function

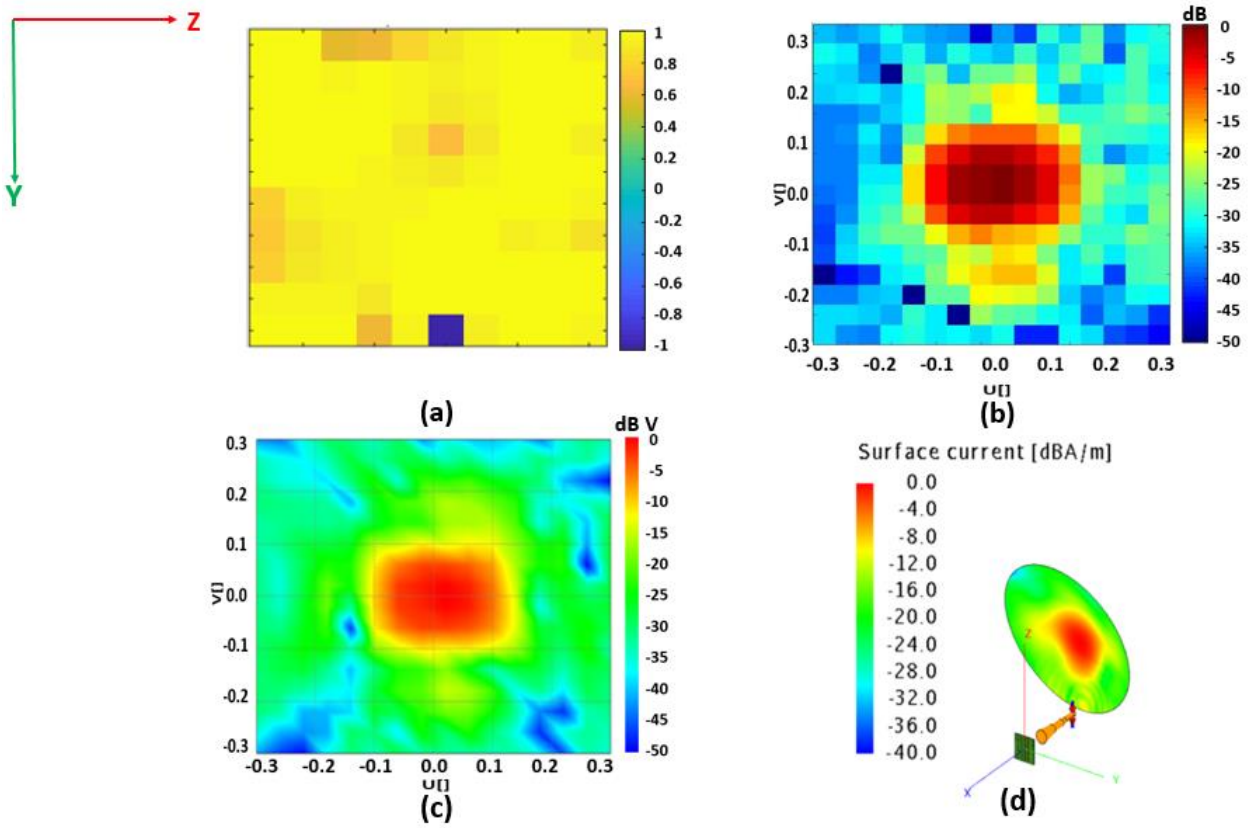

Figure 5.9 (a) Distribution of $\cos\varphi_n$ on the reflectarray elements of the optimized pattern with the reference pattern as the desired pattern, when adding a phase-smoothing term in the cost function, (b) Normalized amplitude of the optimized pattern calculated by PSO, (c) Radiation pattern obtained by simulation of the antenna in FEKO using the phase distribution $\{\varphi_n\}$ in Figure 5.9a, (d) Normalized current distribution on the dish obtained by simulation of the antenna in FEKO using the phase distribution $\{\varphi_n\}$ in Figure 5.9a

It is shown that the phase smoothing condition leads to significant improvement in the quality of the synthesized beams.

5.3.4 Application to the synthesis of shaped and steered beams

This section studies the improved algorithm's beam synthesis performance in terms of beam shaping and beam scanning. Three desired patterns are shown in Figure 5.10 , which are obtained

by hybrid (MoM/MLFMM + PO) simulation of the antenna in Figure 5.2 with FEKO by applying NFF technique. The desired beams include beam steerings of +0.05, -0.1 along the *v* axis, and +0.07 at 45 degrees diagonally in *uv* plane.

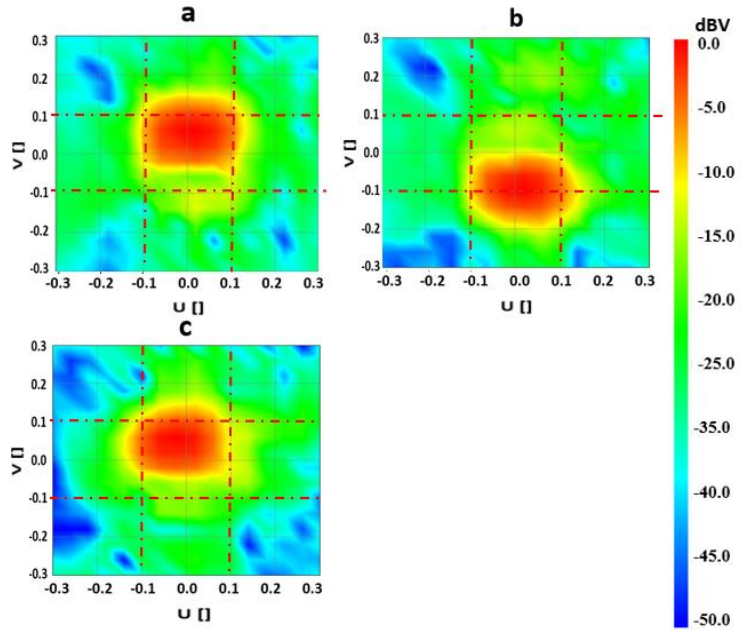

Figure 5.10 Normalized amplitude of radiation patterns obtained by hybrid simulation in FEKO by applying NFF technique: (a) Δu=0, Δv=0.05, (b) Δu=0, Δv=-0.1, (c) Δu=-0.05, Δv=0.05

The beam scanning capability of the algorithm will be investigated first. In all the examples shown, population number of 2000, iteration number of 5000, and α value of 5×10^{-5} are used to synthesize the scanned beams. The selected values for population and iteration numbers have been confirmed after many numerical experiments, giving acceptable results. The results could also be improved with larger iteration and population numbers, but these choices are a compromise between longer simulation times and the quality of the synthesis. Beam steerings of +0.05, -0.1 along the *v* axis, and +0.07 at 45 degrees diagonally in *uv* plane are provided. The normalized far-field patterns calculated by PSO in *uv* plane for these scans are shown in Figure 5.11. The patterns calculated by PSO-optimized phases by using eq. (5.11) with the phase distributions obtained in

the last iteration of PSO in Figure 5.12 are close to the desired patterns. Converged MSE values of 0.00169, 0.0014 and 0.00138 are obtained after 5000 iterations for Figures 5.11a, 5.11b, and 5.11c, respectively.

The phase distributions of the optimized patterns on the reflectarray are shown in Figure 5.12. Progressive phase shift distribution is obtained in the *v* direction in Figures 5.12a and 5.12b. Moreover, a diagonal progressive phase shift can be observed for diagonal scanning, as shown in Figure 5.12c.

The radiation patterns obtained from the PSO optimization are supported by comparing the results with the radiation pattern obtained by simulation in FEKO as provided by using the phases obtained from PSO, see Figure 5.12. Good agreement between the results in Figures 5.11, 5.13, and the desired pattern in Figure 5.10 is observed. In fact, the *uv* shifts, shapes, and sizes of the main beams are comparable in the two sets of figures. The current distributions on the dish related to the radiation patterns in Figure 5.13 are displayed in Figure 5.14. Current distribution on the dish for each case is shifted with respect to the reference case in Figure 5.9

In the interpretation of these figures it is important to realize that the *u* and *v* axes are respectively vertical and horizontal, aligned with *z* and *y*, in the physical representation of Figure 5.14. Consequently, shifts along the *v* direction that appear vertical in Figures 5.11 and 5.13 correspond to horizontal shifts of the current distribution in Figure 5.14.

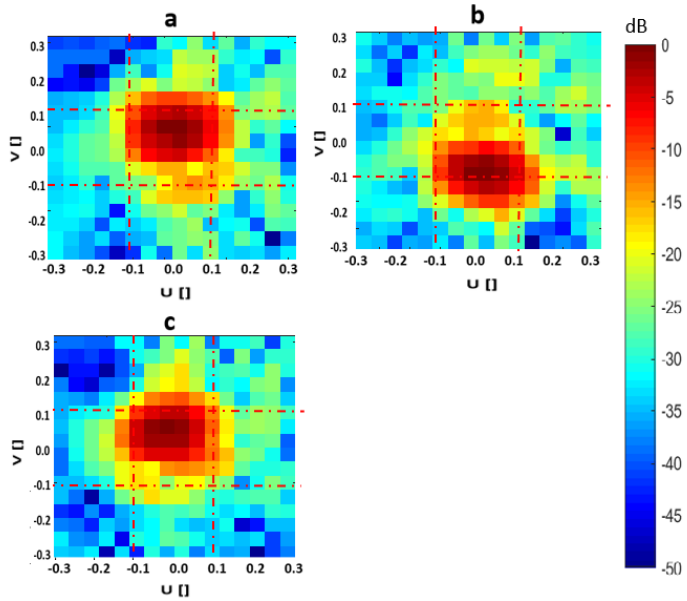

Figure 5.11 Normalized amplitude of the optimized patterns by PSO in MATLAB: (a) Δu=0, Δv=0.05, (b) Δu=0, Δv=-0.1, (c) Δu=-0.05, Δv=0.05

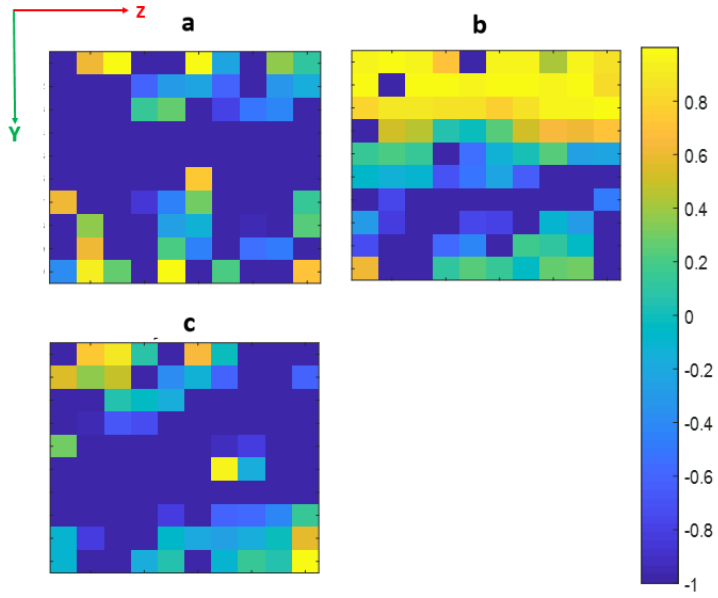

Figure 5.12 Distribution of $\cos\varphi_n$ on the reflectarray for the optimized patterns: (a) Δu=0, Δv=0.05, (b) Δu=0, Δv=-0.1, (c) Δu=-0.05, Δv=0.05

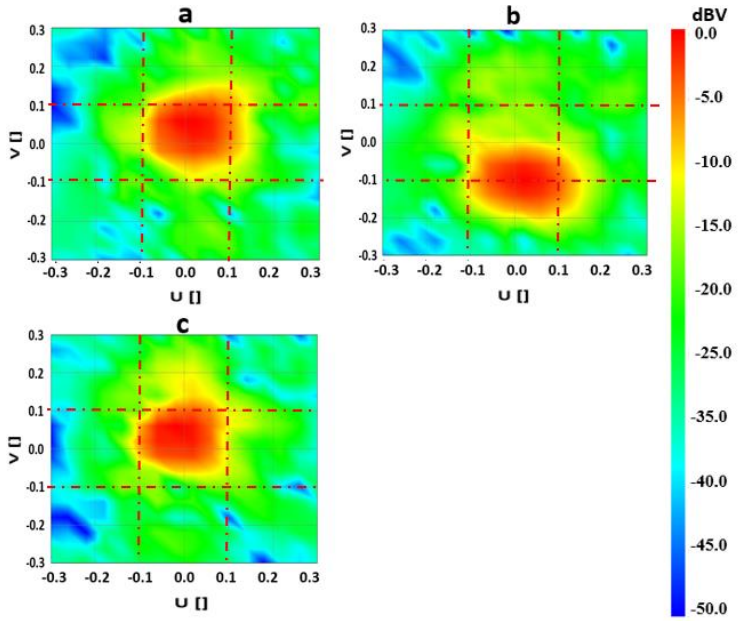

Figure 5.13 Normalized amplitude of radiation patterns obtained by hybrid simulation in FEKO: (a) Δu=0, Δv=0.05, (b) Δu=0, Δv=-0.1, (c) Δu=-0.05, Δv=0.05

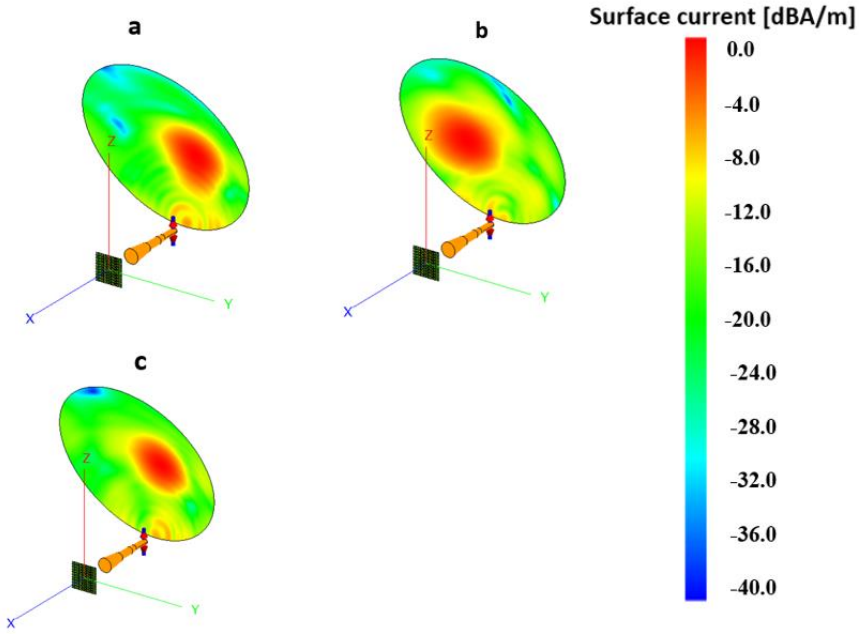

Figure 5.14 Normalized current distribution on the dish for the optimized patterns: (a) Δu=0, Δv=0.05, (b) Δu=0, Δv=-0.1, (c) Δu=-0.05, Δv=0.05

The capability of the algorithm to synthesize scanned beams has been demonstrated. As a second step, the beam shaping property of the algorithm will now be investigated. For this purpose, five patterns are defined as the desired beam, including a square-shaped pattern and four different Gaussian patterns.

Table 5.1 shows the parameters used in the PSO-based algorithm for synthesizing these desired patterns.

In the following examples, four Gaussian patterns are defined as desired patterns following eq. (5.16).

$$F(u,v) = \mathrm{e}^{-\left(\frac{(u-u_0)^2}{2\sigma_u{}^2}+\frac{(v-v_0)^2}{2\sigma_v{}^2}\right)} \tag{5.16}$$

Table 5.1 PSO algorithm's parameters for synthesizing five desired beams

	Desired Pattern	Population Number	Iteration Number	α	MSE
1	Squared Shape	2000	5000	5e-5	0.00109
2	$\sigma_v = 3.5 \quad \sigma_u = 2.5$	3000	6000	5e-5	0.001248
3	$\sigma_v = 3 \quad \sigma_u = 2.5$	3000	6000	5e-5	0.001212
4	$\sigma_v = 2.5 \quad \sigma_u = 2.5$	2000	3000	5e-5	0.00108
5	$\sigma_v = 1.5 \quad \sigma_u = 2.5$	2000	3000	5e-5	0.0026

The selected values for population and iteration numbers in

Table 5.1 have been confirmed after many numerical experiments for each example, giving acceptable MSE and therefore synthesized beams.

In the first example, the square-shaped pattern in Figure 5.15a is defined as the desired beam. Figures 5.15b and 5.15c show the pattern and phase distribution on the reflectarray obtained from PSO. Figures 5.15d and 5.15e show the radiation pattern in uv plane and the current distribution

on the dish obtained by hybrid simulation in FEKO, after applying phase distribution in Figure 5.15c. The radiation pattern calculated by PSO in Figure 5.15b is in good agreement with the radiation pattern obtained by simulation in FEKO in Figure 5.15d. Both figures exhibit a square shape pattern, similar to the desired pattern.

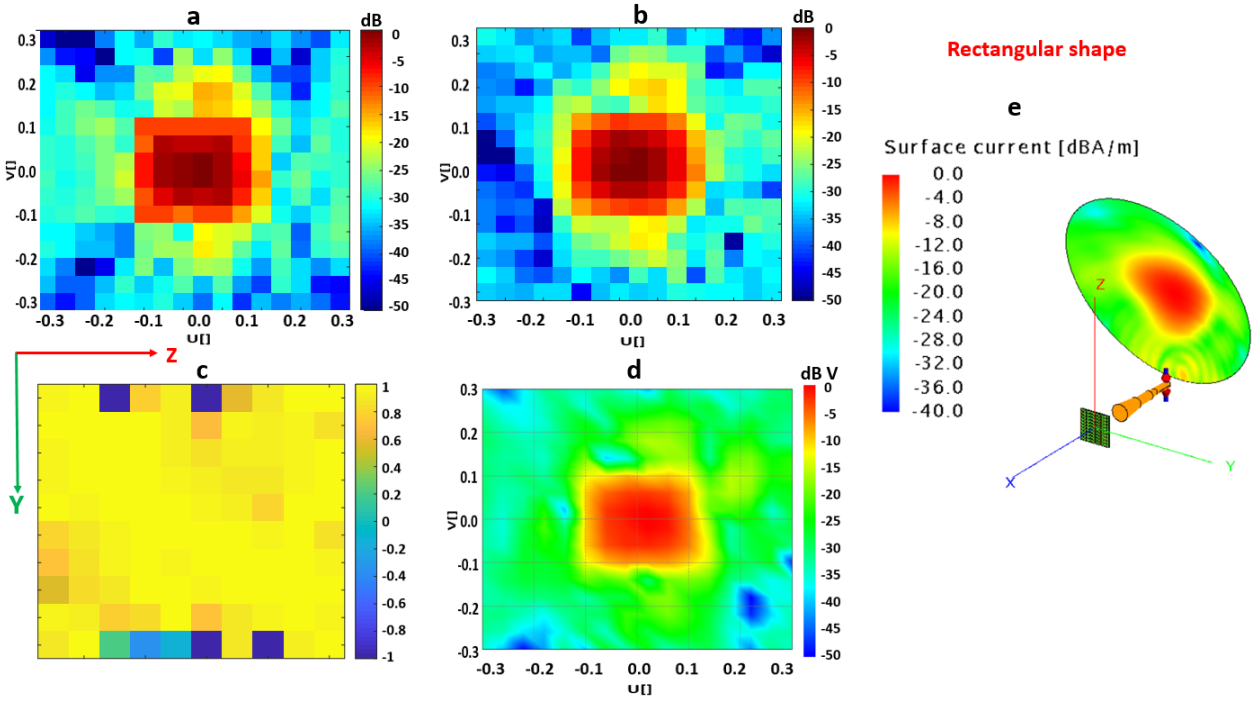

Figure 5.15 (a) Desired square-shaped pattern (b) Normalized amplitude of the optimized pattern by PSO, (c) Distribution of $\cos\varphi_n$ on the reflectarray for the optimized pattern, (d) Normalized amplitude of radiation pattern obtained by simulation of the antenna in FEKO using the phase distribution $\{\varphi_n\}$ in Figure 5.15c, (e) Current distribution on the dish obtained by simulation of the antenna in FEKO, using the phase distribution $\{\varphi_n\}$ in Figure 5.15c

As the second example, the centered (i.e. with u_0 =0 and v_0 =0) Gaussian pattern with σ_v =3.5 and σ_u =2.5 shown in Figure 5.16a is defined as the desired beam. Figures 5.16b and 5.16c show the pattern and phase distribution on the reflectarray obtained from PSO. Figures 5.16d and 5.16e show the radiation pattern in uv plane and the current distribution on the dish obtained by hybrid

simulation in FEKO, after applying proper phase distribution in Figure 5.16c. The radiation pattern obtained from the PSO optimization in Figure 5.16b and the radiation pattern obtained by simulation in FEKO in 5.16d obtained by using the phases obtained from PSO in Figure 5.16c are in good agreement. Both patterns have a wider beam in the *u*=0 cut rather than the *v*=0 cut, similar to the desired pattern.

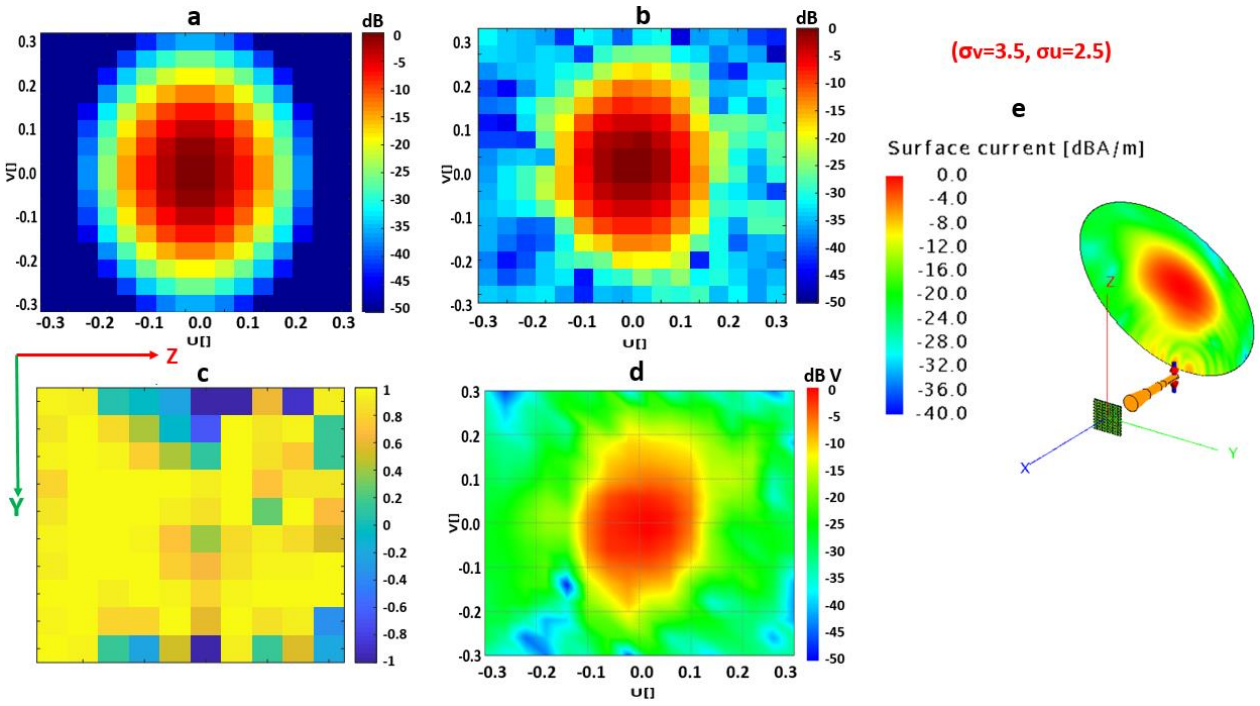

Figure 5.16 (a) Centered Gaussian beam with σ_v =3.5 and σ_u =2.5, (b) Normalized amplitude of the optimized pattern by PSO in MATLAB, (c) Distribution of $\cos\varphi_n$ on the reflectarray for the optimized pattern, (d) Normalized amplitude of radiation pattern obtained by simulation of the antenna in FEKO using the phase distribution $\{\varphi_n\}$ in Figure 5.16c, (e) Current distribution on the dish obtained by simulation of the antenna in FEKO, using the phase distribution $\{\varphi_n\}$ in Figure 5.16c

As the third example, the centered Gaussian pattern with σ_v =3 and σ_u =2.5 shown in Figure 5.17a is defined as the desired pattern, i.e. a beam that is slightly narrower along the *v* axis

compared to Figure 5.16a. Figures 5.17b and 5.17c show the pattern and phase distribution on the reflectarray obtained from PSO. Figures 5.17d and 5.17e show the radiation pattern in uv plane and the current distribution on the dish obtained by hybrid simulation in FEKO, after applying proper phase distribution in Figure 5.17c. The radiation pattern obtained from the PSO optimization in Figure 5.17b and the radiation pattern obtained by simulation in FEKO in Figure 5.17d obtained by using the phases obtained from PSO in Figure 5.17c are in good agreement. Both figures have a wider beam in the u=0 cut rather than the v=0 cut, like the desired pattern. The beamwidth in u=0 cut is narrower in Figure 5.17d compared to Figure 5.16d having a larger σ_v. Both figures have the same beamwidth in v=0, i.e. with the same σ_u.

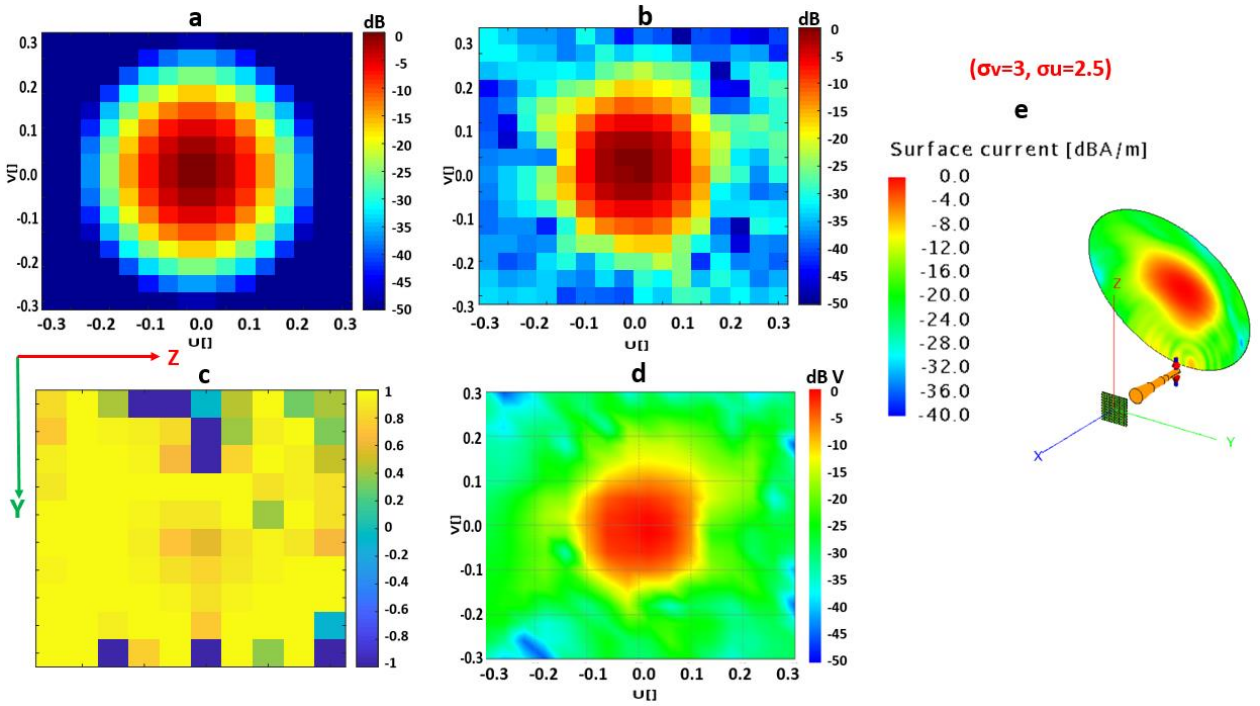

Figure 5.17 (a) Centered Gaussian pattern with σ_v =3 and σ_u =2.5, (b) Normalized amplitude of the optimized pattern by PSO, (c) Distribution of $\cos\varphi_n$ on the reflectarray for the optimized pattern, (d) Normalized amplitude of radiation pattern obtained by simulation of the antenna in FEKO, using the phase distribution $\{\varphi_n\}$ in Figure 5.17c, (e) Current distribution on the dish obtained by simulation of the antenna in FEKO, using the phase distribution $\{\varphi_n\}$ in Figure 5.17c

As the fourth example, the centered Gaussian pattern with σ_v =2.5 and σ_u =2.5 shown in Figure 5.18a is defined as the desired pattern. Figures 5.18b and 5.18c show the pattern and phase distribution on the reflectarray obtained from PSO. Figures 5.18d and 5.18e show the radiation pattern in uv plane and the current distribution on the dish obtained by hybrid simulation in FEKO, after applying proper phase distribution in Figure 5.18c. The radiation pattern obtained from the PSO optimization in Figure 5.18b and the radiation pattern obtained by simulation in FEKO in Figure 5.18d obtained by using the phases obtained from PSO in Figure 5.18c are in good agreement. Both figures exhibit the same beamwidth in u=0 and v=0 cuts, similar to the desired pattern. The beamwidth in u=0 cut is narrower in Figure 5.18d compared to Figures 5.17d and 5.16d with larger σ_v s. Figures 5.18, 5.17, and 5.16 have the same beamwidth in v=0 with the same σ_u .

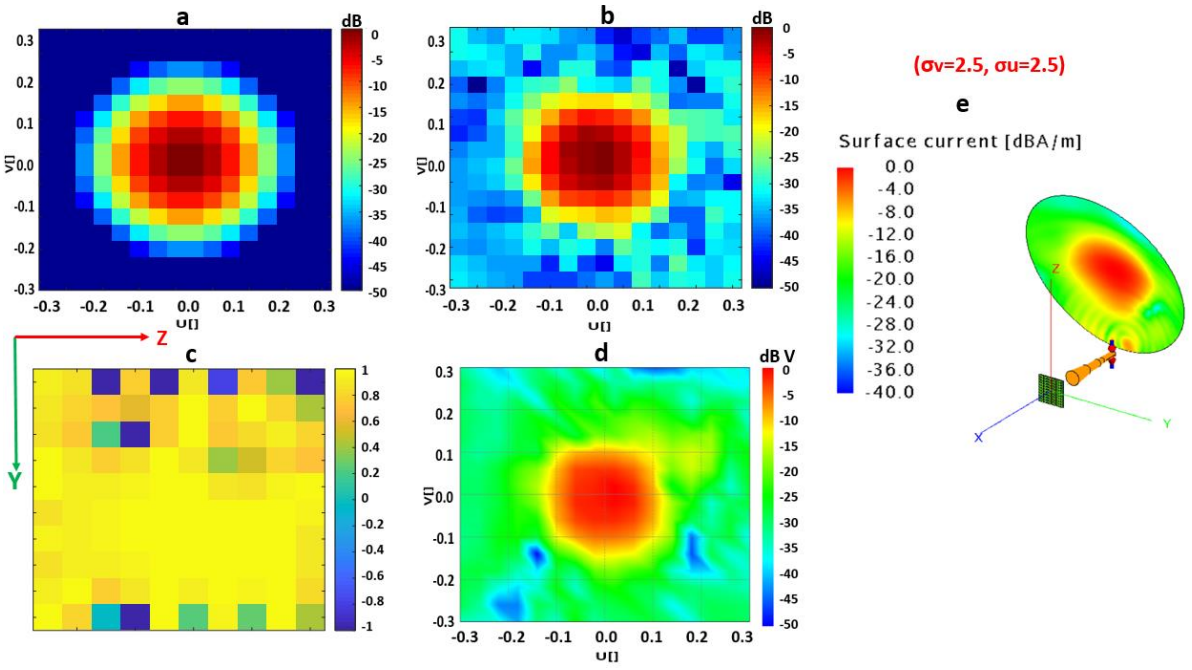

Figure 5.18 (a) Centered Gaussian pattern with σ_v =2.5 and σ_u =2.5, (b) Normalized amplitude of the optimized pattern by PSO, (c) Distribution of $\cos\varphi_n$ on the reflectarray for the optimized pattern, (d) Normalized amplitude of radiation pattern obtained by simulation of the antenna in

FEKO using the phase distribution $\{\varphi_n\}$ in Figure 5.18c, (e) Current distribution on the dish obtained by simulation of the antenna in FEKO, using the phase distribution $\{\varphi_n\}$ in Figure 5.18c

As the last example, the centered Gaussian pattern with σ_v =1.5 and σ_u =2.5 shown in Figure 5.19a is defined as the desired pattern. Figures 5.19b and 5.19c show the pattern and phase distribution on the reflectarray obtained from PSO. Figures 5.19d and 5.19e show the radiation pattern in uv plane and the current distribution on the dish obtained by hybrid simulation in FEKO, after applying proper phase distribution in Figure 5.19c. The radiation pattern obtained from the PSO optimization in Figure 5.19b and the radiation pattern obtained by simulation in FEKO in Figure 5.19d obtained by using the phases obtained from PSO in Figure 5.19c are in good agreement. Both figures have a narrower beam in the u=0 cut rather than the v=0 cut, similar to the desired pattern. The beamwidth in u=0 cut is narrower in Figure 5.19 compared to Figures 5.18, 5.17, and 5.16 with larger σ_v s. All the Figures have the same beamwidth in v=0 with the same σ_u s.

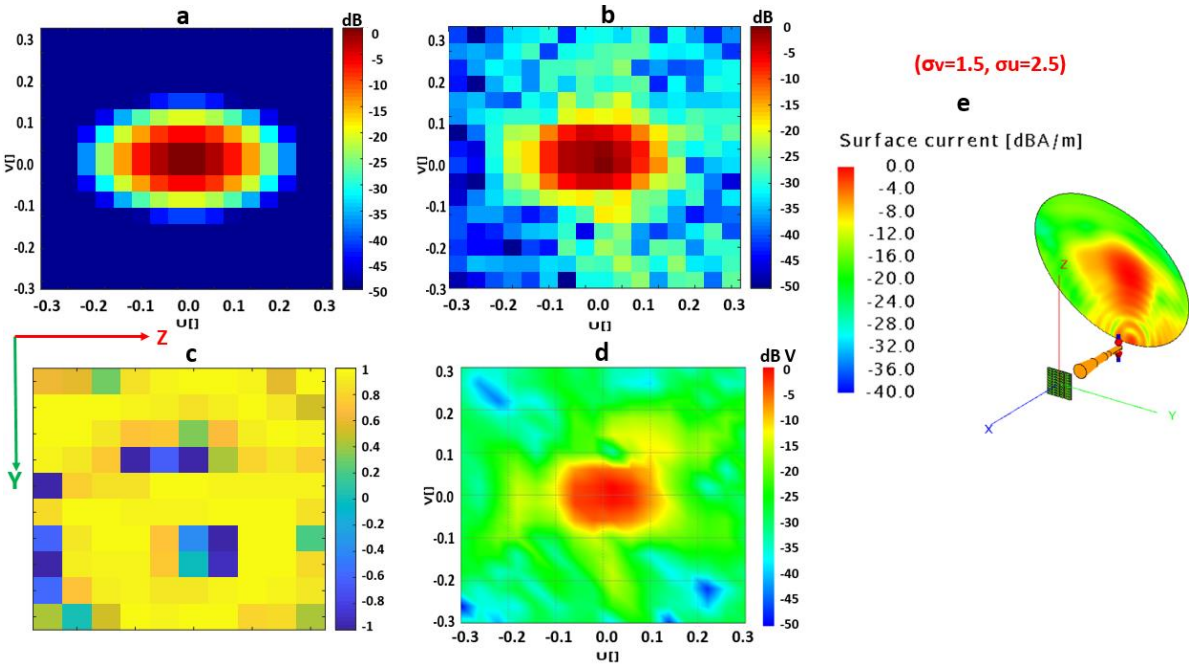

Figure 5.19 (a) Centered Gaussian pattern with σ_V =1.5 and σ_U =2.5, (b) Normalized amplitude of the optimized pattern by PSO, (c) Distribution of $\cos\varphi_n$ on the reflectarray for the optimized pattern, (d) Normalized amplitude of Radiation pattern obtained by simulation of the antenna in FEKO using the phase distribution $\{\varphi_n\}$ in Figure 5.19c, (e) Current distribution on the dish obtained by simulation of the antenna in FEKO, using the phase distribution $\{\varphi_n\}$ in Figure 5.19c

5.4 Conclusion

The results shown in this chapter demonstrate that beam shaping and beam scanning can be realized by a dual-reflector antenna obtained with phase-only synthesis optimized with PSO, using the proposed reconfigurable reflectarray as a subreflector. By using a penalty function only forcing the fitting of the desired and obtained patterns, the algorithm leads to a quasi-random phase distribution on the reflectarray for the optimized pattern and does not result in the desired radiation pattern. The modified MSE function adds a term to minimize the Laplacian of the phase distribution. This modification provides more stable results and leads to desired shaped beams and scanned beams in the desired direction with regular contours.

CHAPTER 6 EXPERIMENTAL VALIDATION OF THE BEAM SYNTHESIS CAPABILITY OF DUAL-REFLECTOR ANTENNA

6.1 Introduction

The previous chapter successfully implemented a PSO-based beam synthesis algorithm for a dual-reflector antenna. This chapter experimentally supports the beam synthesis capability of a dual-reflector antenna based on the algorithm proposed in Chapter 5, considering the limitations in the experimental setup. First, Section 6.2 describes the experimental setup of the dual-reflector antenna. Then, Section 6.3 provides examples to experimentally evaluate the performance of the beam synthesis algorithm for the proposed setup. Finally, Section 6.4 concludes the chapter.

6.2 Description of the experimental setup

This chapter aims at experimentally demonstrating the capability of the PSO-based beam synthesis method proposed in the previous chapter for the dual-reflector antenna in which the subreflector is a reconfigurable reflectarray. For this purpose, the structure in Figure 6.1, which is similar to Figure 4.25 with the uv plane displayed on the figure's left side, is used. In this structure, the major and minor axes of the projected aperture of the elliptical-shaped dish in yz plane are 65 cm (15.18λ) and 43.3 cm (10.11λ), respectively, with the focal distance of 49.2 cm (11.14λ) at the design frequency of 7 GHz. This corresponds to F/D ratios of 0.75 and 1.13 along major and minor dimensions of the aperture, respectively. Configurations in Figures 5.2 and 6.1 have the same reflectarray size. However, the dish size of the measurement setup in Figure 6.1 is smaller than the dish size in Figure 5.2 due to the limited quiet zone size of the CATR of the Poly-Grames Research Center. The quiet zone is the region where the plane wave is created inside the anechoic chamber. In the CATR, the diameter of the quiet zone is 30 cm. Outside this zone, the phase and amplitude of the incoming plane wave are less uniform. This is quite smaller than the dish projected aperture (65 cm x 43.3 cm); therefore, the measured antenna gain will be decreased due to amplitude taper efficiency and phase non-uniformity of the incident wave generated by the CATR reflector. Consequently,

measured antenna beamwidths will be greater than simulated ones. It is also expected that the measured sidelobe levels will be stronger than simulated.

Another difficulty caused by the small dimensions of our CATR is the very limited space to position the reflectarray and feed horn. These elements should be low enough to have an offset in the system that will prevent blockage by the subreflector. This limits the maximum possible size of the subreflector, which in our case has dimensions of 157.5 mm x 157.5 mm. The efficiency of the phase synthesis improves when there are more degrees of freedom to control the phase. Therefore, better synthesis results will be obtained when the reflectarray is uniformly illuminated. However, this will contribute to more spillover loss in the system; therefore, decreasing the gain, and causing higher cross-polarization levels, as discussed in the following pages.

As we have seen in the previous chapter (see, for instance, Figure 5.18), the feed horn, reflectarray, and dish have no supporting structures in the simulated models. In practice, metallic brackets are used to assemble the system, and these elements can cause additional scattering. Absorbing material has been used behind the reflectarray to absorb scattered fields in this region. As we will see, this had a significant positive impact on the antenna cross-polarization performance.

The size of the elliptical reflector's aperture is smaller ($15.18\lambda \times 10.11\lambda$) compared to that used in the simulated case of Chapter 5 (24λ). This simulated dish also had a smaller F/D ratio, i.e. 0.5 versus 0.75 and 1.13. Assuming fixed feed horn and reflectarray sizes, a smaller reflector with a larger F/D will be more uniformly illuminated. We have seen in Chapter 5, particularly in Figures 5.13 and 5.18, that in order to synthesize certain desired beams, the current distribution in the dish has to be translated. This means that better synthesis can be realized if the system has more amplitude tapering. When the illumination is constrained to a smaller aperture, as in the experimental setup at hand, there is less freedom to translate the dish illumination. Consequently, the PSO algorithm will work with a reduced solution space. Therefore, we should not expect the experimental synthesis cases to be as good as in the simulated cases presented in Chapter 5.

Due to these limitations, we cannot expect a good quantitative agreement between measured and simulated results. Nevertheless, it should be possible to observe variations of steering angles and trends in the beamwidth variations created by the beam synthesis.

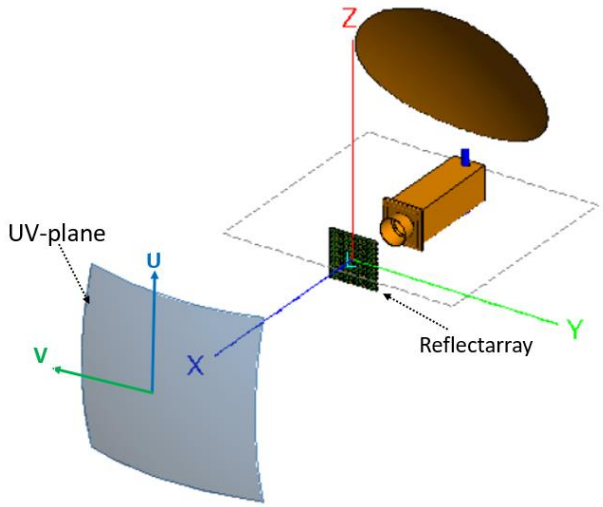

Figure 6.1 Dual-reflector antenna for measurement setup including horn, reconfigurable sub-reflectarray, and solid parabolic dish

Figure 6.2 shows the measurement setup of the structure in Figure 6.1. For all the tests, the antenna positioner rotates the antenna in the horizontal plane. The setup in Figure 6.2a measures the far-field cut along the *v* axis (*u*=0), whereas the setup in Figure 6.2b measures the far-field along the *u* axis (*v*=0). As mentioned in Chapter 4, for simplicity, the reflectarray elements are rotated manually by steps of 11.25 degrees.

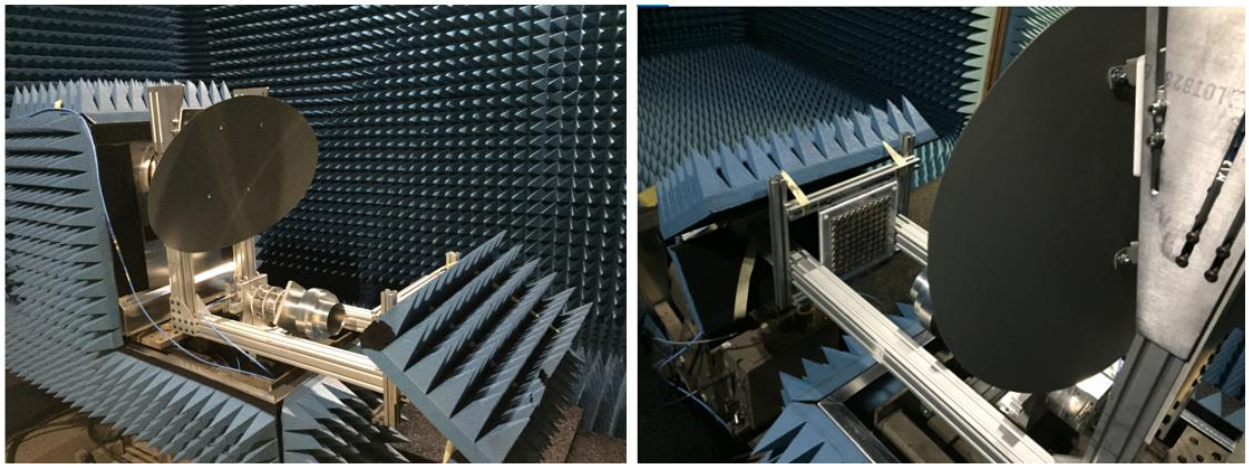

(a)

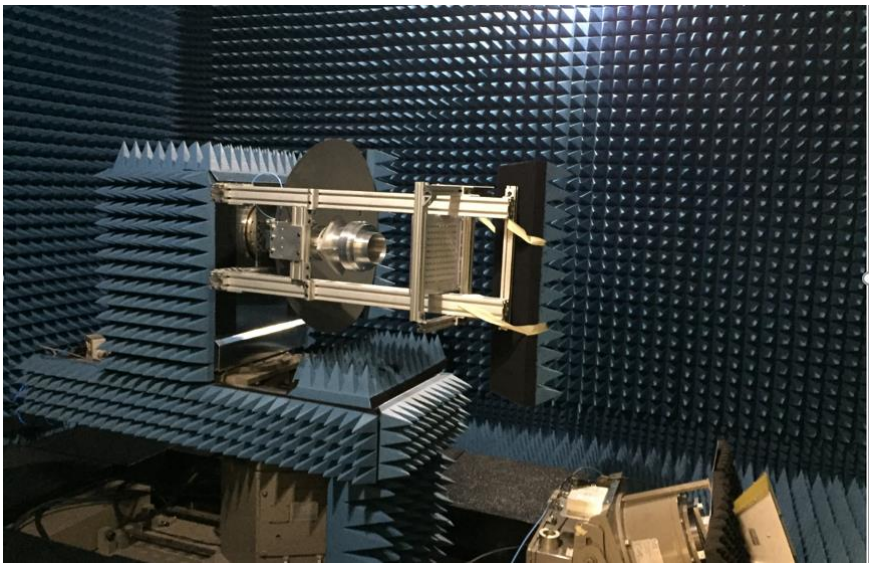

(b)

Figure 6.2 (a) Measurement setup for measuring the far-field pattern cut along *v* axis (*u*=0), (b) Measurement setup for measuring the far-field pattern cut along *u* axis (*v*=0)

6.3 Beam synthesis examples

In order to demonstrate the beam synthesis capability, four Gaussian patterns and one scanned beam along the *v* axis will be considered. Before applying the PSO-based synthesis, a new set of element factors of the 100-elements reflectarray (i.e. functions f_n of the previous chapter) needs to be generated for the dual-reflector structure with the smaller elliptical dish. As a reminder, these functions represent the embedded element pattern of each reflectarray element, taking into consideration the position of the unit cell in the array and scattering by neighboring cells. Once this step is completed, the PSO-based beam synthesis algorithm finds the appropriate phase distribution on the reflectarray. Then, these phases are applied to the reflectarray elements in the experimental antenna. Finally, the agreement between the simulation and measurement results and the change in the beamwidth of the optimized pattern with respect to the reference pattern are studied. All the phases are obtained with respect to the phases of a reference pattern used for the calculations of the element patterns. The reference pattern is related to the state where the elements are adjusted to focus the beam reflected by the reflectarray at the focal point of the dish. Figure 6.3 shows the

reference pattern of the system in the far-field of the antenna structure in Figure 6.1, as calculated by FEKO. All the φ_n's are assumed to be zero when the reflectarray is in that reference state.

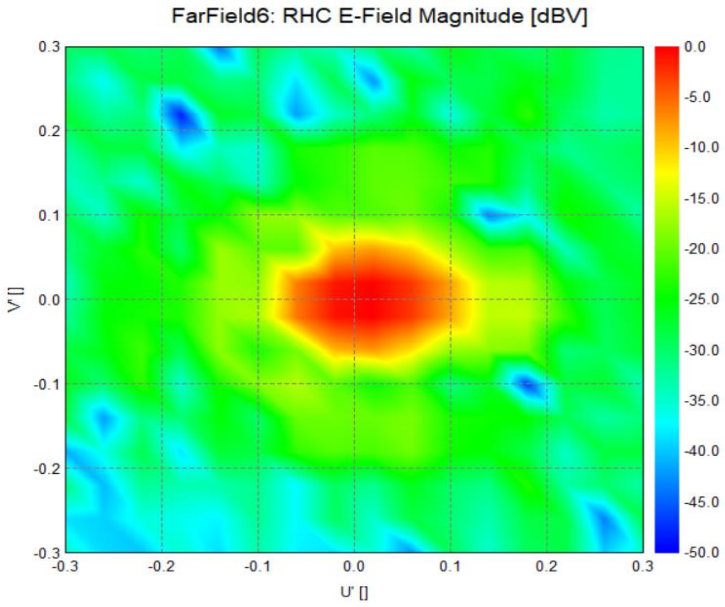

Figure 6.3 Reference radiation pattern related to the structure in Figure 6.1

Having observed the limitations of the experimental setup with the reference pattern, we will now move forward in the measurements, with five examples of beam steering and shaping.

Table 6.1 shows five examples for synthesizing the desired patterns, including one scanned beam and four Gaussian patterns with the function defined in eq. (5.16). In addition, the table shows the parameters related to the PSO-based algorithm for synthesizing desired patterns.

Table 6.1 PSO algorithm's parameters for synthesizing five desired beams

	Desired Pattern	Population Number	Iteration Number	α	MSE
1	$\sigma_v = 4 \quad \sigma_u = 3$	4000	1000	5e-4	0.02537
2	$\sigma_v = 3 \quad \sigma_u = 2$	5000	1000	5e-5	0.0032
3	$\sigma_v = 2 \quad \sigma_u = 3$	5000	1000	5e-5	0.0029
4	$\sigma_v = 2 \quad \sigma_u = 2$	3000	1000	5e-4	0.007
5	Beam steering by $\Delta v = +0.05$	5000	1000	1e-5	0.00074

In the first example, the centered Gaussian pattern with σ_v =4 and σ_u =3 illustrated in Figure 6.4a is defined as the desired beam. PSO algorithm with the population number of 4000 and α =5e-4 gives an MSE of 0.02537 after 1000 iterations. Figures 6.4b and 6.4c show the pattern and phase distribution on the reflectarray obtained from PSO. Figures 6.4d and 6.4e show the radiation pattern in uv plane and the current distribution on the dish obtained by hybrid simulation in FEKO, after applying the proper phase distribution in Figure 6.4c. Compared to the reference pattern in Figure 6.3, the synthesized pattern in Figure 6.4d is wider along the *v* axis.

The normalized patterns along *u* and *v* axes are shown in Figures 6.5a and 6.5b. Each figure displays three curves, including the measured reference beam, the simulated and measured synthesized beams. Results show good agreement between the synthesized pattern's measurement and simulation. The beamwidth increase of the synthesized pattern compared to the reference pattern is clearly visible in the u=0 cut.

Figure 6.6 shows the normalized reference and synthesized patterns along the *v* and *u* axes obtained from measurement. As shown in Figure 6.6, the XPDs of around 18 dB and 13.6 dB within the HPBW along the *v* and *u* axes are obtained respectively for the synthesized beam, while an XPD of about 25 dB is obtained for the reference beam along both axes. The RHCP term is considered as the co-polarization term, and LHCP is deemed to be the cross-polarization term.

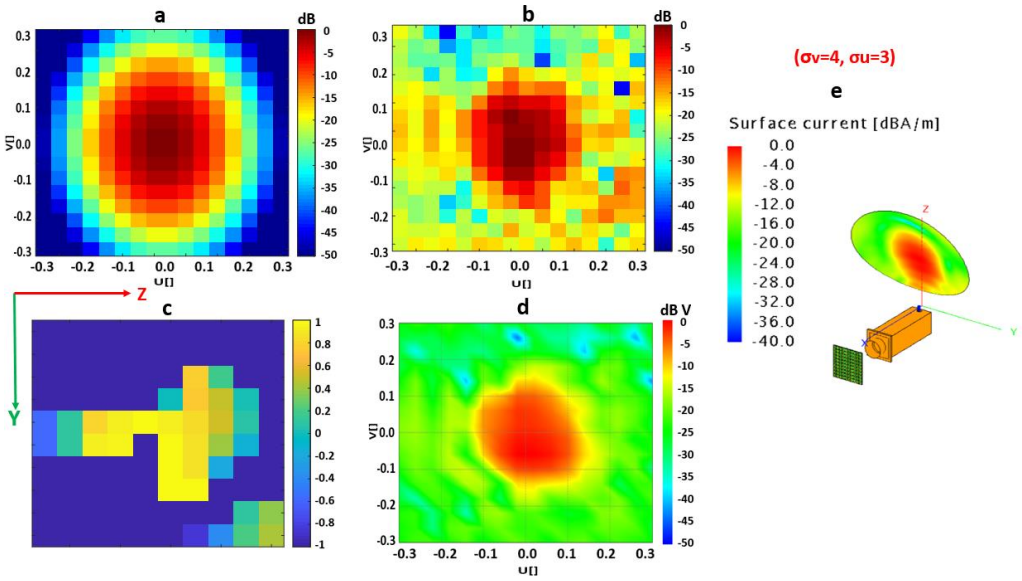

Figure 6.4 (a) Centered Gaussian pattern with σ_v =4 and σ_u =3 , (b) Normalized amplitude of the optimized pattern by PSO, (c) Distribution of $\cos\varphi_n$ on the reflectarray for the optimized pattern, (d) Normalized co-polarization amplitude of radiation pattern obtained by simulation of the antenna in FEKO using the phase distribution $\{\varphi_n\}$ in Figure 6.4c, (e) Current distribution on the dish obtained by simulation of the antenna in FEKO using the phase distribution $\{\varphi_n\}$ in Figure 6.4c

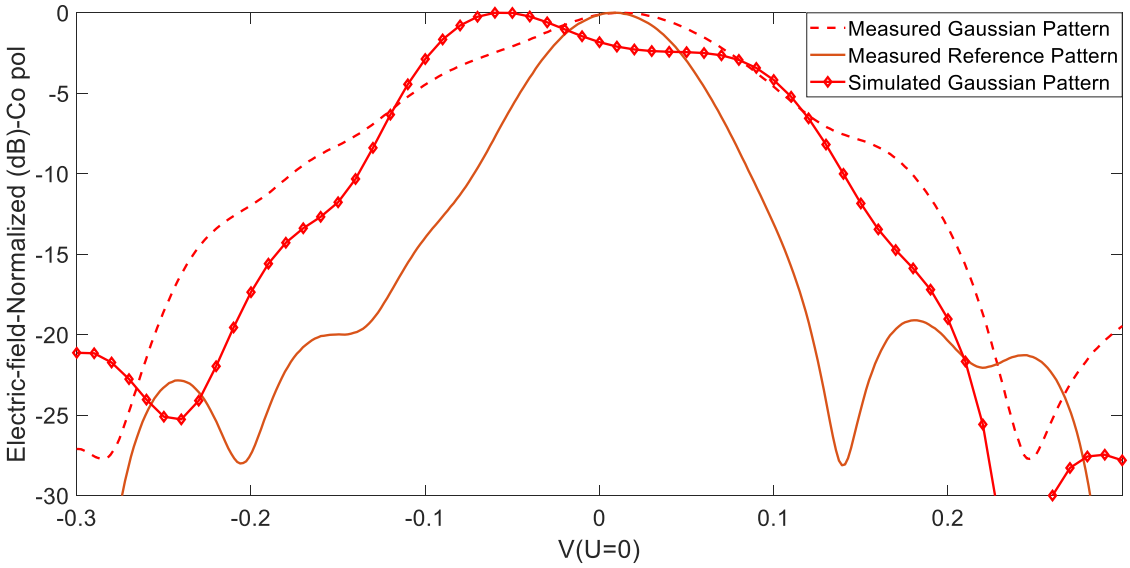

(a)

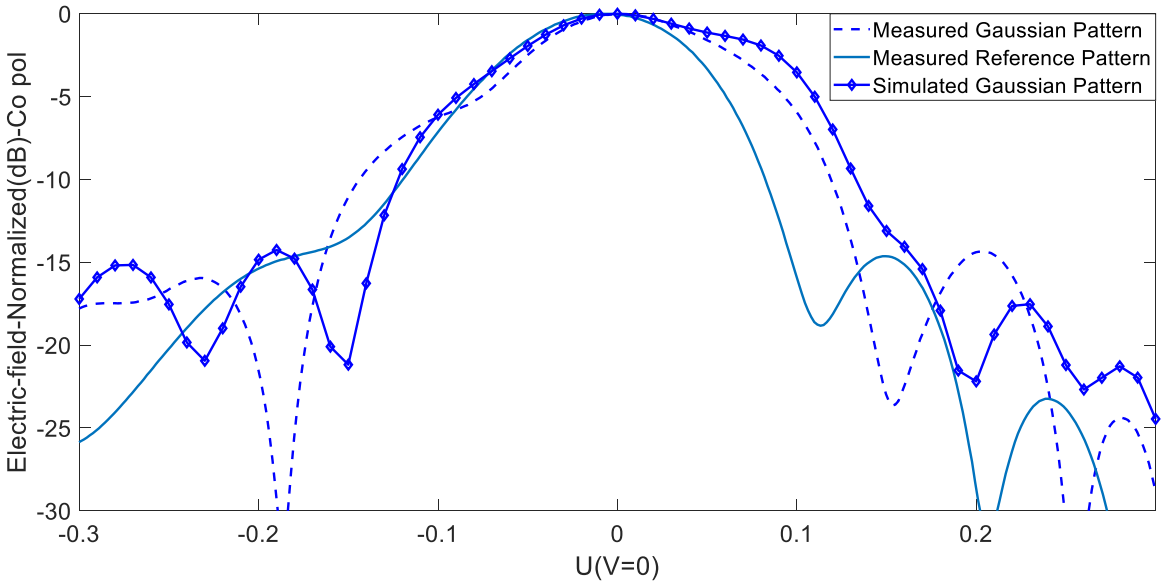

(b)

Figure 6.5 Cuts of Gaussian pattern with σ_v =4 and σ_u =3. (a) Normalized co-polarization electric field along the *v* axis (*u*=0) for the reference beam (measured) and the synthesized beam (measured and simulated) for a desired Gaussian pattern, (b) Same cases but along the *u* axis (*v*=0)

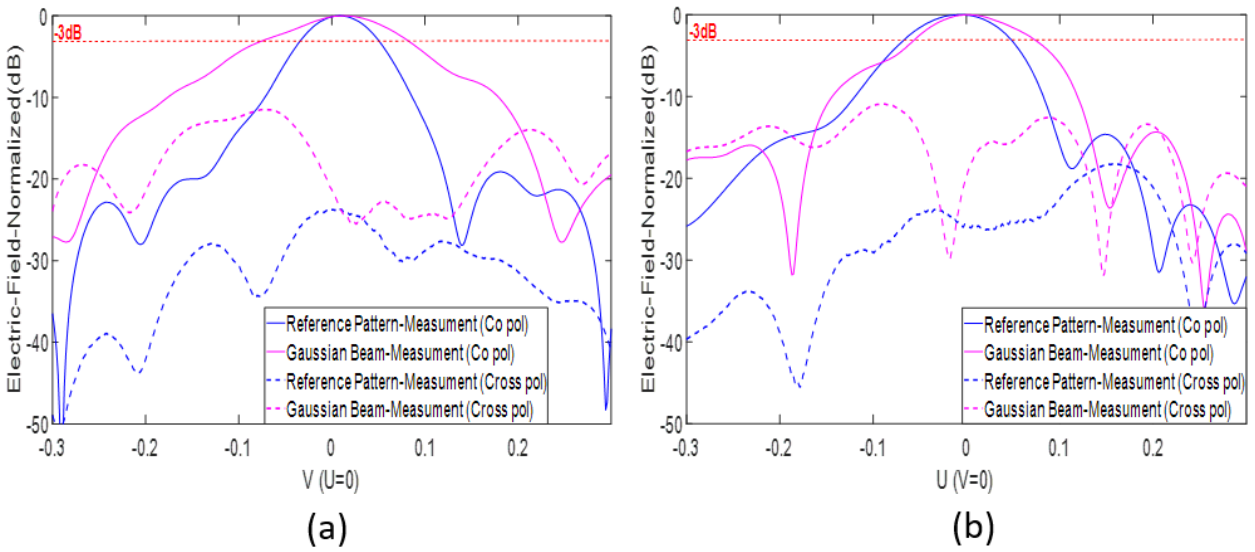

Figure 6.6 Normalized far-field of the reference beam (measured) and desired Gaussian beams with σ_v =4 and σ_u =3 cuts (measurement): (a) along the *v* axis (*u*=0), (b) along the *u* axis (*v*=0)

In the second example, the centered Gaussian pattern with σ_v =3 and σ_u =2 shown in Figure 6.7a is defined as the desired beam. PSO optimization with a population number of 5000 and α =5e-5 gives an MSE of 0.0032 after 1000 iterations. Figures 6.7b and 6.7c show the pattern and phase distribution on the reflectarray obtained from PSO. Figures 6.7d and 6.7e show the radiation pattern in uv plane and the current distribution on the dish obtained by hybrid simulation in FEKO, after applying the proper phase distribution in Figure 6.7c. Compared to the reference pattern in Figure 6.3, the synthesized pattern in Figure 6.7d is wider along the *v* axis while has a similar beamwidth as the reference pattern along the *u* axis.

The normalized patterns along the *u* and *v* axes are shown in Figures 6.8a and 6.8b. Each figure includes three curves; the measured reference beam, the simulated and measured synthesized beams. Results show good agreement between the synthesized pattern's measurement and simulation.

In the *u*=0 cut, simulated and measured synthesized beams have similar beamwidths that are larger than that of the reference case; the three beams are centered near *u*=0, but the simulated beam exhibits some asymmetry.

The beamwidths of the synthesized cases in Figure 6.5a are smaller than in Figure 6.8a in the *u=0* cut, but in that second case, the desired σ_v is smaller; this shows the limitation of the PSO synthesis for this problem. In the *v*=0 cut, compared to Figure 6.5b, the synthesized patterns in Figure 6.8b are narrower, which is in agreement with the smaller σ_u of Figure 6.8b specified in the optimization.

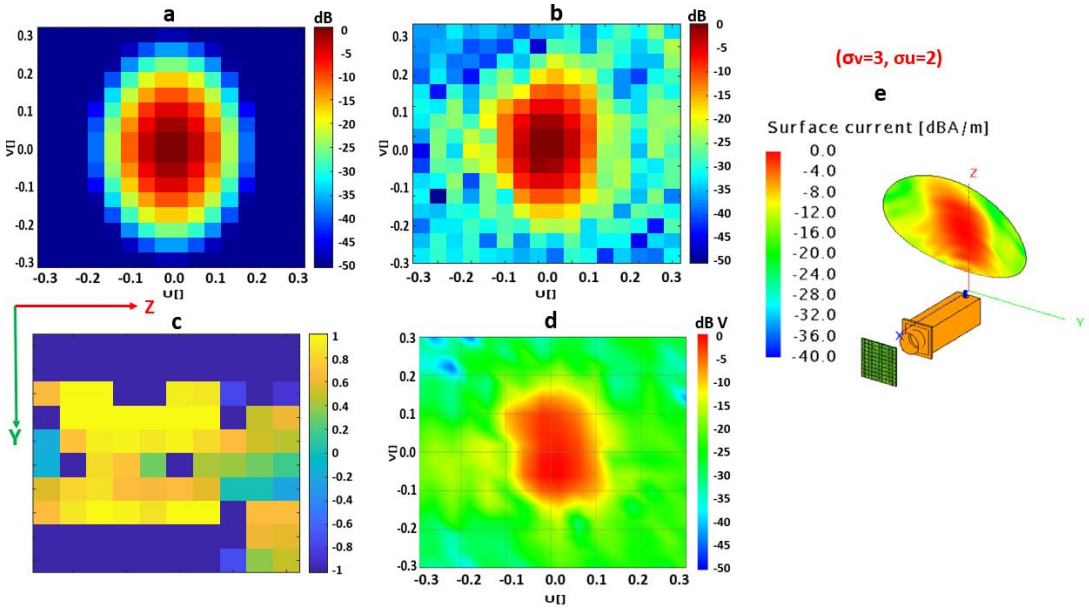

Figure 6.7 (a) Centered Gaussian pattern with σ_v =3 and σ_u =2, (b) Normalized amplitude of the optimized pattern by PSO, (c) Distribution of $\cos\varphi_n$ on the reflectarray for the optimized pattern, (d) Normalized co-polarization amplitude of radiation pattern obtained by simulation of the antenna in FEKO using the phase distribution $\{\varphi_n\}$ in Figure 6.7c, (e) Current distribution on the dish obtained by simulation of the antenna in FEKO, using the phase distribution $\{\varphi_n\}$ in Figure 6.7c

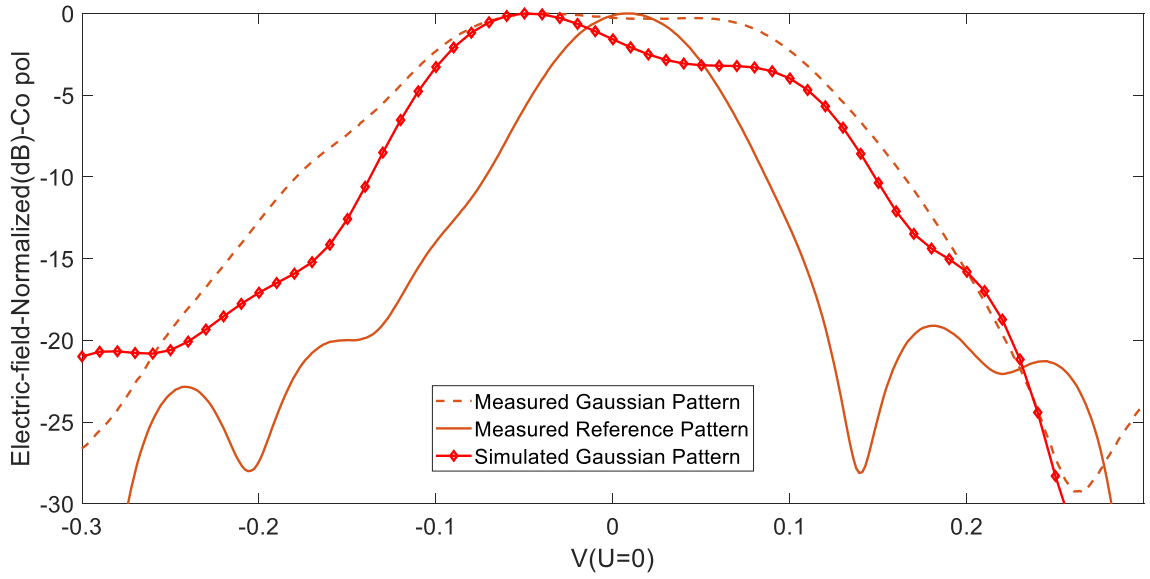

(a)

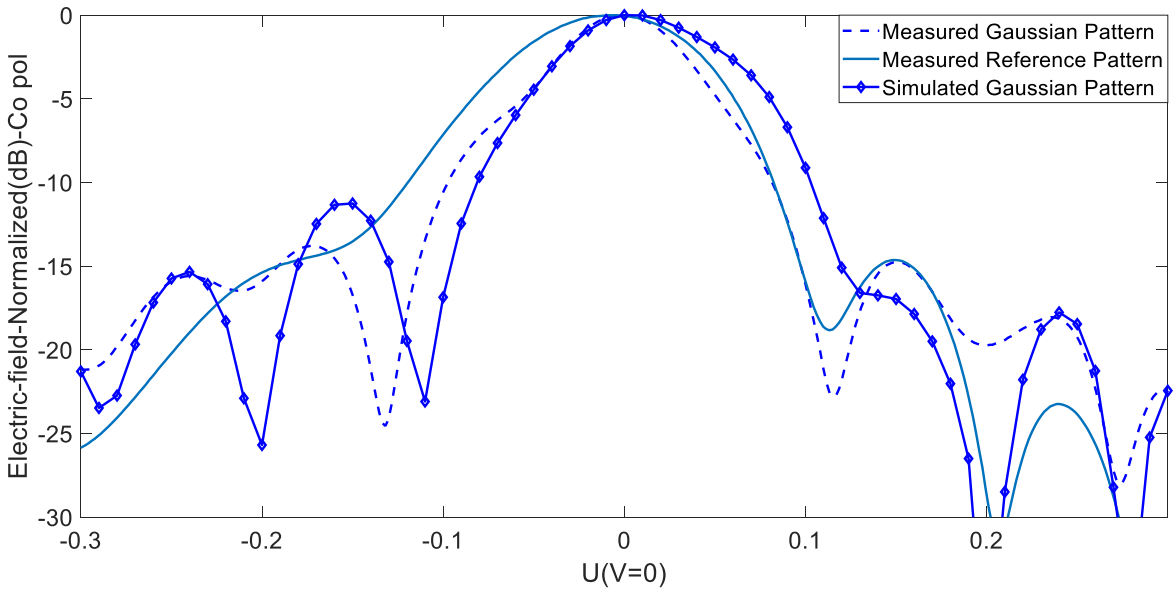

(b)

Figure 6.8 Cuts of Gaussian pattern with σ_v =3 and σ_u =2. (a) Normalized co-polarization electric field along the *v* axis (*u*=0) for the reference beam (measured) and the synthesized beam (measured and simulated) for a desired Gaussian pattern, (b) Same case but along the *u* axis (*v*=0)

Figure 6.9 shows the normalized reference and synthesized patterns along with the *v* and *u* axes obtained from measurement. As shown in Figure 6.9, the XPDs of around 15 dB and 19 dB within the HPBW along with the *v* and *u* axes are obtained, respectively, for the synthesized beam, while an XPD of about 25 dB is obtained for the reference beam along both axes. The RHCP term is considered as the co-polarization term, and LHCP is deemed to be the cross-polarization term.

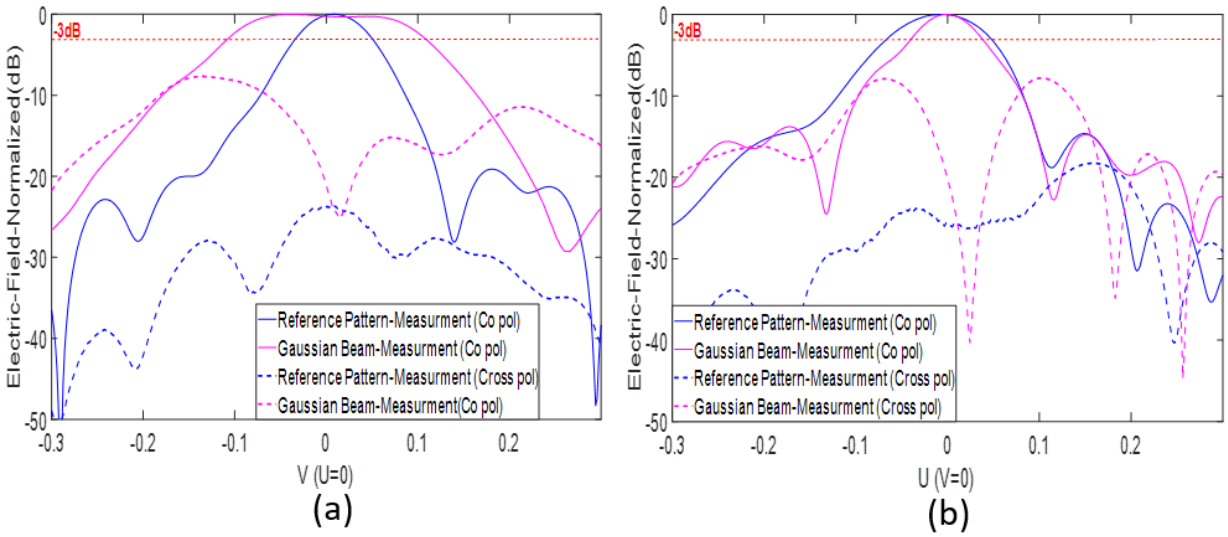

Figure 6.9 Normalized far-field of the reference beam (measured) and desired Gaussian beams with σ_v =3 and σ_u =2 cuts (measured): (a) along the *v* axis (*u*=0), (b) along the *u* axis (*v*=0)

In the third example, the centered Gaussian pattern with σ_u =2 and σ_v =3 shown in Figure 6.10a is defined as the desired beam. PSO algorithm with the population number of 5000 and α =5e-5 gives an MSE of 0.0029 after 1000 iterations. Figures 6.10b and 6.10c show the pattern and phase distribution on the reflectarray obtained from PSO. Figures 6.10d and 6.10e show the radiation pattern in *uv* plane and the current distribution on the dish obtained by hybrid simulation in FEKO, after applying the proper phase distribution in Figure 6.10c. The synthesized pattern in Figure 6.10d has wider beam than the reference pattern in Figure 6.3 along the *v* and *u* axes.

The normalized patterns along the *u* and *v* axes are shown in Figure 6.11. Each figure includes three curves; the measured reference beam, the simulated and measured synthesized beams. Results show good agreement between the synthesized pattern's measurement and simulation results.

In the *u*=0 cut, simulated and measured synthesized beams have similar beamwidths, that are larger than the reference case. In the *u*=0 cut, compared to Figure 6.5a and Figure 6.8a, the measured and simulated synthesized patters in Figure 6.11a are narrower, which is in agreement with the smaller σ_v of Figure 6.11a specified in the optimization.

In the *v*=0 cut, the beamwidths of the synthesized cases in Figure 6.11b are wider than Figure 6.8a, which is in agreement with larger σ_u of Figure 6.11b specified in the optimization. Also, the synthesized cases in Figure 6.11b have the same beamwidth as Figure 6.5b with the same σ_u.

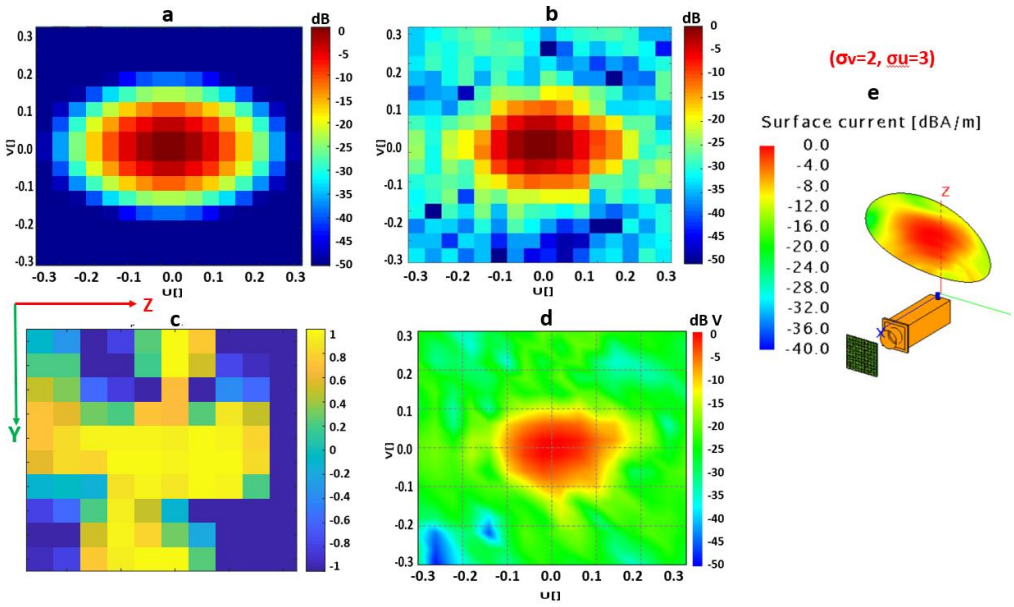

Figure 6.10 (a) Centered Gaussian pattern with σ_v =2 and σ_u =3 , (b) Normalized amplitude of the optimized pattern by PSO, (c) Distribution of $\cos\varphi_n$ on the reflectarray for the optimized pattern, (d) Normalized co-polarization amplitude of radiation pattern obtained by simulation of the antenna in FEKO using the phase distribution $\{\varphi_n\}$ in Figure 6.10c, (e) Current distribution on

the dish obtained by simulation of the antenna in FEKO, using the phase distribution $\{\varphi_n\}$ in Figure 6.10c

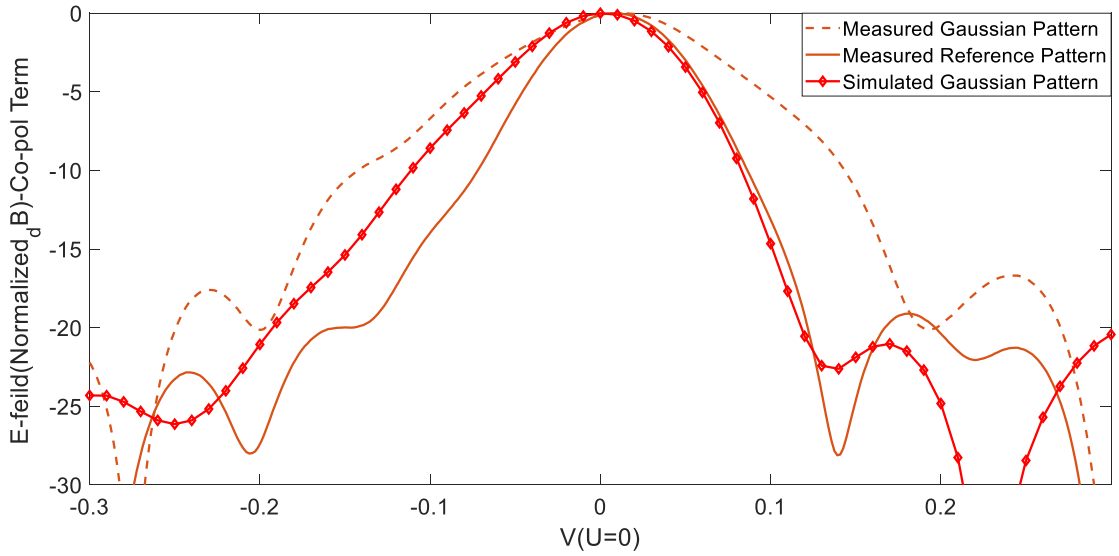

(a)

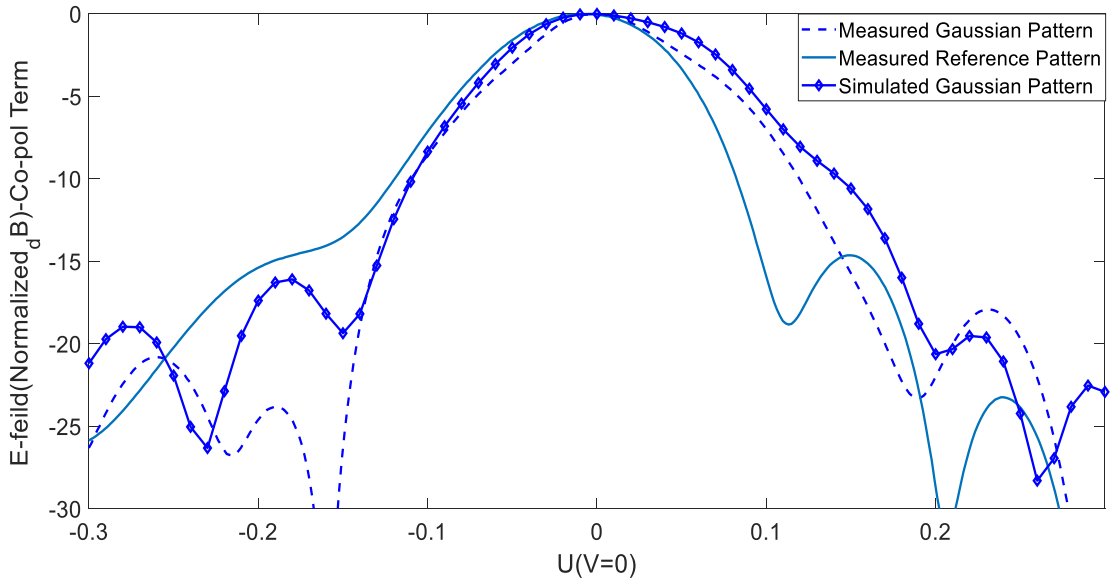

(b)

Figure 6.11 Cuts of Gaussian pattern with σ_v =2 and σ_u =3. (a) Normalized co-polarization electric field along the *v* (*u*=0) axis for the reference beam (measured) and the synthesized beam (measured and simulated) for a desired Gaussian pattern, (b) Same case but along the *u* axis (*v*=0)

Figure 6.12 shows the normalized reference and synthesized patterns along with the *v* and *u* axes obtained from measurement. As shown in Figure 6.12, the XPDs of around 19.5 dB and 20 dB within the HPBW along with the *v* and *u* axes are obtained, respectively, for the synthesized beam, while an XPD of about 25 dB is obtained for the reference beam along both axes. RHCP term is considered as the co-polarization term, and LHCP is deemed to be the cross-polarization term.

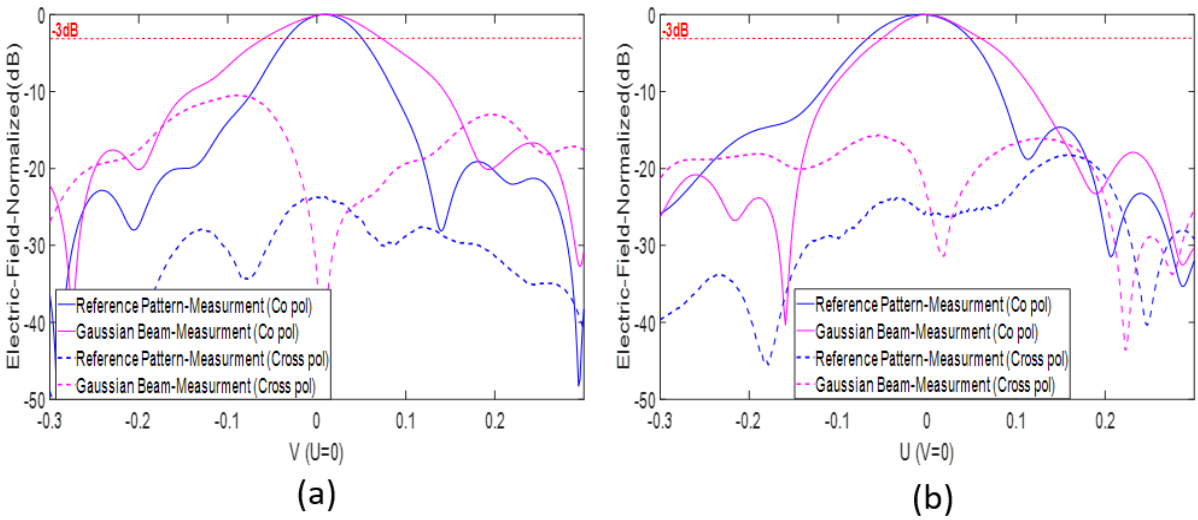

Figure 6.12 Normalized far-field of the reference beam (measured) and desired Gaussian beams with σ_v =2 and σ_u =3 cuts (measured): (a) along the *v* axis (*u*=0), (b) along the *u* axis (*v*=0)

In the fourth example, the centered Gaussian pattern with σ_u =2 and σ_v =2 shown in Figure 6.13a is defined as the desired beam. PSO algorithm with the population number of 3000 and α =5e-4 gives an MSE of 0.007 after 1000 iterations. Figures 6.13b and 6.13c show the pattern and phase distribution on the reflectarray obtained from PSO. Figures 6.13d and 6.13e show the radiation pattern in *uv* plane and the current distribution on the dish obtained by hybrid simulation in FEKO, after applying the proper phase distribution in Figure 6.13c. In contrast with the reference pattern in Figure 6.3, the synthesized pattern in Figure 6.13d is symmetric and has almost the same beamwidth along the *u* and *v* axes.

The normalized patterns along the *u* and *v* axes are shown in Figures 6.14a and 6.14b. Each figure includes three curves; the measured reference beam, the simulated and measured synthesized beams. Results show good agreement between the synthesized pattern's measurement and simulation. As shown in Figure 6.14b in the *v*=0 cut, simulated and measured synthesized beams have similar beamwidths as the reference case. In the *u*=0 cut, the beamwidths of the synthesized cases in Figures 6.5a, 6.8a are wider than 6.14a and 6.11a with the smaller σ_v. In the *v*=0 cut, compared to Figures 6.5b and 6.11b the measured and simulated synthesized patters in Figures

6.14b and 6.8b are narrower, which is in agreement with the smaller σ_u of Figures 6.14a and 6.11a specified in the optimization. As shown in Figure 6.13, the pattern is not centered as the desired Gaussian pattern. The distortion in the optimized beam is due to the small size of the dish. The size of the dish will affect the beam synthesis performance of the antenna since the dish surface cannot cover the total current distribution due to the reflected beam by the reflectarray.

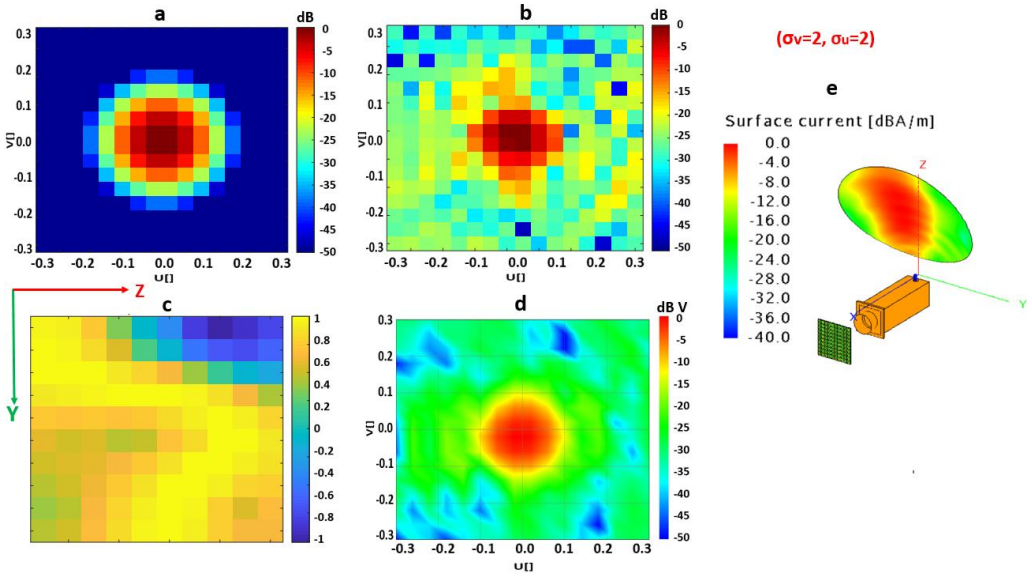

Figure 6.13 (a) Centered Gaussian pattern with σ_u =2 and σ_v =2, (b) Normalized amplitude of the optimized pattern by PSO, (c) Distribution of $\cos\varphi_n$ on the reflectarray for the optimized pattern, (d) Normalized co-polarization amplitude of radiation pattern obtained by simulation of the antenna in FEKO using the phase distribution $\{\varphi_n\}$ in Figure 6.13c, (e) Current distribution on the dish obtained by simulation of the antenna in FEKO, using the phase distribution $\{\varphi_n\}$ in Figure 6.13c

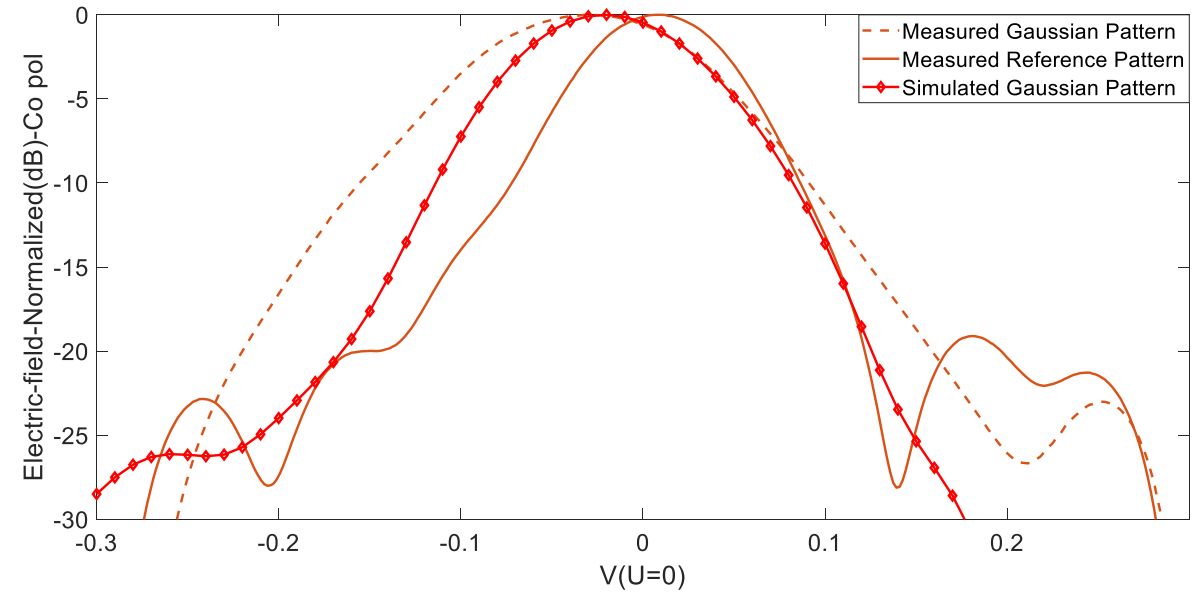

(a)

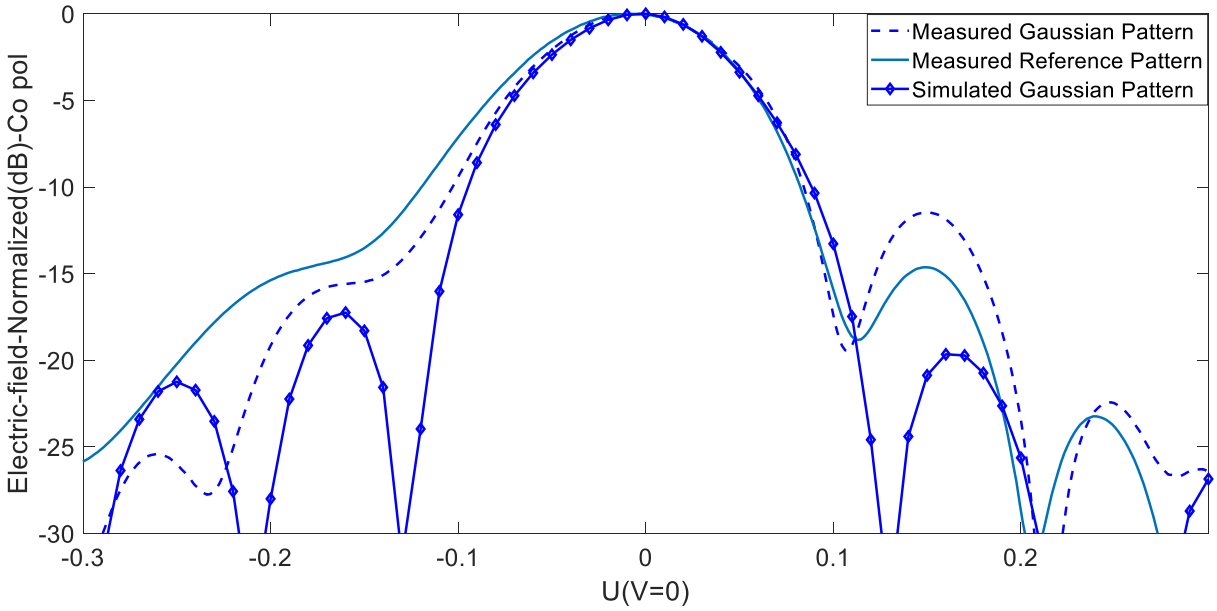

(b)

Figure 6.14 Cuts of Gaussian pattern with σ_v =2 and σ_u =2. (a) Normalized co-polarization electric field along the *v* axis (*u*=0) for the reference beam (measured) and the synthesized beam (measured and simulated) for a desired Gaussian pattern, (b) Same case but along the *u* axis (*v*=0)

Figure 6.15 shows the normalized reference and synthesized patterns along with the *v* and *u* axes obtained from measurement. As shown in Figure 6.15, the XPDs of around 18.5 dB and 20 dB within the HPBW along with the *v* and *u* axes are obtained, respectively, for the synthesized beam, while an XPD of about 25 dB is obtained for the reference beam along both axes. The RHCP term is considered as the co-polarization term, and LHCP is deemed to be the cross-polarization term.

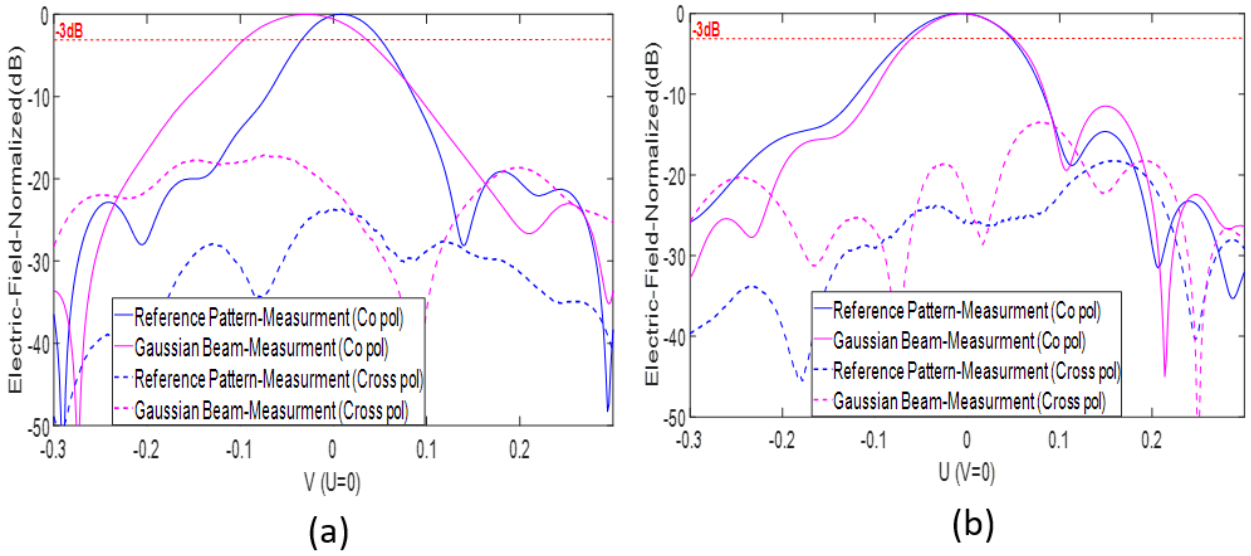

Figure 6.15 Normalized far-field of the reference beam (measured) and desired Gaussian beams with σ_v =2 and σ_u =2 cuts (measured): (a) along the *v* axis (*u*=0), (b) along the *u* axis (*v*=0)

The fifth example demonstrates the performance of the algorithm in synthesizing scanned beams. Beam steering of +0.05 along the *v* axis in *uv* plane is provided in this example. PSO algorithm with the population number of 5000 and α =1e-5 gives an MSE of 0.00074 after 1000 iterations. Figures 6.16b and 6.16c show the pattern and phase distribution on the reflectarray obtained from PSO. Figures 6.16d and 6.16e show the radiation pattern in *uv* plane and the current distribution on the dish obtained by hybrid simulation in FEKO, after applying the proper phase distribution in Figure 6.16c.

Compared to the reference beam in Figure 6.3, the scanned beam in Figure 6.16d is shifted by Δv = +0.05 along the *v* axis. Figure 6.17 shows the normalized patterns along the *v* axes. The figure includes three curves; the measured reference beam, the simulated and measured synthesized

beams. Results show a good agreement between the synthesized pattern's measurement and simulation results and the shift along the *v* axis with respect to the reference pattern. As shown in Figure 6.17, in the *u*=0 cut, simulated and measured synthesized beams have similar beamwidths as the reference case while shifted by $\Delta v = +0.05$ with respect to the reference beam.

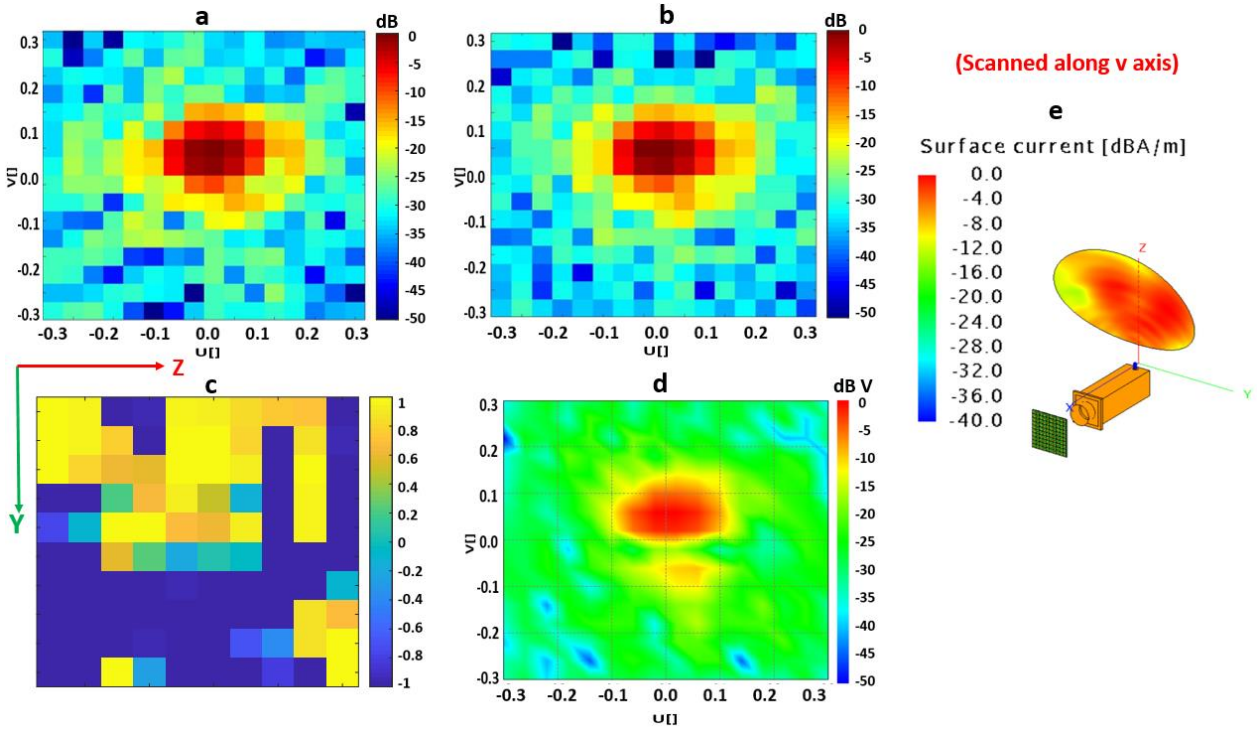

Figure 6.16 (a) Scanned beam patterns by (Δu=0, Δv=0.05), (b) Normalized amplitude of the optimized pattern by PSO, (c) Distribution of $\cos\varphi_n$ on the reflectarray for the optimized pattern, (d) Normalized co-polarization amplitude of radiation pattern obtained by simulation of the antenna in FEKO using the phase distribution $\{\varphi_n\}$ in Figure 6.16c, (e) Current distribution on the dish obtained by simulation of the antenna in FEKO, using the phase distribution $\{\varphi_n\}$ in Figure 6.16c

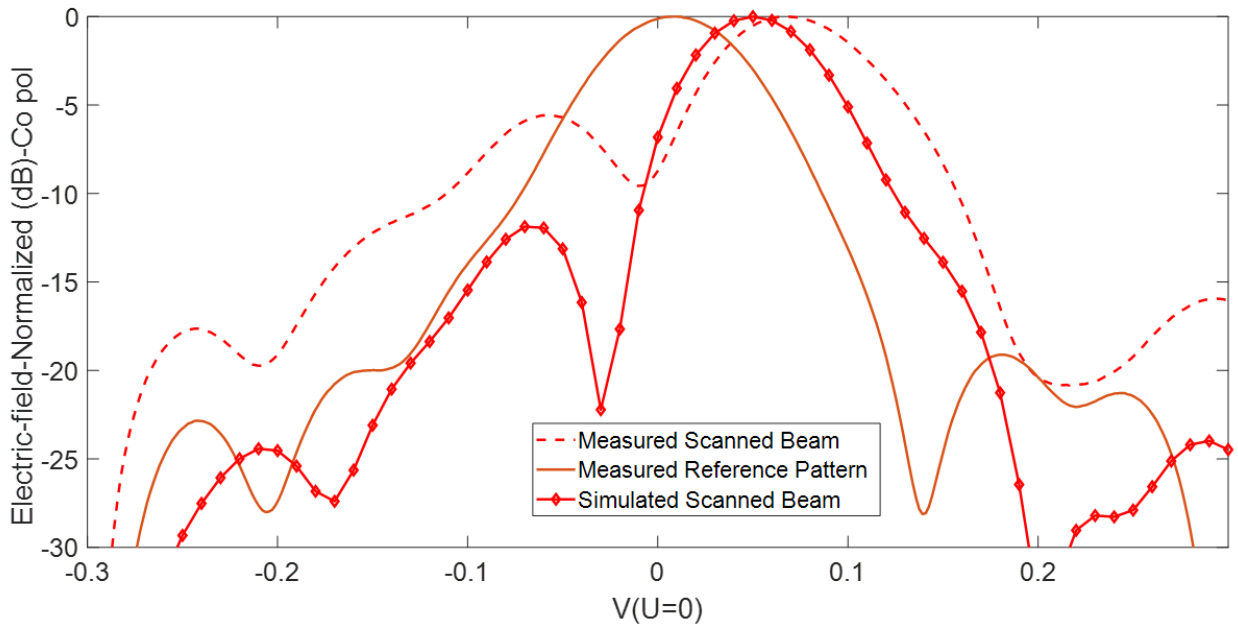

Figure 6.17 Normalized co-polarization electric field along the *v* axis (*u*=0) for the reference beam (measured) and of the synthesized beam (measured and simulated) for a desired scanned beam

Figure 6.18 shows the normalized reference and synthesized patterns along with the *v* axis obtained from measurement. As shown in Figure 6.18, the XPD of around 30 dB within the HPBW along with the *v* axis is obtained for the synthesized beam, while an XPD of about 25 dB is obtained for the reference beam along *v* axis. The RHCP term is considered as the co-polarization term, and LHCP is deemed to be the cross-polarization term.

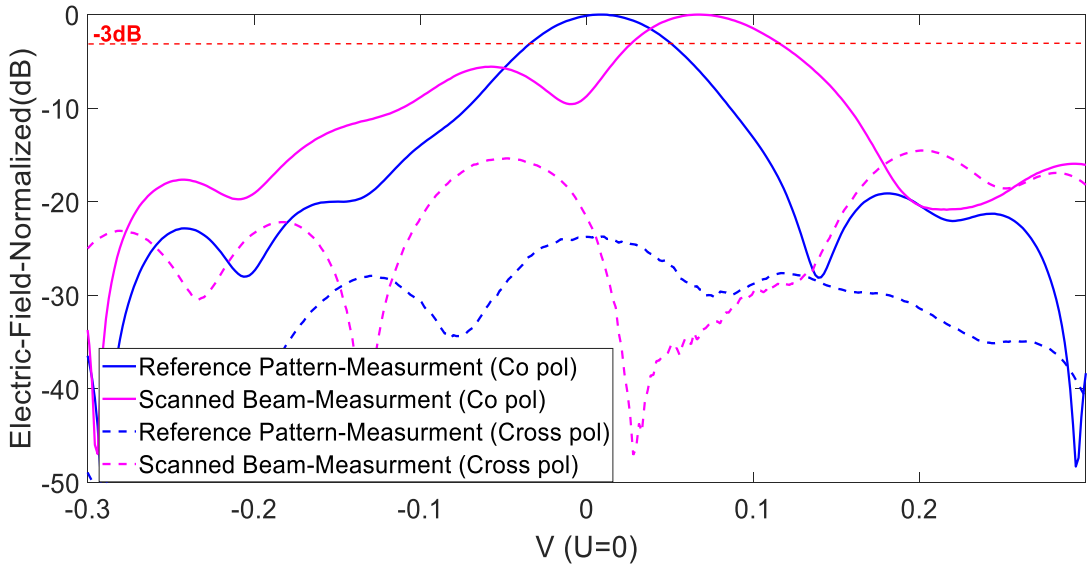

Figure 6.18 Normalized far-field of the reference beam (measured) and desired scanned beam (measured) along the *v* axis (*u*=0)

The performance of the PSO-based bam synthesis algorithm is studied by defining different Gaussian beams as the desired patterns. In addition, section 6.4 studies the improvement in the axial ratio of the antenna system in the simulation compared to the measurement results.

6.4 Improvement in the axial ratio of the antenna system in the measurement setup compared to the simulation

This section confirms the improvement in XPD level in the measurement setup compared to the simulation observed in Chapter 4. The reason for this is the presence of the absorber covering the area behind the reflectarray, which blocks the spillover of cross-polarization term around the reflectarray. The improvement in measurement results is expected to be observed in Chapter 6 with the same setup configuration in Chapter 4 (See Figure 6.2 and Figure 4.30). For example, the simulated and measured beam in *uv* plane for the reference pattern will be considered to study the change in XPD level.

Figures 6.19 and 6.20 show the normalized reference pattern along with the *v* and *u* axes obtained from measurement and simulation. Good agreement is observed between the co-polarization patterns obtained from the measurement and simulation along the *u* and *v* axis. HPBW of 4.5° is observed for the simulated and measured beam along the *v* axis, and HPBW of 5.5° is observed along the *u* axis for the measured and simulated beams. As shown in the figures, the XPDs of about 15dB and 25dB in HPBW are observed for the reference beam along both axes from the simulation and measurement, respectively. The RHCP term is considered as the co-polarization term, and LHCP is deemed to be the cross-polarization term.

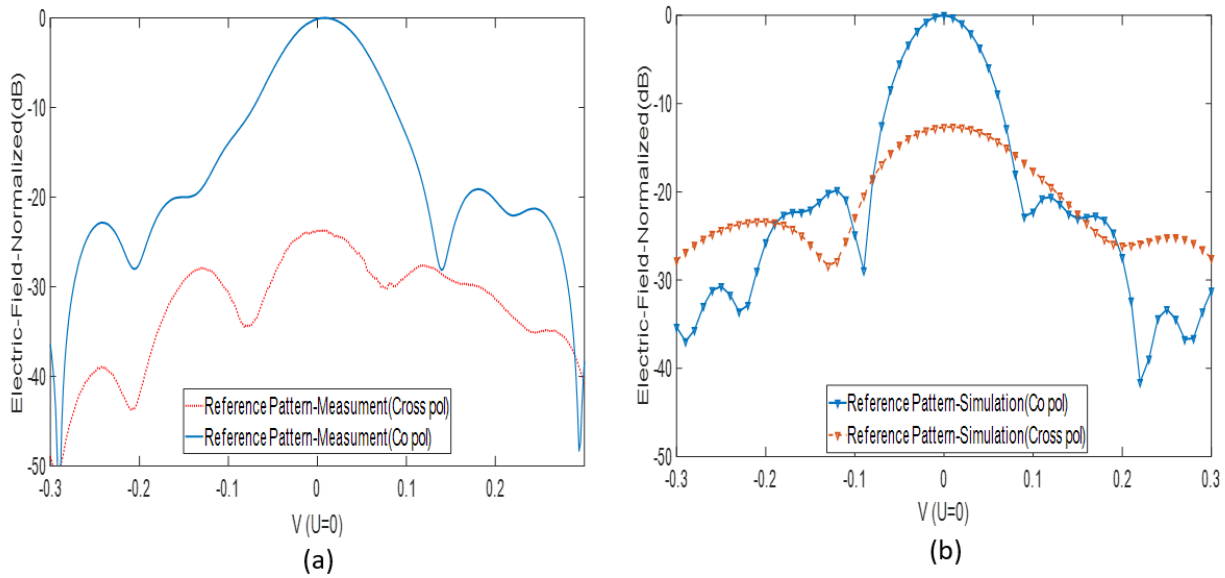

Figure 6.19 Normalized far-field (dB) of the reference case along the *v* axis (*u*=0): (a) Measurement, (b) Simulation

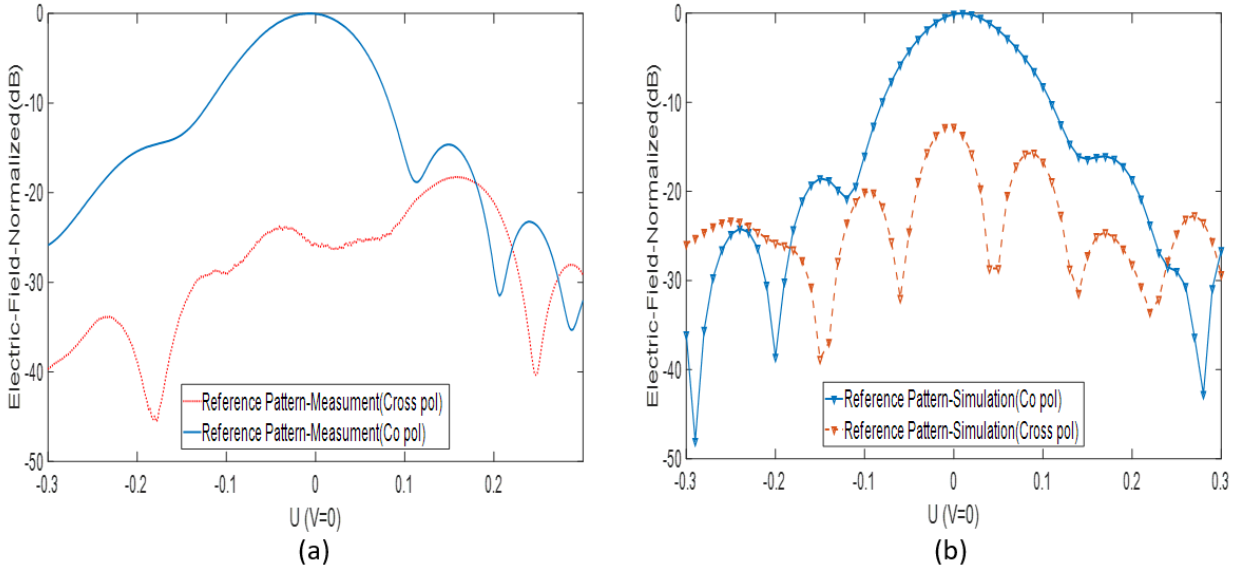

Figure 6.20 Normalized far-field (dB) of the reference case along the *u* axis (*v*=0): (a) Measurement, (b) Simulation

It was conjectured that these higher cross-polarization levels in the simulation are due to the spillover of the beam around the reflectarray. In fact, it should be recalled that reflection on the dish changes the sense of circular polarization, but not the reflection on the reflectarray. Therefore, spillover radiation from the subreflector, which is in the same angular sector as the main beam created by the dish, is contributing to cross-polarization. The main part of this spillover is emitted from the feed horn. Therefore, to decrease the cross-polarization level, absorber material should be placed around the reflectarray to prevent spillover. In the measurement setup, this can be easily implemented, as seen in Figure 6.2a. A simple way to implement an absorber in the FEKO simulation, is to include a Salisbury screen around the reflectarray. This screen consists of an impedance sheet with a surface resistance equal to the plane wave impedance in free space (377Ω) separated form a PEC plate with a distance of λ/4. This Salisbury screen is perfectly absorbing the incident wave at normal incidence, but partially reflects at oblique incidence. It mimics the absorber in the measurement setup. This configuration with the Salisbury screen is shown in Figure 6.21a. Figure 6.22 shows the co-polarization and cross-polarization radiation patterns of the system for three cases, that is simulations with and without Salisbury screen, and measurements with absorber

covering the area behind the reflectarray, as shown in a. It can be seen that the effect of Salisbury screen on the co-polarized patterns is small, especially above the -20 dB level. For the cross-polarization, however, decreases of approximately 5 dB and 12.5 dB near $\theta = 0$ are obtained along the *u* and *v* axes, respectively. This will translate into the improvement of the system axial ratio. The RF pyramidal absorber used in an anechoic chamber does not have the same properties as the Salisbury screen. Still, both of them have the same effect in reducing the cross-polarized spillover radiation around the reflectarray.

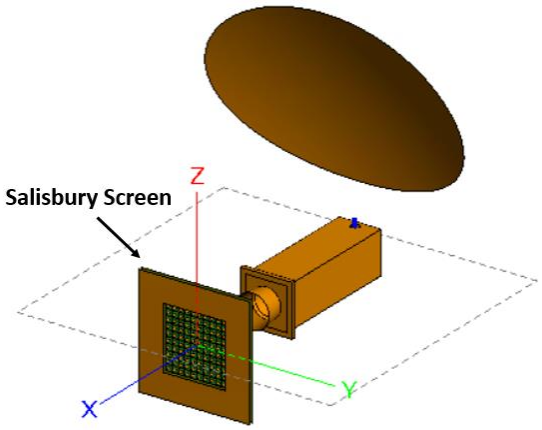

Figure 6.21 Dual-reflector antenna with Salisbury screen around the reflectarray

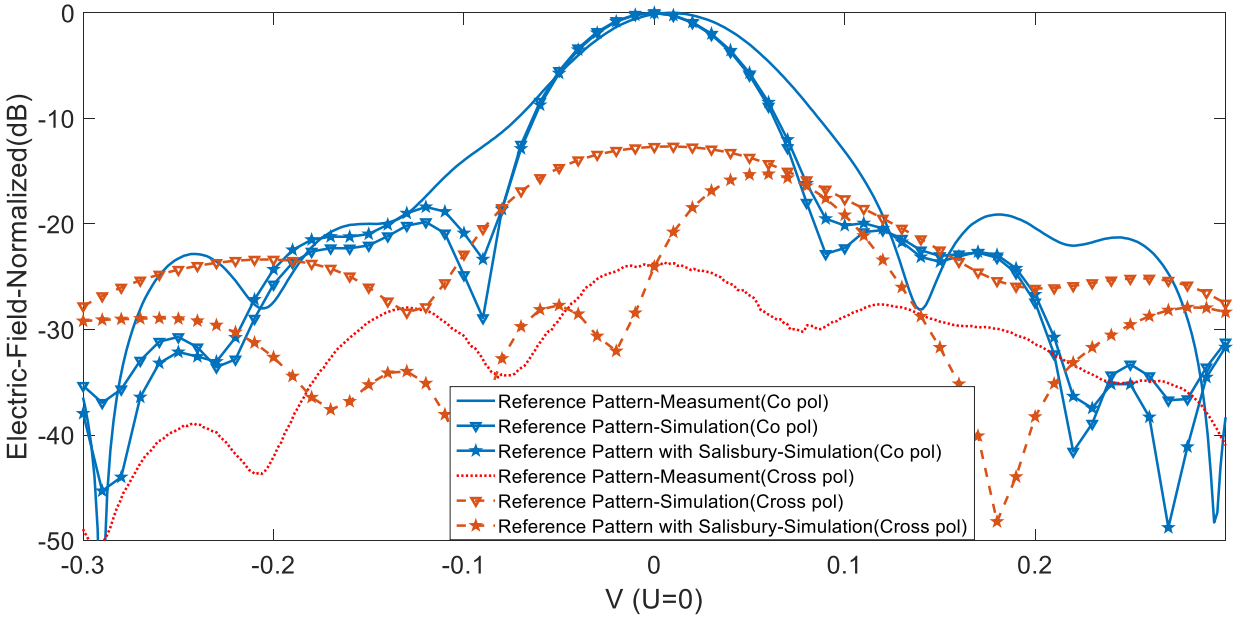

(a)

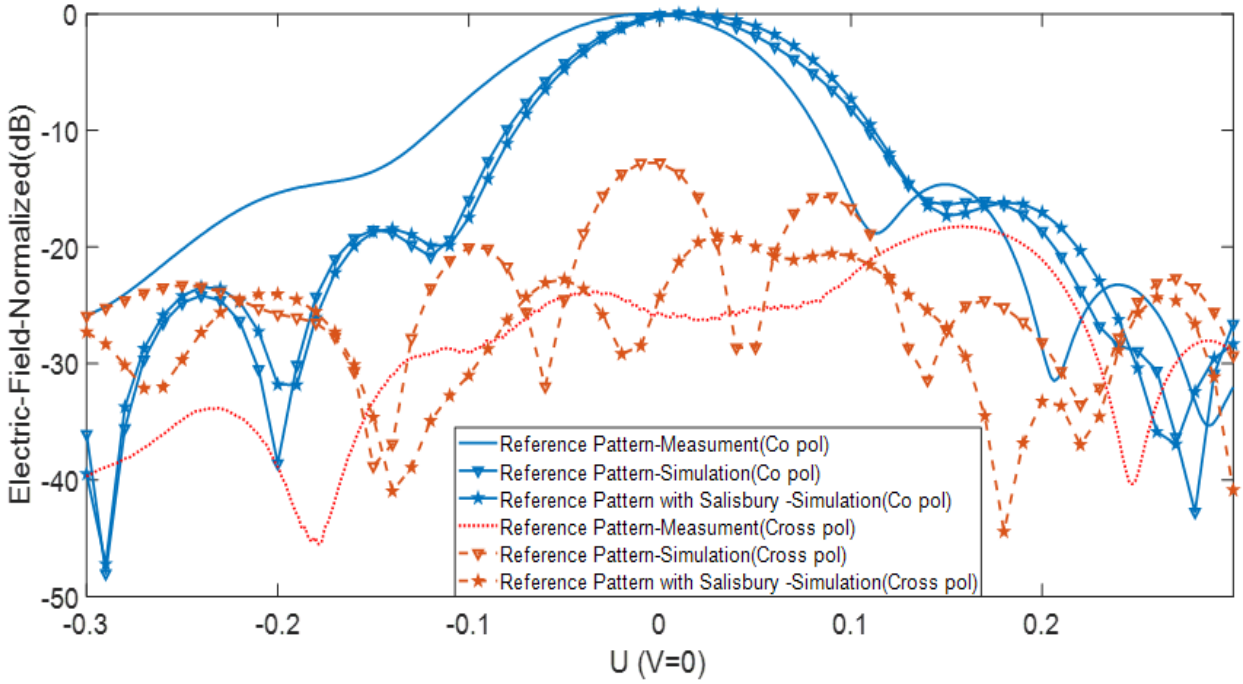

(b)

Figure 6.22 (a) Effect of absorber on the normalized reference patterns along the *v* axis (*u*=0), (b) Effect of absorber on the normalized reference pattern along the *u* axis (*v*=0)

6.5 Conclusion

Beam synthesis of dual-reflector antenna based on the PSO-based beam synthesis algorithm is experimentally studied in this chapter. The proposed algorithm has the ability to control the beamwidth. As a result, the beamwidth of the synthesized beams are matched with the beamwidth of the desired beams, which are Gaussian patterns (the beamwidth of Gaussian distribution is adjusted by varying σ_v and σ_u). The beamwidth control capability of the algorithm is validated by widening the beam with respect to the reference pattern along the *u* and *v* axes by $\Delta v = +0.15$ and $\Delta u = +0.05$ for desired patterns separately. In addition, the beam scanning capability of the algorithm is validated by shifting the beam by $\Delta v = +0.05$ along the *v* axis with respect to the reference beam.

For the proposed setup, the PSO algorithm will work with a reduced solution space due to the limited dish size for the currents on the dish to be translated for synthesizing the beam. As a result, several experiments are needed to adjust the α value, the coefficient of phase gradient term in MSE function. This could be confirmed by finding more variation in α values for different examples in Table 6.1 than the α values in Table 5.1 with the constant value for α in all the cases. Therefore, in the measurement setup with the smaller dish, the algorithm's convergence is more sensitive to the PSO parameters selection, such as α value, than the structure with the larger dish in the previous chapter. In addition, for some cases with the smaller dish, larger population numbers were selected to increase accuracy.

Finally, this chapter studied the effect of RF pyramidal absorber used in an anechoic chamber to improve the proposed system's axial ratio.

CHAPTER 7 CONCLUSION AND FUTURE WORK

This thesis proposes a dual-reflector system with the ability of beam shaping and beam scanning. A reconfigurable reflectarray used as the subreflector in a dual-reflector system has been designed in the C-band where the phase adjustment of the elements is made by mechanical rotation. With the reflectarray as the subreflector of the system, a reduced number of micromotors are needed for the phase adjustment of the system. In counterpart, there is less flexibility and accuracy in the steering and shaping functions.

Different methods have been proposed in the literature to scan the beam out of the dual-reflector structure, including electronic and mechanical approaches [3, 4]. [3] implements beam scanning out of linearly polarized dual-reflector antenna at 94 GHz by tilting the flat metal subreflector, while [4] proposes beam scanning out of linearly polarized dual-reflector antenna by implementing PPS technique at 11.95 GHz. In this work, beam scanning out fo dual-reflector antenna is implemented by applying NFF technique by electromechanical approach.

To evaluate the performance of each method, all the techniques are implemented in the same structure which is the C-band CP dual-reflector antenna structure of our proposed design. As shown in Chapter 4, beam scanning by tilting the flat metal subreflector suffers from a high amount of spillover around the subreflector emitted from the feed horn. Therefore, a limited scan range of ±2 degrees is obtained with this configuration unless the subreflector size is increased. Afterward, by applying the PPS technique, it is observed that the beam scanning is limited to -3 to +3 degrees. The limited scan range in PPS is due to the high cross-polarization level of the beam. This high cross-polarization level is due to offset configuration of the horn and reflectarray with increasing in the incident angles of the beam on the reflectarray elements. In the NFF technique, with the center-fed configuration of the horn and reflectarray, lower incident angles of the beam on the reflectarray elements exist compared to the offset configuration structure of the PPS technique. Therefore, a lower cross-polarization level with more scan range is obtained. With the dish projected aperture size of 24λ, the scan range of up to ±5 degrees is provided by applying the NFF technique. Therefore, in NFF, beam scanning in two planes is possible and is only limited by the dish size. In contrast with the NFF technique, in the PPS technique, the beam scanning in both planes is limited by the high cross-polarization level, while in the vertical plane, it is also limited

by greater feed blockage. Consequently, the NFF technique, the proposed method implemented in this work, can scan the beam in two planes in a wider range compared to the methods introduced in the literature.

Furthermore, the beam shaping and beam synthesis out of the proposed system are implemented by a modified PSO-based algorithm by forcing continuous phase distribution on reflectarray. The beamwidth control capability of the algorithm is validated experimentally by widening the beam with respect to the reference pattern along the *u* and *v* axes by $\Delta v = +0.15$ and $\Delta u = +0.05$ for desired patterns separately. In addition, the beam scanning capability of the algorithm is validated by shifting the beam by $\Delta v = +0.05$ along the *v* axis with respect to the reference beam.

In the following paragraphs, some key recommendations can be given for future work in order to improve the performance of the proposed system.

-Single Feed Multiple Beam (SFMB) Antenna

The proposed antenna in this work has potential to produce multi-beam with a single feed and can be used as 5G base station antennas. Multi-beam array antennas are promising candidate for 5G systems with less complexity in the design and more adaptability with shorter wavelengths compared to the Multiple Input Multiple Output (MIMO) system with phased arrays [73].

Tomura et al. [74] introduces two reflector-based configurations, including Single Feed Per Beam (SFPB) and Multiple Feeds Per Beam (MFPB). In our work, the single feed dual-reflector antenna with the ability of producing multiple beams introduces a new structure called Single Feed Multiple Beam (SFMB). By designing a subreflector with multi-focusing ability in the near-field, multiple virtual source spots can be created. Therefore, each virtual source considered as a non-physical feed and related to a one-directional beam reflected from the main reflector and propagated in specific directions from the base station antenna. Scanning of individual beams is possible by moving the related virtual sources around its primary location. Beam synthesis for multi beams could be implemented by implementing proper beam synthesis algorithm [75]. In [76] and [77] Gregorian dual-reflector antenna is proposed for 5G mobile base stations where multiple feeds are used and controlled by beam switching networks to produce multiple beams. The antenna in this

work can develop a practical, cost-effective, and high gain antenna for the 5G base stations as the single feed multi beam antenna.

-Sustainable Development

By rapidly developing satellite technology, developed countries want to replace old satellites with new and highly developed satellites and remove old satellites from the orbit. The old satellite antennas can still be used before reaching their life span. The useful life of a satellite is typically around 10-15 years. Reconfigurable antennas with the ability of beam steering and beam shaping enable us to change a satellite's coverage map. In this case, instead of removing the satellite from the orbit and sending it to the draft, the satellite coverage map can be switched to other regions, (e.g. from North American to Central or South American countries). Therefore, we can put the old satellites from developed countries to good use and use them for under-developed countries missing telecommunication infrastructure instead of creating space debris.

-Electromechanical System

With the complete implementation of the electromechanical system, we would be able to directly control and shaping the beam to the desired pattern. This will be possible by linking our beam shaping code to the motor control system program for rotating the motors and, therefore, implementing the phase adjustment system for the antenna. This implementation has not been fully completed and is still considered as work in progress. By receiving feedback from the satellite image, the antenna will be adjusted to the desired coverage map.

-Beam Synthesis algorithm

A modified PSO-based beam synthesis algorithm is proposed in this work. Some approaches could be made in order to improve the performance of the algorithm:

1- The proposed algorithm has a better response for larger arrays with higher phase accuracy. Therefore, the algorithm could be implemented for the antenna with a main reflectarray.

2- The limitation of the algorithm in terms of controlling the beamwidth for the narrow beams could be improved by increasing the aperture size of the main reflector.

3- To increase the quality of the shaped beam for the small arrays, MSE, the cost function of the algorithm can be divided into two terms. One term would optimize the beam reflected from the dish as shown in Figure 7.1a (MSE1), and the second term would consider the far-field beam of the reflectarray in the absence of the dish (MSE2), as shown in Figure 7.1b, which is mostly a cross-polarized contribution due to spillover. A separate set of element factor matrices should be defined for each figure by applying the NFF technique.

The cost function of the algorithm is defined in eq. (7.1) by summing MSE1 and MSE2 related to each uv plane in Figures 7.1a and 7.1b. w in the equation is the term in the range of [0,1] to adjust the relative weight of the second term of the cost function.

$$MSE = MSE_1 + w * MSE_2 \tag{7.1}$$

The size and sampling point of each uv plane in Figure 7.1 should be selected based on the spot of the main beam and pattern shape. By applying this approach, both the co-polarized and cross-polarized fields would be taken into account.

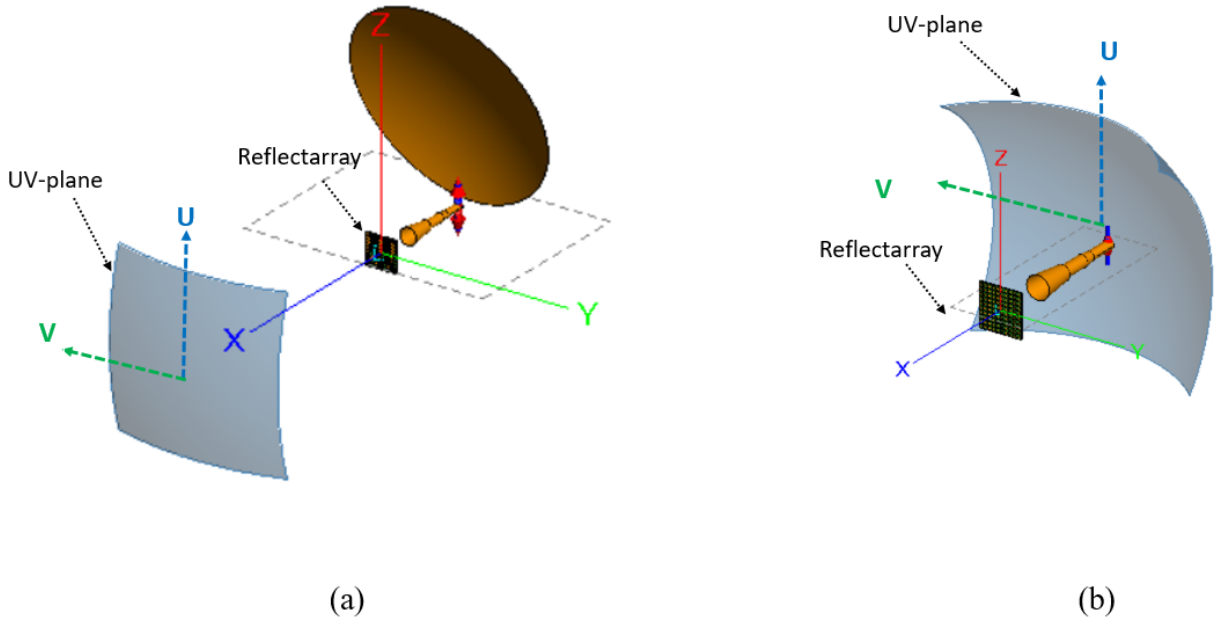

Figure 7.1 (a) Dual-reflector system, with the *uv* plane in the far-field at the left side of the system, (b) The system including the horn and reflectarray with the *uv* plane in the far-field at the right side of the system

4- Thee key parameters of the algorithm including, population number, iteration number, and α values have been selected based on many experiments by running the algorithm. A mathematical solution could be proposed to find the best values for the parameters that are the best fit for the algorithm to minimize the cost function and maximize the smoothness. It is suggested to select the population number 5 times greater than the number of particles which is the number of reflectarray elements. Also, implementing parallel processing optimization instead of sequential optimization would speed up the optimization process.

REFERENCES

[1] Tienda, C., Arrebola, M., & Encinar, J. A., "Review Article: Recent Developments of Reflectarray Antennas in Dual-Reflector Configurations," *International Journal of Antennas and Propagation*, Jan 2012.

[2] M. Arrebola, L. de Haro, J. A. Encinar and L. F. de la Fuente, "Contoured-Beam Gregorian Antenna with a Reflectarray as Subreflector," in *The Second European Conference on Antennas and Propagation, EuCAP 2007*, 2007.

[3] W. H. e. al, "94 GHz Dual-Reflector Antenna With Reflectarray Subreflector," *IEEE Transactions on Antennas and Propagation,* vol. 57, no. 10, pp. 3043-3050, October 2009.

[4] M. Arrebola, L. D. Haro and J. A. Encinar, "Analysis of dual-reflector antennas with a reflectarray as subreflector," *IEEE Antennas and Propagation Magazine,* vol. 50, no. 6, pp. 39-51, December 2008.

[5] Arrebola, M., Hu, W., Encinar, J. A., Cahill, R., Fusco, V., Gamble, H. S., & Grant, N., "94 GHz beam scanning dual-reflector antenna with a sub-reflectarray," in *30th ESA Antenna Workshop 2008*, 2008.

[6] X. Yang et al, "A Broadband High-Efficiency Reconfigurable Reflectarray Antenna Using Mechanically Rotational Elements," *IEEE Transactions on Antennas and Propagation,* vol. 65, no. 8, pp. 3959-3966, 2017.

[7] X. Yang, S. Xu, F. Yang, M. Li, H. Fang and Y. Hou, "Design of a circularly polarized reconfigurable reflectarray using micromotors," in *2015 IEEE International Symposium on Antennas and Propagation & USNC/URSI National Radio Science Meeting*, 2015.

[8] Derakhshan, Aghil, Javad Nourinia, and Changiz Ghobadi, "Electromechanical beamsteering reflectarray antenna for X-band applications," *AEU-International Journal of Electronics and Communications,* vol. 94, pp. 145-149, 2018.

[9] E. R. Schlosser, S. M. Tolfo and M. V. T. Heckler, "Particle swarm optimization for antenna arrays synthesis," in *2015 SBMO/IEEE MTT-S International Microwave and Optoelectronics Conference (IMOC),* Porto de Galinhas, 2015.

[10] L. A. Greda, A. Winterstein, D. L. Lemes and M. V. T. Heckler, "Beamsteering and Beamshaping Using a Linear Antenna Array Based on Particle Swarm Optimization," *IEEE Access,* vol. 7, pp. 141562-141573, 2019.

[11] Bhattacharyya, Arun K, "Projection matrix method for shaped beam synthesis in phased arrays and reflectors," *IEEE Transactions on Antennas and Propagation,* vol. 55, no. 3, pp. 675-683, 2007.

[12] W. Stutzman, "Synthesis of shaped-beam radiation patterns using the iterative sampling method," *IEEE Transactions on Antennas and Propagation,* vol. 19, no. 1, pp. 36-41, 1971.

[13] Zaman, M. A., Mamun, S. A., Gaffar, M., Choudhury, S. M., Alam, M. M., & Matin, M, "Phased Array Synthesis Using Modified Particle Swarm Optimization," *Journal of Engineering Science & Technology Review,* vol. 4, no. 1, 2011.

[14] J. Robinson and Y. Rahmat-Samii, "Particle swarm optimization in electromagnetics," *IEEE Transactions on Antennas and Propagation,* vol. 52, no. 2, pp. 397-407, 2004.

[15] Kadri, B., Brahimi, M, "Patterns antennas arrays synthesis based on adaptive particle swarm optimization and genetic algorithms," *International Journal of Computer Science Issues (IJCSI),* vol. 10, no. 1, p. 21, 2013.

[16] H. M. Elkamchouchi, M. M. Hassan, "Array pattern synthesis approach using a genetic algorithm," *IET Microwaves, Antennas and Propagation,* vol. 8, no. 14, p. 1236–1240, 2014.

[17] T. H. Ismail, Z. M. Hamici, "Array pattern synthesis using digital phase control by quantized particle swarm optimization," *IEEE Transactions on Antennas and Propagation,* vol. 58, no. 6, p. 2142–2145, 2010.

[18] S. Chatterjee, S. Chatterjee, D. R. Poddar, "Synthesis of linear array using Taylor distribution and Particle Swarm Optimisation," *International Journal of Electronics,* vol. 102, no. 3, pp. 514-528, 2015.

[19] D. I. Abu-Al-Nadi, T. H. Ismail, H. Al-Tous, M. J. Mismar, "Design of linear phased array for interference suppression using array polynomial method and particle swarm optimization," *Wireless Personal Communications,* vol. 63, no. 2, pp. 501-513, 2012.

[20] Chuang Han, Ling Wang, "Array Pattern Synthesis Using Particle Swarm Optimization with Dynamic Inertia Weight," *International Journal of Antennas and Propagation,* p. 7 pages, 2016.

[21] S. V. Hum and J. Perruisseau-Carrier, "Reconfigurable Reflectarrays and Array Lenses for Dynamic Antenna Beam Control: A Review," *IEEE Transactions on Antennas and Propagation,* vol. 62, no. 1, pp. 183-198, 2014.

[22] J. P.-C. a. O. C. C. Guclu, "Proof of Concept of a Dual-Band Circularly-Polarized RF MEMS Beam-Switching Reflectarray," *IEEE Transactions on Antennas and Propagation,* vol. 60, no. 11, pp. 5451-5455, 2012.

[23] T. Debogovic and J. Perruisseau-Carrier, "Dual-Polarized Low Loss Reflectarray Cells with MEMS-Based Dynamic Phase Control," in *2015 9th European Conference on Antennas and Propagation (EuCAP),* 2015.

[24] T. Debogovic and J. Perruisseau-Carrier, "Dual-polarized low loss reflectarray cells with MEMS-based dynamic phase control," in *2015 9th European Conference on Antennas and Propagation (EuCAP)*, Lisbon, 2015.

[25] C. Guclu, J. Perruisseau-Carrier and O. A. Civi, "Dual frequency reflectarray cell using split-ring elements with RF MEMS switches," in *2010 IEEE Antennas and Propagation Society International Symposium*, Toronto, 2010.

[26] B. Strassner, C. Han and Kai Chang, "Circularly polarized reflectarray with microstrip ring elements having variable rotation angles," pp. 1122-1125, April 2004.

[27] Yu, A., Yang, F., Elsherbeni, A. Z., & Huang, J, "Design and measurement of a circularly polarized Ka-band reflectarray antenna," in *2009 3rd European Conference on Antennas and Propagation*, 2009.

[28] R. Sorrentino, R. V. Gatti and L. Marcaccioli, "Recent advances on millimetre wave reconfigurable reflectarrays," in *2009 3rd European Conference on Antennas and Propagation*, Berlin, 2009.

[29] H. Legay, B. Pinte, M. Charrier, A. Ziaei, E. Girard and R. Gillard, "A steerable reflectarray antenna with MEMS controls," in *IEEE International Symposium on Phased Array Systems and Technology*, 2003.

[30] S. V. Hum, G. McFeetors and M. Okoniewski, "Integrated MEMS Reflectarray Elements," in *2006 First European Conference on Antennas and Propagation*, 2006.

[31] T. Debogovic and J. Perruisseau-Carrier, "Low Loss MEMS-Reconfigurable 1-Bit Reflectarray Cell With Dual-Linear Polarization," *IEEE Transactions on Antennas and Propagation*, vol. 62, no. 10, pp. 5055-5060, October 2014.

[32] L. Di Palma, A. Clemente, L. Dussopt, R. Sauleau, P. Potier and P. Pouliguen, "Circularly-Polarized Reconfigurable Transmitarray in Ka-Band With Beam Scanning and Polarization

Switching Capabilities," *EEE Transactions on Antennas and Propagation,* vol. 65, no. 2, pp. 529-540, February 2017.

[33] S. V. Hum, M. Okoniewski and R. J. Davies, "Modeling and Design of Electronically Tunable Reflectarrays," *IEEE Transactions on Antennas and Propagation,* vol. 55, no. 8, pp. 2200-2210, Aug 2007.

[34] S. Bildik, S. Dieter, C. Fritzsch, W. Menzel and R. Jakoby, "Reconfigurable Folded Reflectarray Antenna Based Upon Liquid Crystal Technology," *IEEE Transactions on Antennas and Propagation,* vol. 63, no. 1, pp. 122-132, Jan 2015.

[35] J. A. E. M. B. a. E. C. G. Perez-Palomino, "Design and evaluation of multi-resonant unit cells based on liquid crystals for reconfigurable reflectarrays," *IET Microwaves Antennas & Propagation,* vol. 6, no. 3, p. 348–354, February 2012.

[36] R. R. Romanofsky, "Advances in Scanning Reflectarray Antennas Based on Ferroelectric Thin-Film Phase Shifters for Deep-Space Communications," *Proceedings of the IEEE,* vol. 95, no. 10, pp. 1968-1975, 2007.

[37] Huang, John, and Ronald J. Pogorzelski, "A Ka-band microstrip reflectarray with elements having variable rotation angles," *IEEE transactions on antennas and propagation,* vol. 46, no. 5, pp. 650-656, 1998.

[38] X. Liu, Y. Ge, X. Chen and L. Chen, "Design of Folded Reflectarray Antennas Using Pancharatnam-Berry Phase Reflectors," *IEEE Access,* vol. 6, pp. 28818-28824, 2018.

[39] A. Yu, F. Yang, A. Z. Elsherbeni and J. Huang, "A single layer broadband circularly polarized reflectarray based on the element rotation technique," in *2009 IEEE Antennas and Propagation Society International Symposium*, Charleston, 2009.

[40] A. Roxer, "Design of 3D printed circularly polarized waveguide antenna," Czech Technical University, Prague, 2016.

[41] "A High-Performance Dual-Mode Feed Horn for Parabolic Reflectors with a Stepped-Septum Polarizer in a Circular Waveguide [Antenna Designer's Notebook]," *IEEE Antennas and Propagation Magazine,* vol. 53, no. 3, pp. 142-146, 2011.

[42] Kim, J. M. Kovitz and Y. Rahmat-Samii, "Enhancing the Power Capabilities of the Stepped Septum Using an Optimized Smooth Sigmoid Profile," *IEEE Antennas and Propagation Magazine,* vol. 56, no. 5, pp. 16-42, 2014.

[43] A. I. Sandhu, "Design of an orthomode transducer in gap waveguide technology," 2010.

[44] Jensen F, Frandsen A, "On the number of modes in spherical wave expansions," in *26th AMTA*, 2004.

[45] Elmansouri, M., Filipovic, D. S, "Design of combined-antennas using spherical modes," in *Proceedings of 2014 Antenna application symposium*, Monticello, IL, 2014.

[46] H. Yang et al., "A 1-Bit 10×10 Reconfigurable Reflectarray Antenna: Design, Optimization, and Experiment," *IEEE Transactions on Antennas and Propagation,* vol. 64, no. 6, pp. 2246-2254, 2016.

[47] H. Yang et al, "A Study of Phase Quantization Effects for Reconfigurable Reflectarray Antennas," *IEEE Antennas and Wireless Propagation Letters,* vol. 16, pp. 302-305, 2017.

[48] H. Kamoda, T. Iwasaki, J. Tsumochi, T. Kuki and O. Hashimoto, "60-GHz Electronically Reconfigurable Large Reflectarray Using Single-Bit Phase Shifters," *IEEE Transactions on Antennas and Propagation,* vol. 59, no. 7, pp. 2524-2531, July 2011.

[49] H. Luyen, J. H. Booske and N. Behdad, "2-Bit Phase Quantization Using Mixed Polarization-Rotation/Non-Polarization- Rotation Reflection Modes for Beam-Steerable Reflectarrays," *IEEE Transactions on Antennas and Propagation,* vol. 68, no. 12, pp. 7937-7946, December 2020.

[50] N. Pucci-Barbeau, "AUTOMATISATION D'ANTENNE RÉSEAU-RÉFLECTEUR RECONFIGURABLE," Montreal, 2017.

[51] C. Tienda, M. Arrebola, J.A. Encinar, G. Toso, "Analysis of a dual-reflectarray antenna," *IET Microwaves, Antennas & Propagation,* vol. 5, no. 13, p. 1636–1645, 21 October 2011.

[52] J. L. MM Dehnavi, "Beam scanning dual reflector antenna with a circularly polarized reconfigurable reflectarray as subreflector," in *70th Int. Astron, Cong. (IAC 2019),* Washington, DC, 2019.

[53] Stutzman, Warren L., and Gary A, Antenna theory and design, John Wiley & Sons, 2012.

[54] Rudge, A. W., Adatia, N. A, "Offset-parabolic-reflector antennas: A review," in *Proceedings of the IEEE*, 1978.

[55] D. -. Duan and Y. Rahmat-Samii, "Beam squint determination in conic-section reflector antennas with circularly polarized feeds," *IEEE Transactions on Antennas and Propagation,* vol. 39, no. 5, pp. 612-619, May 1991.

[56] S. Xu and Y. Rahmat-Sami, "A Novel Beam Squint Compensation Technique for Circularly Polarized Conic-Section Reflector Antennas," *IEEE Transactions on Antennas and Propagation*, vol. 58, no. 2, pp. 307-317, Feb 2010.

[57] M. M. Dehnavi and J. Laurin, "Near Field Focusing using a Circularly Polarized Reconfigurable Reflectarray," in *2019 IEEE International Symposium on Antennas and Propagation and USNC-URSI Radio Science Meeting*, Atlanta, 2019.

[58] Nepa, P., Buffi, A., Michel, A, "Technologies for near-field focused microwave antennas," *International Journal of Antennas and Propagation,* March 2017.

[59] P. Nepa and A. Buf, "Near-field focused microwave antennas," *IEEE Antennas and Propagation Magazine,* vol. 59, 2017.

[60] P. Nepa, "Near-Field Focused Antennas for Wireless Communications and Power Transfer," MRL (Microwave Radiation Laboratory), Pisa, Italy, 2016.

[61] Nepa, Paolo, Alice Buffi, "Near-field-focused microwave antennas: Near-field shaping and implementation," *IEEE Antennas and Propagation Magazine,* vol. 59, no. 3, pp. 42-53, April 2017.

[62] S. Clauzier, E. Rochefort, S. Avrillon, L. Le Coq, M. Himdi and F. Colombel, "A loaded sectoral horn antenna using near-field focusing technique," in *2013 European Microwave Conference*, Nuremberg, 2013.

[63] Buffi, A., Paolo Nepa, and Giuliano Manara, "Design criteria for near-field-focused planar arrays," *IEEE Antennas and Propagation Magazine,* vol. 54, no. 1, pp. 40-50, 2012.

[64] N. G. Sunkurh, "ITSO - Basics of Satellite Communications," ITSO, 2017.

[65] J. Budhu and Y. Rahmat-Samii, "Understanding the appearance of specular reflection in offset fed reflectarray antennas," in *2011 IEEE International Symposium on Antennas and Propagation (APSURSI)*, Pokane, 2011.

[66] R. El hani and J. Laurin, "Specular Reflection Analysis for Off-Specular Reflectarray Antennas," *in IEEE Transactions on Antennas and Propagation,* vol. 61, no. 7, pp. 3575-3581, July 2013.

[67] Dinh Le Doan, B.E (Hons.I), "DUAL REFLECTOR ANTENNAS : A STUDY OF FOCAL FIELD AND EFFICIENCY," 1997.

[68] John A R Legon, "Calculation of the focal length of an offset satellite dish antenna," 2006.

[69] G. Ihninger, "76.032 GHz transverter," OE2IGL, Salzburg, 2018.

[70] T. B. Chen, Y. B. Chen, Y. C. Jiao and E. S. Zhang, "Synthesis of antenna array using particle swarm optimization," in *2005 Asia-Pacific Microwave Conference Proceedings*, Suzhou, 2005.

[71] Hsu, C. H., Chen, C. H., Shyr, W. J., Kuo, K. H., Chung, Y. N., & Lin, T. C., "Optimizing beam pattern of linear adaptive phase array antenna based on particle swarm optimization," in *2010 Fourth International Conference on Genetic and Evolutionary Computing*, Shenzhen, 2010.

[72] Y. Rahmat-Samii, D. Gies and J. Robinson, "Particle swarm optimization (PSO): A novel paradigm for antenna designs," vol. 2003, no. 306, pp. 14-22, 2003.

[73] M. H. Dahri, M. H. Jamaluddin, M. I. Abbasi and M. R. Kamarudin, "A review of wideband reflectarray antennas for 5G communication systems," vol. 5, pp. 17803-17815, 2017.

[74] T. Tomura, M. Takikawa, Y. Inasawa and H. Miyashita, "Trade-off of multibeam reflector antenna configuration for satellite onboard application," in *2016 URSI Asia-Pacific Radio Science Conference (URSI AP-RASC)*, 2016.

[75] Comisso, Massimiliano, Gabriele Palese, Fulvio Babich, Francesca Vatta, and Giulia Buttazzoni, "3D multi-beam and null synthesis by phase-only control for 5G antenna arrays," *Electronics*, vol. 8, no. 6, p. 656, 2019.

[76] K. Quzwain, Y. Yamada, K. Kamardin, N. H. A. Rahman and T. A. Rahman, "Design of Shaped Offset Dual-Reflector Antenna for 5G Mobile Base Station," in *018 IEEE International RF and Microwave Conference (RFM)*, 2018.

[77] Y. Yamada, K. Quzwain, F. Ansarudin, K. Kamardin and N. H. Abd Rahman, "Aperture Antennas for 5G Mobile Base Stations," in *2019 IEEE Asia-Pacific Conference on Applied Electromagnetics (APACE)*, 2019.

[78] "sparkfun Start Smoothing," sparkfun, 8 July 2013. [Online]. Available: https://learn.sparkfun.com/tutorials/i2c/all.

APPENDIX A DIMENSIONS OF THE SEPTUM POLARIZER

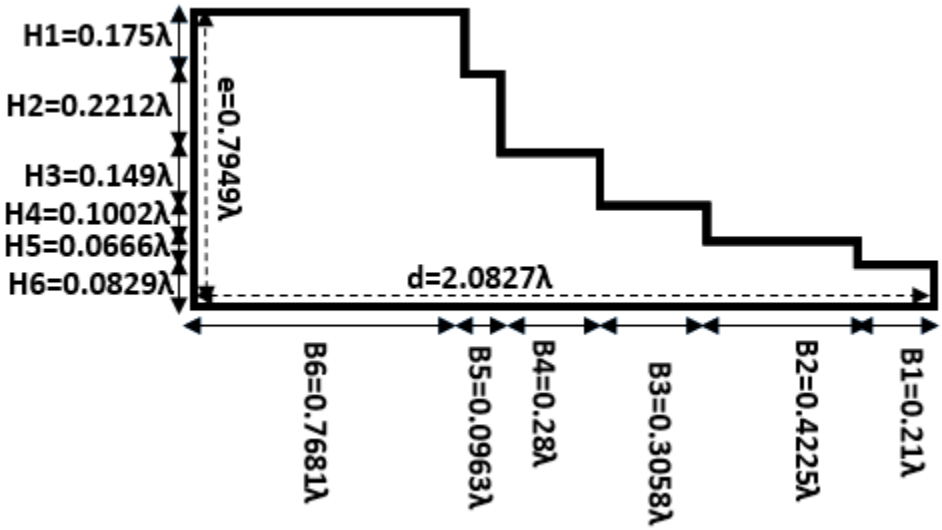

Figure A.1 The dimensions of the septum polarizer

The thickness of the septum is 0.0043λ ($\lambda = 42.8\text{mm}$)

APPENDIX B DIMENSIONS OF THE FEED HORN

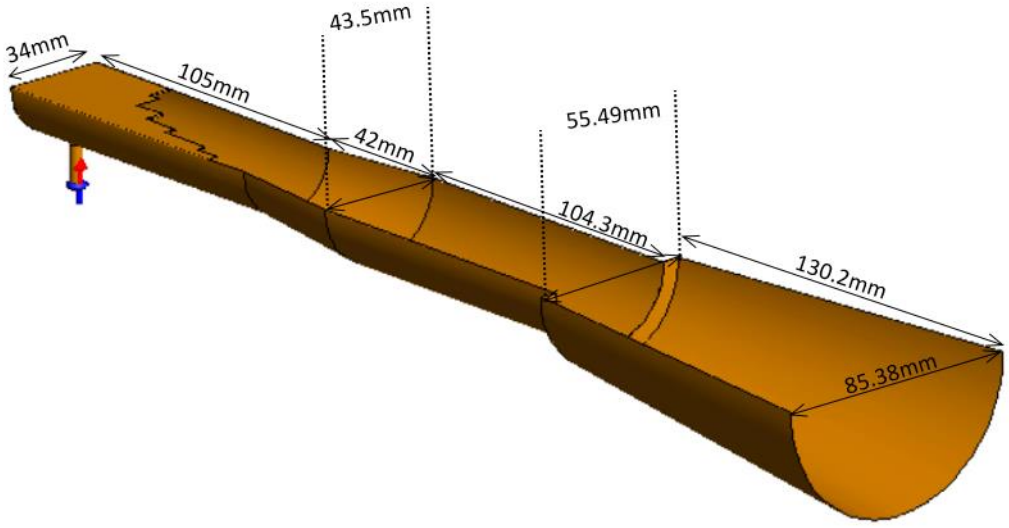

Figure B.1 Dimensions of the feed horn

APPENDIX C SPHERICAL MODE EXPANSION

The antenna far-field can be express in terms of spherical modes. The electric and magnetic fields can be express as the sum of orthogonal spherical modes in spherical coordinate system [44, 45]

$$\boldsymbol{E}(r,\theta,\varphi) = k\sqrt{\eta}\sum_{c=3}^{4}\sum_{s=1}^{2}\sum_{m=-n}^{n}\sum_{n=1}^{\infty} Q_{smn}^{(c)}\, \boldsymbol{F}_{smn}^{(c)}(r,\theta,\varphi) \tag{C.1}$$

$$\boldsymbol{H}(r,\theta,\varphi) = j\frac{k}{\sqrt{\eta}}\sum_{c=3}^{4}\sum_{s=1}^{2}\sum_{m=-n}^{n}\sum_{n=1}^{\infty} Q_{smn}^{(c)}\, \boldsymbol{F}_{3\text{-}s,m,n}^{(c)}(r,\theta,\varphi) \tag{C.2}$$

The field is characterized by the Q_{smn}, the modal coefficient, to the, the spherical wave functions $\boldsymbol{F}_{smn}$. *s*, *m* and n are the mode indices with *s*=1 indicating the TE-modes and *s*=2 the TM-modes; c represents the propagation direction: *c*=3 is inward while *c*=4 is outward. *k* is the propagation constant and η is the wave impedance of the propagation medium.

APPENDIX D AUTOMATION OF RECONFIGURABLE NETWORK ANTENNA

UNIVERSITÉ DE MONTRÉAL

AUTOMATISATION D'ANTENNE RÉSEAU-RÉFLECTEUR RECONFIGURABLE

RAPPORT DE STAGE

NICOLAS PUCCI-BARBEAU
DÉPARTEMENT DE GÉNIE ÉLECTRIQUE
ÉCOLE POLYTECHNIQUE DE MONTRÉAL

Table des matières

D.1 Design mécanique

D.1.1 Choix des moteurs :

Afin de répondre à la demande de précision et de mouvement angulaire, l'approche privilégiée est celle du servo-moteur. Celui-ci est présente certains avantages dans les circonstances précise de ce projet comparé à un moteur pas-à-pas. En outre, le servo-moteur ne requière qu'un seul signal de contrôle, comparé aux trois signaux nécessaires pour un pas-à-pas. Cela permettra donc de faciliter le circuit et le programme nécessaire au fonctionnement du prototype.

Ainsi, le moteur choisi est le SER0039 de DFRobot. Le critère principal motivant le choix du moteur est la taille de celui-ci, car les éléments du réseau réflecteur sont très proche les uns des autres. Ainsi, ce moteur est le meilleur rapport qualité-prix-dimension.

D.1.2 Design du support :

Le support conçu et proposé dans le cadre de ce stage répond aux différentes contraintes du projet. Il est réalisé par impression 3D afin de faciliter l'évolution du prototype et la rapidité de fabrication. Ici-bas est présenté le modèle du support. Cette architecture est choisie afin de respecter l'écart demandé entre les éléments variable. Le choix d'une structure en escalier est la solution trouvée afin de respecter l'espacement entre les éléments réflecteur du réseau, tout en utilisant des moteurs bons marchés. Une solution plus simple serait possible si des moteurs plus petits étaient utilisés. Par contre, l'achat de moteur plus cher n'était pas nécessaire à cette étape du projet.

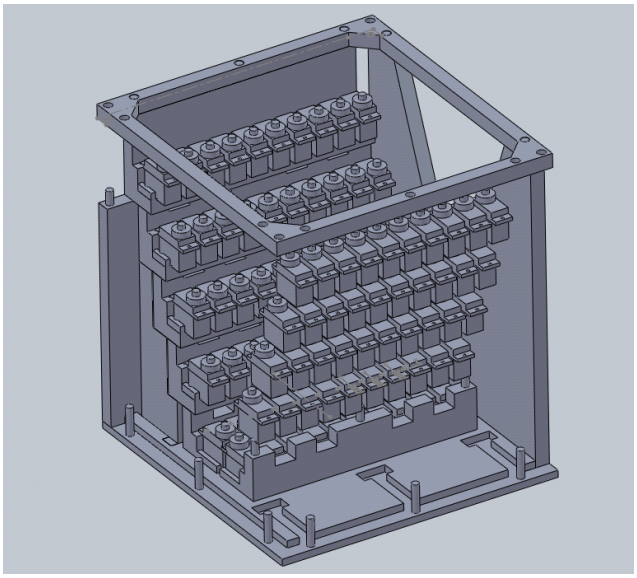

Figure D. 1 Modèle 3D du support

D.2 Design électrique

D.2.1 Choix du microcontrôleur :

Le microcontrôleur choisi est le Atmega328P monté sur un Arduino. Ce format a l'avantage d'être simple et très répandu, ce qui en facilitera la programmation dû à l'abondance de bibliothèques existantes. De plus, ce microcontrôleur est assez puissant pour l'utilisation qui est prévue dans ce contexte et est disponible à bas prix. Le modèle exact est l'Elegoo Uno R3.

D.2.2 Contrôle des moteurs :

Puisque le microcontrôleur ne possède pas assez de sortie physique pour connecter 100 moteurs, le design fera appelle au PCA9685, un driver de DEL pouvant être utilisé afin de contrôler des servomoteurs. Ce driver utilise la communication par protocole I^2C, ce qui permet de de n'utiliser que 2 sorties du microcontrôleur afin de contrôler l'ensemble des drivers nécessaires. Ce modèle de driver permet de contrôler 16 moteurs par carte et ils peuvent prendre des adresses allant de 100 0000 à 111 1101. Il est donc possible d'avoir jusqu'à 62 cartes différentes sur le même bus de communication.

Il est possible d'ajuster plusieurs paramètres de fonctionnement de ce contrôleur, comme la fréquence du signal de sortie, la valeur de chaque sortie et le moment d'application d'un changement sur la sortie. Afin d'assurer le fonctionnement du prototype, la fréquence de sortie est fixée à 50Hz et l'application du changement est lors de la condition d'arrêt (voir section I^2C).

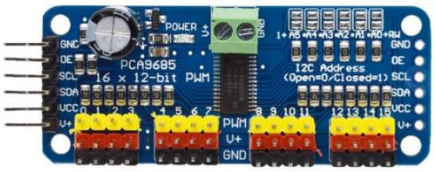

Figure D. 2 PCA9685

D.2.3 I^2C

L'I2C est un protocole de communication entre maitres et esclaves. Il est réalisé par la connexion de 2 canaux entre chaque membre du réseau; le premier canal est le SDL (serial data line) et le second est le SCL (serial clock line). Le fonctionnement de ce protocole est simple, Le maitre génère en signal d'horloge qu'il propage sur le SCL. Lorsqu'il veut parler, le maitre émet une condition de départ sur le SDL et annonce l'adresse de l'esclave ciblé. Les échanges se font sur 8 bits plus un bit de ACK. Voici un schéma simple du protocole.

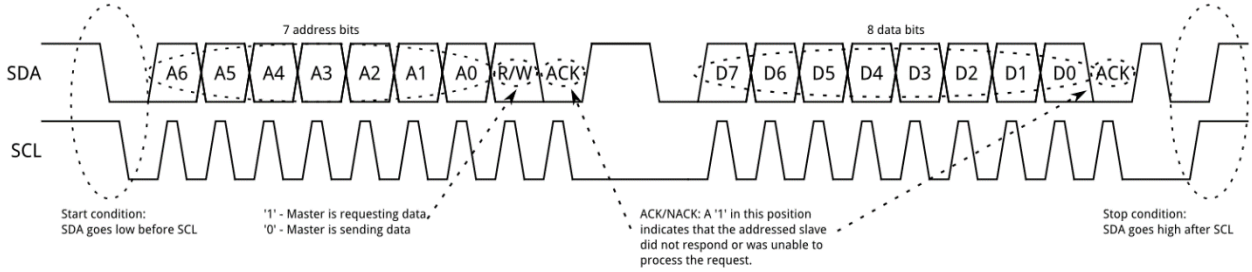

Figure D. 3 Fonctionnement du bus I^2C [78]

L’utilisation de ce protocole permettra l’utilisation d’adressage numérique afin de pouvoir communiquer avec chaque moteur individuellement. Cette implémentation est plus efficace que l’utilisation de multiplexeur analogique, car le circuit physique est grandement simplifié, au prix d’un script de contrôle plus complexe. Par contre, étant donnée l’utilisation d’un microcontrôleur grand public, ce protocole de communication est déjà disponible dans la librairie Wire. Ainsi, le circuit électronique est simplifié et la programmation supplémentaire est déjà réalisée.

D.2.4 Schéma global :

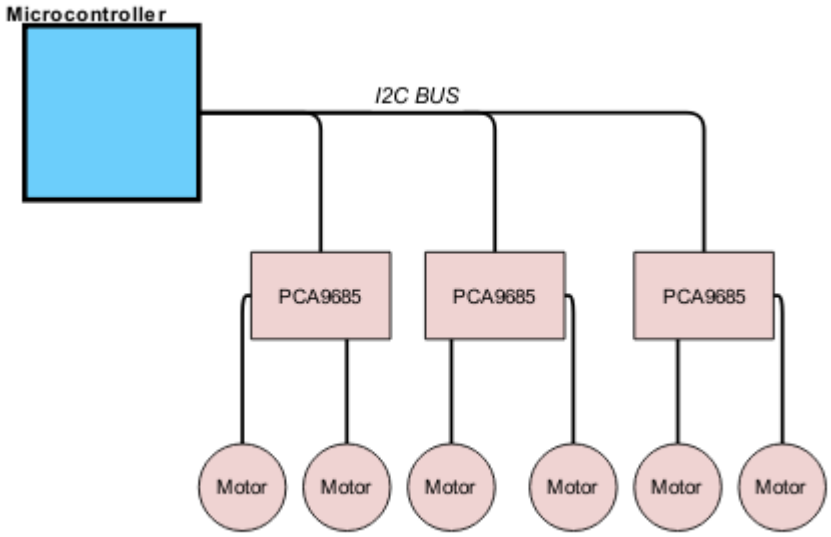

Figure D. 4 Schéma global